



HAL
open science

3D elastic full waveform inversion for subsurface characterization. Study of a shallow seismic multicomponent field data

Theodosius Marwan Irnaka

► **To cite this version:**

Theodosius Marwan Irnaka. 3D elastic full waveform inversion for subsurface characterization. Study of a shallow seismic multicomponent field data. Earth Sciences. Université Grenoble Alpes [2020-..], 2021. English. NNT: 2021GRALU004 . tel-03202027

HAL Id: tel-03202027

<https://theses.hal.science/tel-03202027>

Submitted on 19 Apr 2021

HAL is a multi-disciplinary open access archive for the deposit and dissemination of scientific research documents, whether they are published or not. The documents may come from teaching and research institutions in France or abroad, or from public or private research centers.

L'archive ouverte pluridisciplinaire **HAL**, est destinée au dépôt et à la diffusion de documents scientifiques de niveau recherche, publiés ou non, émanant des établissements d'enseignement et de recherche français ou étrangers, des laboratoires publics ou privés.

THÈSE

Pour obtenir le grade de

DOCTEUR DE L'UNIVERSITÉ GRENOBLE ALPES

Spécialité : **Sciences de la Terre et de l'Univers et de l'Environnement
(CESTUE)**

Arrêté ministériel : 25 Mai 2016

Présentée par

Theodosius Marwan Irnaka

Thèse dirigée par **Romain Brossier**
et codirigée par **Ludovic Métivier**

préparée au sein du **Laboratoire Institut des Sciences de la Terre**
dans l'**École doctorale Terre, Univers, Environnement**

3D elastic full waveform inversion for subsurface characterization

Study of a shallow seismic multicomponent
field data

Thèse soutenue publiquement le **23 Février 2021**,
devant le jury composé de :

Donatienne Leparoux

Directrice de Recherche Université Gustave Eiffel, Rapporteur

Hansruedi Maurer

Prof. Ecole polytechnique fédérale de Zurich, Rapporteur

Stéphane Garambois

Prof. Université Grenoble Alpes, Président

Daniel Köhn

Christian Albrecht Universität zu Kiel, Examineur

Thomas Bohlen

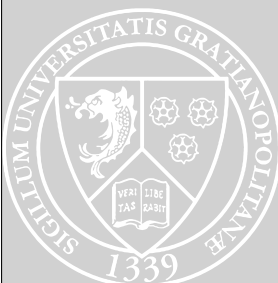
Prof. Karlsruhe Institut für Technologie, Examineur

Romain Brossier

Maître de Conférences Université Grenoble Alpes, Directeur de thèse

Ludovic Métivier

Chargé de Recherche CNRS Université Grenoble Alpes, Co-directeur de thèse



Acknowledgments

There is no destination without a journey, and there are many who helped me along the way on this journey. I want to take a brief moment to acknowledge and thank them properly. Without them, there will not be any story to be told.

First, I would like to express my sincere gratitude to both of my advisor, Romain Brossier and Ludovic Métivier, for the continuous support of my Ph.D. study and related research, for their patience, motivation, ideas, and immense knowledge. Their guidance helped me in all the time of my research and writing of this thesis. I could not have imagined having better advisors and mentors for my Ph.D study. I wish to thank the members of thesis committee: Daniel Köhn, Donatienne Leparoux, Hansruedi Maurer, Stéphane Garambois, and Thomas Bohlen for generously offering their time, support, guidance and good will throughout the review and the public defense of my Ph.D.

I am deeply grateful to the SEISCOPE consortium and its sponsors AKERBP, CGG, CHEVRON, EQUINOR, EXXON-MOBIL, JGI, PETROBRAS, SCHLUMBERGER, SHELL, SINOPEC, SIS-PROBE, and TOTAL, for the funding opportunity to undertake my studies at École doctorale Terre, Univers, Environnement (TUE) Université Grenoble Alpes. I am also profoundly grateful to the Wave Phenomena consortium, especially for Prof. Thomas Bohlen and his team from Karlsruhe Institute of Technology (KIT) for the opportunity to have a collaborative seismic data acquisition, processing, as well as many fruitful discussion during my studies.

I would like to offer my special thanks to Prof. Jean Virieux, Pengliang Yang, and Yudi Pan. They become my mentor and give insightful comments, discussions, and suggestions. I would like to express my appreciation to Tilman Steinweg and Svenja Schaneng for collaborating as a student, field engineer, and friend during the seismic data acquisition.

I will not forget the dynamic of my office mates, Arnaud Pladys, Julien Thurin, Phuong-Thu Trinh, and Sylvain Fiolleau. Thank you for giving me a comfortable research atmosphere, providing many random discussions during the past four years. Thank you for giving me support and motivation during my downtime.

I am really grateful to be a part of SEISCOPE, more than a consortium, but a family, especially for Alizia Tarayoun, Andrzej Górszczyk, Giuseppe Provenzano, Hugo Samuel Sanchez Reyes, Jet-Hoe Tang, Jian Cao, Laure Tavard, Longfei Gao, Nishant Kamath, Peng Yong, Philippe Le Bouiteiller, Sandrine Nadau, Serge Sambolian, Wei Zhou, Weiguang He, Yang Li, and Yubing Li. I hope our path will cross a thousand times again in the future. Thank you, thank you for all my labmates, especially Marco Salcedo Arciniega, Yang Lu, Qing Yu.

From the bottom of my heart, I would like to give my thanks to Pradityo Adi Wicaksono, Dwiria Wahyuni, and Sonny Aribowo, and all members of PPI Grenoble for becoming a blind external reviewer of my manuscript and for all the activities. Some words of gratitude go to Prima Wira Kusuma

Wardhani, Donata Nariswari Wardani, Siti Fatimah, and Maria Rosalita Sudiby. They have always been actively engaged in small scientific and non-scientific discussions.

I am also very grateful to my family-like colleagues in the Geophysics sub-department, Universitas Gadjah Mada. They have allowed me to pursue this higher education. I hope my presence there in the future might bring benefits to all of us.

I thank my family, my parents and my parents in law for their love and support. *Terima kasih Bapak dan Ibu yang sudah mendukung anakmu ini untuk mengejar mimpi setinggi-tingginya, tanpa menuntut apapun. Terima kasih sudah membesarkan dan mendidiku tanpa pamrih, memberikan kesempatan yang seluas-luasnya dan motivasi yang tiada hentinya. Matur nuwun.*

Above all, I would like to thank my wife, Veronica Dwi Adityarini, for her love, constant support, and sacrifice. Thank you for being my soulmate, partner, friend, editor, proofreader, and shadow advisor. I owe you everything.

November 2020

Theodosius Marwan Iznaka

Abstract

Full Waveform Inversion (FWI) is an iterative data fitting procedure between the observed data and the synthetic data. The synthetic data is calculated by solving the wave equation. FWI aims at reconstructing the detailed information of the subsurface physical properties. FWI has been rapidly developed in the past decades, thanks to the increase of the computational capability and the development of the acquisition technology. FWI also has been applied in a broad scales including the global, lithospheric, crustal, and near surface scale.

In this manuscript, we investigate the inversion of a multicomponent source and receiver near-surface field dataset using a viscoelastic full waveform inversion algorithm for a shallow seismic target. The target is a trench line buried at approximately 1 m depth. We present the pre-processing of the data, including a matching filter correction to compensate for different source and receiver coupling conditions during the acquisition, as well as a dedicated multi-step workflow for the reconstruction of both P-wave and S-wave velocities. Our implementation is based on viscoelastic modeling using a spectral element discretization to accurately account for the wave propagation's complexity in this shallow region. We illustrate the inversion stability by starting from different initial models, either based on dispersion curve analysis or homogeneous models consistent with first arrivals. We recover similar results in both cases. We also illustrate the importance of taking into account the attenuation by comparing elastic and viscoelastic results. The 3D results make it possible to recover and locate precisely the trench line in terms of interpretation. They also exhibit another trench line structure, in a direction forming an angle at 45 degrees with the direction of the targeted trench line. This new structure had been previously interpreted as an artifact in former 2D inversion results. The archaeological interpretation of this new structure is still a matter of discussion.

We also perform three different experiments to study the effect of multicomponent data on this FWI application. The first experiment is a sensitivity kernel analysis of several wave packets (P-wave, S-wave, and surface wave) on a simple 3D model based on a Cartesian based direction of source and receiver. The second experiment is 3D elastic inversion based on synthetic (using cartesian direction's source) and field data (using Galperin source) with various component combinations. Sixteen component combinations are analyzed for each case. In the third experiment, we perform the acquisition's decimation based on the second experiment. We demonstrate a significant benefit of multicomponent data FWI in terms of model and data misfit through those experiments. In a shallow seismic scale, the inversions with the horizontal components give a better depth reconstruction. Based on the acquisition's decimation, inversion using heavily decimated 9C seismic data still produce similar results compared to the inversion using 1C seismic of a dense acquisition.

Résumé

L'inversion de forme d'onde complète (FWI) est une procédure d'ajustement itératif des données entre les données observées et les données synthétiques. Les données synthétiques sont calculées en résolvant une équation d'onde. La FWI vise à reconstruire les informations détaillées des propriétés physiques du sous-sol. La méthode FWI a été développée au cours des dernières décennies, grâce à l'augmentation de la capacité de calcul et au développement de la technologie d'acquisition. La FWI a également été appliquée à des échelles variées, allant de l'échelle globale, lithosphérique, crustale, jusqu'à la proche surface, c'est à dire quelques mètres de profondeur.

Dans ce manuscrit, nous étudions l'inversion d'un jeu de données de source et de récepteur multi-composantes en utilisant un algorithme d'inversion de forme d'onde complète viscoélastique pour une cible sismique peu profonde. La cible est une ligne de tranchée enterrée à environ 1 m de profondeur. Nous présentons le pré-traitement des données, y compris une correction par déconvolution pour compenser les différentes conditions de couplage de la source et du récepteur pendant l'acquisition, ainsi qu'un procédé d'inversion en plusieurs étapes pour la reconstruction des vitesses des ondes P et S. Notre mise en œuvre est basée sur une modélisation viscoélastique utilisant une discrétisation par éléments spectraux pour rendre compte avec précision de la complexité de la propagation des ondes dans cette région peu profonde. Nous illustrons la stabilité de l'inversion en partant de différents modèles initiaux, soit basés sur l'analyse des courbes de dispersion, soit des modèles homogènes cohérents avec les premières arrivées. Nous obtenons des résultats similaires dans les deux cas. Nous illustrons également l'importance de la prise en compte de l'atténuation en comparant les résultats élastiques et viscoélastiques. Les résultats 3D permettent de localiser précisément la ligne de tranchée en termes d'interprétation. Ils montrent également une autre structure de ligne de tranchée, dans une direction formant un angle de 45 degrés avec la direction de la ligne de tranchée ciblée. Cette nouvelle structure avait été précédemment interprétée comme un artefact dans les anciens résultats d'inversion 2D. L'interprétation archéologique de cette nouvelle structure est actuellement en discussion.

Nous réalisons également trois expériences différentes pour comprendre l'effet des données à composantes multiples sur la FWI. La première expérience est une analyse de sensibilité de plusieurs paquets d'ondes (onde P, onde S et onde de surface) sur un modèle 3D simple basé sur une direction cartésienne de la source et du récepteur. La seconde expérience est une inversion élastique 3D basée sur des données synthétiques (utilisant la source de direction cartésienne) et de champ (utilisant la source Galperin) avec diverses combinaisons de composantes. Seize combinaisons de composantes sont analysées pour chaque cas. Dans la troisième expérience, nous effectuons la décimation de l'acquisition sur la base de la deuxième expérience. Nous démontrons un avantage significatif des données multi-composantes FWI grâce à ces expériences. Dans une échelle sismique peu profonde, les inversions avec les composantes horizontales donnent une meilleure reconstruction en profondeur. En se basant sur la décimation de l'acquisition, l'inversion utilisant des données sismiques 9C fortement décimées produit des résultats similaires à l'inversion utilisant des données sismiques 1C sur l'acquisition complète.

Contents

General Introduction	1
Seismic imaging	1
Near surface full waveform inversion	6
Multicomponent seismic data	7
Problematics	10
Outlines of the manuscript	11
1 Viscoelastic wave simulation and Full Waveform Inversion	13
1.1 Elastodynamics equation	15
1.1.1 Elastic modeling	16
1.1.2 Viscoelastic modeling	16
1.2 Discretization of the viscoelastic wave equation using Spectral Element Method	19
1.2.1 Mapping the reference to the physical space	20
1.2.2 Integration points and Gauss-Lobatto-Legendre (GLL) quadrature	21
1.2.3 Global system of the weak formulation	22
1.3 Full waveform inversion	24
1.3.1 Solving the constrained local minimization problem	25
1.3.2 Preconditioning application	30
1.4 Implementation: SEM46 code	30
2 The Ettlingen Line and 9C seismic data	33
2.1 The Ettlingen Line	35
2.2 Previous geophysical investigations	38
2.3 3D 9C Seismic Acquisition	40
2.3.1 Motivation	40
2.3.2 Data acquisition	40
2.4 Pre-processing and data correction	44
2.4.1 Data evaluation	44
2.4.2 Data correction using matching filter	44
3 3D 9C elastic Full Waveform Inversion Application	49
3.1 Introduction	53
3.2 Data Acquisition and Pre-processing	56
3.2.1 Target	56
3.2.2 Acquisition	57
3.2.3 Data evaluation	58

CONTENTS

3.2.4	Data correction using matching filter	58
3.3	Full Waveform Inversion methodology	60
3.3.1	Modeling of elastic and viscoelastic waves	60
3.3.2	Inverse problem	62
3.3.3	Implementation: SEM46 code	65
3.4	Application	66
3.4.1	Initial model building	66
3.4.2	Source estimation	66
3.4.3	Multi-scale strategy	67
3.4.4	Model reconstruction	67
3.4.5	Quality control: data fit	69
3.5	Discussion and interpretation	72
3.5.1	Model interpretation	72
3.5.2	Is it reasonable to start from a homogeneous model?	74
3.5.3	Elastic or viscoelastic FWI?	74
3.5.4	Other limitations and prospects	76
3.6	Conclusions	79
3.A	Parameter binding FWI	80
3.B	Non-linear model constraints FWI	80
3.C	Source estimation	81
3.D	Computational cost	82
4	Analysis of the use of multicomponent sources and receivers in the frame of shallow seismic Full Waveform Inversion	85
4.1	Introduction	89
4.2	Full Waveform Inversion	91
4.2.1	Elastic wave modeling	91
4.2.2	Inverse problem	91
4.2.3	SEM46 code	92
4.3	Sensitivity kernel investigation on multicomponent data	92
4.3.1	Sensitivity kernel	92
4.3.2	Synthetic model and experiment setup	93
4.3.3	Results	95
4.4	Application of multicomponent Full Waveform Inversion	98
4.4.1	Experiment setup	98
4.4.2	Assessment methods	103
4.4.3	Results	106
4.5	Acquisition's decimation	114
4.5.1	Source's and receiver's decimation setup	114
4.5.2	Results	114
4.6	Conclusions	121
5	The source subsampling and encoding toolbox	123
5.1	Introduction	125
5.2	Theory	126
5.2.1	Source encoding	126
5.2.2	Subsampling on sources	127

5.2.3	Code implementation	128
5.3	Application on the Ettlingen Line data	131
5.3.1	Parameter setup	131
5.3.2	Results	137
5.4	Conclusions	140
5.A	Computational time tables	141
Conclusions and prospects		145
	Conclusions	145
	Prospects	147
List of Figures		149
References		157

General Introduction

Seismic imaging

Geophysical imaging is a set of non-invasive techniques to investigate the subsurface properties of the Earth. It can be carried out by detecting a measurable physical quantity from the observable location, e.g., from the surface, airborne, or satellite. Different measured physical quantity leads to a different geophysical method (Parasnis, 1962; Telford et al., 1990).

Several examples of popular geophysics methods are gravity, magnetic, and seismic methods. We are not going to discuss the detail of the gravity and magnetic methods. However, measuring gravity force at a specific area may give us the knowledge about the subsurface's mass and density distribution (LaFehr, 1980; Li and Oldenburg, 1998). Earth's magnetic field measurement may help us to differentiate different types of rocks based on the ability to produce an induced magnetic field from the main Earth's magnetic field (Reford, 1980; Nabighian et al., 2005). On the other hand, the seismic method studies the mechanical waves' interaction that propagates through a medium. A mechanical wave itself is defined as the oscillation of matter that transfers energy through a medium. With a very small strain, the medium's oscillation behaves elastically; therefore, it does not create a permanent deformation. Seismic method is interesting because the seismic waves is one of the 'geophysical wave' that have the shortest wavelength which can be detected accurately compared to the other geophysical methods (Lay and Wallace, 1995). This fact implies the high-resolution potential of the seismic method.

The early development of the seismic method is based on interpreting the recorded waves coming from earthquakes. At the end of 19th and the beginning of 20th century, the number of equipment and recording technology were still limited. Nevertheless, the seismic wave analysis helped the early geoscientist prefiguring the first global structure of the Earth (Romanowicz and Dziewonski, 2010). The analysis they performed at that time were based on the comparison of seismic wave travel times and the identification of particular waves. Notable discoveries encompass the discontinuity between the Earth's crust and the mantle by Mohorovicic discontinuity (a transition zone that is now known as Moho) (Mohorovicic, 1909; Jarchow and Thompson, 1989), and the liquid structure of the Earth's outer core, detected through the absence of recorded shear waves, typical propagation's type in a fluid medium (Oldham, 1906). Figure 1 shows the simplified model of the Earth and its particular body wave's raypath.

The knowledge of the seismic wave's type is a key to understand the seismic method. A sample of an earthquake recording is given in Figure 2. This figure shows three seismograms on an earthquake recording with the magnitude of 6.4 and angular distance of 88.7°. The seismograms consist of the ground velocities in three orthogonal directions, with the horizontal directions rotated to the longitudinal and transverse components. The longitudinal component is the component pointing to the direction of the earthquake, whereas the transverse component is the one that is perpendicular with the longitudinal

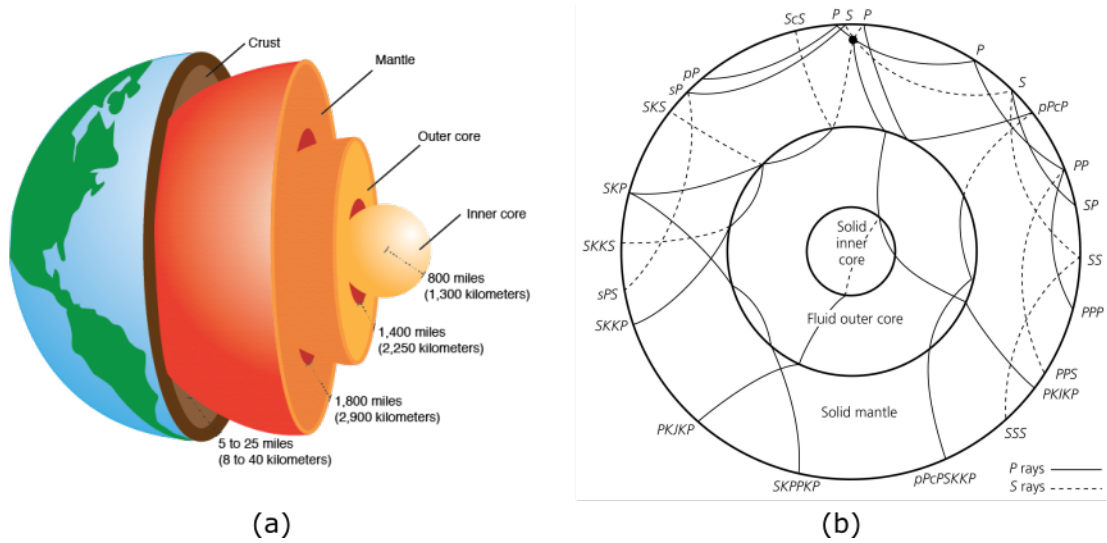


Figure 1: The simplified illustration of the 3D internal structure of the Earth as a layered model (a). The simplified 2D section structure of the Earth and the examples of the body wave's seismic phases (b). The names of the raypath is given by the wave type, the propagated layer, and the interaction with the discontinuities (Stein and Wysession, 2003).

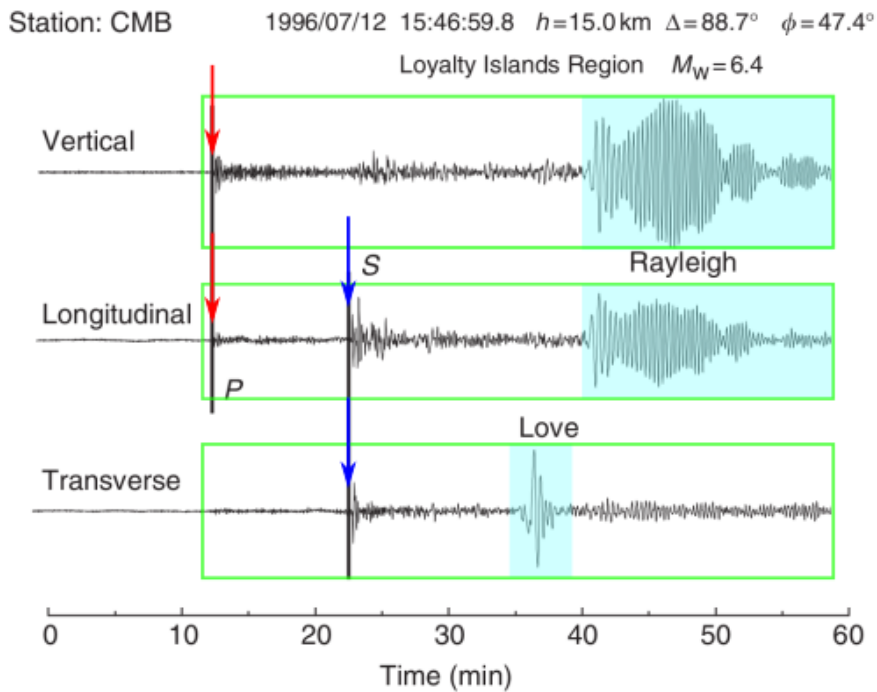


Figure 2: Example on an earthquake recorded using a multicomponent seismometer (Lee et al., 2002). The horizontal component is rotated to the longitudinal and transverse direction with respect to the earthquake. Red arrows indicate the first arrival of the P-wave. Blue arrows indicate the first arrival of S-wave. Cyan blocks represent the surface waves. Green blocks represent the windows data for full waveform inversion (FWI). Note that in FWI, all parts of the dataset are taken into account.

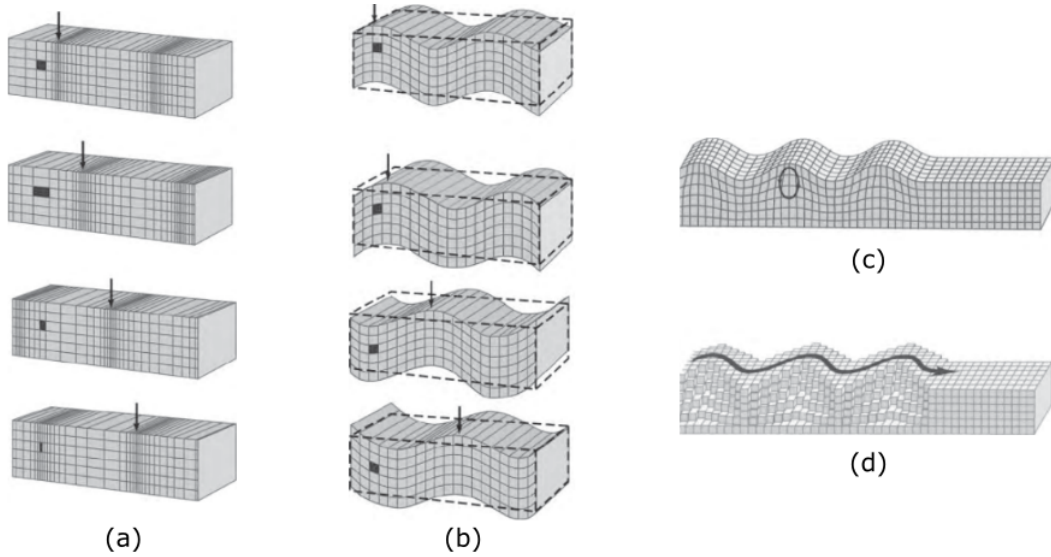


Figure 3: Particle motion of P-wave (a), S_V -wave (b), Rayleigh wave (c), and Love Wave (d). The direction of the propagation is from the left to the right of the model. The S-wave is consist of two different polarizations S_V and S_H -waves. In this illustration, only S_V -wave is given. After Everett (2013).

component. This figure shows two main body waves (P and S waves) and two surface waves (Rayleigh and Love waves). P-waves are visible from the vertical and longitudinal components (red arrows). S-waves are visible from the longitudinal and transverse components (blue arrows). The two different types of the surface waves are well-separated. Due to the direction of its propagation, the Rayleigh waves can be seen in the vertical and longitudinal components, whereas the Love wave can be seen in the transverse component (both are shown as cyan blocks). The distinction between body and surface waves as well as the illustration of each of the above mentioned propagation modes are given in Figure 3.

Full waveform inversion (FWI) is a seismic method that take advantage of the whole information of the recorded data (Virieux and Operto, 2009). It is a high-resolution seismic imaging with the potential resolution up to half of the propagated wavelength, according to the diffraction theory's limit (Wu and Toksöz, 1987). It was designed in the 1980s by Lailly (1983) and Tarantola (1984a). FWI may bridge the gap between a high wavenumber Claerbout (1971)'s migration imaging principle and a low wavenumber approach of the first arrival traveltome tomography (FATT) (Aki et al., 1974).

FWI is formulated as an iterative data fitting procedure between the observed seismograms with the corresponding synthetics, computed by solving the wave equation. In its early development, even 2D FWI was shown to be a computationally demanding problem, given by the available resources (Gauthier et al., 1986; Cary and Chapman, 1988; Crase et al., 1990; Jin et al., 1991; Lambaré et al., 1992). At that time, aside from the computational challenge, the data availability is also limited to short offset seismic reflection surveys which were not designed for FWI purposes. These problems have made the early FWI applications even more challenging and required more accurate initial models. In recent years, we observe rapid methodology developments and applications of FWI, thanks to the availability of the wide-angle and broadband frequency seismic acquisition devices, as well as the high-performance computing (HPC) platform development.

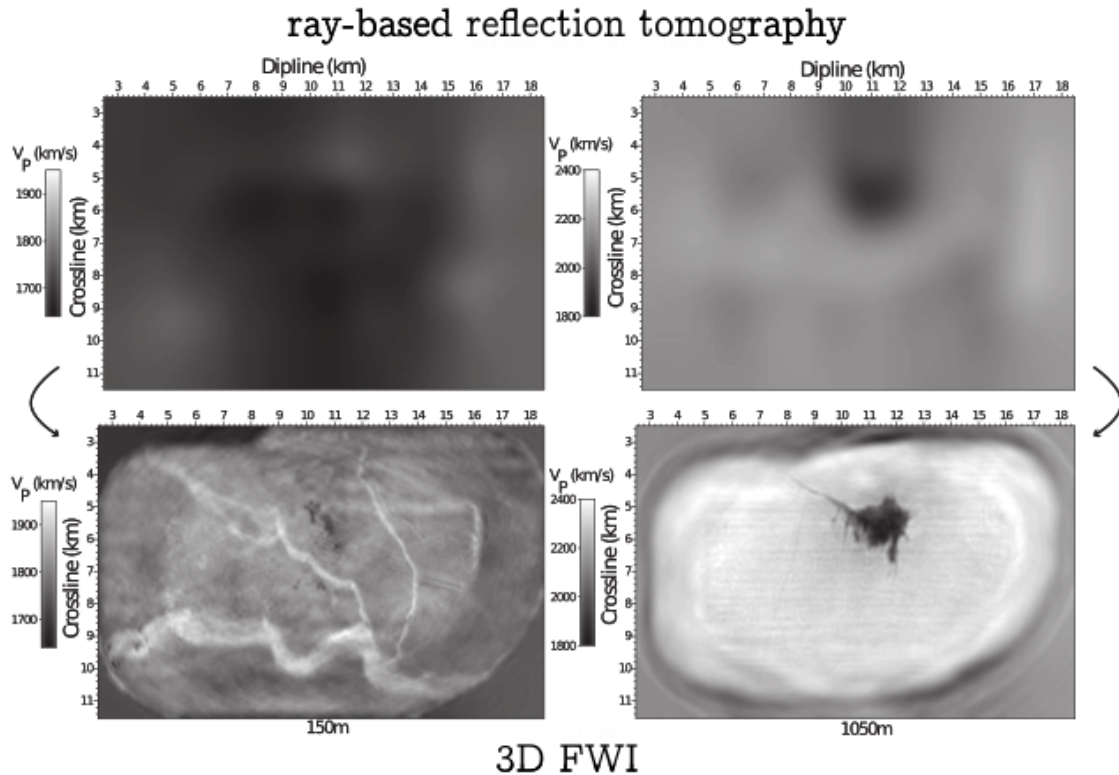


Figure 4: Example of 3D acoustic FWI from (Operto et al., 2015). Top figures represent the initial V_P models from the reflection tomography, bottom figures represent the final reconstructed V_P models using FWI. Left and right figures represent the horizontal sections at 150 m and 1050 m depth, respectively.

FWI has pioneered its first impressive applications at the exploration scale, especially for the oil and gas industry (Sirgue et al., 2010; Etienne et al., 2012; Prioux et al., 2013b; Vigh et al., 2014; Górszczyk et al., 2017; He et al., 2019b; Trinh et al., 2019a). The scale of the investigation on such size is few kilometers to tens of kilometers. One of the successful 3D FWI application examples for the exploration scale was carried out by Operto et al. (2015). They used an acoustic approximation for marine seismic data. The data was recorded using hydrophones, a pressure-sensitive receiver which only sensitive to the acoustic wave (P-wave). Figure 4 shows the initial V_P model (top) and the reconstructed V_P model (bottom) at two different depth slices, 150 m and 1050 m, respectively. The initial models are obtained from the reflection tomography. In the end, they were able to obtain a much higher resolution of the V_P model, as indicated by a clearer glacial sand channel deposits at 150 m depth slice and gas cloud at 1050 m depth slice.

In other cases, the elastic approximation is required because the acoustic approximation is not accurate to mimic the recorded data. The acoustic modeling is not able to simulate elastic wave features, such as the S-wave, the converted phase between P and S waves, and the surface waves. Those type of data are present when our recording apparatus is sensitive with the ground movement (displacement, velocity, or acceleration). In marine environment, Ocean Bottom Cable (OBC) and Ocean Bottom Seismometer (OBS) are used to record the elastic response of the seismic signal. The FWI itself can be performed by taking advantage on both hydrophone and OBS (Sears et al., 2008, 2010; Prioux et al., 2013b; Vigh et al., 2014). In land environment, the data acquisition is performed using geophones,

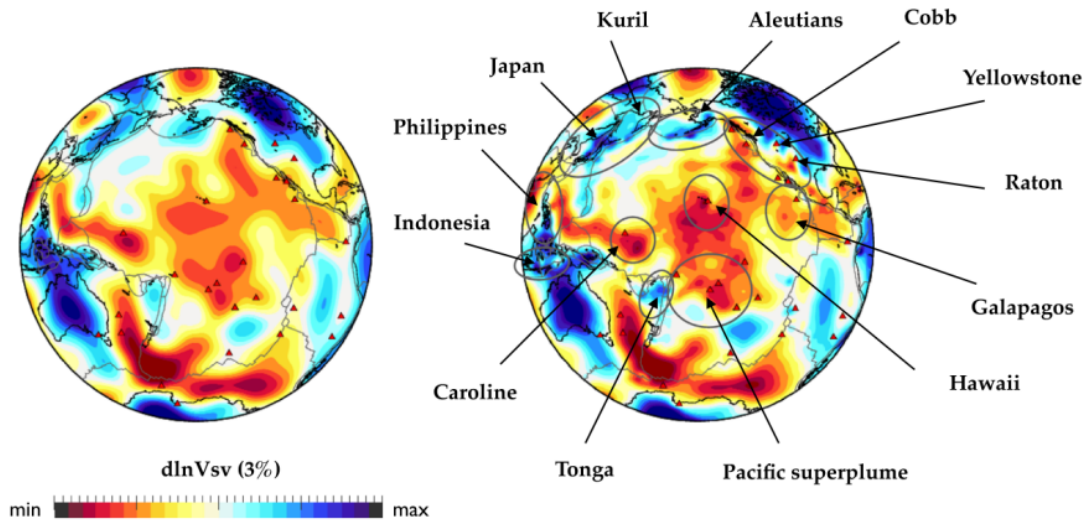


Figure 5: Example of global FWI showing the vertically polarized V_S perturbations in the initial mantle model S362ANI (left) and the reconstructed model using FWI - GLAD-M15 (right) at 250 km depth. Notable slabs and hotspots enhanced in the reconstructed model are marked. This image is taken from Bozdağ et al. (2016).

which also record the elastic response. The application of elastic FWI in land data, especially in complex topography, using synthetic data exist (Borisov et al., 2018, 2019; Trinh et al., 2018), but the application using field data is still limited (He et al., 2019b; Borisov et al., 2019; Trinh et al., 2019a).

Several FWI applications for lithospheric and global scales have also been performed for a decade (Tape et al., 2010; Beller et al., 2018; Fichtner et al., 2008; Bozdağ et al., 2016; Modrak and Tromp, 2016; Lu et al., 2020). In these scales, the artificial source is challenging to be feasibly deployed because one need a very high energy source that can propagate in a long distance. Alternatively, we can rely on the natural sources. Earthquakes and ambient noise are the two most common sources for the FWI application at this scale (Fichtner et al., 2008; Bozdağ et al., 2016; Beller et al., 2018; Lu et al., 2020). Using earthquakes as the sources of the FWI require an accurate definition of the source. In practice, an accurate estimation of such source is also challenging to be performed if the earthquake is too small or the network is not sufficiently large to cover the mechanism which limit the accessibility of the FWI using this approach. Yet, several researches are able to produce meaningful images from this limited information. Figure 5 shows an example of global FWI by Bozdağ et al. (2016). Through FWI, they were able to enhance the resolution of the reference model S362ANI. Several notable slabs and hotspots are remarked in the reconstructed model. Lu et al. (2020) carried out another application of FWI in a lithospheric scale. They performed FWI using the observed data which were taken from the cross-correlation technique of the ambient noise data. They called the method as the ambient noise wave-equation tomography. Their result is a 3D shear wave velocity model (V_S) of the Western Europe, especially around the Alps. They showed that the FWI are able to refine the shear wave velocity model which were obtained by a traditional ambient noise tomography based on surface wave dispersion curve analysis (Lu et al., 2018).

I have shown that FWI is now a mature seismic imaging technique, especially in the exploration scale. FWI also rapidly developed in global and lithospheric scale in the recent years. In the next section, we focus on the development of FWI in the near surface scale, which is the main interest of

this PhD thesis.

Near surface full waveform inversion

The near surface or shallow seismic scale spans from a few meters to several hundreds of meters. The application of seismic imaging in this scale is well-known for geotechnical applications (Kramer, 1996; Stokoe et al., 2000), ground characterization (Foti et al., 2003; Roberts and Asten, 2004; Chapman et al., 2006), infrastructure planning (Stewart et al., 1997; Martínez and Mendoza, 2011; Pegah and Liu, 2016), subsurface feature detection (Cardarelli et al., 2010), agriculture (Allred et al., 2008; Weil et al., 2012), archaeological studies (Wynn, 1986; Vafidis et al., 2003; Signanini and Torrese, 2004), and shallow-seismic hazard assessment (Göktürkler et al., 2008; Samyn et al., 2012). Despite of the broad applications of the seismic imaging in this scale, currently FWI is not the most popular seismic imaging method. Nevertheless, there are several FWI applications in shallow seismic scale and the FWI starts to gain more interest in the recent years (Smithyman et al., 2009; Romdhane et al., 2011; Bretaudeau et al., 2013a; Fathi et al., 2016; Köhn et al., 2018; Lamert and Friederich, 2019; Nguyen and Tran, 2018; Wittkamp et al., 2018; Smith et al., 2019; Pan et al., 2019; Wang et al., 2019).

The FWI application in shallow seismic scale has its advantages and disadvantages. The advantage is related to the frequency content of the data. In exploration scale, one of the critical difficulties is the lack of low frequency content leading to the problem of cycle skipping and local minima. In shallow seismic scale, the frequency content is sufficiently low compared with the scale of the target. This fact makes it possible to avoid this problems. The disadvantages are related to the acquisition and the propagated wave. In shallow seismic scale, the targets are often sparsely covered due to the few number of available sources and receivers. In academic or small geotechnical surveys, the equipment is limited due to the lack of material and financial capability compared to the oil and gas industry at the exploration scale. In most of shallow seismic applications, cheap 2D seismic profiles are used. In this case, 3D effects are neglected leading to an inaccurate reconstruction of the subsurface properties. At this scale, the signal to noise ratio is often low due to the weak seismic sources (sledgehammer, small vibroseis), the lack of repeatability of the source, and high variability of receiver-soil (source-soil) coupling. The second difficulty is due to the high complexity of the elastic wave propagation at the near-surface. The propagation of surface waves dominates the recorded data in amplitude by several order of magnitudes. With the limited offset (source-receiver distance), we might not be able to separate between the body waves and the surface waves. Aside from the elastic effects, the medium at shallow seismic scale is also known to have a strong attenuation effect.

The strong elastic effect and attenuation in the data require proper modeling and inversion tools. A modeling tool which is capable to perform an accurate elastic wave simulation is required. With the strong attenuation, viscoelastic modeling is also required, especially at high frequency, where the effect of the attenuation is more substantial. Since the elastic waves are influenced by more parameters than the acoustic waves, more parameters are needed to be reconstructed (V_P , V_S , and density for the elastic isotropic medium).

Figure 6 shows one example of a shallow seismic 2D FWI application for an archaeological target (Köhn et al., 2018). Starting from the initial model obtained from FATT and employing the LBL strategy (low-pass, band-pass, low-pass), they were able to reconstruct the detailed feature in the final model (Fig. 6b) which can be physically correlated with the archaeological investigation (Fig. 6a). LBL strategy is a strategy which consists of two L-workflow (low-pass filtered data) inversions and B-workflow (band-pass filtered data) inversion.

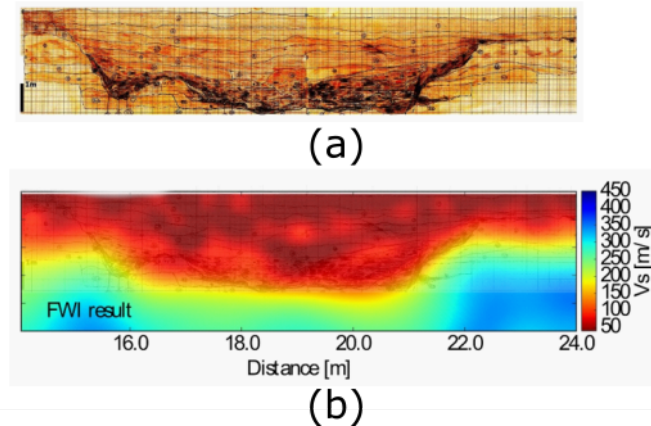


Figure 6: 2D FWI in shallow seismic experiment (Köhn et al., 2018).

Although FWI has been successfully applied to various targets, field data, and scales, it remains an ill-posed inverse problem. The issue regarding the partial illumination of the target and band-limited data sometimes leads to local minima convergence. In practice, the uncertainty attached to the reconstructed model can be significant. Besides the methodological developments that aim to mitigate the ill-posedness of FWI (modification of misfit function or introducing the domain extension strategies), access to more complete data that can constrain the inversion (such as multicomponent data) is also essential.

Multicomponent seismic data

Multicomponent receiver

The seismometer has a long development history starting from a visual seismoscope to the microelectromechanical systems (MEMS). The earliest known seismic instrument is the Zhang Heng seismoscope (Dewey and Byerly, 1969). It was built in 132 AD during the Han dynasty era. This instrument is aimed to detect the occurrence and the direction of the earthquake. It can detect the azimuth of the earthquake by releasing a ball from the dragons into the open mouth of the toads (Fig. 7). In Europe and Japan, the development of earthquake detecting instruments can be traced from eighteen to early nineteen centuries (Dewey and Byerly, 1969).

A component in the seismic recording device refers to the direction where the mechanical vibration is recorded. A single component (1C) seismometer only records the vibration in a single direction, resulting in a scalar recording. In comparison, a multicomponent seismometer refers to a multi directions recording. In this sense, the Zhang Heng seismoscope is a multicomponent seismic detector because it has multiple horizontal sensors, even if it lacks the vertical component and the ability to record the time series.

In an elastic medium, the seismic wavefield, which is propagated beneath the earth, is a vectorial field in 3D. Three orthogonal directions are sufficient to represent the 3D particle movement in that vectorial field. In fluid, which behaves as an acoustic media, 1C sensors are sufficient because the wavefield can be represented in a scalar valued pressure field. The hydrophone is an example of a popular 1C seismic recorder which is sensitive to pressure (Fig. 8). The hydrophone is used for seismic



Figure 7: The replica of Zhang Heng seismoscope featured in Chabot Space and Science center in Oakland, California (Wikipedia contributors, 2020b).



Figure 8: A sample of hydrophone, a pressure sensitive seismic recorder device. It is usually used in marine environment (Wikipedia contributors, 2020a).

applications in marine environments. In these environments, the recorders are located beneath the body of water (e.g. sea, lake, or river). Inside the water, pressure-sensitive sensors are sufficient because the seismic waves are propagated in the form of an acoustic wave.

The seismic vibration in the land environment is usually recorded by geophone. The geophone is sensitive towards the motion in a specific direction(s). Since the seismic wave in the land is a 3D vectorial field, recording using 1C geophones only extract one vectorial field projection in a specific direction. Despite that, taking into account 1C receiver is a common practice in seismic exploration (crustal-scale) or near-surface scale because it is cheap to build and deploy in the field. We may take an example of V_P reconstruction using the FATT method. One can use 1C vertical geophone (Fig. 9b) in order to obtain the first arrival of P-wave. Another example is V_S reconstruction using the multichannel analysis of the surface wave (MASW) method (Park et al., 1999). 1C horizontal geophone might be sufficient to capture the Love wave, given the source's correct direction.

In global scale seismology, especially the study of earthquake and its mechanism, multicomponent receivers are more common. One reason is that seismometers for earthquake recording purposes are sparsely installed; therefore, having a full vectorial recording is beneficial for earthquake analysis. Aside from the multicomponent factor, receivers used for earthquake recording have a lower eigenfrequency than the exploration or shallow seismic scale. It makes it possible to have a more accurate

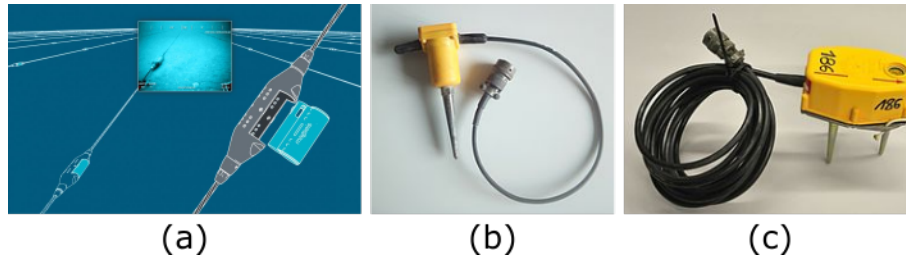


Figure 9: Ocean bottom cable (OBC), courtesy of Magseis (Duey, 2017) (a). 1C (b), and 3C geophone made by SENSOR Netherland (c) (GFZ, 2020).

recording at a longer periods.

At the crustal-scale, multicomponent receiver gains attraction when we are interested in V_S image reconstruction. In marine environments, multicomponent receivers exist in the form of multicomponent Ocean Bottom Cable (OBC). OBC are installed at the bottom of the sea. They directly record the vibration of the sea-bed as three geophone components. Figure 9a shows the installation of the Magseis OBC sensor at the bottom of the sea. OBC can be combined with the hydrophone, resulting in a 4C component seismic. In onshore seismic, where the receiver is installed at the top of the rock/soil, having 3C geophones are important because of the elastic wave propagation. An example of 3C geophones is shown in Figure 9c. In the framework of FWI, multicomponent data has a potential benefit as an additional information. Several applications of multicomponent FWI have been performed (Choi et al., 2008; Sears et al., 2010; Kamath and Tsvankin, 2013; Vigh et al., 2014; Prioux et al., 2013a,b; Górszczyk et al., 2017; Smith et al., 2019). All of them consistently suggest that FWI using multicomponent data can improve the inversion result.

At a shallow-seismic scale, multicomponent receivers have been shown to improve the reconstructed model. Nuber et al. (2017) proposes a way to efficiently design the acquisition through an optimized experimental design for a 2D synthetic case. An optimized experimental design aims at predicting the most optimum source location for the seismic acquisition. They demonstrate that multicomponent data can increase the efficiency of the acquisition with a fewer number of sources. Smith et al. (2019) also perform both synthetic and field experiment with the underground tunnel as the target. Their synthetic test demonstrates that using multicomponent sources and multicomponent receivers can improve the image, especially at depth. In their field experiment, they use vertical sources while using two types of geophones. The first is vertical geophones, and the second is horizontal geophones. The horizontal geophones were set longitudinally to the direction of the target. Thanks to the second horizontal geophones, they were able to better reconstruct the underground tunnel.

Multicomponent source

The component of the source is defined as the direction where the source is excited. In a multicomponent source application, the seismic wave, which is generated at the same location, is excited from several different directions and recorded separately. The development of multicomponent seismic source technologies is tightly linked with industrial demand, especially in the oil and gas exploration scale. The multicomponent source technology became feasible in the period of 1960s to 1970s when Conoco, an oil company, introduces its horizontal vibrator truck (Hardage et al., 2011). Figure 10 shows multicomponent vibrator trucks. The vertical vibrator truck excites the vertical source direction, whereas the inline and crossline horizontal vibrator trucks excite horizontal directions.

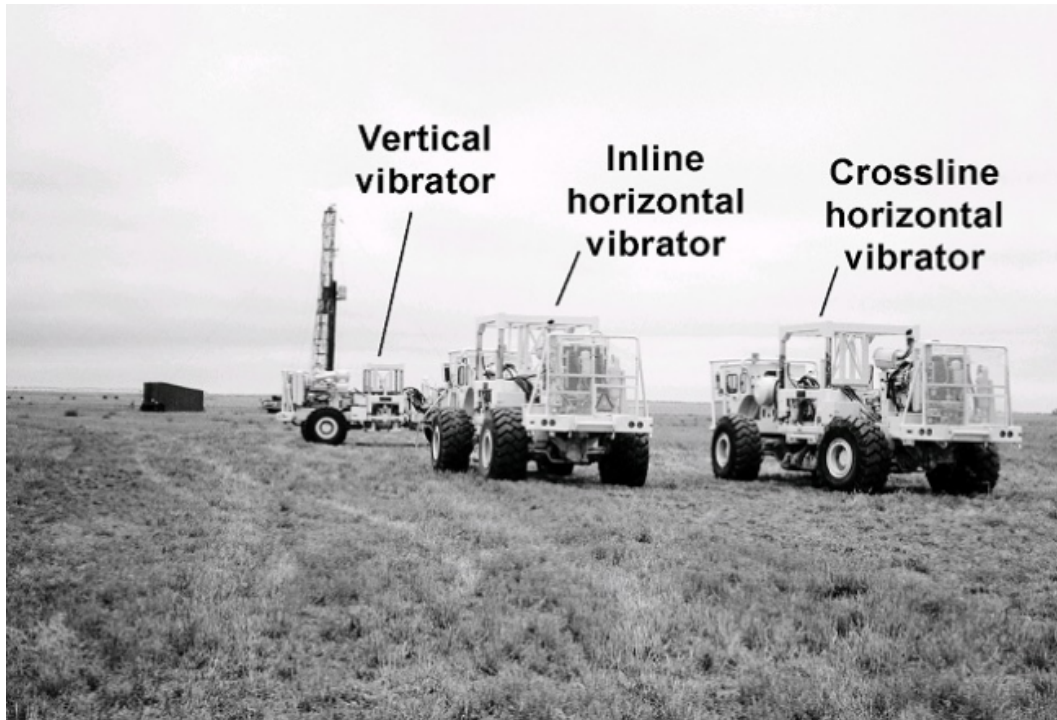


Figure 10: Example of three orthogonal vector sources which can produce 9C seismic data when recorded using 3C receivers (Hardage et al., 2011).

At a shallow seismic scale, multicomponent sources have also been introduced. Classically, we only use the vertical source. This type of source can be easily produced by hitting a horizontal metal plate with the sledgehammer. The horizontal direction source is not usually performed. When it is performed, normally, the horizontal source requires a vertical metal plate hit by a horizontal force. Performing vertical to horizontal sources requires the metal plate's movement from the horizontal direction to the vertical direction and vice versa. This installation process might reduce the source's consistency and efficiency in terms of the source-ground coupling, location, and direction. Therefore, Schmelzbach et al. (2016) proposes a prismatic source. A prismatic source can produce two sources' directions in a single installation process. The data can be rotated in the preprocessing step to produce the true vertical and horizontal component. The prismatic source is later improved by adding the third direction. The new type of source is called the Galperin source (Häusler et al., 2018). The Galperin source consists of three orthogonal directions in a single source's installation. It can increase the data consistency, as well as the acquisition's efficiency.

In the next section, I discuss more detail about the application of FWI for a specific shallow seismic case that became the focus of my study in this manuscript. We take advantage of the Galperin source and multi component receiver in order to obtain a 9C seismic data.

Problematics

This manuscript focuses on one specific 3D 9C dense dataset acquired to investigate a very shallow archaeological target called the Ettlingen Line. The acquisition was lead by Karlsruhe Institute

of Technology (KIT) in collaboration with GFZ Potsdam, ETH Zurich, and Univ. Grenoble Alpes (UGA)/SEISCOPE in terms of the equipment and work forces. Through contact with Prof. Thomas Bohlen, Yudi Pan, and the team from KIT, I was able to participate in the field experiment directly. The receivers were standard 3C geophones, whereas the sources are the 3C Galperin source (Häusler et al., 2018). Two seismic acquisitions with different acquisition geometries were performed.

Based on this original and relatively dense 3D multicomponent field dataset for the imaging of the shallow target Ettlingen line, my PhD work has been dedicated to investigate two main questions.

The first question is: can we design an efficient FWI workflow, for the simultaneous reconstruction of both P-wave and S-wave velocities, based on this dataset, for this shallow target? Associated with this question, I investigate the importance of accounting for viscous attenuation effects in the first meters of the subsurface where unconsolidated soil is present. I also discuss the requirement in terms of initial model building in this specific context of near-surface imaging from seismic data. The question behind is the ability for FWI to exploit the low-frequency information content of the data with respect to the target, which in principle should make possible to start the inversion from very simplistic models (1D vertically varying models). This is a very contrasted situation compared with what is usually met at exploration scale, where (visco-)elastic FWI has been already tested for the inversion of land data. Finally, I analyze the inverted 3D P-wave and S-wave velocities in the light of previous 2D GPR investigations and 3D MASW results to assess what such higher resolution 3D models bring in terms of geological interpretation. In particular, my reconstructed 3D models make a second trench-like structure apparent, which forms a 45 degree angle with the targeted trench structure, which was previously interpreted as an artifact. The geometrical coherency of this structure along the inline direction makes it likely a true structure, whose historical/archeological interpretation is currently a matter of discussion.

The second main question I investigate in this PhD work, is the information brought by the multicomponent aspect of the field data. In particular, I investigate what can be expected, for such shallow target, from horizontal receivers components, and more originally, from the horizontal source components. The first main result from the study of this second question is the importance of recording and inverting the Love waves, which has a deeper penetration depth than the Rayleigh wave, and thus make possible to illuminate the target at greater depth. The second main result is that thanks to multicomponent data, it is possible to reduce relatively drastically the number of receiver and source devices used to perform the acquisition. Indeed, decimated multicomponent acquisition yields similar results as a corresponding dense single component acquisition.

Outlines of the manuscript

Chapter 1 introduces the well-established theory of the elastic and visco-elastic full waveform modeling and inversion. The work performed in this PhD relies on computational tools developed in the frame of the SEM46 code. This modeling and inversion code relies on a spectral element discretization of the visco-elastic wave equations. I recall the main principles of this method in this chapter. I also describe the computational tools I use to perform the modeling and inversion in this manuscript.

Chapter 2 describes the Ettlingen Line as the main object of the experiment in this manuscript. It begins with the history of the Ettlingen Line. I continue the discussion with the previous geophysical investigations that have been done in the past. After that, I explain in detail the seismic acquisition in this location. Then, I present the required preprocessing before the FWI application.

Chapter 3 contains the application of 3D FWI at the Ettlingen Line using 9C data. I begin with the

strategy to perform multiparameter FWI and tackle shallow seismic data, which has a strong elastic response, mainly in the form of the surface waves. I also analyze the result of inversions starting from two different initial models. In addition, I assess the necessity to use viscoelastic medium compared to the elastic medium.

In **Chapter 4**, I explore in detail the effect of multicomponent data on FWI. The discussion starts with the analysis of the sensitivity kernel for each wave type and each component. I continue with the practical example of FWI using various component's combinations. Both synthetic and field experiments are demonstrated in this experiment. Then, I test the limit of the multicomponent data inversion by performing acquisition decimation.

In **Chapter 5**, I explain other activity during my PhD studies. In particular, I discuss the theory and implementation of the source subsampling and source encoding. Source subsampling and source encoding are two methods to reduce the computational time of FWI by reducing the amount of simulation required in each iteration during the inversion.

Finally, I close the manuscript with conclusions and prospects.

Chapter 1

Viscoelastic wave simulation and Full Waveform Inversion

Contents

1.1	Elastodynamics equation	15
1.1.1	Elastic modeling	16
1.1.2	Viscoelastic modeling	16
1.2	Discretization of the viscoelastic wave equation using Spectral Element Method	19
1.2.1	Mapping the reference to the physical space	20
1.2.2	Integration points and Gauss-Lobatto-Legendre (GLL) quadrature	21
1.2.3	Global system of the weak formulation	22
1.3	Full waveform inversion	24
1.3.1	Solving the constrained local minimization problem	25
1.3.2	Preconditioning application	30
1.4	Implementation: SEM46 code	30

1.1 Elastodynamics equation

Shallow seismic data is generally dominated by strong elastic effects. This effect is manifested in the form of the shear wave and the strong amplitude of the surface wave. At exploration scale, where the wave phases are well-separated, a specific preprocessing and tuning needs to be applied in order to be able to perform FWI using acoustic approximation (Barnes and Charara, 2008). One of the strategy is by applying time window to early arrival (Gao et al., 2006, 2007; Smithyman et al., 2009). By doing so, we neglect the presence of the elastic effect. In our experiment, the surface wave is hardly separable with the body wave, therefore performing time window strategy only for the acoustic wave is not suitable. In addition, we lose the V_S information inside the data if we remove the elastic response. Reconstructing V_S in shallow seismic scale is often preferable because of the resolution benefit. V_S has lower velocity than V_P which can be translated into a potential higher resolution of the reconstructed model. It is due to the fact that V_S wavelength is shorter than its V_P counterpart at the same frequency. Therefore, elastic wave equation is more suitable to represent the shallow seismic data than the acoustic wave equation.

Shallow seismic data also suffers from a high anelastic attenuation due to the presence of the unconsolidated soil (El Yadari et al., 2008; Xia et al., 2012; Gao et al., 2020). The attenuation itself is considered as an energy loss per cycle of the wave. Therefore a high frequency data suffers attenuation more than low frequency data at the same propagated length due to a shorter wavelength. Considering this fact, we consider elastic and viscoelastic approach in the context of my manuscript. The investigation of whether elastic or viscoelastic modeling is sufficient is studied later in Chapter 3.

The elastodynamic equation governs the propagation of the wave in elastic or viscoelastic medium. The equation is valid within the range of linearity of Hooke's law, implying non-permanent deformation of the medium. It can be written as a set of equation:

$$\begin{aligned}\rho(\mathbf{x})\partial_{tt}u_i(\mathbf{x}, t) &= \partial_j\sigma_{ij}(\mathbf{x}, t) + f_i(\mathbf{x}, t), \\ \sigma_{ij}(\mathbf{x}, t) &= M_{ijkl}(\mathbf{x}, t) *_t \varepsilon_{kl}(x, t) + \mathcal{T}_{ij}(\mathbf{x}, t),\end{aligned}\tag{1.1}$$

where ρ is the density, u is the displacement field, σ and ε are the second order stress and strain tensors, f is the external force, and \mathcal{T} is the stress failure. The effect of the attenuation is denoted by a relaxation rate M_{ijkl} , and symbol $*_t$ represents a convolution operator in time domain. We follow Einstein convention (summation over repeated indices) for these equations.

The strain and the deformation of previous equation (Eq. 1.1) is linked through the Hooke's Law as

$$\varepsilon_{kl} = \frac{1}{2}(\partial_k u_l + \partial_l u_k) = \frac{1}{2}\left(\frac{\partial u_k}{\partial x_l} + \frac{\partial u_l}{\partial x_k}\right)\tag{1.2}$$

Due to the symmetry of the stress and strain tensors, Voigt notation can be used to reduce the tensor's order as

$$\begin{aligned}11 \rightarrow 1, \quad 22 \rightarrow 2, \quad 33 \rightarrow 3, \\ 23 \text{ or } 32 \rightarrow 4, \quad 13 \text{ or } 31 \rightarrow 5, \quad 12 \text{ or } 21 \rightarrow 6.\end{aligned}\tag{1.3}$$

The stress and strain tensor become

$$\begin{aligned}\sigma &= \begin{bmatrix} \sigma_{11} & \sigma_{12} & \sigma_{13} \\ \sigma_{21} & \sigma_{22} & \sigma_{23} \\ \sigma_{31} & \sigma_{32} & \sigma_{33} \end{bmatrix} \equiv (\sigma_1, \sigma_2, \sigma_3, \sigma_4, \sigma_5, \sigma_6)^T, \\ \varepsilon &= \begin{bmatrix} \varepsilon_{11} & \varepsilon_{12} & \varepsilon_{13} \\ \varepsilon_{21} & \varepsilon_{22} & \varepsilon_{23} \\ \varepsilon_{31} & \varepsilon_{32} & \varepsilon_{33} \end{bmatrix} \equiv (\varepsilon_1, \varepsilon_2, \varepsilon_3, \varepsilon_4, \varepsilon_5, \varepsilon_6)^T,\end{aligned}\tag{1.4}$$

where the superscript T is the transpose. Here we introduce the spatial derivative operator D as operator given as

$$D = \begin{pmatrix} \partial_1 & 0 & 0 & 0 & \partial_3 & \partial_2 \\ 0 & \partial_2 & 0 & \partial_3 & 0 & \partial_1 \\ 0 & 0 & \partial_3 & \partial_2 & \partial_1 & 0 \end{pmatrix},\tag{1.5}$$

so that Equation 1.2 can be rewritten as

$$\varepsilon = D^T u.\tag{1.6}$$

1.1.1 Elastic modeling

In a purely elastic wave propagation we have $M_{ijkl}(\mathbf{x}, t) = c_{ijkl}(\mathbf{x})\delta(t)$, and equation 1.1 simplifies into

$$\begin{aligned}\rho \partial_{tt} u_i &= \partial_j \sigma_{ij} + f_i, \\ \sigma_{ij} &= c_{ijkl} \varepsilon_{kl} + \mathcal{T}_{ij},\end{aligned}\tag{1.7}$$

where c_{ijkl} is the elastic (unrelaxed) stiffness tensor.

Using Voigt indexing and matrix notations, equation 1.7 can be rewritten as

$$\rho \partial_{tt} \mathbf{u} = D C D^T \mathbf{u} + S,\tag{1.8}$$

where S is the external source and C is the stiffness tensor. In subsurface medium, it is known to exhibit anisotropic behavior due to microscopic oriented heterogeneities or macroscopic oriented structures Babuska and Cara (1991). However, in this PhD thesis, we assume a specific form of C which represents an isotropic medium as

$$C = \begin{bmatrix} \lambda + 2\mu & \lambda & \lambda & 0 & 0 & 0 \\ \lambda & \lambda + 2\mu & \lambda & 0 & 0 & 0 \\ \lambda & \lambda & \lambda + 2\mu & 0 & 0 & 0 \\ 0 & 0 & 0 & \mu & 0 & 0 \\ 0 & 0 & 0 & 0 & \mu & 0 \\ 0 & 0 & 0 & 0 & 0 & \mu \end{bmatrix}.\tag{1.9}$$

1.1.2 Viscoelastic modeling

In viscoelastic media, the loss of amplitude in the signal is not only caused by the geometric spreading and scattering, but also an additional anelastic attenuation. This attenuation is characterized by the energy loss per cycle of the wave, and measured by the quality factor tensor $Q_{ijkl}(\mathbf{x})$ (Carcione et al.,

1988). In frequency domain, the inverse of this quality factor is the ratio between the imaginary and the real part of the relaxation rate $\hat{M}_{ijkl}(\mathbf{x}, \omega)$ as

$$\hat{Q}_{ijkl}^{-1}(\mathbf{x}, \omega) = \frac{\mathcal{I}[\hat{M}_{ijkl}(\mathbf{x}, \omega)]}{\mathcal{R}[\hat{M}_{ijkl}(\mathbf{x}, \omega)]}, \quad (1.10)$$

where the hat symbol $\hat{\cdot}$ represents the Fourier transformed variable.

1.1.2.1 Constant Q approximation

For a simple wave modeling for seismic application, a constant Q over the considered frequency band $[\omega_{min}, \omega_{max}]$ is usually accepted. We can use the L standard-linear-solid systems (SLS), at particular reference frequencies $\omega_\Lambda \in [\omega_{min}, \omega_{max}]$, to fit a constant Q parameter over the frequency band. Anelastic coefficients Y_Λ^{ijkl} may be introduced in the definition of the complex relaxation rate $\hat{M}_{ijkl}(\mathbf{x}, \omega)$ as

$$\hat{M}_{ijkl}(\mathbf{x}, \omega) = c_{ijkl}(\mathbf{x}) \left(1 - \sum_{\Lambda=1}^L Y_\Lambda^{ijkl}(\mathbf{x}) \frac{\omega_\Lambda}{\omega_\Lambda + i\omega} \right), \quad (1.11)$$

where $\Lambda = 1, \dots, L$ (Emmerich and Korn, 1987; Blanch et al., 1995; Moczo and Kristek, 2005; van Driel and Nissen-Meyer, 2014). Plugging the complex relaxation rate to the quality factor (Eq. 1.10) gives

$$\hat{Q}_{ijkl}^{-1}(\mathbf{x}, \omega) = \frac{\sum_{\Lambda=1}^L Y_\Lambda^{ijkl}(\mathbf{x}) \frac{\omega_\Lambda \omega}{\omega_\Lambda^2 + \omega^2}}{1 - \sum_{\Lambda=1}^L Y_\Lambda^{ijkl}(\mathbf{x}) \frac{\omega_\Lambda \omega}{\omega_\Lambda^2 + \omega^2}}. \quad (1.12)$$

In the assumption where $Q \gg 1$, the denominator of the $\hat{Q}_{ijkl}^{-1}(\mathbf{x}, \omega)$ can be neglected which leads to

$$\hat{Q}_{ijkl}^{-1}(\mathbf{x}, \omega) \approx \sum_{\Lambda=1}^L Y_\Lambda^{ijkl}(\mathbf{x}) \frac{\omega_\Lambda \omega}{\omega_\Lambda^2 + \omega^2}. \quad (1.13)$$

Instead of computing a set of L anelastic coefficients $Y_\Lambda^{ijkl}(\mathbf{x})$ for each spatial location \mathbf{x} , Yang et al. (2016) proposes the approximation

$$Y_\Lambda^{ijkl}(\mathbf{x}) \approx y_\Lambda Q_{ijkl}^{-1}(\mathbf{x}) \quad (1.14)$$

for the entire medium. In this case, the scalars y_Λ are L dimensionless anelastic coefficients. Inserting Equation 1.14 into Equation 1.13 gives

$$\hat{Q}_{ijkl}^{-1}(\mathbf{x}, \omega) \approx \sum_{\Lambda=1}^L y_\Lambda Q_{ijkl}^{-1}(\mathbf{x}) \frac{\omega_\Lambda \omega}{\omega_\Lambda^2 + \omega^2}. \quad (1.15)$$

In their formulation, Yang et al. (2016) compute the coefficient y_Λ , which minimize the distance between the frequency independent quality factor $Q_{ijkl}^{-1}(\mathbf{x})$ with the one which is frequency dependent $\hat{Q}_{ijkl}^{-1}(\mathbf{x}, \omega)$. The coefficients y_Λ over the frequency band $[\omega_{min}, \omega_{max}]$ are estimated using generalized least-squares minimization problem

$$\min_{y_\Lambda} \left\{ \int_{\omega_{min}}^{\omega_{max}} \left[Q_{ref}^{-1} \left(y_\Lambda \frac{\omega_\Lambda \omega}{\omega^2 + \omega_\Lambda^2} \right) \right]^2 \right\}. \quad (1.16)$$

According to Trinh (2018), the value of this constant is usually chosen such that

$$Q_{ref} \approx \sqrt{\min_{ijkl, \mathbf{x}} Q_{ijkl}(\mathbf{x}) \times \max_{ijkl, \mathbf{x}} Q_{ijkl}(\mathbf{x})}. \quad (1.17)$$

1.1.2.2 Isotropic and anisotropic viscoelastic equation using SLS approximation

By considering the scalars y_Λ into Equation 1.11, we obtain

$$\hat{M}_{ijkl}(\mathbf{x}, \omega) = c_{ijkl}(\mathbf{x}) - c_{ijkl}(\mathbf{x})Q_{ijkl}^{-1}(\mathbf{x}) \sum_{\Lambda=1}^L y_\Lambda \frac{\omega_\Lambda}{\omega_\Lambda + i\omega}. \quad (1.18)$$

The product between $c_{ijkl}(\mathbf{x})$ and $Q_{ijkl}^{-1}(\mathbf{x})$ are a term-by-term product. In this equation, the attenuation mechanisms is shown by the second part of the right-hand side in Equation 1.18. As mentioned previously, following the strategy of Yang et al. (2016), an explicit storing of the 21 anelastic coefficients $Y_\Lambda^{ijkl}(\mathbf{x})$ (Komatitsch and Tromp, 1999) related to the $M_{ijkl}(\mathbf{x})$ at each spatial direction is avoided. In this implementation, we only need to store L scalar y_Λ for the entire medium and the heterogeneous attenuation parameters $Q_{ijkl}(\mathbf{x})$ over the medium. We also store L reference frequencies ω_Λ associated with the number of L in the SLS.

From Equation 1.18, we can separate the elastic rheology (unrelaxed stiffness coefficients $c_{ijkl}(\mathbf{x})$) with the frequency-dependent attenuation mechanism, by introducing the attenuative stiffness coefficient $c_{ijkl}^R(\mathbf{x})$ (Trinh, 2018). In the case of fully anisotropic attenuation, the parameters can be linked with the $c_{ijkl}(\mathbf{x})$ as

$$c_{ijkl}^R(\mathbf{x}) = c_{ijkl}(\mathbf{x})Q_{ijkl}^{-1}(\mathbf{x}). \quad (1.19)$$

The relationship between stress and strain in Equation 1.1 becomes

$$\sigma_{ij}(\mathbf{x}, t) = c_{ijkl}(\mathbf{x})\varepsilon_{kl}(\mathbf{x}, t) - c_{ijkl}^R(\mathbf{x}) \sum_{\Lambda=1}^L \psi_{\Lambda;kl}(\mathbf{x}, t), \quad (1.20)$$

where the memory variable $\psi_{\Lambda;kl}(\mathbf{x}, t)$ satisfies the first-order ordinary differential equation (ODE)

$$\partial_t \psi_{\Lambda;kl}(\mathbf{x}, t) + w_\Lambda \psi_{\Lambda;kl}(\mathbf{x}, t) = w_\Lambda y_\Lambda \varepsilon_{kl}(\mathbf{x}, t). \quad (1.21)$$

Note that we neglect the source term $\mathcal{T}_{ij}(\mathbf{x}, t)$ in the Equation 1.20. Trinh (2018) has given a detailed mathematical demonstration which is coherent with Moczo and Kristek (2005) and Yang et al. (2016). Following Voigt notation, the second-order visco-elastic wave equation can be written as

$$\begin{aligned} \rho \partial_{tt} \mathbf{u} &= DCD^T \mathbf{u} - DC^R \sum_{\Lambda=1}^L \psi_\Lambda + \mathbf{S}, \\ \partial_t \psi_\Lambda + w_\Lambda \psi_\Lambda &= y_\Lambda w_\Lambda D^T \mathbf{u}, \quad \text{with } \Lambda = 1, \dots, L, \end{aligned} \quad (1.22)$$

where ψ_Λ is the memory-variable vector associated with each Λ in SLS

$$\psi_\Lambda = (\psi_{\Lambda;1}, \psi_{\Lambda;2}, \psi_{\Lambda;3}, \psi_{\Lambda;4}, \psi_{\Lambda;5}, \psi_{\Lambda;6})^T. \quad (1.23)$$

The matrix $C^R = (C_{ij}^R)_{6 \times 6}$ contains the attenuative stiffness coefficients with 21 independent component for the case of fully anisotropic medium.

In practice, we use a simpler isotropic attenuation description in this PhD thesis, such that the corresponding relaxed stiffness-tensor can be written as

$$C^R = \begin{bmatrix} \lambda^R + 2\mu^R & \lambda^R & \lambda^R & 0 & 0 & 0 \\ \lambda^R & \lambda^R + 2\mu^R & \lambda^R & 0 & 0 & 0 \\ \lambda^R & \lambda^R & \lambda^R + 2\mu^R & 0 & 0 & 0 \\ 0 & 0 & 0 & \mu^R & 0 & 0 \\ 0 & 0 & 0 & 0 & \mu^R & 0 \\ 0 & 0 & 0 & 0 & 0 & \mu^R \end{bmatrix}, \quad (1.24)$$

where λ^R and μ^R are the relaxed Lamé coefficients. The isotropic attenuation implies that the attenuative stiffness tensor $(C_{ij}^R)_{6 \times 6}$ is isotropic but not the inverse quality factor matrix $(Q_{ij}^{-1})_{6 \times 6}$ (Moczo et al., 1997). We consider the effective mechanism with

$$\begin{aligned} \lambda^R + 2\mu^R &= \frac{1}{3}Q_P^{-1}(C_{11} + C_{22} + C_{33}) \\ \text{and } \mu^R &= \frac{1}{3}Q_S^{-1}(C_{44} + C_{55} + C_{66}), \end{aligned} \quad (1.25)$$

where the Q_P and Q_S are the attenuation parameters associated with the compressional and shear wave velocity (V_P and V_S).

The viscoelastic equation in Equation 1.22 is not self-adjoint due to the presence of memory variables. This property is related to energy dissipation. Later, we can show that the corresponding adjoint system can be transformed into a similar structure as for the forward problem.

1.2 Discretization of the viscoelastic wave equation using Spectral Element Method

The elastic or viscoelastic partial differential equation (PDE) given in Equation 1.7 and 1.22 need to be solved by choosing a suitable numerical method. When acoustic approximation with a flat free surface is considered, one can choose the finite difference (FD) discretization in space. In this particular case, FD is appealing due to its numerical efficiency and relatively simple implementation. Even when we consider the elastic wave equation, fluid-solid interaction can be easily implemented, considering a simple bathymetry. However, the standard FD formulation is limited to a regular grid-spacing, although there are some applications of deformed grid FD with the trade-off of increasing complexity and computational cost Moczo (1989); de la Puente et al. (2014); Petersson and Sjögreen (2015). An extra effort also needs to be considered when considering a complex topography (Robertsson, 1996; Bohlen and Saenger, 2006; Zhang and Chen, 2006).

As an alternative, there is another numerical method based on the weak formulation of the PDE called Finite Element (FE). The weak form on which FE is based, ensures to satisfy the free surface condition for any topography and irregular tetrahedral meshes makes possible to take into account both irregular topography and internal discontinuities.

For this reason, we adopt spectral element method (SEM), which is a very specific FE technique. The main restriction of the method is the use of hexahedral meshes, which do not allow to conform to arbitrary discontinuities. However, it is possible to use deformed elements to represent accurately an irregular topography, and SEM benefits from other very appealing properties, such as spectral convergence, which makes it a very popular method in Earth Sciences in general and geophysics in particular (Faccioli et al., 1997; Komatitsch and Vilotte, 1998; Komatitsch and Tromp, 1999; Trinh et al., 2019b). We detail after the specific properties of SEM.

In SEM, the seismic wavefield's discretization is based on Lagrange interpolants on hexahedral elements, whereas the integration over elements is based on Gauss-Lobatto-Legendre (GLL) points. As an illustration, Figure 1.1 shows the example of discretized medium in 2D. Figure 1.1a represents the 2D physical medium in Cartesian coordinate $\{\mathbf{x}; (x, y) \in \mathbb{R}^2\}$. In standard SEM, it can be discretized using several non-overlapped deformed quadrilateral elements Ω_e with Γ as the boundary. Figure 1.1b shows the *reference square* in GLL-space $\{\boldsymbol{\xi}; (\xi, \eta) \in \mathbb{R}^2\}$. In 3D, the medium is discretized using

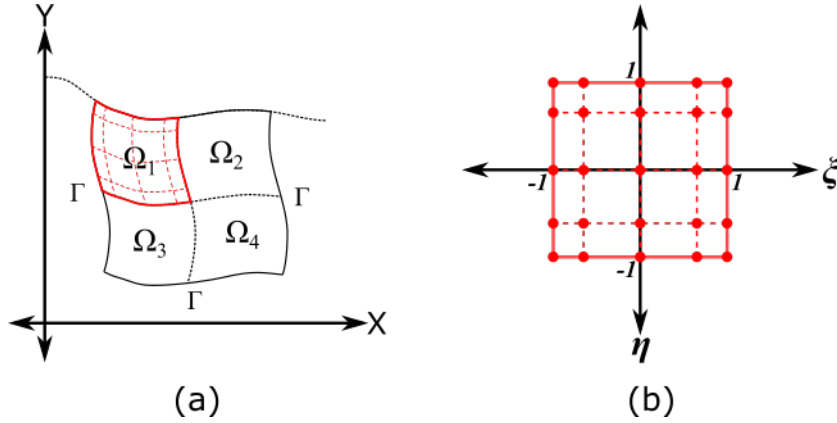


Figure 1.1: The physical model Ω in Cartesian coordinate is divided into a set of tensorial element $\Omega_e (e = 1, \dots, 4)$ (a). Example of GLL points in 2D element with interpolation order $N = 4$ (b).

hexahedral elements Ω_e . The physical space is represented by $\{\mathbf{x}; (x, y, z) \in \mathbb{R}^3\}$, and the GLL space is represented by $\{\boldsymbol{\xi}; (\xi, \eta, \zeta) \in \mathbb{R}^3\}$.

1.2.1 Mapping the reference to the physical space

SEM has the flexibility to use deformed elements. In practice, this feature is beneficial for representing a complex topography and geological features. Komatitsch and Tromp (1999) state that the shape of each hexahedral element is defined by a set of n_a control points $\mathbf{x}_a = \mathbf{x}(\xi_a, \eta_a, \zeta_a); a = 1, \dots, n_a$ and a set of n_a shape functions $N_a(\xi, \eta, \zeta)$. The general mapping between the reference cube and the hexahedral element can be written as

$$\mathbf{x}(\xi, \eta, \zeta) = \sum_{a=1}^{n_a} N_a(\xi, \eta, \zeta) \mathbf{x}_a. \quad (1.26)$$

Jacobian matrix $\mathbf{J}(\boldsymbol{\xi})$ associated with the mapping in Equation 1.26 for each position can be defined as

$$\mathbf{J}(\boldsymbol{\xi}) = \begin{bmatrix} \partial_\xi z & \partial_\eta z & \partial_\zeta z \\ \partial_\xi x & \partial_\eta x & \partial_\zeta x \\ \partial_\xi y & \partial_\eta y & \partial_\zeta y \end{bmatrix}. \quad (1.27)$$

An element of volume dx in the physical space is related to an element of volume $d\boldsymbol{\xi}$ in the reference cube through

$$dzdxdy = J_e(\boldsymbol{\xi}) d\xi d\eta d\zeta, \quad (1.28)$$

with $J_e(\boldsymbol{\xi})$ is the determinant of the Jacobian matrix $\mathbf{J}(\boldsymbol{\xi})$.

In fully deformed elements in physical space, the Jacobian matrix $\mathbf{J}(\boldsymbol{\xi})$ is full of non-zero terms. On the other hand, the Jacobian matrix $\mathbf{J}(\boldsymbol{\xi})$ is diagonal when the element is regular (rectangular parallelepiped shape). By exploiting this behavior, we have better computational efficiency by combining fully deformed elements and regular elements.

1.2.2 Integration points and Gauss-Lobatto-Legendre (GLL) quadrature

SEM utilize Gauss-Lobatto-Legendre (GLL) integration points, which are defined in the reference cube. In 1D, the $(N + 1)$ GLL points are roots of the polynomial

$$(1 - \xi^2)L_N(\xi) = 0, \quad (1.29)$$

where L_N is Legendre polynomial of degree N . Based on Canuto et al. (2006), Legendre polynomial can be defined by the following recursion relation with $L_0(x) = 1$ and $L_1(x) = x$ as

$$L_{k+1}(x) = \frac{2k+1}{k+1}xL_k(x) - \frac{k}{k+1}L_{k-1}(x). \quad (1.30)$$

In 2D or 3D case, the GLL points are defined based on the tensorial products of GLL points in 1D. Figure 1.1b shows the GLL points in 2D element at interpolation order $N = 4$.

In 3D, the reference cube is discretized into a set of $(N + 1)^3$ GLL points

$$\boldsymbol{\xi}_{\hat{k}} = (\xi_{k_1}, \eta_{k_2}, \zeta_{k_3}) \quad \hat{k} \text{ stands for the triple indexes } \{k_1, k_2, k_3 = 0, \dots, N\} \quad (1.31)$$

where k_1 , k_2 , and k_3 are the indexing of GLL points in z , x , and y dimensions, respectively. These collocation points are used to define $(N_1)^3$ basis function $\mathfrak{l}_{\hat{k}}(\boldsymbol{\xi})$

$$\mathfrak{l}_{\hat{k}}(\boldsymbol{\xi}) = \mathfrak{l}_{k_1}(\xi)\mathfrak{l}_{k_2}(\eta)\mathfrak{l}_{k_3}(\zeta), \quad (1.32)$$

where each function is a product of Lagrange polynomial of degree N

$$\mathfrak{l}_j(\xi) = \prod_{i=0; i \neq j}^N \frac{\xi - x_i}{\xi_j - x_i}. \quad (1.33)$$

Lagrange polynomials have the property that its values at GLL nodes are equal to 0 when $i \neq j$ and 1 when $i = j$.

In SEM, the spatial interpolation and numerical integration use the same collocation points. The approximation of a vector $\mathbf{v}(\boldsymbol{\xi}) = (v_1(\boldsymbol{\xi}), v_2(\boldsymbol{\xi}), v_3(\boldsymbol{\xi}))^T$ over the reference cube can be written as follows

$$\mathbf{v}(\boldsymbol{\xi}) \approx \sum_{h_1=0}^N \sum_{h_2=0}^N \sum_{h_3=0}^N \mathbf{v}_{\hat{h}} \mathfrak{l}_{h_1}(\xi)\mathfrak{l}_{h_2}(\eta)\mathfrak{l}_{h_3}(\zeta) = \sum_{\hat{h}=0}^N \mathbf{v}_{\hat{h}} \mathfrak{l}_{\hat{h}}(\boldsymbol{\xi}), \quad (1.34)$$

where $\mathbf{v}_{\hat{h}} = \mathbf{b}(\xi_{h_1}, \eta_{h_2}, \zeta_{h_3})$. Equation 1.34 shows that we can consider heterogeneous medium inside each element at each collocation points.

The integral of any continuous function $f(\boldsymbol{\xi})$ over the reference cube can be approximated using Gauss-Lobatto-Legendre quadrature as

$$\int \int \int_{-1}^1 f(\boldsymbol{\xi}) d\boldsymbol{\xi} \approx \sum_{\hat{q}=0}^N w_{\hat{q}} f(\boldsymbol{\xi}_{\hat{q}}), \quad (1.35)$$

where $w_{\hat{q}}$ stands for the product of quadrature weights associated with the GLL integration points $\boldsymbol{\xi}_{\hat{q}}$. The weight of each GLL points are defined as

$$w_j = \frac{2}{N(N+1)} \frac{1}{[L_N(\xi_j)]^2} \quad \text{for } \xi_j \neq \pm 1$$

$$w_j = \frac{2}{N(N+1)} \quad \text{for } \xi_j = \pm 1. \quad (1.36)$$

The spectral convergence property of SEM are guaranteed for polynomial functions up to the degree $(2N + 1)$, in which the Equation 1.35 is exact.

1.2.3 Global system of the weak formulation

We can form a weak formulation of the viscoelastic wave equation (Eq. 1.22) in integral form by considering the choice of Lagrange basis functions $l_{\hat{k}}(\mathbf{x})$ as

$$\begin{aligned} \int_{\Omega} l_{\hat{k}}(\mathbf{x}) \rho(\mathbf{x}) \partial_{tt} \mathbf{u}(\mathbf{x}) d\mathbf{x} &= \int_{\Omega} l_{\hat{k}}(\mathbf{x}) D C D^T \mathbf{u}(\mathbf{x}) d\mathbf{x} - \int_{\Omega} l_{\hat{k}}(\mathbf{x}) D C^a \sum_{\Lambda=1}^L \psi_{\Lambda}(\mathbf{x}) d\mathbf{x} + \int_{\Omega} l_{\hat{k}}(\mathbf{x}) \mathbf{S}(\mathbf{x}) d\mathbf{x}, \\ \int_{\Omega} l_{\hat{k}}(\mathbf{x}) \partial_t \psi_{\Lambda}(\mathbf{x}) d\mathbf{x} + \omega_{\Lambda} \int_{\Omega} l_{\hat{k}}(\mathbf{x}) \psi_{\Lambda}(\psi) d\mathbf{x} &= y_{\Lambda} \omega_{\Lambda} \int_{\Omega} l_{\hat{k}}(\mathbf{x}) D^T \mathbf{u}(\mathbf{x}) d\mathbf{x}. \end{aligned} \quad (1.37)$$

Through the integration by part technique, we obtain

$$\begin{aligned} \int_{\Omega} l_{\hat{k}}(\mathbf{x}) \rho(\mathbf{x}) \partial_{tt} \mathbf{u}(\mathbf{x}) d\mathbf{x} &= - \int_{\Omega} [D l_{\hat{k}}(\mathbf{x})] C D^T \mathbf{u}(\mathbf{x}) d\mathbf{x} + \int_{\Omega} [D l_{\hat{k}}(\mathbf{x})] C^a \sum_{\Lambda=1}^L \psi_{\Lambda}(\mathbf{x}) d\mathbf{x} \\ &\quad + \underbrace{\int_{\Gamma_{\Omega}} [I_D l_{\hat{k}}(\mathbf{x})] \tau_B(\mathbf{x}) d s_{\mathbf{x}}}_{\text{Boundary term B}} + \int_{\Omega} l_{\hat{k}}(\mathbf{x}) \mathbf{S}(\mathbf{x}) d\mathbf{x}, \\ \int_{\Omega} l_{\hat{k}}(\mathbf{x}) \partial_t \psi_{\Lambda}(\mathbf{x}) d\mathbf{x} + \omega_{\Lambda} \int_{\Omega} l_{\hat{k}}(\mathbf{x}) \psi_{\Lambda}(\psi) d\mathbf{x} &= y_{\Lambda} \omega_{\Lambda} \int_{\Omega} l_{\hat{k}}(\mathbf{x}) D^T \mathbf{u}(\mathbf{x}) d\mathbf{x}. \end{aligned} \quad (1.38)$$

The free surface and the absorbing boundary is controlled by the boundary term **B**. In the free surface boundary, the traction τ_B is 0; therefore, the boundary term vanishes. In the absorbing boundary condition, the traction τ_B is used to attenuate the outgoing wavefield. For simplicity, we temporarily ignore the boundary term **B** in the next steps.

By moving the physical space \mathbf{x} to the reference space $\boldsymbol{\xi}$, we obtain

$$\begin{aligned} \int_{\Omega} l_{\hat{k}}(\boldsymbol{\xi}) \rho(\boldsymbol{\xi}) \partial_{tt} \mathbf{u}(\boldsymbol{\xi}) J_e(\boldsymbol{\xi}) d\boldsymbol{\xi} &= - \int_{\Omega} \sum_{j=1}^3 \frac{\partial l_{\hat{k}}(\boldsymbol{\xi})}{\partial r_j} G_j(\boldsymbol{\xi}) C D^T \mathbf{u}(\boldsymbol{\xi}) J_e(\boldsymbol{\xi}) d\boldsymbol{\xi} \\ &\quad + \int_{\Omega} \sum_{j=1}^3 \frac{\partial l_{\hat{k}}(\boldsymbol{\xi})}{\partial r_j} G_j(\boldsymbol{\xi}) C^a \sum_{\Lambda=1}^L \psi_{\Lambda}(\boldsymbol{\xi}) J_e(\boldsymbol{\xi}) d\boldsymbol{\xi} + \int_{\Omega} l_{\hat{k}}(\boldsymbol{\xi}) \mathbf{S}(\boldsymbol{\xi}) J_e(\boldsymbol{\xi}) d\boldsymbol{\xi}, \\ \int_{\Omega} l_{\hat{k}}(\boldsymbol{\xi}) \partial_t \psi_{\Lambda}(\boldsymbol{\xi}) J_e(\boldsymbol{\xi}) d\boldsymbol{\xi} + \omega_{\Lambda} \int_{\Omega} l_{\hat{k}}(\boldsymbol{\xi}) \psi_{\Lambda}(\boldsymbol{\xi}) J_e(\boldsymbol{\xi}) d\boldsymbol{\xi} &= y_{\Lambda} \omega_{\Lambda} \int_{\Omega} l_{\hat{k}}(\boldsymbol{\xi}) D^T \mathbf{u}(\boldsymbol{\xi}) J_e(\boldsymbol{\xi}) d\boldsymbol{\xi}, \end{aligned} \quad (1.39)$$

where $[D l_{\hat{k}}(\boldsymbol{\xi})]$ is defined as

$$[D l_{\hat{k}}(\boldsymbol{\xi})] = \sum_{j=1}^3 \frac{\partial l_{\hat{k}}(\boldsymbol{\xi})}{\partial r_j} G_j(\boldsymbol{\xi}), \quad (1.40)$$

and $G_j(\boldsymbol{\xi})$ is defined as

$$G_j \boldsymbol{\xi} = \begin{pmatrix} \frac{\partial r_j}{\partial p_1} & 0 & 0 & 0 & \frac{\partial r_j}{\partial p_3} & \frac{\partial r_j}{\partial p_2} \\ 0 & \frac{\partial r_j}{\partial p_2} & 0 & \frac{\partial r_j}{\partial p_3} & 0 & \frac{\partial r_j}{\partial p_1} \\ 0 & 0 & \frac{\partial r_j}{\partial p_3} & \frac{\partial r_j}{\partial p_2} & \frac{\partial r_j}{\partial p_1} & 0 \end{pmatrix}. \quad (1.41)$$

The (p_1, p_2, p_3) is the redefinition of $(z, x, y) = \mathbf{x}$ in physical space, and (r_1, r_2, r_3) is the redefinition of $(\xi, \eta, \zeta) = \boldsymbol{\xi}$.

Afterward, we may approximate the physical field, \mathbf{u} , \mathbf{S} , and ψ_Λ , by the spatial interpolation over the basis function from Equation 1.34 and taking into account Equation 1.40, we obtain

$$\begin{aligned}
 \sum_{\hat{h}=1}^N \int_{\Omega} \mathbf{l}_{\hat{k}}(\boldsymbol{\xi}) \rho(\boldsymbol{\xi}) \mathbf{l}_{\hat{h}}(\boldsymbol{\xi}) \partial_{tt} \mathbf{u}_{\hat{h}} J_e(\boldsymbol{\xi}) d\boldsymbol{\xi} &= - \int_{\Omega} \sum_{j=1}^3 \frac{\partial \mathbf{l}_{\hat{k}}(\boldsymbol{\xi})}{\partial r_j} G_j(\boldsymbol{\xi}) C \sum_{\hat{h}=1}^N \sum_{i=1}^3 G_i^T(\boldsymbol{\xi}) \frac{\partial \mathbf{l}_{\hat{h}}(\boldsymbol{\xi})}{\partial r_i} \mathbf{u}_{\hat{h}} J_e(\boldsymbol{\xi}) d\boldsymbol{\xi} \\
 &+ \int_{\Omega} \sum_{j=1}^3 \frac{\partial \mathbf{l}_{\hat{k}}(\boldsymbol{\xi})}{\partial r_j} G_j(\boldsymbol{\xi}) C^a \sum_{\hat{h}=1}^N \mathbf{l}_{\hat{h}}(\boldsymbol{\xi}) \sum_{\Lambda=1}^L \psi_{\Lambda; \hat{h}} J_e(\boldsymbol{\xi}) d\boldsymbol{\xi} + \sum_{\hat{h}=1}^N \int_{\Omega} \mathbf{l}_{\hat{k}}(\boldsymbol{\xi}) \mathbf{l}_{\hat{h}}(\boldsymbol{\xi}) \mathbf{S}_{\hat{h}} J_e(\boldsymbol{\xi}) d\boldsymbol{\xi}, \\
 \sum_{\hat{h}=1}^N \int_{\Omega} \mathbf{l}_{\hat{k}}(\boldsymbol{\xi}) \mathbf{l}_{\hat{h}}(\boldsymbol{\xi}) \partial_t \psi_{\Lambda; \hat{h}} J_e(\boldsymbol{\xi}) d\boldsymbol{\xi} + \omega_\Lambda \sum_{\hat{h}=1}^N \int_{\Omega} \mathbf{l}_{\hat{k}}(\boldsymbol{\xi}) \mathbf{l}_{\hat{h}}(\boldsymbol{\xi}) \psi_{\Lambda; \hat{h}} J_e(\boldsymbol{\xi}) d\boldsymbol{\xi} \\
 &= y_\Lambda \omega_\Lambda \int_{\omega} \mathbf{l}_{\hat{k}}(\boldsymbol{\xi}) \sum_{\hat{h}=1}^N \sum_{i=1}^3 G_i^T(\boldsymbol{\xi}) \frac{\partial \mathbf{l}_{\hat{h}}(\boldsymbol{\xi})}{\partial r_i} \mathbf{u}_{\hat{h}} J_e(\boldsymbol{\xi}) d\boldsymbol{\xi}.
 \end{aligned} \tag{1.42}$$

The next step is the application of GLL quadrature (Eq. 1.36), using the property of Lagrange polynomial (the values at GLL nodes are equal to 0 when $i \neq j$ and 1 when $i = j$), simplifying the Kronecker delta function, and removing $w_{\hat{k}} J_e(\boldsymbol{\xi}_{\hat{k}})$ from both sides of the second equation and changing the index \hat{k} to \hat{q} , we have

$$\begin{aligned}
 \underbrace{w_{\hat{k}} \rho_{\hat{k}} J_e(\boldsymbol{\xi}_{\hat{k}})}_{M_{\hat{k}\hat{k}}} \partial_{tt} \mathbf{u}_{\hat{k}} &= - \overbrace{\sum_{\hat{q}=1}^N w_{\hat{q}} J_e(\boldsymbol{\xi}_{\hat{q}}) \sum_{j=1}^3 \frac{\partial \mathbf{l}_{\hat{k}}(\boldsymbol{\xi}_{\hat{q}})}{\partial r_j} G_j(\boldsymbol{\xi}_{\hat{q}}) C}^{\mathcal{D}_{\hat{k}\hat{q}}^w} \overbrace{\sum_{\hat{h}=1}^N \sum_{i=1}^3 G_i^T(\boldsymbol{\xi}_{\hat{q}}) \frac{\partial \mathbf{l}_{\hat{h}}(\boldsymbol{\xi}_{\hat{q}})}{\partial r_i} \mathbf{u}_{\hat{h}}}^{\mathcal{D}_{\hat{q}\hat{h}}} \\
 &+ \sum_{\hat{q}=1}^N w_{\hat{q}} J_e(\boldsymbol{\xi}_{\hat{q}}) \sum_{j=1}^3 \frac{\partial \mathbf{l}_{\hat{k}}(\boldsymbol{\xi}_{\hat{q}})}{\partial r_j} G_j(\boldsymbol{\xi}_{\hat{q}}) C^a \sum_{\hat{q}=1}^N \sum_{\Lambda=1}^L \psi_{\Lambda; \hat{q}} + \underbrace{w_{\hat{k}} J_e(\boldsymbol{\xi}_{\hat{k}}) \mathbf{S}_{\hat{k}}}_{F_{\hat{k}\hat{k}}}, \\
 \partial_t \psi_{\Lambda; \hat{q}} + \omega_\Lambda \psi_{\Lambda; \hat{q}} &= y_\Lambda \omega_\Lambda \sum_{\hat{h}=1}^N \sum_{i=1}^3 G_i^T(\boldsymbol{\xi}_{\hat{q}}) \frac{\partial \mathbf{l}_{\hat{h}}(\boldsymbol{\xi}_{\hat{q}})}{\partial r_i} \mathbf{u}_{\hat{h}}.
 \end{aligned} \tag{1.43}$$

From the Equation 1.43, we can introduce the global mass matrix \mathbf{M} which is diagonal by construction. The diagonal term is

$$M_{\hat{k}\hat{k}} = w_{\hat{k}} \rho(\boldsymbol{\xi}_{\hat{k}}) J_e(\boldsymbol{\xi}_{\hat{k}}). \tag{1.44}$$

The weighted spatial derivative matrix \mathcal{D}^w and the spatial derivative matrix \mathcal{D} are written as

$$\mathcal{D}_{\hat{k}\hat{q}}^w = \sum_{\hat{q}=1}^N w_{\hat{q}} J_e(\boldsymbol{\xi}_{\hat{q}}) \sum_{j=1}^3 \frac{\partial \mathbf{l}_{\hat{k}}(\boldsymbol{\xi}_{\hat{q}})}{\partial r_j} G_j(\boldsymbol{\xi}_{\hat{q}}), \tag{1.45}$$

$$\mathcal{D}_{\hat{q}\hat{h}} = \sum_{\hat{h}=1}^N \sum_{i=1}^3 G_i^T(\boldsymbol{\xi}_{\hat{q}}) \frac{\partial \mathbf{l}_{\hat{h}}(\boldsymbol{\xi}_{\hat{q}})}{\partial r_i} \mathbf{u}_{\hat{h}}. \tag{1.46}$$

The operator \mathcal{D} estimates the spatial derivatives of a vector in the Cartesian space. The operator \mathcal{D}^w is the spatial derivatives operator, weighted by GLL weights $w_{\hat{q}}$ and the local Jacobiand determinant $J_e(\boldsymbol{\xi}_{\hat{q}})$. The stiffness matrix can be defined through the spatial derivative matrices as

$$\mathbf{K} = \mathcal{D}^w C \mathcal{D}. \quad (1.47)$$

The source term is taken into account inside the matrix \mathbf{F} with

$$F_{\hat{k}\hat{k}} = w_{\hat{k}} J_e(\boldsymbol{\xi}_{\hat{k}}) \mathbf{S}_{\hat{k}}. \quad (1.48)$$

The boundary term \mathbf{B} in Equation 1.38 can be discretized using the similar manner. After discretization in the reference space, an example of the boundary term for the points located at one face of the model can be provided as

$$B_{\hat{k}\hat{k}} = w_{k_1} w_{k_2} J_e^S(\boldsymbol{\xi}_{\hat{k}}) \tau_B(\boldsymbol{\xi}_{\hat{k}}). \quad (1.49)$$

Now, the weak form of the second-order viscoelastic wave in Equation 1.22 can be given as

$$\begin{aligned} M \partial_{tt} \mathbf{u} &= -\mathbf{K} \mathbf{u} + \mathcal{D}^w C^a \sum_{\Lambda=1}^L \psi_{\Lambda} + \mathbf{F} + \mathbf{B}, \\ \partial_t \psi_{\Lambda} + w_{\Lambda} \psi_{\Lambda} &= \omega_{\Lambda} y_{\Lambda} \mathcal{D} \mathbf{u}. \end{aligned} \quad (1.50)$$

In elastic medium, the attenuation contribution $\mathcal{D}^w C^a \sum_{\Lambda=1}^L \psi_{\Lambda}$ vanishes, leading to

$$M \partial_{tt} \mathbf{u} = -\mathbf{K} \mathbf{u} + \mathbf{F} + \mathbf{B}, \quad (1.51)$$

as described by Komatitsch and Tromp (1999). The outgoing wavefield at the model boundaries is absorbed by the combination of sponge layers Cerjan et al. (1985) and radiative boundary condition (Lysmer and Kuhlemeyer, 1969; Kouroussis et al., 2011). A second-order explicit viscoelastic Newmark scheme is used for the time integration to compute the displacement field at each time step (Komatitsch, 1997).

1.3 Full waveform inversion

Full waveform inversion (FWI) is a data fitting procedure between the observed seismograms with the corresponding synthetics, computed by solving the wave equation, given by

$$\chi(\mathbf{m}) = \frac{1}{2} \|\mathbf{d}_{cal}(\mathbf{m}) - \mathbf{d}_{obs}\|^2 = \frac{1}{2} \|R \mathcal{W}(\mathbf{m}) - \mathbf{d}_{obs}\|^2, \quad (1.52)$$

where \mathbf{d}_{cal} is the synthetic data given model \mathbf{m} , \mathbf{d}_{obs} is the observed data, R is the extraction operation which extract the full wavefield \mathcal{W} at receiver positions for each source. \mathcal{W} is defined as the modified incident wavefield which take into account both displacement \mathbf{u} and memory variables fields ψ_{Λ} associated with L -SLS mechanism as

$$\mathcal{W} = \underbrace{(u_1, u_2, u_3)}_{\mathbf{u}}, \underbrace{(\psi_{1;1}, \dots, \psi_{1;6})}_{\psi_1}, \dots, \underbrace{(\psi_{L;1}, \dots, \psi_{L;6})}_{\psi_L}^T. \quad (1.53)$$

With this definition, we can recast Equation 1.22 into a forward problem with variable \mathcal{W} , and rewritten as

$$\begin{aligned}
 & \overbrace{\begin{pmatrix} \rho I_3 & 0 & \dots & 0 \\ 0 & 0 & \dots & 0 \\ \dots & \dots & \dots & \dots \\ 0 & 0 & \dots & 0 \end{pmatrix}}^{\mathbf{B}_2(\mathbf{m})} \partial_{tt} \mathcal{W} + \overbrace{\begin{pmatrix} 0 & 0 & \dots & 0 \\ 0 & I_6 & \dots & 0 \\ \dots & \dots & \dots & \dots \\ 0 & 0 & \dots & I_6 \end{pmatrix}}^{\mathbf{B}_1} \partial_t \mathcal{W} \\
 & + \underbrace{\begin{pmatrix} -DCD^T & DC^a & \dots & DC^a \\ -y_1 \omega_1 D^T & \omega_1 I_6 & \dots & 0 \\ \dots & \dots & \dots & \dots \\ -y_L \omega_L D^T & \omega_L I_6 & \dots & \omega_L I_6 \end{pmatrix}}_{\mathbf{B}_0(\mathbf{m})} \mathcal{W} = \mathbf{S}.
 \end{aligned} \tag{1.54}$$

We can rewrite Equation 1.54 in a more compact form by substituting the matrices with $\mathbf{B}_2(\mathbf{m})$, \mathbf{B}_1 , and $\mathbf{B}_0(\mathbf{m})$ as

$$F(\mathbf{m}, \mathcal{W}) = \mathbf{B}_2(\mathbf{m}) \partial_{tt} \mathcal{W} + \mathbf{B}_1 \partial_t \mathcal{W} + \mathbf{B}_0(\mathbf{m}) \mathcal{W} - \mathbf{S} = 0. \tag{1.55}$$

In the context of my PhD, there are only two model parameters that are taken into account (V_P and V_S). In practice, the parameterization is performed on the independent components of the unrelaxed stiffness components (C_{ij}) as

$$\mathbf{m} = (C_{ij}; (1 \leq i \leq j \leq 6)). \tag{1.56}$$

It is important to be noted that in general cases, we can include other model parameter, e.g. density ρ , Q_P^{-1} , and Q_S^{-1} (Trinh, 2018).

1.3.1 Solving the constrained local minimization problem

The iteration in an inversion based on the Newton method is given by

$$\mathbf{m}_{k+1} = \mathbf{m}_k + \alpha \Delta \mathbf{m}. \tag{1.57}$$

where \mathbf{m} is the model parameters, k is the number of iteration, and α is the step length. We consider that the $\Delta \mathbf{m}$ is pointing towards the descent direction, and specified as

$$\Delta \mathbf{m} = -\mathcal{H}^{-1} \nabla \chi_k, \tag{1.58}$$

where \mathcal{H} is the Hessian of the misfit with respect to the model parameters and $\nabla \chi_k$ is the gradient of misfit with respect to the model parameters. The presence of inverse Hessian \mathcal{H}^{-1} might mitigate the cross-talk between parameter. However, the computation of Hessian is unfeasible, especially in 3D case. Therefore, Hessian approximation is often used in practice for Equation 1.58.

I use the SEISCOPE optimization toolbox, an optimization kernel developed by Métivier and Brossier (2016). This toolbox employs the Wolfe condition to determine the step length α and implement various non-linear optimization methods. However, prior to calculating the model update, we need to calculate the gradient of each parameter with respect to the misfit function.

1.3.1.1 Gradient computation

Lagrangian definition and adjoint state formulation

The gradient computation can be performed through the adjoint state approach (Plessix, 2006; Trinh, 2018). The Lagrangian function with the Lagrangian multiplier vector ν , subjected to the wave equation constraint as

$$\mathcal{L}(\mathbf{m}, \mathcal{W}, \nu) = \frac{1}{2} \|R\mathcal{W} - \mathbf{d}_{obs}\|^2 + \langle \nu, F(\mathbf{m}, \mathcal{W}) \rangle. \quad (1.59)$$

The inner product $\langle \cdot, \cdot \rangle$ is defined over the space and time domain $\Omega \times [0 - t]$. This definition of the Lagrangian multiplier is not unique and do not represent a certain physical meaning.

Let $\mathcal{W}(\mathbf{m})$ be the solution of the forward problem 1.55 for the model parameter \mathbf{m} . Then the second term of the Lagrangian function is cancelled,

$$\mathcal{L}(\mathbf{m}, \mathcal{W}(\mathbf{m}), \nu) = \frac{1}{2} \|R\mathcal{W}(\mathbf{m}) - \mathbf{d}_{obs}\|^2 = \chi(\mathbf{m}), \quad (1.60)$$

and giving us the misfit function $\chi(\mathbf{m})$. Therefore, the gradient of the misfit function can be calculated from the derivative of the Lagrangian function with respect to model parameters \mathbf{m} as

$$\frac{\partial \chi(\mathbf{m})}{\partial \mathbf{m}} = \frac{\partial \mathcal{L}(\mathbf{m}, \mathcal{W}(\mathbf{m}), \nu)}{\partial \mathbf{m}}. \quad (1.61)$$

Using the chain rule, the Equation 1.61 can be transformed into

$$\frac{\partial \chi(\mathbf{m})}{\partial \mathbf{m}} = \left\langle \nu, \frac{\partial F(\mathbf{m}, \mathcal{W}(\mathbf{m}))}{\partial \mathbf{m}} \right\rangle + \frac{\partial \mathcal{L}(\mathbf{m}, \mathcal{W}(\mathbf{m}), \nu)}{\partial \mathcal{W}(\mathbf{m})} \frac{\partial \mathcal{W}(\mathbf{m})}{\partial \mathbf{m}}, \quad (1.62)$$

where the adjoint fields are considered as independent with the model parameters (i.e. $\partial \nu / \partial \mathbf{m} = 0$).

Similar to the construction of the incident wavefield $\mathcal{W}(\mathbf{m})$, we define the Lagrangian multiplier from the adjoint displacement $\bar{\mathbf{u}}$ and memory variable fields $\bar{\phi}_\Lambda$ as

$$\nu = (\bar{\mathbf{u}}, \bar{\phi}_1, \dots, \bar{\phi}_L)^T, \quad (1.63)$$

which satisfies

$$\frac{\partial \mathcal{L}(\mathbf{m}, \mathcal{W}(\mathbf{m}), \nu)}{\partial \mathcal{W}(\mathbf{m})} = 0. \quad (1.64)$$

Then the gradient of misfit function on model parameters \mathbf{m} in Equation 1.62 can be simplified into

$$\frac{\partial \chi(\mathbf{m})}{\partial \mathbf{m}} = \left\langle \nu, \frac{\partial F(\mathbf{m}, \mathcal{W}(\mathbf{m}))}{\partial \mathbf{m}} \right\rangle. \quad (1.65)$$

Now, we would like to construct the adjoint systems. Prior to a detailed discussion, there are some important properties of adjoint operators \cdot^\dagger with respect to time and spatial derivatives that we use in the next developments

$$D^\dagger = -D^T, \quad (\partial_t)^\dagger = -\partial_t, \quad (1.66)$$

where D is the first order spatial derivative operator discribed in Equation 1.5. From Equation 1.64 and the adjoint operator's properties in Equation 1.66, we can compute the adjoint fields ν through

$$0 = \frac{\partial \mathcal{L}(\mathbf{m}, \mathcal{W}(\mathbf{m}), \nu)}{\partial \mathcal{W}(\mathbf{m})} = R^\dagger (R\mathcal{W}(\mathbf{m}) - \mathbf{d}_{obs}) + \left(\frac{\partial F(\mathbf{m}, \mathcal{W}(\mathbf{m}))}{\partial \mathcal{W}(\mathbf{m})} \right)^\dagger \nu. \quad (1.67)$$

Considering the properties of the adjoint operator in Equation 1.66, we get

$$\mathbf{B}_2^\dagger(\mathbf{m})\partial_{tt}\nu - \mathbf{B}_1^\dagger\partial_t\nu + \mathbf{B}_0(\mathbf{m})^\dagger\nu = -R^\dagger(R\mathcal{W}(\mathbf{m}) - \mathbf{d}_{obs}). \quad (1.68)$$

Since no contribution of data residual is coming from the memory variables Δd_{ϕ_Λ} , the overall data residual can be simplified to

$$R\mathcal{W}(\mathbf{m}) - \mathbf{d}_{obs} = [\Delta d_{\mathbf{u}}, \Delta d_{\phi_1}, \dots, \Delta d_{\phi_L}]^T = [\Delta d_{\mathbf{u}}, 0, \dots, 0]^T. \quad (1.69)$$

Similar to the expansion on Equation 1.54, the Equation 1.68 can be expanded as

$$\begin{aligned} & \overbrace{\begin{pmatrix} \rho I_3 & 0 & \dots & 0 \\ 0 & 0 & \dots & 0 \\ \dots & \dots & \dots & \dots \\ 0 & 0 & \dots & 0 \end{pmatrix}}^{\mathbf{B}_2^\dagger(\mathbf{m})} \partial_{tt} \begin{bmatrix} \bar{\mathbf{u}} \\ \bar{\phi}_1 \\ \dots \\ \bar{\phi}_L \end{bmatrix} - \overbrace{\begin{pmatrix} 0 & 0 & \dots & 0 \\ 0 & I_6 & \dots & 0 \\ \dots & \dots & \dots & \dots \\ 0 & 0 & \dots & I_6 \end{pmatrix}}^{\mathbf{B}_1^\dagger} \partial_t \begin{bmatrix} \bar{\mathbf{u}} \\ \bar{\phi}_1 \\ \dots \\ \bar{\phi}_L \end{bmatrix} + \\ & \underbrace{\begin{pmatrix} -DCD^T & y_1\omega_1 D & \dots & y_L\omega_L D \\ -C^a D^T & \omega_1 I_6 & \dots & 0 \\ \dots & \dots & \dots & \dots \\ -C^a D^T & 0 & \dots & \omega_L I_6 \end{pmatrix}}_{\mathbf{B}_0^\dagger} \begin{bmatrix} \bar{\mathbf{u}} \\ \bar{\phi}_1 \\ \dots \\ \bar{\phi}_L \end{bmatrix} = \begin{bmatrix} -R^\dagger \Delta d_{\mathbf{u}} \\ 0 \\ \dots \\ 0 \end{bmatrix}, \end{aligned} \quad (1.70)$$

resulting in the second order adjoint system

$$\begin{aligned} \rho\partial_{tt}\bar{\mathbf{u}} &= DCD^T\bar{\mathbf{u}} - D \sum_{\Lambda=1}^L y_\Lambda \omega_\Lambda \bar{\phi}_\Lambda - R^\dagger \Delta d_{\mathbf{u}}, \\ \partial_t \bar{\phi}_\Lambda - \omega_\Lambda \bar{\phi}_\Lambda &= -C^a D^T \bar{\mathbf{u}}. \end{aligned} \quad (1.71)$$

In this adjoint system the residual at the receiver positions behave as the source terms. We introduced the modified adjoint memory variable $\bar{\psi}_\Lambda$ such that

$$y_\Lambda \omega_\Lambda \bar{\phi}_\Lambda = C^a \bar{\psi}_\Lambda, \quad (1.72)$$

which transforms the adjoint system in Equation 1.71 into

$$\begin{aligned} \rho\partial_{tt}\bar{\mathbf{u}} &= DCD^T\bar{\mathbf{u}} - DC^a \sum_{\Lambda=1}^L \bar{\psi}_\Lambda - R^\dagger \Delta d_{\mathbf{u}}, \\ \partial_t \bar{\psi}_\Lambda - \omega_\Lambda \bar{\psi}_\Lambda &= -y_\Lambda \omega_\Lambda D^T \bar{\mathbf{u}}. \end{aligned} \quad (1.73)$$

If we look carefully, this adjoint system is similar to the forward problem in Equation 1.22. The difference is the negative sign in the memory variable ODE and the adjoint source. It is important to be noted that we need to be sure that the adjoint field equation is stable in terms of the energy. The reverse sign in this ODE means an exponential increase of the amplitude of the adjoint field. However, the adjoint field backpropagates in time. Thus, the reversed sign in the ODE corresponds to the attenuation. The adjoint field is also attenuated, but reversely in time; therefore, it is still a computationally stable equation.

Gradient formulation

In my PhD work, I am only interested in reconstructing two elastic parameters, V_P and V_S . The gradient of both parameters can be estimated by calculating the gradient on stiffness coefficients C_{ij} as

$$\frac{\partial \chi(\mathbf{m})}{\partial C_{ij}} = \left\langle \nu, \frac{F(\mathbf{m}, \mathcal{W}(\mathbf{m}))}{\partial C_{ij}} \right\rangle. \quad (1.74)$$

The derivative of the forward problem (Eq. 1.55) on C_{ij} coefficients is given by

$$\begin{aligned} \frac{\partial F(\mathbf{m}, \mathcal{W}(\mathbf{m}))}{\partial C_{ij}} &= \overbrace{\begin{pmatrix} -D \frac{\partial C}{\partial C_{ij}} D^T & D \frac{\partial C^a}{\partial C_{ij}} & \cdots & D \frac{\partial C^a}{\partial C_{ij}} \\ 0 & 0 & \cdots & 0 \\ \cdots & \cdots & \cdots & \cdots \\ 0 & 0 & \cdots & 0 \end{pmatrix}}^{\partial \mathbf{B}_0(\mathbf{m}) / \partial C_{ij}} \begin{bmatrix} \mathbf{u} \\ \psi_1 \\ \cdots \\ \psi_L \end{bmatrix} \\ &= \begin{bmatrix} -D \frac{\partial C}{\partial C_{ij}} D^T \mathbf{u} + \sum_{\Lambda=1}^L D \frac{\partial C^a}{\partial C_{ij}} \psi_{\Lambda} \\ 0 \\ \cdots \\ 0 \end{bmatrix}. \end{aligned} \quad (1.75)$$

By considering the Lagrangian multiplier vector ν , the elementary C_{ij} gradient in Equation 1.74 becomes

$$\begin{aligned} \frac{\partial \chi(\mathbf{m})}{\partial C_{ij}} &= \left\langle \begin{bmatrix} \bar{\mathbf{u}} \\ \bar{\phi}_1 \\ \cdots \\ \bar{\phi}_L \end{bmatrix}, \begin{bmatrix} -D \frac{\partial C}{\partial C_{ij}} D^T \mathbf{u} + \sum_{\Lambda=1}^L D \frac{\partial C^a}{\partial C_{ij}} \psi_{\Lambda} \\ 0 \\ \cdots \\ 0 \end{bmatrix} \right\rangle, \\ &= \left\langle \bar{\mathbf{u}}, -D \frac{\partial C}{\partial C_{ij}} D^T \mathbf{u} \right\rangle + \left\langle \bar{\mathbf{u}}, \sum_{\Lambda=1}^L D \frac{\partial C^a}{\partial C_{ij}} \psi_{\Lambda} \right\rangle. \end{aligned} \quad (1.76)$$

Considering the properties of the adjoint operator in Equation 1.66, we obtain

$$\frac{\partial \chi(\mathbf{m})}{\partial C_{ij}} = \left\langle D^T \bar{\mathbf{u}}, \frac{\partial C}{\partial C_{ij}} D^T \mathbf{u} \right\rangle - \left\langle D^T \bar{\mathbf{u}}, \sum_{\Lambda=1}^L \frac{\partial C^a}{\partial C_{ij}} \psi_{\Lambda} \right\rangle. \quad (1.77)$$

We simplify this expression by considering the adjoint $\bar{\boldsymbol{\varepsilon}} = D^T \bar{\mathbf{u}}$ and forward strain $\boldsymbol{\varepsilon} = D^T \mathbf{u}$. The gradient on stiffness coefficient C_{ij} becomes

$$\frac{\partial \chi(\mathbf{m})}{\partial C_{ij}} = \left\langle \bar{\boldsymbol{\varepsilon}}, \frac{\partial C}{\partial C_{ij}} \boldsymbol{\varepsilon} \right\rangle - \left\langle \bar{\boldsymbol{\varepsilon}}, \sum_{\Lambda=1}^L \frac{\partial C^a}{\partial C_{ij}} \psi_{\Lambda} \right\rangle. \quad (1.78)$$

In elastic medium, the second term on the right-hand side related to the memory variables vanishes. The gradient of V_P and V_S can be computed by chain rule using

$$\begin{aligned} \frac{\partial \chi(\mathbf{m})}{\partial V_P} &= \sum_{i=1}^6 \sum_{j=1}^6 \frac{\partial \chi}{\partial C_{ij}} \frac{\partial C_{ij}}{\partial V_P} \\ \frac{\partial \chi(\mathbf{m})}{\partial V_S} &= \sum_{i=1}^6 \sum_{j=1}^6 \frac{\partial \chi}{\partial C_{ij}} \frac{\partial C_{ij}}{\partial V_S} \end{aligned} \quad (1.79)$$

Note that the other parameter's gradient (density ρ , Q_P^{-1} , Q_S^{-1}) can also be calculated using a similar manner (Trinh, 2018).

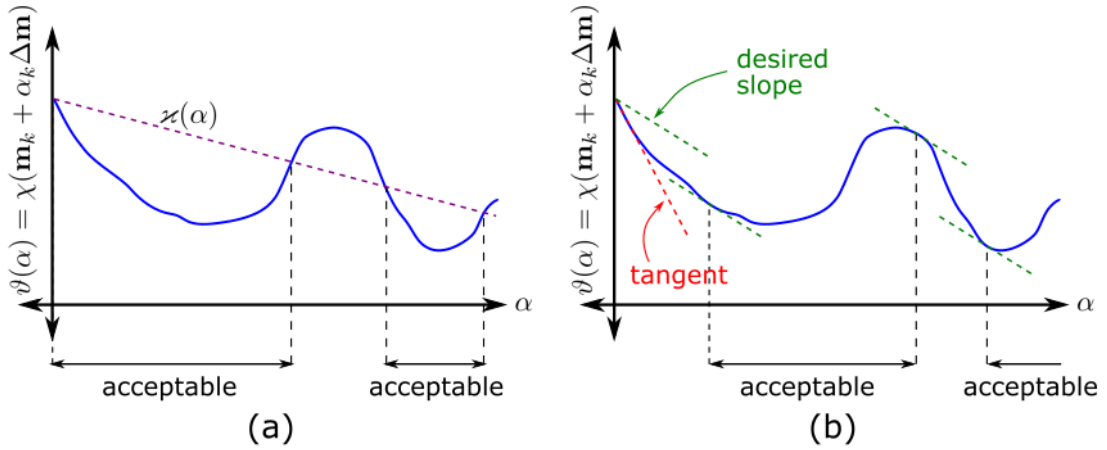


Figure 1.2: Sufficient decrease condition (a) and the curvature condition (b). Two condition for satisfying the Wolfe condition. The picture is adapted from Nocedal and Wright (2006).

1.3.1.2 Step-length estimation

The step length controls the magnitude of movement along the descent direction $\Delta \mathbf{m}_k$ at each iteration. The step-length α_k is computed using line search method following Wolfe conditions (Wolfe, 1969). Nocedal and Wright (2006) write two criteria that need to be satisfied:

- Sufficient decrease condition: for a given size of step-length, the misfit function reduction should be proportional to both the step length and the directional derivative

$$\chi(\mathbf{m}_k + \alpha_k \Delta \mathbf{m}_k) \leq \chi(\mathbf{m}_k) + b_1 \alpha_k \nabla \chi_k^T \Delta \mathbf{m}_k \quad (1.80)$$

In practice, the constant b_1 is chosen to be a small quantity as $b_1 = 10^{-4}$. This condition is illustrated in Figure 1.2a as a linear line $\varkappa(\alpha)$.

- Curvature condition: avoiding very small step length, which could slow down or prevent the convergence.

$$\nabla \chi(\mathbf{m}_k + \alpha_k \Delta \mathbf{m}_k)^T \Delta \mathbf{m}_k \geq b_2 \nabla \chi(\mathbf{m}_k)^T \Delta \mathbf{m}_k \quad (1.81)$$

The left-handside of Equation 1.81 is the derivative of $\vartheta(\alpha)$. This curvature condition ensure that the slope of ϑ at α_k is greater than b_2 times the initial slope $\vartheta(0)$. In practice, the constant b_2 is chosen to be close to 1 as $b_2 = 0.9$. The illustration of this condition can be seen in Figure 1.2b.

The Wolfe condition ensure the convergence of the inversion with an arbitraty initial guess as long as the misfit function is bounded and twice continuously differentiable.

1.3.1.3 Descent direction computation through Quasi-Newton *l*-BFGS

The idea behind the *l*-BFGS method is taking into account the information inside the Hessian without paying the full price of the Hessian calculation itself. The concept can be realized by considering several gradients from the previous iterations and using it to approximate the inverse Hessian (Byrd et al., 1995; Métivier and Brossier, 2016). The information is included inside the descent direction as

$$\Delta \mathbf{m}_k = -\mathbf{Q}_k \nabla \chi(\mathbf{m}_k), \quad (1.82)$$

where the \mathcal{Q} is the approximation of the inverse Hessian \mathcal{H}^{-1} at iteration k . This approach significantly improves the convergence compared to the standard steepest descent and non-linear conjugate gradient, even though the number of the previous gradients which are taken into account are small (5 to 20). The numerical implementation follows a two-loops recursion strategies, which avoids any explicit estimation of the inverse Hessian.

I consider the l -BFGS as the balance between fast and stable convergence for my cases. Therefore, all synthetic and field data applications in this manuscript use l -BFGS to compute its descent direction.

1.3.2 Preconditioning application

In our application, we employ a smoothing of the gradient and a preconditioning for the l -BFGS optimization where we provide an estimation of the inverse Hessian matrix.

1.3.2.1 Bessel gradient smoothing

From a mathematical perspective, FWI is an ill-posed inverse problem with a highly non-unique solution. In practice, regularization strategies are required to reduce the size of the solution space. Trinh et al. (2017) proposes a gradient smoothing through the Bessel filter. This smoothing strategy is an anisotropic filter that benefits from taking into account prior information of the geological structure. Bessel filter is applied within the spectral element meshes framework through its standard weak formulation; therefore, avoiding the projection loop of SEM meshes in Gauss Lobatto Legendre points and Cartesian coordinate or an explicit windowed convolution in SEM meshes. Variable coherent lengths and orientation are required as the input of this Bessel filter.

1.3.2.2 Depth preconditioning

Depth preconditioning is widely used to enhance the model estimation with depth. Formally, it introduces an approximation of the inverse Hessian \mathcal{Q} as a diagonal operator with the increasing weights over depth. The standard formulation is given as

$$\mathcal{Q} \approx \mathcal{P}(z, x, y) = (\varrho + z)^\varphi \quad (1.83)$$

where \mathcal{P} is the optimization preconditioning, ϱ is a pre-defined constant related to the depth compensation, and φ is a pre-defined constants related to mathematical power. In the 3D application, the φ constant is usually chosen as 2. In marine applications, ϱ can be set as 0 since the zero-depth is located inside the water column. The depth preconditioning appears to be robust and efficient for a flat-topography condition. Since my applications are small cases with flat topography, I consider this depth preconditioning for my synthetic and field experiments.

1.4 Implementation: SEM46 code

The waveform modeling and inversion methodology that I have briefly described is implemented in the SEM46 package (Fig 1.3). It is a 3D viscoelastic full waveform modeling and inversion software based on a spectral element discretization of the elastodynamics equation (Trinh et al., 2019b). It is written in

Fortran with MPI (Message Passing Interface). For the inversion part, it is coupled to the SEISCOPE optimization toolbox (Métivier and Brossier, 2016).

SEM46 has several specificities aside from the intrinsic benefit of the spectral element method that has been explained in Section 1.2. SEM46 has a cartesian-based mesh which is easy to implement. SEM46 is also has an efficient and scalable parallelism over the sources and domains.



Figure 1.3: The logo of SEM46 (Brossier and Trinh, 2017).

Chapter 2

The Ettlingen Line and 9C seismic data

Contents

2.1	The Ettlingen Line	35
2.2	Previous geophysical investigations	38
2.3	3D 9C Seismic Acquisition	40
2.3.1	Motivation	40
2.3.2	Data acquisition	40
2.4	Pre-processing and data correction	44
2.4.1	Data evaluation	44
2.4.2	Data correction using matching filter	44

2.1 The Ettlingen Line

This study's target is a historical defensive trench line (Fig. 2.1) located at Rheinstetten, Germany. German troops built it during the War of the Spanish Succession in 1707 (Lang et al., 1907). It spans from the Fort of Philippsburg in the northwest to the Schwarzwald (Black Forest) in the southeast part of Figure 2.2. Twenty years later, this defensive trench line is reactivated during the War of the Polish Succession from 1733 to 1735. The majority of the Ettlingen Line is destroyed in May 1734, when the French troops pushed back the German forces.

Along the original Ettlingen Line, there are three types of defensive structures. The first type is bulky wood obstacles; the second type is a V-shaped trench combined with the sturdy wood obstacles, and the last is a V-shaped trench with the palisades wall. The southeast part of the Ettlingen line is dominated by the first type, whereas the northwest part of the Ettlingen Line is dominated by the second and the third structure's types. Figure 2.1a shows the original shape of the third type of the Ettlingen Line's structure. Most of the Ettlingen Line remains which are still exist nowadays have been eroded (Fig. 2.1b), and at some locations, the Ettlingen Line has been leveled to the ground as depicted in Figure 2.1c.

Figure 2.2 shows the comparison between the ancient map between the period of winter 1707 to the winter 1708 and the modern era taken from Google Maps in October 2020. The historical site of the Ettlingen Line is still preserved at some locations, indicated by the red circles on both maps. There are several significant differences between ancient and modern maps. For example, Karlsruhe city has not been founded in 1707; the road system and populated area are also seen to be expanded in the modern era. Nowadays, the Ettlingen Line can only be seen in the preserved area.

My field experiment is located at the preserved area of the Ettlingen Line. It is located inside the red circle in Figure 2.2, and later detailed as the white rectangle in the base map plot in Figure 2.3a. Some parts of the Ettlingen Line have been leveled to the ground (dashed red line), probably due to the glider airfield's development. Fortunately, at the northwest and southeast of the experiment, we can observe the existing trench line (solid red lines), albeit the vegetation covers it (Fig. 2.3b).

Based on the geological map from Hüttner et al. (1968), the trench is surrounded by Pleistocene fluvial sediment deposits from the Rhine River, which can be seen at the west from the trench location. Typically, the war trench is not a deep structure. There might not be any other significant geological structure and formation in our experiment with only a few meters depth.

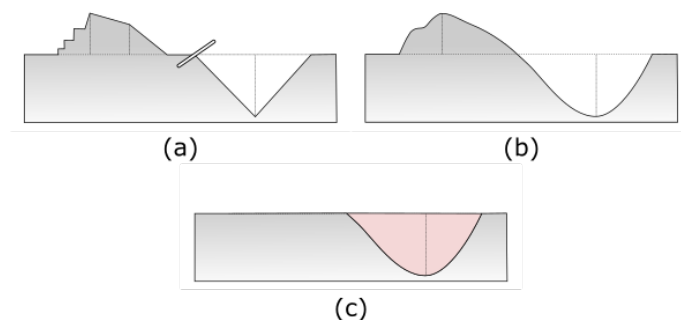


Figure 2.1: The original shape of the trench (a), the shape of the existing trench (b), and the current shape of the buried trench (c) redrawn from Lang et al. (1907). The trench's existing shape is smoother due to erosion, and the wooden palisade wall also does not exist anymore. Our target is the buried trench (c) in which I do not know any more the boundary and the geometry of the original trench.

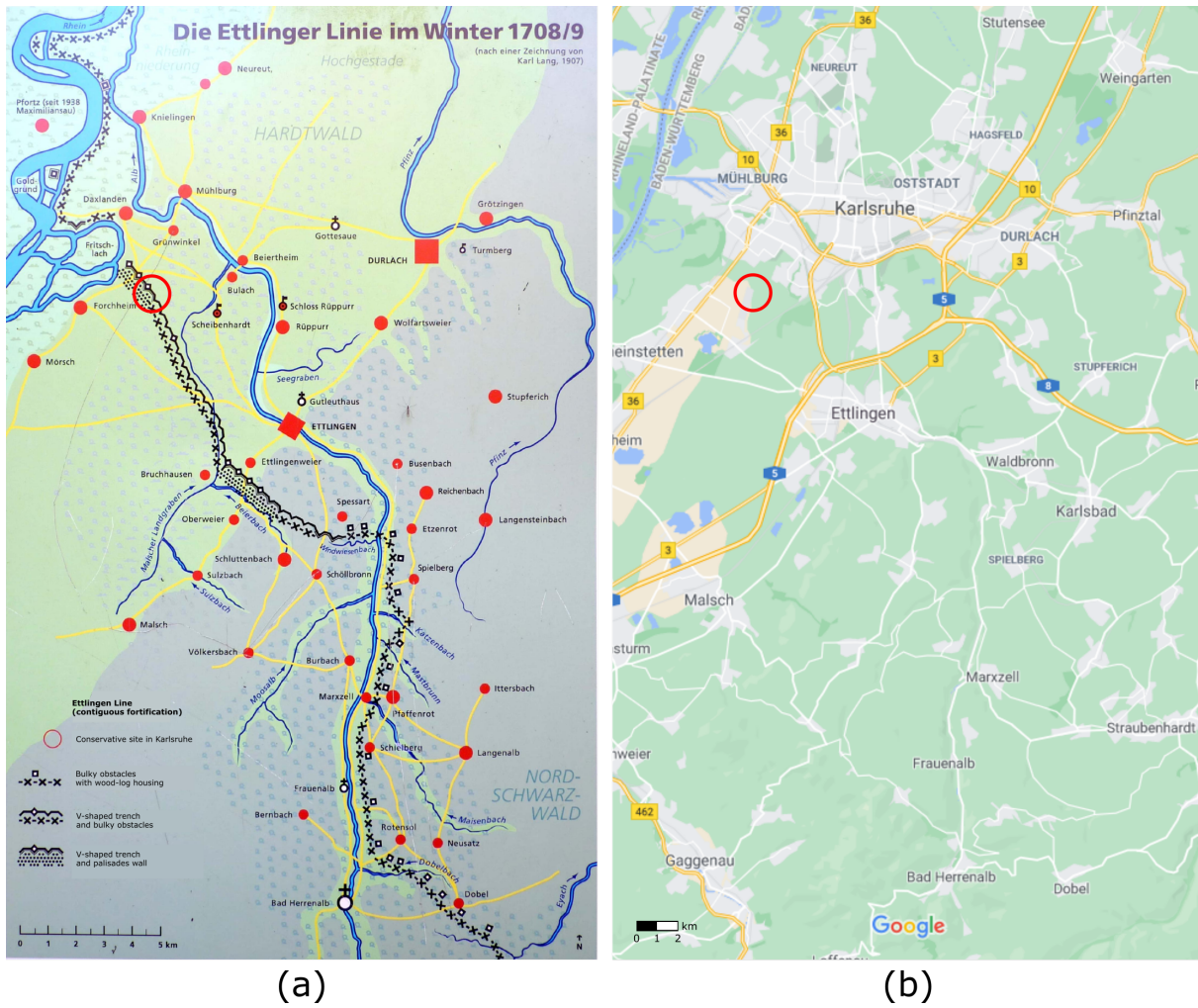


Figure 2.2: Photo of the information panel of the Ettlingen Line showing the old map between the period of winter 1707 to 1708 (a). Modern map of Karlsruhe and Ettlingen taken from Google Maps in October 2020 (b). The red circle indicates the preserved area of the trench and the approximate location of the field experiment. At the time of the Ettlingen Line’s construction, the city of Karlsruhe has not been founded.

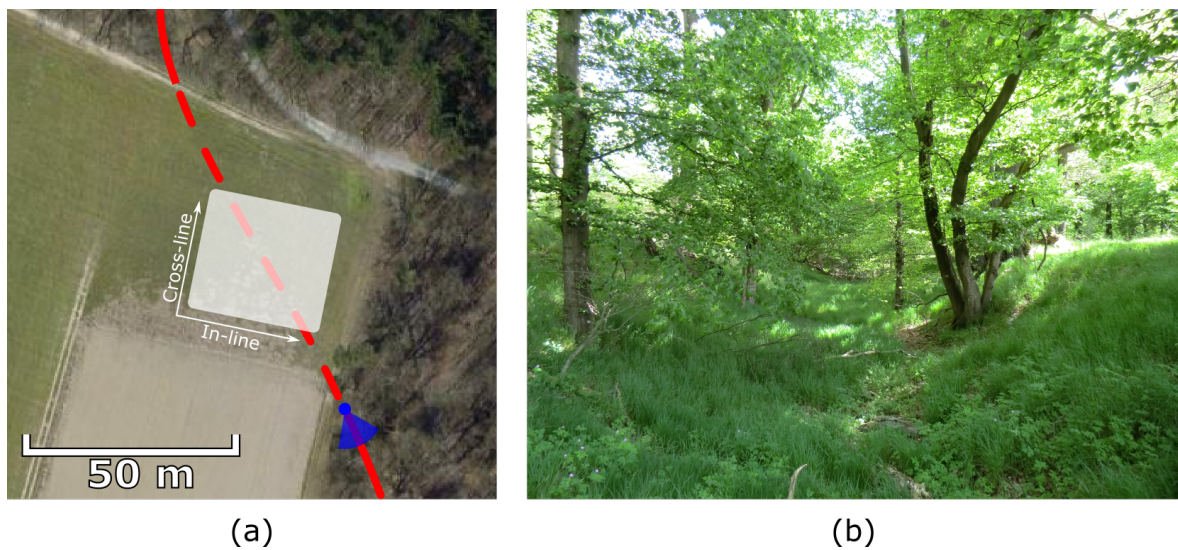


Figure 2.3: Basemap of the acquisition at Rheinstetten (a). Red solid line represents the existing location of the trench, red dashed line represents the possible buried location of the trench line, and the white rectangle represents seismic acquisition location. The existing V-shaped trench of the Ettlingen Line at the south-east of the study area (b). Blue circle in (a) represents the approximate location of the photo, whereas its translucent cone depicts the estimated field of view of the photo in (b).

2.2 Previous geophysical investigations

Several experiments have been performed in this area to uncover the geometry of the buried trench. Binnig (2015) performed 2D FWI on two seismic lines (profile 1 and 2 on Fig. 2.4). The seismic lines were acquired across the possible location of the Ettlingen Line. Vertical direction sources excited using sledgehammer are recorded using vertical geophones. In his experiment, he performed 2D multicomponent FWI in viscoelastic medium up to 30 Hz. Figure 2.5 shows the reconstructed V_S on two seismic profiles. The Ettlingen Line is reconstructed as a low-velocity anomaly with an inverted triangle shape.

Wittkamp et al. (2018) performed 2D seismic acquisition using single-component vertical source and 3C receiver on profile 3 (Fig. 2.4). They used vertical hammer blows on a steel plate to excite the P-SV dataset and horizontal hammer blows in the crossline direction to excite the SH dataset. They performed three different FWI experiments on viscoelastic medium up to 130 Hz. The first is an inversion using the Love wave from the SH dataset, the second is an inversion using the Rayleigh wave from the P-SV dataset, and the last is a joint inversion that combines both Love and Rayleigh wave. From their study, they demonstrate that the joint FWI yields better Ettlingen Line's reconstruction. Wegscheider (2017) also performed GPR measurement and data processing for the Ettlingen Line field. His GPR section shows an inverted triangle structure, which was interpreted as the Ettlingen Line. Figure 2.6 shows the final reconstructed V_S model (in colour) overlaid by the previous GPR data processing by Wegscheider (2017).

Pan et al. (2018) performed a detailed 3D MASW, producing a 3D V_S cube. They worked using the same dataset that I have used during my PhD work (Sec. 2.3). Using a multi-channel analysis of the surface wave (MASW), they are able to reconstruct the Ettlingen Line in 3D. They used a boxcar spatial window to localize the dispersion curve after observing that the boxcar spatial window provides the same resolution compared to the gaussian window. They were able to delineate the 3D structure of the Ettlingen Line (Fig. 2.7).

Throughout all these studies, the Ettlingen Line is consistently reconstructed as an inverted triangle shape trench line with a lower velocity anomaly than the surrounding area, which may correspond to a lower soil consolidation level of the filling material. 3D reconstruction of the Ettlingen Line provides a better spatial extension than the 2D velocity model. The width of the Ettlingen Line reaches approximately 6 meters, while the depth is around 5 meters.

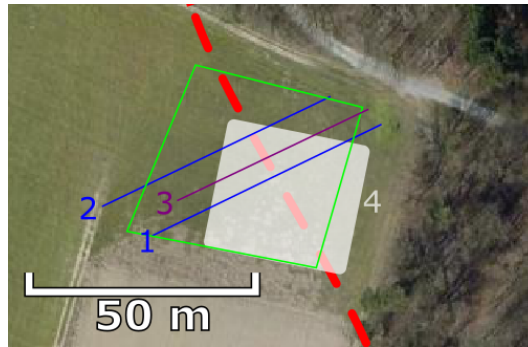


Figure 2.4: Basemap of the acquisition at the Ettlingen Line, Rheinstetten from the previous geophysical experiments. The Red dashed line represents the possible buried location of the trench line. The white rectangle represents seismic acquisition location on Pan et al. (2018) and the study on this PhD thesis. The blue line represents the approximate location of the seismic line in Binnig (2015). The Green rectangle represents the approximate location of the GPR survey in Wegscheider (2017). The purple line depicts the seismic acquisition line in Wittkamp et al. (2018).

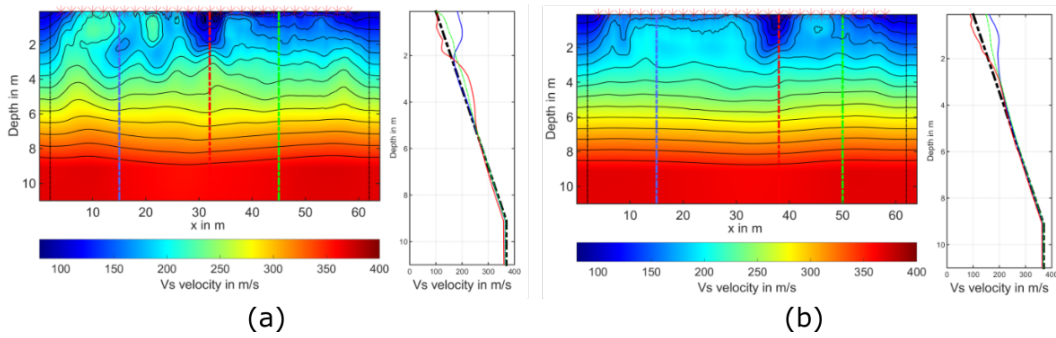


Figure 2.5: Reconstructed V_S on seismic profile 1 (a) and 2 (b) taken from Binnig (2015). The location of each profile can be seen on Figure. 2.4. The vertical lines on each subfigure correspond to the depth profile with the same color. The black dashed lines at the edge of the model are the perfectly matched layer (PML).

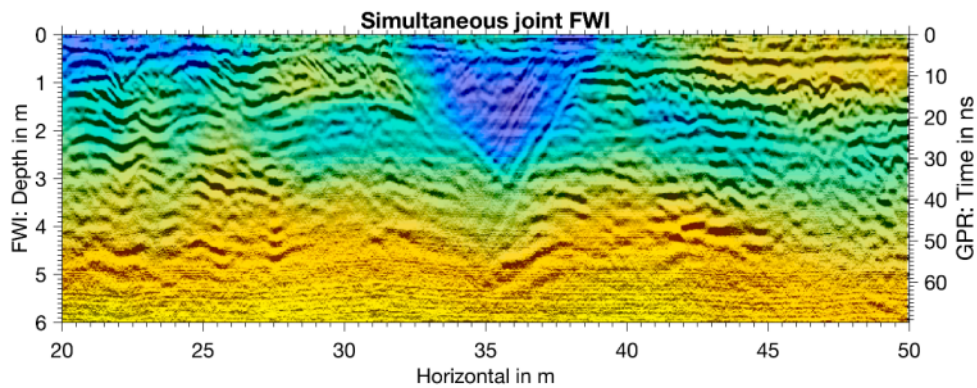


Figure 2.6: Reconstructed V_S overlaid with the GPR section on profile 3 taken from Wittkamp et al. (2018). The GPR experiment was performed by Wegscheider (2017).

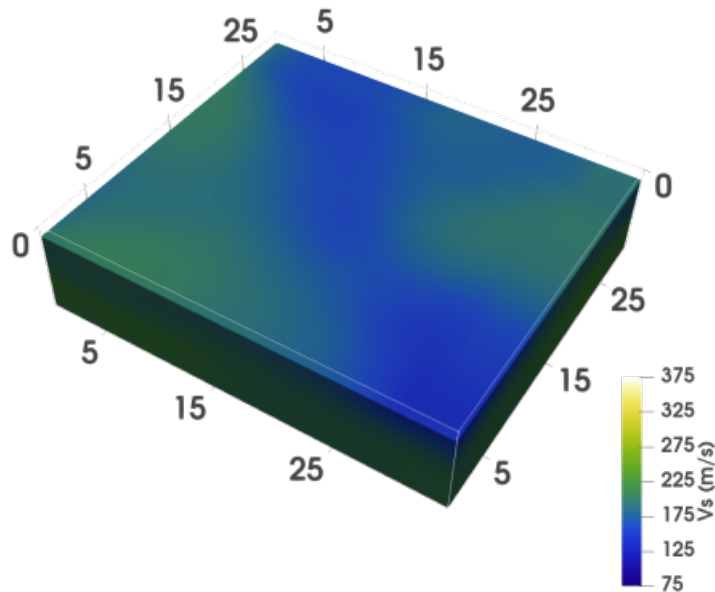


Figure 2.7: 3D reconstructed V_S from MASW data processing by Pan et al. (2018). The Ettligen Line is indicated by a low velocity zone.

2.3 3D 9C Seismic Acquisition

2.3.1 Motivation

Karlsruhe Institute of Technology (KIT) has performed several geophysical investigations on Ettligen Line field. Their previous experiments consistently confirm the shape of the Ettligen Line. The simple and geologically known target makes it interesting to be treated as a benchmark model to investigate 3D elastic FWI in the shallow seismic context. The first 3D model reconstruction using MASW technique has shown benefit by showing the ability to see the lateral extension of the Ettligen Line, as demonstrated by Pan et al. (2018).

This time, I have been able to join in the field to perform the 3D dense multicomponent seismic acquisition. The acquisition campaign was lead by KIT, with equipment support from GFZ Potsdam, ETH Zurich, and Univ. Grenoble Alpes (UGA) in April 2017.

2.3.2 Data acquisition

This experiment performed a 3D seismic acquisition with three-component Galperin sources and three-component (3C) receivers, resulting in 9C seismic data.

A Galperin source is a multicomponent source which is designed for shallow seismic applications (Häusler et al., 2018). It has three different source directions (U, V, and W), which are not aligned with the Cartesian coordinate axis. An illustration of this particular type of source is given in Figure 3.3a. It is built from iron and filled with wood inside. The wood inside the Galperin source helps to reduce the reverberation during seismic acquisition. The orientation of each source direction is depicted in Figure 3.3b. The source directions (U, V, and W) form 120° angles with each other, from the horizontal

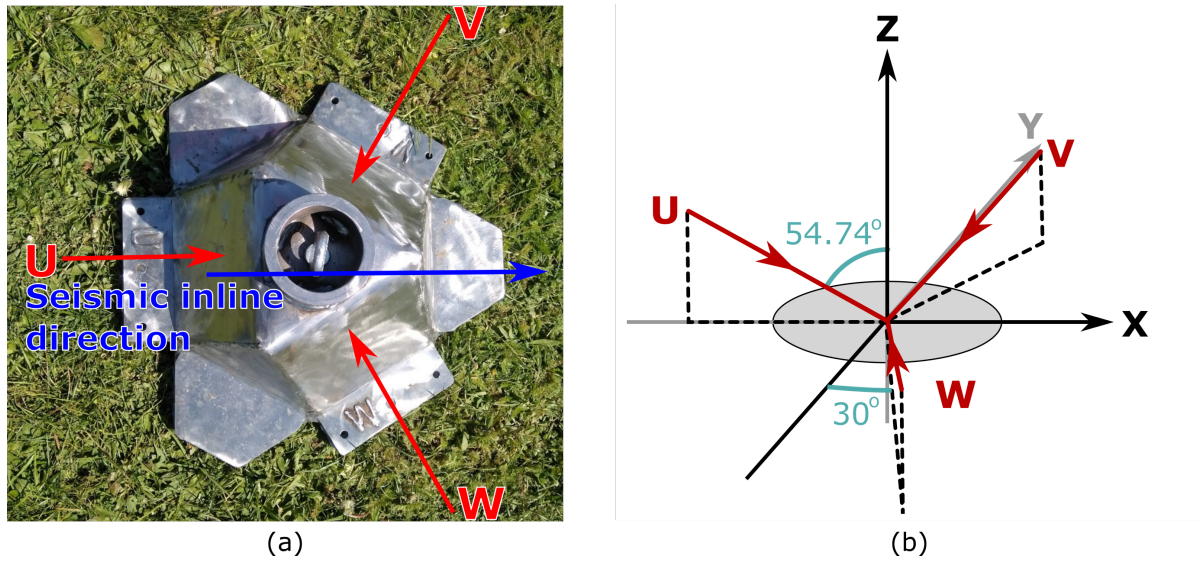


Figure 2.8: The Galperin source used in 9C seismic acquisition (a), and its schematic explaining the three principal orthogonal direction of the source (b) (Häusler et al., 2018).

plane's perspective. Furthermore, all source directions form an angle θ of 54.74° with the vertical axis (Z). Source directions V and W form an angle ϕ of 30° with the Y axis. The theoretical force distribution along Cartesian coordinates is given in Table 3.1, assuming a point force F on each source direction.

Table 2.1: Cartesian point source weights to represent a directional point source.

Source Direction	F_Z	F_X	F_Y
U	$F \cos \theta$	$F \sin \theta$	0
V	$F \cos \theta$	$-F \sin \theta \cos \phi$	$-F \sin \theta \sin \phi$
W	$F \cos \theta$	$-F \sin \theta \cos \phi$	$F \sin \theta \sin \phi$

The 3C geophones record seismic vibrations along the vertical and the horizontal components aligned with the Cartesian axis of Z, X, and Y (Fig. 2.9a and b). Two different types of receivers with the same eigenfrequency of 4.5 Hz have been used. For each source location and direction, three seismic stacks have been performed. The total recording time is $T = 1$ second with 4 kHz frequency sampling. Tabel 2.2 presents the complete list of the equipment which were used during the acquisition campaign.

We have performed two sequential seismic acquisitions: each with different receiver geometries. Both acquisitions use 36 Galperin sources in the same positions. They are indicated by black circles in Figure 3.4. The sources have been installed following a staggered pattern resulting in a minimum source spacing of about 5.66 m. The first acquisition uses a coarse repartition of receivers with 2 m inline and 4 m crossline spacing, giving 128 3C geophone positions in total (Fig. 3.4a). The second uses a dense repartition of receivers, with 1 m inline and crossline spacing, giving 888 3C geophone positions in total (Fig. 3.4b). Because of the limited number of available pieces of equipment (160 3C geophones), the dense acquisition has been split into six acquisition subsets (color-coded on Fig. 3.4b) acquired during five days in total, repeating all source locations for each subset.

Table 2.2: List of equipment used during the acquisition.

Type	Owner	Item description
Source	GPI KIT	3C Galperin Source
Receiver	ETH Zurich	40 3C geophones, eigenfrequency of 4.5 Hz, brand: Geo Space (Houston,TX USA), 5 geophone cables, 5 interface cables, 5 geodes (ver. 7.15), 7 batteries, and 7 connection cables.
	GFZ Potsdam (GIPP)	34 3C geophones, eigenfrequency of 4.5 Hz, brand: SENSOR (Netherlands) with 34 adapters, 10 geophone cables, 12 interface cables, 10 geodes (ver. 9.28), 10 batteries, 10 connection cables, and 2 dual interface boxes.
	GPI KIT	51 3C geophones, eigenfrequency of 4.5 Hz, brand: Geo Space (Houston, TX USA), 5 geophone cables, 5 interface cables, 3 geodes (2 geodes with Ver. 9.30 and 1 geode with Ver. 9.04), 3 batteries, and 3 connection cables.
	Univ. Grenoble Alpes	38 3C geophones, eigenfrequency of 4.5 Hz, brand: Geo Space (Houston, TX USA) 1 interface cable, 2 geodes (Ver. 9.14 and Ver. 7.06), 2 batteries, and 2 connection cables.

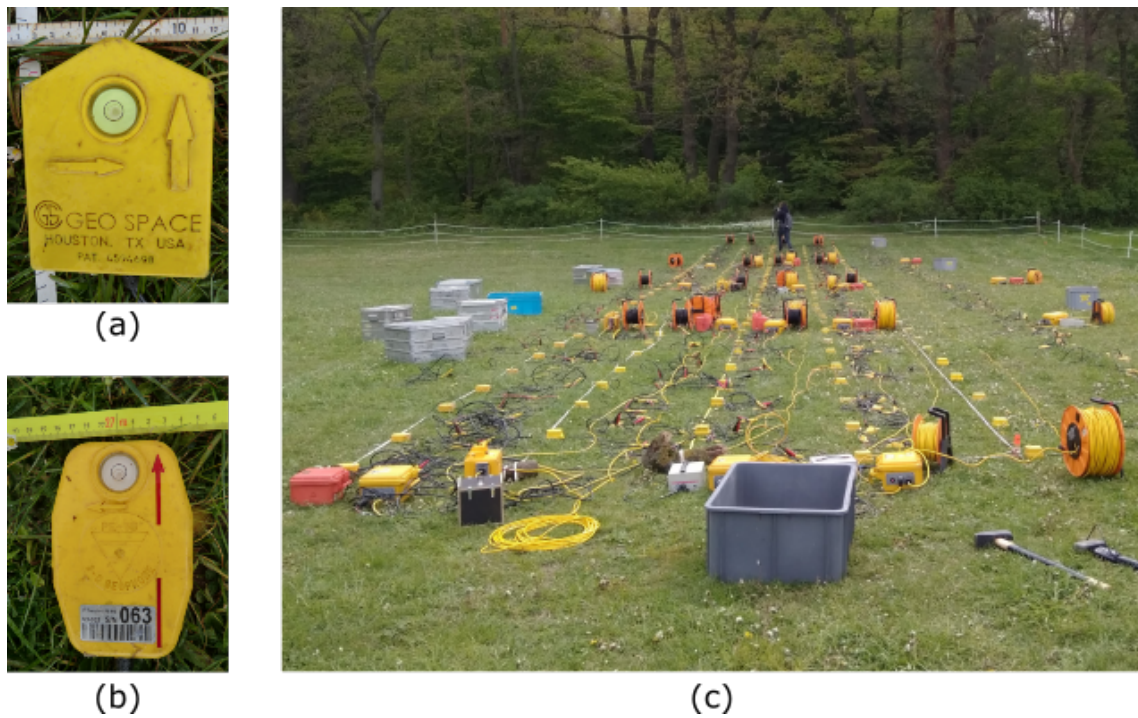


Figure 2.9: The Galperin source used in 9C seismic acquisition (a), and its schematic explaining the three principal orthogonal direction of the source (b) (Häusler et al., 2018).

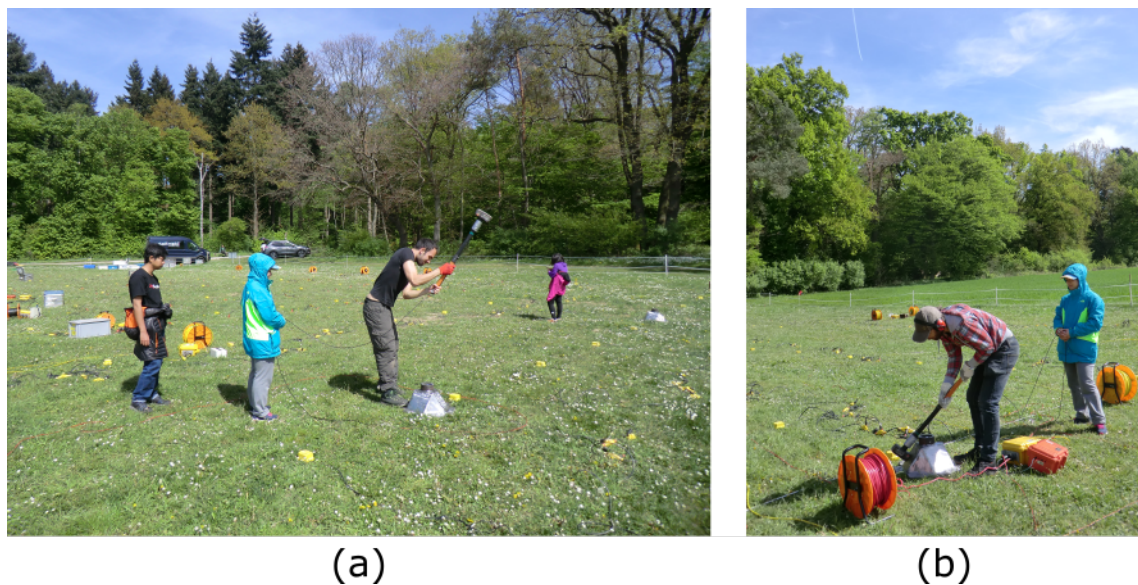


Figure 2.10: Seismic data acquisition at the Ettlingen Line field. The figure shows the Galperin source is hit by the sledgehammer.

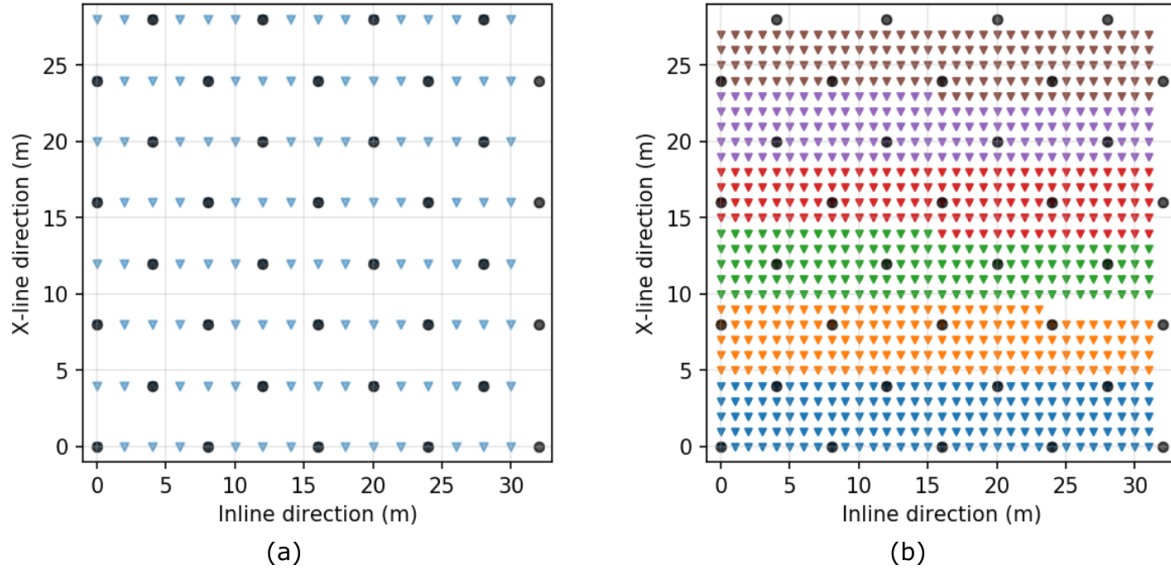


Figure 2.11: Coarse grid acquisition (a) and dense grid acquisition (b). Triangles represent receiver's locations, whereas circles represent source's locations. Different receiver's color shows different acquisition time; 1st day = blue, 2nd day = orange, 3rd day = green, 4th day = red, 5th day = purple and brown.

2.4 Pre-processing and data correction

2.4.1 Data evaluation

The noise level is estimated by comparing the windows where we can separate signal and noise. Signal windows are taken from relatively far offset data (> 25 m) with two windows. Noise windows are taken from ambient noise data at the same trace before the first arrival of the seismic wave. The length of the windows is 40 ms and 100 ms for noise and signal windows, respectively. SNR is then calculated using both noise and signal window as follows

$$SNR_{dB} = 10 \log_{10} \left(\frac{S_{signal}}{S_{noise}} \right)^2, \quad (2.1)$$

where S is the spectral amplitude of the given window, and SNR_{dB} is the signal to noise ratio given in dB .

Figure 3.5a presents the distribution of signal (orange line \pm standard deviation) and the ambient noise (blue line \pm standard deviation). We can see a relatively high SNR from 15 Hz (green line) to 145 Hz (red line). In practice, I define 3 Hz (Orange line) as the lowest bound of the signal, which will be used for inversion.

2.4.2 Data correction using matching filter

Splitting the acquisition into six patches for the dense acquisition requires source repetition at the same location. The acquisition's separation raises difficulties in terms of source repeatability because of potential differences in the source-ground coupling, triggering time, and the surface condition itself. The

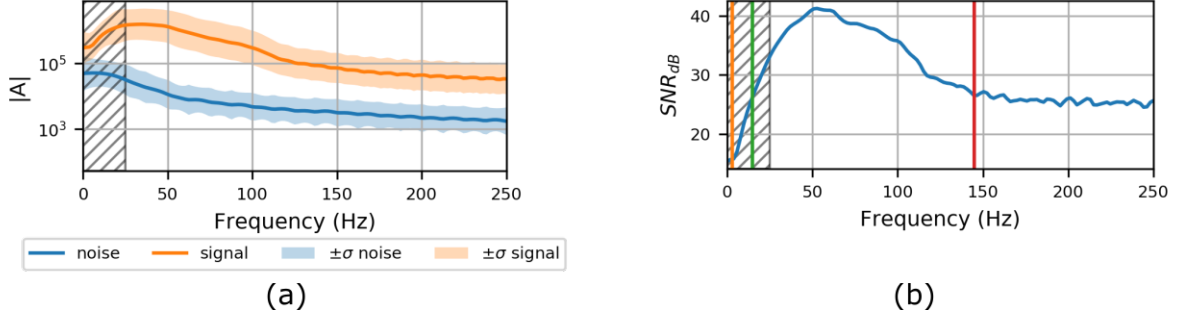


Figure 2.12: Signal (orange) and noise (blue) spectrum together with its standard deviation of Ettlingen Line 9C seismic data (a). SNR_{dB} of the seismic data (b). The good signal ($SNR_{dB} > 27$) ranging from 15 Hz (green line) to 145 Hz (red line). I started our FWI from 3 Hz (orange line) based on the strong coherent signal. The grey hatches represent unreliable SNR estimation.

latter is particularly problematic for an acquisition spread on five days with rain occurring at night. In practice, these limitations prevent us from combining the dense data into a single consistent dataset directly. I illustrate this issue in Figures 3.6 and 3.7 where the vertical red lines represent subset boundaries. Figure 3.6a shows rough seismic data before any correction. Half of the seismic data (the left part) has been acquired on April 28th, 2017, whereas the other half (the right part) has been acquired on May 2nd, 2017. Both subsets generally have the same amplitude level, but there is a visible kinematic offset or phase change. Another example of data inconsistencies can be seen in Figure 3.7a, where a crossline section of the data exhibits amplitude inconsistencies from one subset to another.

In order to handle such inconsistencies, one could have used the 6 subsets independently, hence increasing the total computational cost by a factor of 6. To avoid this extra cost, I have chosen to correct the data before FWI, thanks to the common receiver locations between the coarse and the dense acquisition. Taking advantage of having those common receiver locations for each patch of acquisition, I assume that there exists a matching filter $f_{i,sc,s}(t)$ which can satisfy a minimization problem given by

$$\mathcal{C}(f_{i,sc,s}(t)) = \sum_{j, sr} \frac{1}{2} \left\| c_{i,sc,j, sr}(t) - f_{i,sc,s}(t) * \hat{d}_{i,sc,s,j, sr}(t) \right\|^2, \quad (2.2)$$

where $\mathcal{C}(f_{i,sc,s}(t))$ is the least-square misfit function, $c_{i,sc,j, sr}(t)$ coarse acquisition data, $\hat{d}_{i,sc,s,j, sr}(t)$ is the dense acquisition data for each patch s , source's location i , source's component sc , receiver position j and component sr . In frequency domain, the convolution operator ($*$) will simply become a multiplication and the equation becomes

$$\mathcal{C}(f_{i,sc,s}(\omega)) = \sum_{j, sr} \frac{1}{2} \left\| c_{i,sc,j, sr}(\omega) - \hat{f}_{i,sc,s}(\omega) \hat{d}_{i,sc,s,j, sr}(\omega) \right\|^2. \quad (2.3)$$

The solution of Equation 2.3 can be analytically determined by deriving the gradient given by

$$\frac{\partial \mathcal{C}(f_{i,sc,s}(\omega))}{\partial \hat{f}_{i,sc,s}(\omega)} = \sum_{j, sr} -\overline{\hat{d}_{i,sc,s,j, sr}(\omega)} (c_{i,sc,j, sr}(\omega) - \hat{f}_{i,sc,s}(\omega) \hat{d}_{i,sc,s,j, sr}(\omega)) = 0. \quad (2.4)$$

The matching filter can be calculated by rearranging Equation 2.4 into

$$\hat{f}_{i,sc,s}(\omega) = \frac{\sum_{j, sr} \overline{\hat{d}_{i,sc,s,j, sr}(\omega)} \hat{c}_{i,sc,j, sr}(\omega)}{\sum_{j, sr} \overline{\hat{d}_{i,sc,s,j, sr}(\omega)} \hat{d}_{i,sc,s,j, sr}(\omega) + \varepsilon}, \quad (2.5)$$

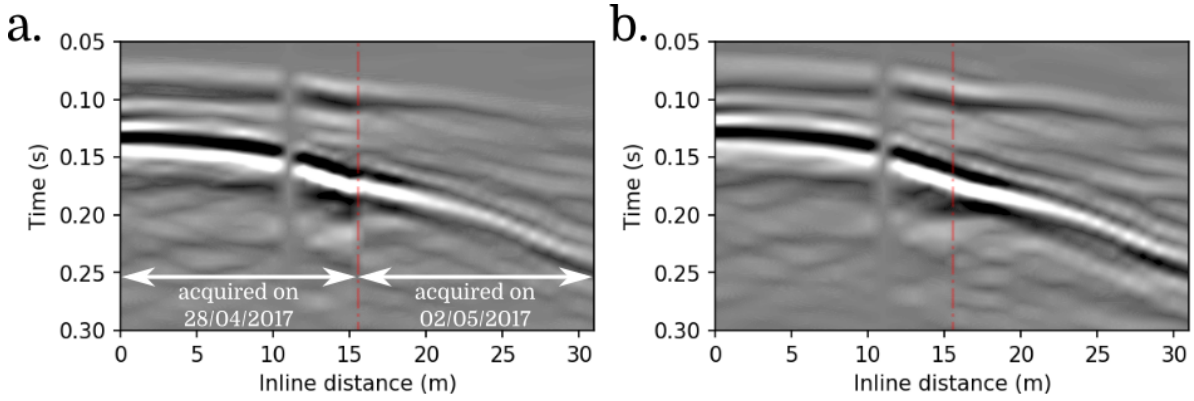


Figure 2.13: Seismic data before data correction (a) shows travel time shift between acquisition's subsets, and after data correction (b) where the data is more consistent.

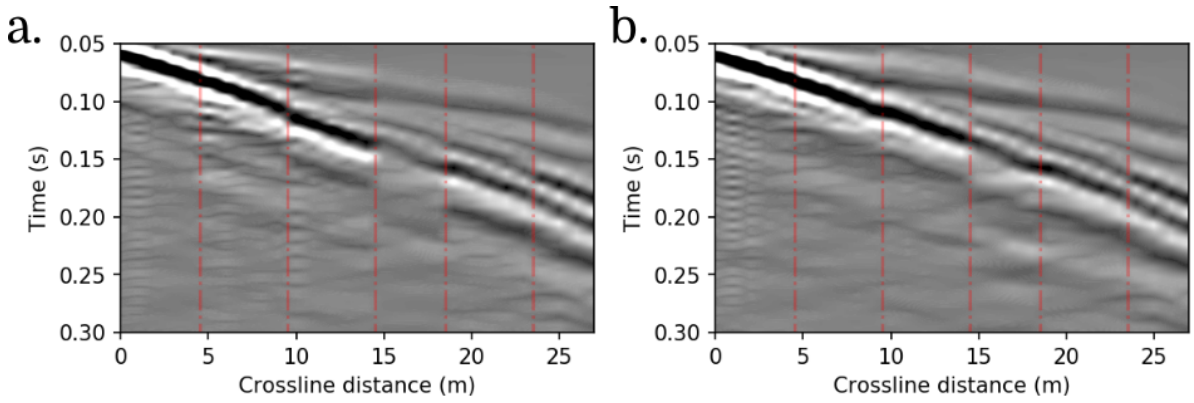


Figure 2.14: Seismic data before data correction (a), and after data correction (b). This seismic line is taken from the first crossline on the first source location on UZ component. Red vertical lines represent acquisition subset separation. Consistency improvements can be seen on the corrected data.

where ε is the stabilization factor for the matching filter. Finally, the corrected dense acquisition data can be calculated through convolution

$$d_{ij_p} = d_{ij_t} * f_{i,sc,s}(t). \quad (2.6)$$

This matching filter approach is similar to the source time function estimation proposed by Pratt (1999) and elastic correction towards acoustic data by Agudo et al. (2018).

Once computed, the matching filters are used to correct the dense grid data through convolution. This matching filter approach corrects both time and amplitude inconsistencies. Figure 3.6b shows a time shift correction from the matching filter, Figure 3.7b shows an amplitude correction between each patch of acquisition. While this strategy improves the data's consistency, I also observe that it increases the noise level, especially on the lower SNR data. However, the noise before the first arrival can be muted during the inversion. I have found that this matching filter strategy globally enhances our inversion results while avoiding the extra cost of considering each subset of acquisition independently.

In Chapter 1, I have already introduced the methodologies that are used in this PhD thesis. In this chapter, I have already present the target and the available dataset. I present the main results of my PhD

work in the next two chapters (Ch. 3 and 4). Both chapters correspond to the two articles which are submitted to the journal.

Chapter 3

3D 9C elastic Full Waveform Inversion Application

Contents

3.1	Introduction	53
3.2	Data Acquisition and Pre-processing	56
3.2.1	Target	56
3.2.2	Acquisition	57
3.2.3	Data evaluation	58
3.2.4	Data correction using matching filter	58
3.3	Full Waveform Inversion methodology	60
3.3.1	Modeling of elastic and viscoelastic waves	60
3.3.2	Inverse problem	62
3.3.3	Implementation: SEM46 code	65
3.4	Application	66
3.4.1	Initial model building	66
3.4.2	Source estimation	66
3.4.3	Multi-scale strategy	67
3.4.4	Model reconstruction	67
3.4.5	Quality control: data fit	69
3.5	Discussion and interpretation	72
3.5.1	Model interpretation	72
3.5.2	Is it reasonable to start from a homogeneous model?	74
3.5.3	Elastic or viscoelastic FWI?	74
3.5.4	Other limitations and prospects	76
3.6	Conclusions	79
3.A	Parameter binding FWI	80
3.B	Non-linear model constraints FWI	80
3.C	Source estimation	81
3.D	Computational cost	82

We have seen that the Chapter 2 gives a detailed history and previous experiments on the Ettlingen Line. The previous experiments demonstrate the Ettlingen Line's existence as a low-velocity anomaly with an inverted triangle shape. Afterward, we perform a 3D dense seismic acquisition using multicomponent sources (Galperin source) and multicomponent receivers. We demonstrate that our acquired data has a relatively broad usable frequency range (3 to 145 Hz). We also perform an additional data correction through matching filters in order to combine the part by part acquisition into a single consistent seismic acquisition.

In this chapter, we investigate the first main question in the problematics at the end of the General Introduction, namely: design an efficient FWI workflow for the reconstruction of P-wave and S-wave velocities from the Ettlingen field data. We propose a robust and dedicated 3D elastic FWI workflow for shallow seismic data. This experiment is calculated using SEM46, a (visco)elastic modeling and inversion tool based on spectral element discretization to obtain an accurate wave propagation simulation in shallow seismic scale (Chapter 1 Section 3.3.3). We perform two different inversions with two different initial models, the homogeneous model and the model obtained using multi-channel analysis of the surface wave (MASW) in order to see the effectiveness of our workflow. We also perform two more additional inversions to assess the result between two modeling approaches based on the elastic and viscoelastic medium. Finally, we obtain reconstructed V_P and V_S , which reveal a 3D extension of the Ettlingen Line as well as another trench line structure that has not been interpreted by the previous experiments.

This chapter is based on the extended abstract and paper:

- Irnaka, T., Brossier, R., Métivier, L., Bohlen, T., and Pan, Y. (2019a). Towards 3D 9C elastic Full Waveform Inversion of shallow seismic wavefields - case study Ettlingen Line. In *Expanded Abstracts, 81th Annual EAGE Conference & Exhibition, London*, page We P01 04. EAGE.118.
- Irnaka, T. M., Brossier, R., Métivier, L., Bohlen, T., and Pan, Y. (submitted). 3D 9C Full Waveform Inversion for Shallow Seismic Target: Ettlingen Line Case Study. *submitted to Geophysical Journal International*.

Abstract

We investigate the inversion of a multi-component source and receiver near-surface dataset using a viscoelastic full waveform inversion algorithm. The target is a trench line buried at approximately 1 m depth. We present the pre-processing of the data, including a matching filter correction to compensate for different source and receiver coupling conditions during the acquisition, as well as a dedicated multi-step workflow for the reconstruction of both P-wave and S-wave velocities. Our implementation is based on viscoelastic modeling using a spectral element discretization to accurately account for the wave propagation's complexity in this shallow region. We illustrate the inversion stability by starting from different initial models, either based on dispersion curve analysis or homogeneous models consistent with first arrivals. We recover similar results in both cases. We also illustrate the importance of taking into account the attenuation by comparing elastic and viscoelastic results. The 3D results make it possible to recover and locate precisely the trench line in terms of interpretation. They also exhibit another trench line structure, in a direction forming an angle at 45 degrees with the direction of the targeted trench line. This new structure had been previously interpreted as an artifact in former 2D inversion results. The archaeological interpretation of this new structure is still a matter of discussion.

3.1 Introduction

Accurate and efficient seismic imaging techniques are crucial for near surface applications. Geotechnical applications (Kramer, 1996; Stokoe et al., 2000), ground characterization (Foti et al., 2003; Roberts and Asten, 2004; Chapman et al., 2006), infrastructure planning (Stewart et al., 1997; Martínez and Mendoza, 2011; Pegah and Liu, 2016), subsurface feature detection (Cardarelli et al., 2010), agriculture (Allred et al., 2008; Weil et al., 2012), archaeological studies (Wynn, 1986; Vafidis et al., 2003; Signanini and Torrese, 2004), and shallow-seismic hazard assessment (Göktürkler et al., 2008; Samyn et al., 2012) are instances of applications which focus on shallow targets from several meters to few tens of meters deep.

Conventional methods for this type of application encompass seismic refraction (Palmer, 1980), first arrival travel-time tomography (FATT) (Aki et al., 1974), and multi-channel analysis of surface wave (MASW) (Park et al., 1999). All these methods suffer from several limitations. Seismic refraction technique uses a very crude assumption by assuming a layered subsurface, with homogeneous layers, and the velocity in each layer increases with depth. Interpreting the first arrivals using Snell's law, it aims at inferring the velocity of each layer. FATT, which only considers the first arrival signal (from P or S-wave), is only sensitive to the direct and diving waves. In the context of shallow-seismic, FATT is limited because the maximum offset for such application is often too short to sample the subsurface at sufficient depth. In addition, FATT requires picking on P or S waves, and the resolution depends on the distribution of the ray path. MASW focuses on the surface waves instead of interpreting body waves. It takes advantage of the dispersive behavior of the surface waves. MASW is generally limited to the reconstruction of V_S , based on the assumption of a local 1D model, and relies on a pre-processing stage which transfers the seismic data to the frequency-velocity domain that makes possible to pick the phase or group velocity.

Another seismic imaging method called Full Waveform Inversion (FWI) (Tarantola, 1984a; Virieux and Operto, 2009) has started to gain popularity for shallow-seismic applications. FWI has already been successfully applied on many crustal-scale targets (Sirgue et al., 2010; Etienne et al., 2012; Prioux et al., 2013b; Vigh et al., 2014; Górszczyk et al., 2017; He et al., 2019b; Trinh et al., 2019a), as well as

in seismology for lithospheric scale study (Tape et al., 2010; Beller et al., 2018; Lu et al., 2018), or for regional and global tomography (Fichtner et al., 2008; Modrak and Tromp, 2016). FWI is based on the iterative minimization between observed data and data calculated through the solution of wave propagation equations. As such, it aims at interpreting the whole signal, contrary to previously mentioned seismic imaging methods.

The interest for FWI comes from its high-resolution power up to half of the wavelength, the fact that it does not rely on prior assumptions regarding the subsurface geometry/configuration, and the possibility of estimating 3D quantitative subsurface models. Conventional difficulties for FWI applications are related to the design of sufficiently accurate initial subsurface models, and the risk to converge to local minima (also referred to as cycle skipping issue in the FWI community as discussed in Virieux and Operto (2009)), as well as the need for a sufficiently accurate modeling engine to take into account the complexity of wave propagation and the consequently higher computational cost of the whole procedure.

Even if the lack of low frequency may not be so strong for shallow targets, the application of 3D FWI in the near-surface context may suffer from two specific difficulties. The first is related to the seismic acquisition: the targets are often sparsely covered due to a limited number of available sources and receivers. 2D profiles are often used rather than full 3D acquisition. The signal to noise ratio is often poor due to weak seismic sources (sledgehammer, small vibroseis), the sources generally lack repeatability, and variable receiver-soil coupling effects can be observed. The second difficulty is due to the high complexity of the elastic wave propagation in the near-surface, where highly dispersive surface waves dominate the recorded signal, and attenuation effects can be strong. Despite these difficulties, several 2D FWI studies in shallow-seismic have been performed on synthetic and field data (Bretaudeau et al., 2013b; Köhn et al., 2016, 2019; Wittkamp et al., 2018; Lamert and Friederich, 2019; Wang et al., 2019). The extension to the 3D case has also proven to be feasible (Fathi et al., 2016; Nguyen and Tran, 2018; Smith et al., 2019). One of the most recent examples, Smith et al. (2019) performed 3D elastic FWI for tunnel detection on synthetic and field data. They use SPECFEM package as the waveform modeling tool (Peter et al., 2011) and SeisFlows as the inversion engine (Modrak et al., 2018). They use multi-component geophones with vertical force sources. Their initial models are obtained from travel-time tomography for V_P and MASW for V_S . Up to 20 Hz, they can reconstruct a nice 3D model of the underground tunnel using field data. They also emphasize using horizontal source components to improve the reconstruction at depth on their synthetic test.

Our study focuses on a specific 3D dataset that has been acquired to investigate a very shallow target, the Ettlingen Line, Germany (Fig. 4.10). The expected investigation depth reaches only 6 meters. Compared with more conventional acquisitions for this type of targets, we benefit here a rather dense coverage, implying a total number of 36 3C source and 888 3C receiver positions, for a maximum offset of 41 m. In addition, the acquisition uses multi-component receivers and multi-directional sources. In this context, the seismic signal recorded mainly contains surface waves.

Contrary to conventional exploration case-studies, the frequency content of the data, considering the target we have, is sufficiently low to avoid cycle skipping issues. Moreover, the difficulty is to accurately invert the surface waves to extract the information on both V_P and V_S . We show how, based on an accurate spectral element modeling and inversion tool, we can set up an efficient multi-parameter inversion workflow, making it possible to retrieve high-resolution 3D models for both parameters. Thanks to the data's low-frequency content, we show how we can perform FWI from homogeneous V_P and V_S initial models. Starting from such simple models considerably reduces the complexity of the FWI workflow, which conventionally relies on a substantial pre-processing step to build accurate enough initial velocity models, using tomography or MASW techniques. The results we obtain reveal a detailed 3D



Figure 3.1: Basemap of the acquisition at Rheinstetten. Red solid line represents the existing location of the trench, red dashed line represents the possible buried location of the trench line, and the white rectangle represents seismic acquisition location.

structure of the Ettlingen Line, compatible with results obtained in previous studies. The reconstructed models exhibit a new low-velocity trench, which has been previously considered an artifact in a previous 2D FWI inversion, and which is not visible on a previous MASW inversion. This new trench's 3D coherency makes it a very plausible structure that was previously ignored on this site. We also discuss the stability of the inversion regarding the initial model design and the integration of attenuation in the numerical modeling engine through different numerical experiments.

The structure of the paper is as follows. In Section 2, we introduce the target specificities, the acquisition setup, and a pre-processing operation we have applied to the data. In Section 3, we present a short overview of the methodology we apply: elastic and viscoelastic wave modeling using a spectral element discretization, multi-parameter inversion using a specific two-steps workflow. Section 4 presents this methodology's application on the Ettlingen Line field data, analysis of the reconstructed models, and the data fit. In Section 5, we discuss the geological and archaeological interpretation of the reconstructed models. We also present numerical experiments discussing the method's sensitivity regarding the starting model's choice and an elastic or viscoelastic modeling engine, and discuss the limitation of the method. The conclusion is proposed in Section 6.

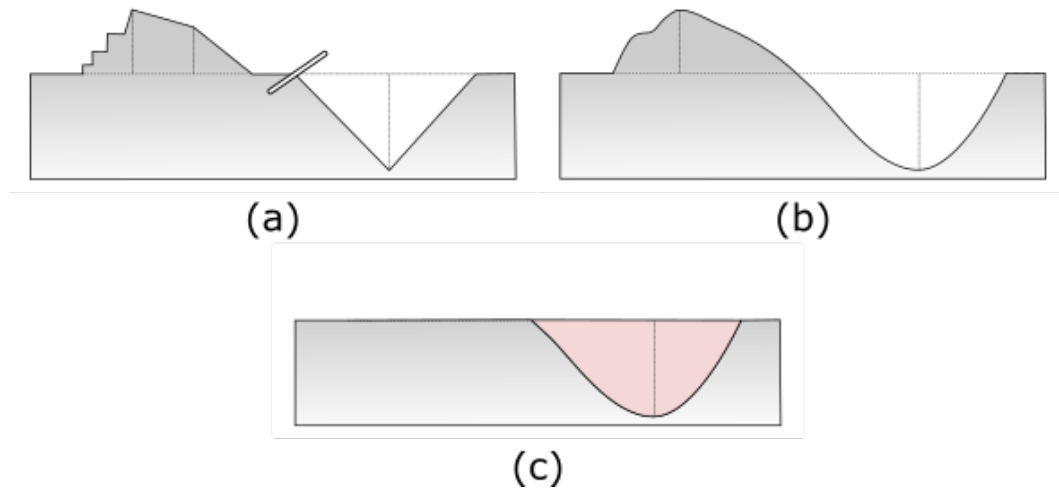


Figure 3.2: The original shape of the trench (a), the current shape of trench (b), and the current shape of buried trench (c) redrawn from Lang et al. (1907). In general, the current shape is smoother due to erosion. The wood palisade wall also do not exist anymore. Our target is the buried trench in which we do not know anymore the boundary and the geometry of the original trench.

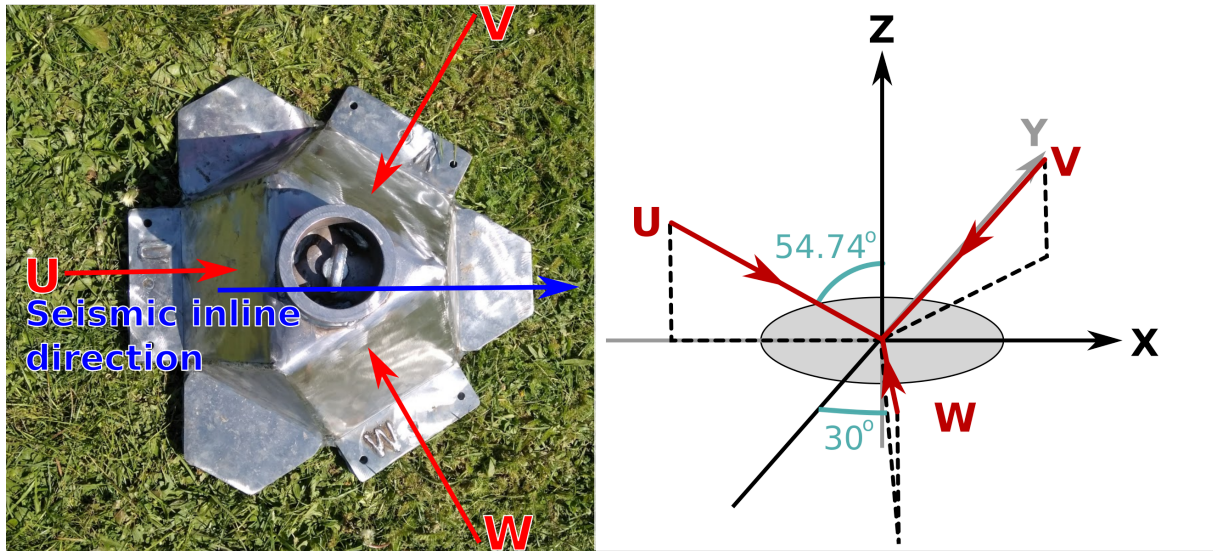


Figure 3.3: The Galperin source used in 9C seismic acquisition (a), and its schematic explaining the three principal orthogonal direction of the source (b) (Häusler et al., 2018).

3.2 Data Acquisition and Pre-processing

3.2.1 Target

The target of this study is a historical defensive trench line located at Rheinstetten, Germany. German troops built it during the War of the Spanish Succession in 1707 (Lang et al., 1907). It has been leveled to ground in the area of our investigation (Fig. 3.2). The trench is surrounded by Pleistocene fluvial sediment deposits from the Rhine River, west of the trench. Several experiments have been performed

Table 3.1: Cartesian point source weights to represent a directional point source.

Source Direction	F_Z	F_X	F_Y
U	$F \cos \theta$	$F \sin \theta$	0
V	$F \cos \theta$	$-F \sin \theta \cos \phi$	$-F \sin \theta \sin \phi$
W	$F \cos \theta$	$-F \sin \theta \cos \phi$	$F \sin \theta \sin \phi$

in this area to uncover the geometry of the buried trench. Wegscheider (2017) reveals the trench's 2D shape by performing a ground penetrating radar (GPR) investigation. Wittkamp et al. (2018) estimate a 2D V_S model using 2D elastic FWI focused on Love and Rayleigh waves. Pan et al. (2018) performs a detailed 3D MASW, producing a 3D V_S cube. From these studies, the Ettlingen Line appears as an inverted triangle shape trench with a lower velocity than the surrounding area (consistent with a weaker consolidation of the subsurface in the trench due to the excavation before being filled in again). The width of the trench reaches approximately 6 meters, while the depth is around 3 meters.

3.2.2 Acquisition

The seismic data acquisition was organized by GPI Karlsruhe Institute of Technology (KIT), collaborating with GFZ Potsdam, ETH Zurich, and Univ. Grenoble Alpes (UGA) in April 2017. This experiment performed a 3D seismic acquisition with three-component (3C) Galperin sources and three-component receivers, resulting in a 9C seismic data.

A Galperin source is a multi-component source designed for shallow-seismic applications (Häusler et al., 2018). It has three different source directions (U , V , and W), which are not aligned with the Cartesian coordinate axis. An illustration of this particular type of source is given in Figure 3.3a. It is built from iron and filled with wood inside. The wood inside the Galperin source helps to reduce the reverberation during seismic acquisition. The orientation of each source direction is depicted in Figure 3.3b. The source directions (U , V , and W) form 120° angles with each other, with respect to the horizontal plane. Furthermore, all source directions form an angle θ of 54.74° with the vertical axis (Z). Source directions V and W form an angle ϕ of 30° with the Y axis. The force distribution along Cartesian coordinates is given in Table 3.1, assuming a point force F on each source direction.

The 3C geophones record seismic vibrations along the vertical and the horizontal components aligned with the Cartesian axis of Z , X , and Y . Two different types of receivers with the same eigenfrequency of 4.5 Hz have been used. For each source location and direction, three seismic stacks have been performed. The total recording time is $T = 1$ second with 4 kHz frequency sampling.

We have performed two sequential seismic acquisitions: each with different receiver geometries. Both acquisitions use 36 Galperin sources at the same positions. They are indicated by black circles in Figure 3.4. The sources have been installed following a staggered pattern resulting in a minimum source spacing about 5.66 m. The first acquisition uses a coarse repartition of receivers with 2 m inline and 4 m crossline spacing, giving 128 3C geophone positions in total (Fig. 3.4a). The second uses a dense repartition of receivers, with 1 m inline and crossline spacing, giving 888 3C geophone positions in total (Fig. 3.4b). Because of the limited number of available equipment (160 3C geophones), the dense acquisition has been split into six acquisition subsets (color-coded on Fig. 3.4b) acquired during 5 days in total, repeating all source locations for each subset.

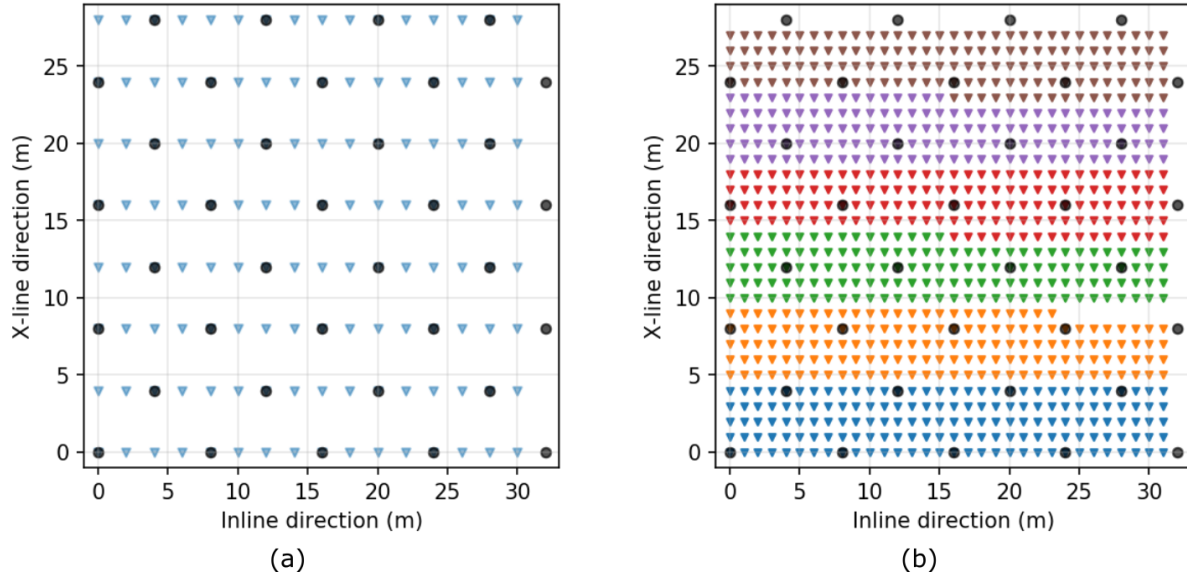


Figure 3.4: Coarse grid acquisition (a) and dense grid acquisition (b). Triangles represent receiver's locations, whereas circles represent source's locations. Different receiver's color shows different acquisition time; 1st day = blue, 2nd day = orange, 3rd day = green, 4th day = red, 5th day = purple and brown.

3.2.3 Data evaluation

The noise level is estimated by comparing the windows where we can clearly separate signal and noise. Signal windows are taken from relatively far offset data ($> 25m$) with two windows. Noise windows are taken from ambient noise data at the same trace before the seismic wave's first arrival. The length of the windows is 40 ms and 100 ms for noise and signal windows, respectively. SNR is then calculated using both noise and signal window as follows

$$SNR_{dB} = 10 \log_{10} \left(\frac{S_{signal}}{S_{noise}} \right)^2, \quad (3.1)$$

where S is the spectral amplitude of the given window and SNR_{dB} is the signal to noise ratio given in dB .

Figure 3.5a presents the distribution of signal (orange line \pm standard deviation) and the ambient noise (blue line \pm standard deviation). We can see a relatively high SNR from 15 Hz (green line) to 145 Hz (red line). In practice, we define 3 Hz (orange line) as the lowest bound of the signal, which will be used for inversion.

3.2.4 Data correction using matching filter

Splitting the acquisition into six patches for the dense acquisition requires source repetition at the same location. The acquisition's separation raises difficulties in source repeatability because of potential differences in the source-ground coupling, triggering time, and surface condition. The latter is particularly problematic for an acquisition spread on five days with rain occurring at night. In practice, these limitations prevent us to directly combine the dense data into a single consistent dataset. We illustrate this

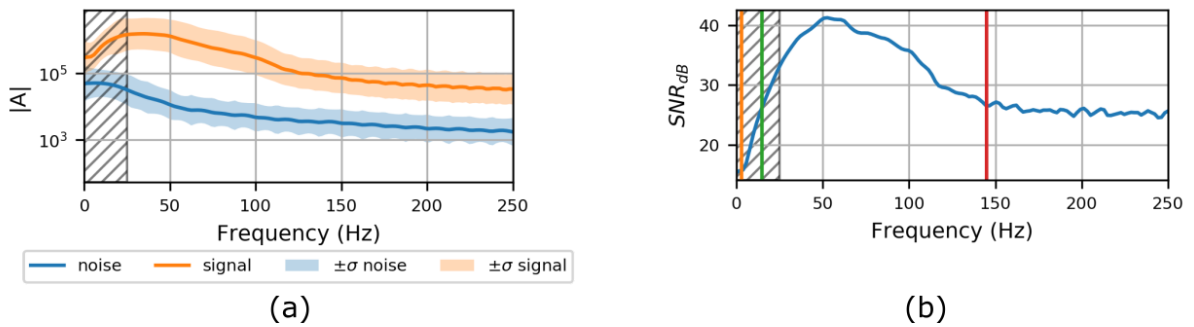


Figure 3.5: Signal (orange) and noise (blue) spectrum together with its standard deviation of Ettlingen Line 9C seismic data (a). SNR_{dB} of the seismic data (b). The good signal ($SNR_{dB} > 27$) ranging from 15 Hz (green line) to 145 Hz (red line). We started our FWI from 3 Hz (orange line) based on the strong coherent signal. They grey hatches represents unreliable SNR estimation.

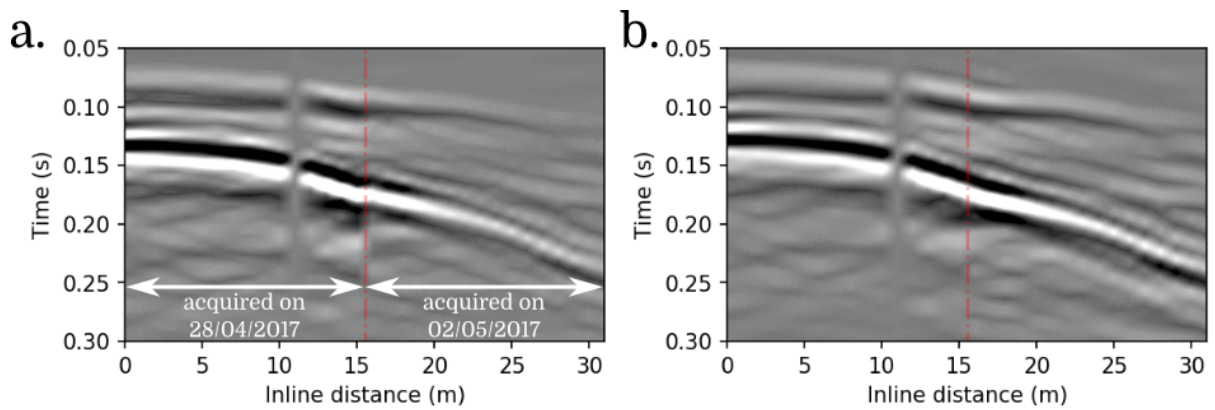


Figure 3.6: Seismic data before data correction (a) shows travel time shift between acquisition's subsets, and after data correction (b) where the data is more consistent.

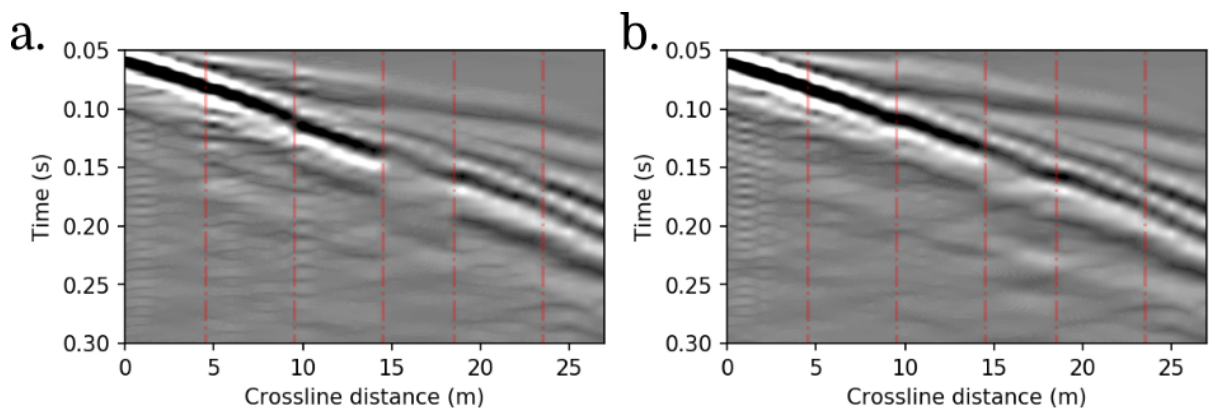


Figure 3.7: Seismic data before data correction (a), and after data correction (b). This seismic line is taken from the first crossline on the first source location on UZ component. Red vertical lines represent acquisition subset separation. Consistency improvements can be seen on the corrected data.

issue in Figures 3.6 and 3.7 where the vertical red lines represent subset boundaries. Figure 3.6a shows rough seismic data before any correction. Half of the seismic data (the left part) has been acquired on April 28th, 2017, whereas the other half (the right part) has been acquired on May 2nd, 2017. Both subsets generally have the same amplitude level, but there is a visible kinematic offset or phase change. Another example of data inconsistencies can be seen in Figure 3.7a, where a crossline section of the data exhibits amplitude inconsistencies from one subset to another.

In order to handle such inconsistencies, one could have used the 6 subsets independently, hence increasing the total computational cost by a factor of 6. To avoid this extra cost, we have chosen to correct the data before FWI, thanks to the common receiver locations between the coarse and the dense acquisition. Taking advantage of having those common receiver locations for each patch of acquisition, we can design a matching filter which can transform our dense grid data to match the coarse grid data, for each acquisition patch (s), source's component (sc), and source's location (i). The coarse grid's data acquisition has been performed all at once on the same day, with a ground condition relatively equivalent for each receiver. Therefore the coarse grid data can be used as the baseline for the correction. The matching filters $f_{i,sc,s}(t)$ can be computed through a frequency-domain deconvolution

$$\hat{f}_{i,sc,s}(\omega) = \frac{\sum_{j, sr} \hat{d}_{i,sc,s,j, sr}(\omega) \hat{c}_{i,sc,j, sr}(\omega)}{\sum_{j, sr} \hat{d}_{i,sc,s,j, sr}(\omega) \hat{d}_{i,sc,s,j, sr}(\omega) + \varepsilon}, \quad (3.2)$$

where $\hat{f}_{i,sc,s}(\omega)$ is the frequency-domain of $f_{i,sc,s}(t)$, $d_{i,sc,s,j, sr}(\omega)$ is the dense grid data associated with the receiver position j and component sr , while $c_{i,sc,j, sr}$ is the coarse grid data for the same source/receiver location/component. ε is the stabilization factor of the matching filter. This matching filter approach is similar to the source time function estimation proposed by Pratt (1999) and elastic correction towards acoustic data by Agudo et al. (2018). The detailed formulation of the matching filter technique is given in Section 2.4.2.

Once computed, the matching filters are used to correct the dense grid data through convolution. This matching filter approach corrects both time and amplitude inconsistencies. Figure 3.6b shows a time shift correction from the matching filter, Figure 3.7b shows an amplitude correction between each patch of acquisition. While this strategy improves the data's consistency, we also observe that it increases the noise level, especially on the data with lower SNR. However, the noise before the first arrival can be muted during the inversion. In general, we have found that this matching filter strategy globally enhances our inversion results while avoiding the extra cost of considering each subset of acquisition independently.

Now that we have introduced the target, the acquisition details, and the pre-processing strategy, we present a rapid overview of the methodology we apply to invert the Ettlingen data.

3.3 Full Waveform Inversion methodology

3.3.1 Modeling of elastic and viscoelastic waves

3.3.1.1 Formulation

The general viscoelastic wave equations are

$$\begin{aligned} \rho \partial_{tt} u_i &= \partial_j \sigma_{ij} + f_i, \\ \sigma_{ij} &= M_{ijkl} *_t \varepsilon_{kl} + \mathcal{T}_{ij}, \end{aligned} \quad (3.3)$$

where ρ is the density, u is the displacement field, σ and ε is the second order stress and strain tensors, f is the external force, and \mathcal{T} is the stress failure. The effect of the attenuation is denoted by a relaxation rate M_{ijkl} , and symbol $*_t$ represents a convolution operator in time domain. We follow Einstein convention (summation over repeated indices) for these equations.

In a purely elastic wave propagation we have $M_{ijkl}(x, t) = c_{ijkl}(x)\delta(t)$, and equation 3.3 simplifies into

$$\begin{aligned}\rho\partial_{tt}u_i &= \partial_j\sigma_{ij} + f_i, \\ \sigma_{ij} &= c_{ijkl}\varepsilon_{kl} + \mathcal{T}_{ij},\end{aligned}\quad (3.4)$$

where c_{ijkl} is the elastic (unrelaxed) stiffness-coefficient.

Using Voigt indexing and matrix notations, equation 4.1 can be rewritten as

$$\rho\partial_{tt}\mathbf{u} = DCD^T\mathbf{u} + S, \quad (3.5)$$

where S is the external source, D is the spatial derivative operator

$$D = \begin{pmatrix} \partial_1 & 0 & 0 & 0 & \partial_3 & \partial_2 \\ 0 & \partial_2 & 0 & \partial_3 & 0 & \partial_1 \\ 0 & 0 & \partial_3 & \partial_2 & \partial_1 & 0 \end{pmatrix}, \quad (3.6)$$

and C is the stiffness tensor in isotropic medium

$$C = \begin{bmatrix} \lambda + 2\mu & \lambda & \lambda & 0 & 0 & 0 \\ \lambda & \lambda + 2\mu & \lambda & 0 & 0 & 0 \\ \lambda & \lambda & \lambda + 2\mu & 0 & 0 & 0 \\ 0 & 0 & 0 & \mu & 0 & 0 \\ 0 & 0 & 0 & 0 & \mu & 0 \\ 0 & 0 & 0 & 0 & 0 & \mu \end{bmatrix}. \quad (3.7)$$

In viscoelastic medium, the quality factor is denoted by Q . For P and S body wave, it is denoted by Q_P and Q_S . These Q_P and Q_S are assumed to be constant over the considered frequency band, as is generally the case in seismic. In terms of modeling, we approximate the attenuation by introducing a set of L standard linear solid (SLS) mechanisms. This amounts to add ordinary differential equations (ODE) and memory variables $\psi_{s;ij}$ in equation 3.3 resulting in

$$\begin{aligned}\rho\partial_{tt}u_i &= \partial_j\sigma_{ij} + f_i, \\ \sigma_{ij} &= c_{ijkl}\varepsilon_{kl} - c_{ijkl}^R \sum_{s=1}^L \psi_{s;ij} + \mathcal{T}_{ij}, \\ \partial_t\psi_{s;ij} + \omega_s\psi_{s;ij} &= \omega_s y_s \varepsilon_{kl},\end{aligned}\quad (3.8)$$

where the scalar y_s is the dimensionless anelastic coefficient (Yang et al., 2016).

We consider in our case an isotropic attenuation (as usually done), and the corresponding isotropic relaxed stiffness-tensor can be written as

$$C^R = \begin{pmatrix} \lambda^R + 2\mu^R & \lambda^R & \lambda^R & 0 & 0 & 0 \\ \lambda^R & \lambda^R + 2\mu^R & \lambda^R & 0 & 0 & 0 \\ \lambda^R & \lambda^R & \lambda^R + 2\mu^R & 0 & 0 & 0 \\ 0 & 0 & 0 & \mu^R & 0 & 0 \\ 0 & 0 & 0 & 0 & \mu^R & 0 \\ 0 & 0 & 0 & 0 & 0 & \mu^R \end{pmatrix}. \quad (3.9)$$

Following Moczo et al. (1997), the relaxed Lamé coefficients λ^R and μ^R can be estimated from the unrelaxed values as

$$\begin{aligned}\lambda^R + 2\mu^R &= \frac{1}{3}Q_P^{-1}(C_{11} + C_{22} + C_{33}) \\ \text{and } \mu^R &= \frac{1}{3}Q_S^{-1}(C_{44} + C_{55} + C_{66}).\end{aligned}\quad (3.10)$$

3.3.1.2 Spectral element discretization

The spectral element method (SEM) is a numerical method that combines the Finite Element Method's benefits, with the added value of spectral accuracy. The foundation for SEM is the weak formulation of the second-order wave equation. The seismic wavefield's discretization is based on Lagrange interpolants, whereas the integration over elements is based on Gauss-Lobatto-Legendre points. In SEM, the medium is discretized using hexahedral elements. After discretization using the spectral element method, the elastic wave equation can be represented as

$$\mathbf{M}\partial_{tt}\mathbf{u} = -\mathbf{K}\mathbf{u} + \mathbf{F}, \quad (3.11)$$

where \mathbf{M} and \mathbf{K} are the mass and stiffness matrices, and \mathbf{F} is the source term. In SEM, \mathbf{M} is diagonal by construction, which makes it possible to use efficiently explicit time discretization schemes. We use here the Newmark time integration method. The computationally demanding step is the computation of the product between the displacement vector and the stiffness matrix ($\mathbf{K}\mathbf{u}$) (Komatitsch et al., 2000; Trinh et al., 2019b). This product can be calculated efficiently using a matrix-free implementation based on the factorization

$$\mathbf{K} = \mathcal{D}^w \mathbf{C} \mathcal{D}, \quad (3.12)$$

where \mathcal{D} stands for the spatial derivatives of a vector in the Cartesian space, and \mathcal{D}^w is the spatial derivative weighted by GLL weights (Deville et al., 2002; Trinh et al., 2019b). This factorization can be interpreted as a three-step computation: calculating the strain from the estimation of the spatial derivatives, calculating the stress component from the product of the stiffness coefficient, and a second estimation of the spatial derivatives.

After discretization using spectral element method, the viscoelastic second-order wave equation can be written as

$$\begin{aligned}\mathbf{M}\partial_{tt}\mathbf{u} &= -\mathbf{K}\mathbf{u} + \mathcal{D}^w C^R \sum_{s=1}^L \psi_s + \mathbf{F}, \\ \partial_t \psi_s + w_s \psi_s &= w_s y_s \varepsilon.\end{aligned}\quad (3.13)$$

3.3.2 Inverse problem

3.3.2.1 Generalities

FWI is formulated as a minimization problem. We focus on a simple least squares misfit function $f(m)$, which measures the discrepancy between the calculated data $d_{cal}(m)$ and the observed data d_{obs} as

$$f(m) = \frac{1}{2} \|d_{cal}(m) - d_{obs}\|^2. \quad (3.14)$$

FWI is defined as the minimization of $f(m)$ with respect to the model parameters m .

The calculated data $d_{cal}(m)$ are obtained through the solution of the viscoelastic equations 3.13 and the extraction of the wavefield values at the receiver locations. The parameters m gathers the density ρ , and any combination of the stiffness tensor coefficients C_{ij} .

FWI is a local optimization problem which is conventionally solved using Newton-based methods. It starts with an initial model m_0 , which is then updated through the iterative scheme

$$m_{k+1} = m_k + \alpha_k \Delta m_k, \quad (3.15)$$

where k is the iteration number, α_k is the step length obtained using the line search method (Nocedal and Wright, 2006) and Δm_k (Eq. 3.16) is the model parameter update. Following the quasi-Newton l -BFGS approach, the latter is represented as a product between the inverse Hessian estimated using l -BFGS, denoted by Q_k (Byrd et al., 1995; Métivier and Brossier, 2016), and the gradient of the misfit function ∇f

$$\Delta m_k = -Q_k \nabla f(m_k). \quad (3.16)$$

We follow the adjoint-state method to compute the gradient $\nabla f(m)$ (Plessix, 2006). The gradient of the least-squares misfit function with respect to the coefficients C_{ij} in viscoelastic medium is given by the zero-lag cross-correlation between the adjoint displacement field $l(m)$ (solution of the adjoint viscoelastic wave equations) and the incident acceleration field $\ddot{u}(m)$ plus an additional term related to the memory variables ψ_s as

$$\nabla f(m) = \frac{\partial \chi(m)}{\partial m} = \left\langle l(m), \frac{\partial C}{\partial C_{ij}} u(m) \right\rangle - \left\langle l(m), \sum_{s=1}^L \frac{\partial C^R}{\partial C_{ij}} \psi_s \right\rangle. \quad (3.17)$$

For purely elastic media the second term of the right hand side vanishes.

The gradient with respect to any parameter p , function of the density and the stiffness matrix coefficients C_{ij} can be determined following the chain-rule as

$$\frac{\partial f(m)}{\partial p} = \sum_{I=1}^6 \sum_{J=1}^6 \frac{\partial f}{\partial C_{ij}} \frac{\partial C_{ij}}{\partial p} + \frac{\partial f}{\partial \rho} \frac{\partial \rho}{\partial p}, \quad (3.18)$$

3.3.2.2 Bessel gradient smoothing

From a mathematical perspective, FWI is an ill-posed inverse problem, with a highly non-unique solution. In practice, regularization strategies are required to reduce the size of the solution space. Trinh et al. (2017) proposed a gradient smoothing through Bessel filter. This smoothing strategy is an anisotropic filter which has the benefit of taking into account the shape of prior information of the geological structure. Bessel filter is applied within the spectral element meshes framework through its standard weak formulation; therefore, avoiding the projection loop of SEM meshes in Gauss Lobatto Legendre points and Cartesian coordinate or an explicit windowed convolution in SEM meshes. Variable coherent lengths and orientation are required as the input of this Bessel filter.

3.3.2.3 Multi-parameter inversion strategy

Inverting shallow-seismic data with limited offset comes with inherent challenges. Even in a relatively simple model, the surface wave can exhibit a complex waveform due to its dispersive behavior. The surface wave dispersion implies the medium properties at different depth depending on the data's frequency

content. Low-frequency surface wave has a deeper penetration depth and brings low wavenumber content. High-frequency surface wave brings higher-resolution information, however, at a shallower depth. This complex behavior can quickly drive the inversion towards local minima (cycle skipping at a higher frequency). To avoid this problem, we follow a standard multi-scale approach, where the inversion is carried out from the lowest frequency band to the broader frequency band (Bunks et al., 1995).

In this shallow-seismic imaging context, given the sufficient amount of low-frequency content, the multi-scale approach is sufficient to avoid any cycle skipping issues throughout the inversion (which is much different from exploration scale targets). However, this strategy does not solve the problem of the unbalanced sensitivity between V_P and V_S on the surface wave dominated data. In the exploration scale, with a sufficiently large offset, one can perform a dynamic windowing strategy, in which we can separate the body and the surface wave (He et al., 2019b; Trinh et al., 2019a). Unfortunately, this approach is not feasible for our case study, and a direct multi-parameter FWI is not ideal.

For this reason, we design a specific two steps strategy. In the first step, we invert only for V_S , however, updating also for V_P by strictly enforcing an assumed linear relationship between V_P and V_S . This first step is what we denote as the parameter binding strategy in the following. In the second step, we perform a true multi-parameter inversion, updating simultaneously both V_P and V_S , while incorporating non-linear constraints to bound not only V_P and V_S values, but also the ratio of V_P over V_S .

More in details, the parameter binding strategy assumes the linear relationship

$$V_P(x, y, z) = \gamma(x, y, z)V_S(x, y, z) \quad (3.19)$$

The gradient of the misfit function with respect to V_S can thus be written as

$$\frac{\partial f(m)}{\partial V_S} = -\left\langle l(m), \frac{\partial A}{\partial V_S} u(m) \right\rangle + \gamma \left\langle l(m), \frac{\partial A}{\partial V_P} u(m) \right\rangle, \quad (3.20)$$

where A is the forward operator.

The derivatives through the Lagrangian formalism can be found in Appendix 3.A. Implementing this strategy makes it possible to perform FWI that simultaneously updates V_P and V_S based on the scaling parameter γ .

This parameter binding strategy makes it possible to perform stable FWI in shallow-seismic case, but the relation between V_P and V_S (γ) remains fixed during the inversion. With the limited knowledge of the true γ , FWI with parameter binding can lead to an incorrect model update. The second step of multi-parameter inversion is used to mitigate this issue. To stabilize this multi-parameter inversion, we apply bound constraints on V_P , V_S , and V_P/V_S . The bound for each of these quantities parameters can be deduced from prior geological knowledge of the area. Enforcing these bounds amounts to define a set of non-linear constraints, as is done in Peters and Herrmann (2017) and Trinh et al. (2019a).

The non-linear constraints inversion is formulated as a minimization of the misfit function $f(m)$ over a restricted model space Ω which simultaneously satisfies:

- Bounds constraint \mathcal{C}_1 : V_P and V_S should vary within a pre-defined range

$$\mathcal{C}_1 = \{V_P, V_S, V_{P_{min}} \leq V_P \leq V_{P_{max}} \text{ and } V_{S_{min}} \leq V_S \leq V_{S_{max}}\}, \quad (3.21)$$

- Ratio constraint \mathcal{C}_2 : The value of V_P/V_S should vary within a pre-defined range

$$\mathcal{C}_2 = \{V_P, V_S, \quad r_1 \leq V_P/V_S \leq r_2\}, \quad (3.22)$$

where $V_P, V_S \in \mathcal{C}_1 \cap \mathcal{C}_2$.

In terms of the non-linear constraint, the projected parameter of V_P and V_S can be determined by solving the following equation

$$\begin{aligned} \min_{V_P, V_S} f(V_P, V_S) &= \frac{(\overline{V}_P - V_P)^2}{V_P^2} + \frac{(\overline{V}_S - V_S)^2}{V_S^2}, \\ \text{subject to} \quad & r_1 \leq V_P/V_S \leq r_2, \end{aligned} \quad (3.23)$$

where \overline{V}_P and \overline{V}_S is the updated V_P and V_S value given by the optimization for each iteration, V_P and V_S represent a projected value with respect to the r_1 and r_2 boundary.

Trinh (2018) uses the Dykstra algorithm to solve this non-linear model constraint (Boyle and Dykstra, 1986). This approach is used in our experiment in order to obtain a reasonable multi-parameter inversion for the shallow-seismic application. Appendix 3.B contains more detailed information regarding the non-linear model constraint and the Dykstra algorithm.

This non-linear constraint strategy is crucial because the V_S gradient is still relatively strong, even after the first FWI. Another reason is the limitation of V_P information inside the data itself (relatively weak early body wave arrivals are recorded). Although V_P might be recovered from the surface wave, as Irnaka et al. (2018) had demonstrated it on a synthetic case, with the influence of the noise level and the accuracy of the acquisition, the information on V_P from the gradient remains weak compared to the information on V_S . Another source of V_P update is the body wave or P-wave, which can be seen on the data. This body wave feature is masked by the strong surface wave at low frequency, and this information is difficult to retrieve. At higher frequency, the body waves are well separated with the surface wave (see Figure 3.8). Without proper estimation of the V_P at the low frequency, the multi-parameter inversion has difficulty estimating the correct V_P at the higher frequency cycles.

Our approach tries to find a balance between FWI with parameter binding and FWI with multiple model constraints. We want to ensure that we would get the update from both parameters V_P , V_S , and V_P/V_S for each cycle. The new value of V_P/V_S is used as the input parameter for the next frequency band of FWI with parameter binding. It is essential to note that for both FWI steps, we only use top window muting to reduce the matching filter artifacts before the first arrival. With this approach, we take all available information of both V_P and V_S from each frequency band.

3.3.3 Implementation: SEM46 code

The methodology that we have briefly described is implemented in the SEM46 package. It is a 3D viscoelastic full waveform modeling and inversion tool based on the spectral element method and the SEISCOPE optimization toolbox (Métivier and Brossier, 2016) written in Fortran (Trinh et al., 2019b). SEM46 offers simplicity in mesh design by automatically designing the computational domain mesh on a Cartesian base. Such a Cartesian based mesh is suitable for smooth varying medium, which applies for most FWI applications. It uses a two-level MPI parallelization, combining parallelization over sources and domain decomposition based parallelization.

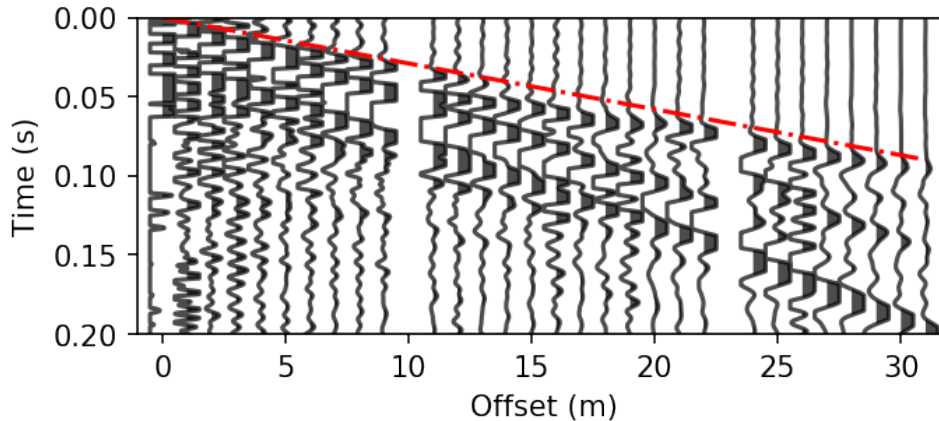


Figure 3.8: Seismic section on the first source location with U source direction. This seismic section is used to estimate the V_P for the homogeneous initial model. Red dashed line represents the direct P-wave arrival from the estimated homogeneous model.

3.4 Application

This section discusses how we apply the FWI method described in the previous section in a consistent workflow. We use a hierarchical approach based on frequency continuation, and for each frequency band, the two steps approach based on parameter binding, then non-linear model constraints are applied (Fig. 3.9). We describe in detail each stage of this workflow in the following.

3.4.1 Initial model building

The Ettlingen Line has relatively simple geology and flat topography. Our goal is to have a simple but consistent starting homogeneous velocity model.

To design it, we pick the first P-wave arrival at the longest offset on inline seismic section (Fig. 3.8). From this arrival, we estimate a homogeneous V_P model directly, resulting in a value of 345 m.s^{-1} . We estimate the other elastic parameters (V_S and density ρ) using a fixed Poisson's ratio $\nu = 0.25$ and the Gardner's relationship, resulting in $V_S = 199 \text{ m.s}^{-1}$ and $\rho = 1336 \text{ kg.m}^{-3}$.

An initial attenuation model is obtained based on the previous experiment of Gao et al. (2020), who have implemented multi-mode surface waves Q estimation (Gao et al., 2018). The Q_S model is 12 for the first 1 m depth. Then it linearly increases up to 80 until 5 m depth and remains constant from this depth. A constant ratio of 1.5 is used to estimate Q_P from Q_S based on Hauksson and Shearer (2006). During FWI, only V_P and V_S are reconstructed; the density ρ , Q_P , and Q_S models are considered as passive parameters (used for the modeling but not updated).

3.4.2 Source estimation

We assume to have directional point sources (U, V, W) with known and fixed source direction for each location (Table 3.1). We also assume to have equivalent source energy and fixed source location. In order to obtain such source time function, we follow a strategy with three steps: raw source time

function estimation for each source location using deconvolution operation (Pratt, 1999), amplitude normalization to equalize the amplitude contribution of each source, and spatial weighting average to reduce the local effect and over-estimation of the source. The technical detail of the source estimation is written in Appendix 3.C. These steps produce single-source time functions for each location and direction of the source, making a total of 108 source signals.

3.4.3 Multi-scale strategy

The lowest frequency band we start with is 3-15 Hz. We increase the frequency band by 10 Hz increments at each FWI stage. In total, we perform six FWI stages. The highest frequency band in this experiment is thus 3-65 Hz.

We apply the multi-parameter strategy for each frequency band described in the previous section (Figure 3.9). The first inversion is FWI with parameter binding, and the second is non-linear model constraint multi-parameter inversion. We specify the initial γ as a fixed value of 1.732 (which corresponds to the constant Poisson's ratio $\nu = 0.25$). The γ value is updated each time the non-linear model constraints multi-parameter inversion is carried out. The lower and upper boundary values we use are 100 m.s^{-1} and 2000 m.s^{-1} respectively for V_P , 50 m.s^{-1} and 800 m.s^{-1} respectively for V_S . The lower and upper boundary values for the ratio between V_P and V_S are 1.633 and 10, respectively. A short offset data muting up to 1.5 m offset is applied to remove some unreliable data. An additional top window muting is used to remove a strong noise on some part of the data, which might be increased by the matching filter correction.

In terms of numerical optimization parameters, we set the maximum line search to 20, and the number of the stored gradient for *l*-BFGS to 10. The Bessel filter based gradient smoothing uses coherent lengths of 0.1λ , 0.7λ , and 0.7λ with respect to the local velocity and dominant frequency in vertical, inline, and crossline direction, respectively. A depth preconditioner is applied to the gradient with the depth power of 2.

3.4.4 Model reconstruction

We carry out a complete FWI workflow with both parameter binding and non-linear constraint strategies to obtain the reconstructed model for the respective frequency band for each scale.

Figure 3.10 shows the evolution of the reconstructed models. We present V_S on the top row, V_P on the middle row, and Poisson's ratio ν on the bottom row. The Poisson's ratio is calculated from the reconstructed V_P and V_S . The columns represent the updated model throughout the different FWI stages, starting from the initial model on the left, 3-25 Hz band on the 2nd column, 3-45 Hz band on the 3rd column, and the final 3-65 Hz band on the 4th column. All 3D views are presented with a 1 m depth section. The locations of the source are indicated as red points on the initial models.

We observe a gradual reconstruction of the Ettlingen line structure through the frequency continuation strategy. On lower frequency bands (up to 25 Hz), the updates are mainly dominated by the background velocity update, which corresponds to a vertical velocity gradient. This vertical velocity gradient can be observed in the final vertical section, as given in Figure 3.11.

The Ettlingen line, which corresponds to the low V_S and V_P velocity zone appearing at 1 m depth, oriented along the diagonal of the model, starts to be visible at 45 Hz. We also observe the appearance of a second low-velocity zone aligned with the crossline direction at this frequency. However, already

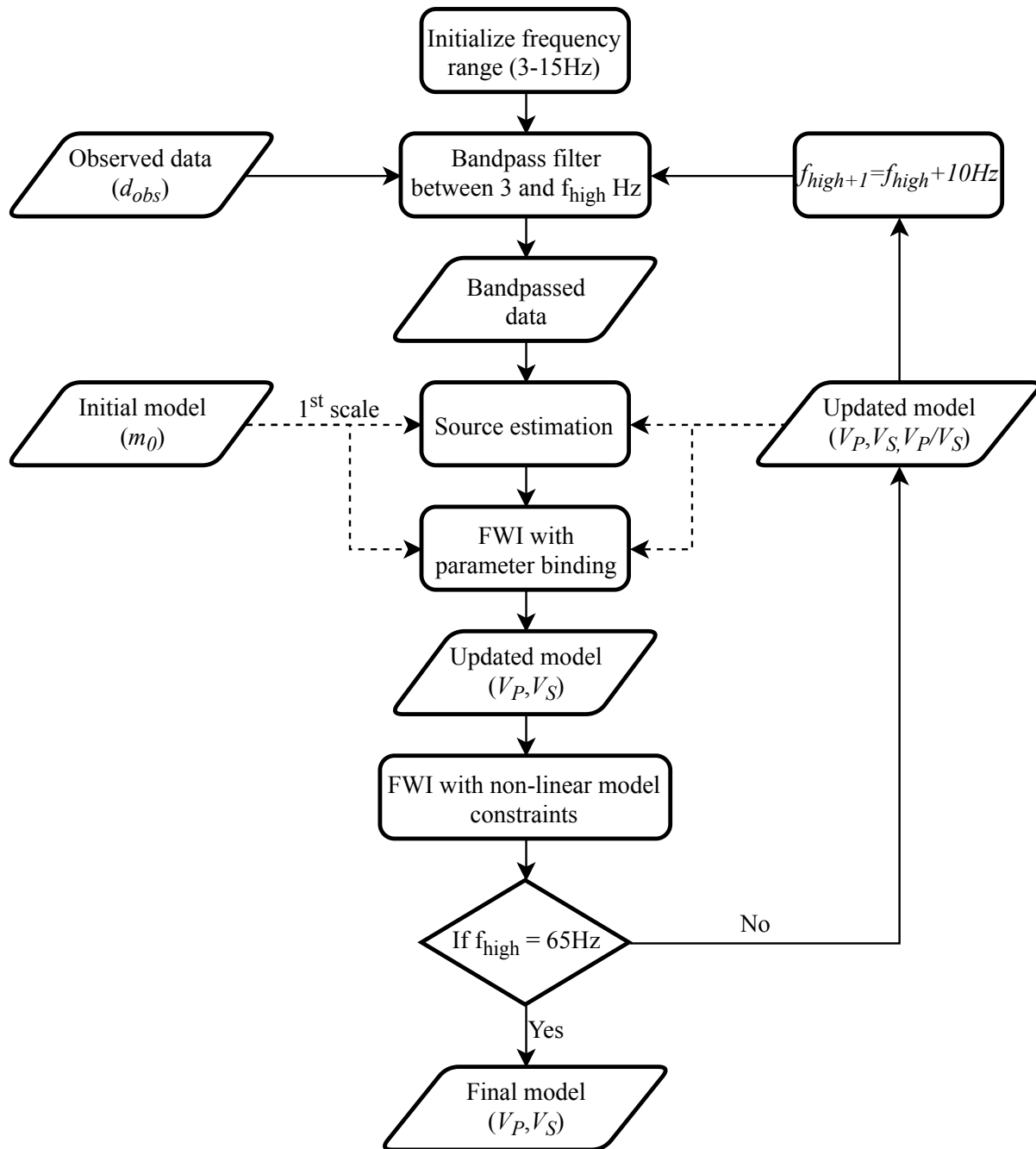


Figure 3.9: The proposed FWI Workflow for shallow-seismic application. We test this workflow with 9C data on Ettlingen Line case.

in the V_S gradient in the initial model, we can detect information regarding the presence of the Ettlingen line (Fig. 3.12).

As expected, the Poisson ratio is constant at the beginning of the inversion, while the multi-parameter workflow we design allows us to relax the linear relationship initially imposed between V_P and V_S . Higher values of the Poisson ratio (close to 0.4) along the two trench structures are consistent

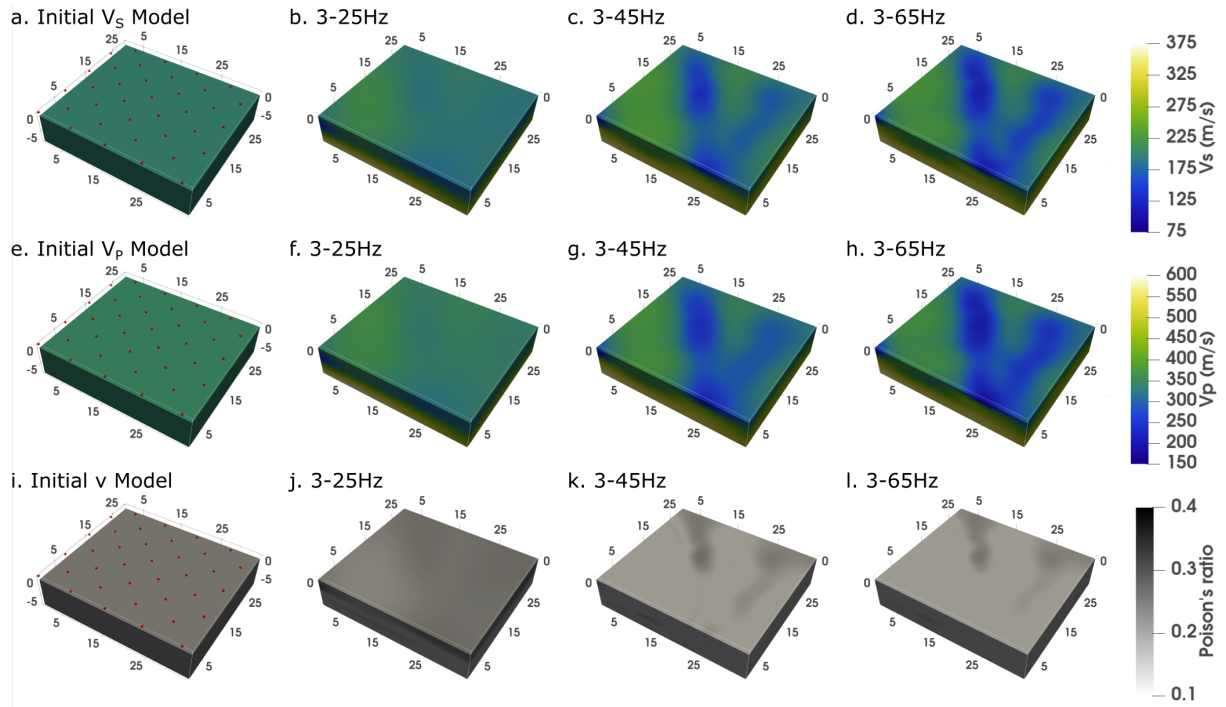


Figure 3.10: Reconstructed parameters (V_S at the top row, V_P at the middle row, and ν at the bottom row) at 1 m depth section. Each column is associated with a specific FWI stage (initial model on the 1st column, 3-25 Hz band on the 2nd column, 3-45 Hz band on the 3rd column, 3-65 Hz band on the 4th column).

with the trench's interpretation as less consolidated zones.

Throughout the different frequency bands, we can also observe a relative insensitivity of the model's shallowest part. This insensitive zone might correspond to the expected FWI resolution. Figure 3.12 also illustrates this behavior. In the case of the 3-25 Hz frequency band, we observe a negative gradient value in the shallowest part of the model. It is the opposite of the intended direction since the seismic velocity at the near-surface is supposed to be slower than the one in the model's deeper part.

3.4.5 Quality control: data fit

In Figure 3.13a, we present a comparison between the 9C observed data (grey traces) and the 9C synthetic data calculated in the initial model (red traces) on the last frequency band (3 - 65 Hz). Both data are recorded using the source at the location inline 0 m and crossline 16 m for all nine components. The displayed seismic data is the seismic data with inline direction. The source orientations are represented in the row (U,V,W), and the receiver components are represented in columns (Z,X,Y). We perform a trace by trace normalization in order to better see the fit at a longer offset.

In this figure, we see clearly that the strong surface wave dominates the waveform. Although the homogeneous model produces a simple waveform propagation, we still observe a good surface wave matching and no evidence of cycle skipping. The good match is an indication that starting from a homogeneous model is feasible in this context.

In Figure 3.13b, we perform the same comparison, but this time the synthetic is calculated using

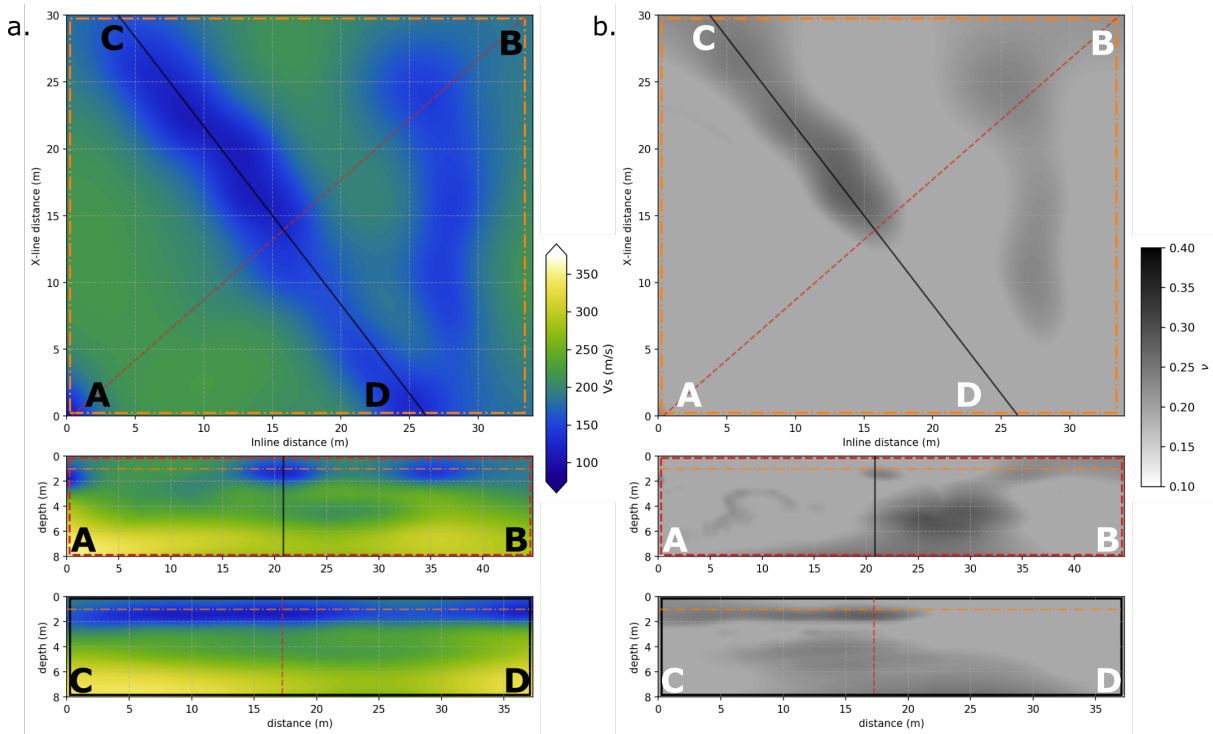


Figure 3.11: A horizontal slice of reconstructed V_S (left) and Poisson's ratio ν (right) at 1 m depth shows clear presence of the Ettlingen Line trench as well as a trench-like structure with north-south direction (top). Vertical slice of reconstructed V_S perpendicular (middle) and parallel (bottom) with the direction of Ettlingen Line.

the final reconstructed V_P and V_S models. We can observe a significant improvement of the data fit in all components. The vertical components (first column), in which the waveforms are the least complex, have a relatively better match than the horizontal component. In this seismic section, the Ettlingen Line is located approximately between trace numbers 10 and 20. Between those traces, we can observe that the FWI can reconstruct the small disturbances in the recorded data. Starting from a homogeneous model, we observe that we can obtain a satisfactory data fit.

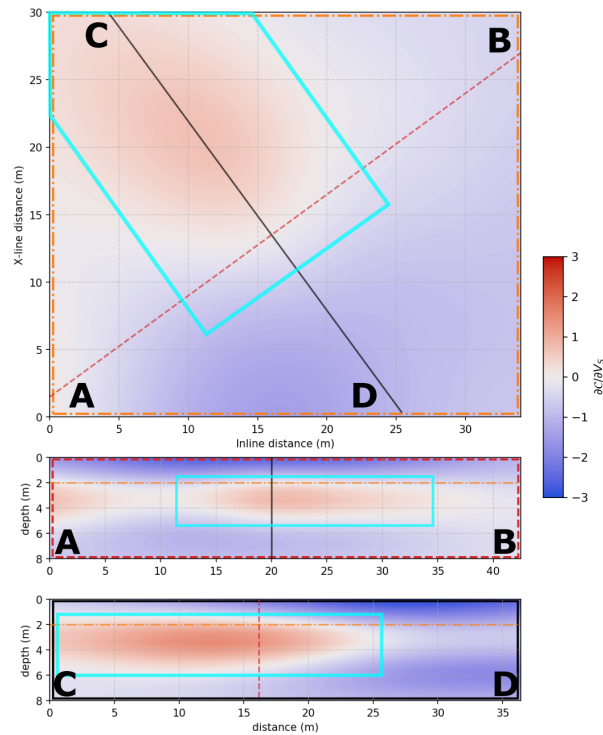


Figure 3.12: First V_S gradient at 3-25 Hz frequency band. The top figure represents a horizontal slice at 2m depth, the middle figure represents a vertical crossline section AB , and the bottom figure represents a vertical inline section CD . Cyan rectangles on each figure depict the positive value which correspond with the presence of the low velocity anomaly of the Ettlingen Line.

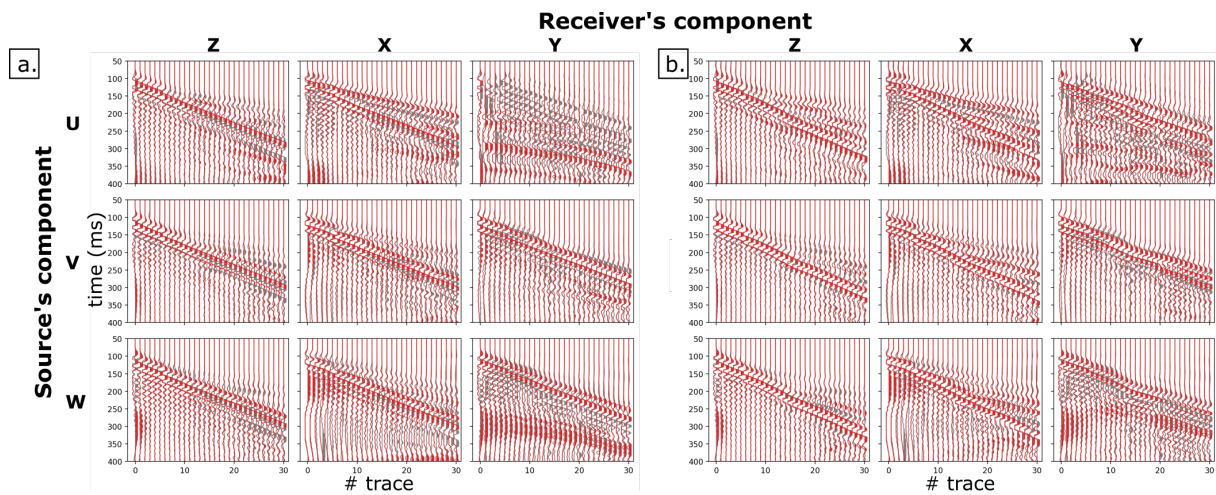


Figure 3.13: Comparison between 9C observed data (grey) and 9C calculated data (red) in (a) the initial model (b) the reconstructed model. A trace by trace normalization is used to plot the data. The larger overlap between red and grey in the final model shows a better data match.

3.5 Discussion and interpretation

3.5.1 Model interpretation

Several experiments at the Ettlingen Line have been performed already with different approaches and methods. A 3D GPR experiment has been performed by Wegscheider (2017), and 2D elastic FWI from 2D seismic data has been lead by Wittkamp et al. (2018). A 3D MASW has also been performed by Pan et al. (2018) using the same data.

Figure 3.14 shows a comparison between these results. In Figure 3.14a, an overlay between the GPR results and the 2D V_S model obtained by Wittkamp et al. (2018) is presented. GPR measurement shows an inverted triangle shape in the middle of the section, interpreted as the Ettlingen Line. The 2D FWI was carried out using joint inversion from both Rayleigh and Love waves up until 130 Hz. The low-velocity anomaly represents the Ettlingen Line in the middle of the model. The sharp boundary and shallow model reconstruction can be seen thanks to the higher frequency inversion. In Figure 3.14b, the corresponding 2D slice extracted from the 3D MASW V_S model is presented. In Figure 3.14c, we present the corresponding slice of the V_S model we have estimated through 3D multi-parameter viscoelastic FWI.

While we do not recover the high resolution coming from both GPR and high-frequency surface waves from the first experiment, we can still locate the V_S anomaly at a similar location. This result is also in agreement with the MASW result, with, in our case, a significantly higher resolution, as expected.

However, our approach's added value relies on the fact that we estimate 3D models, both for V_P and V_S . Both our reconstructed V_P and V_S show a distinct presence of the low-velocity anomaly. Analyzing the model from the final frequency band, we can infer the geometry of the trench line. It has a consistent northwest-southeast direction, with a width of around five meters and two meters depth.

Interestingly, we can also observe an additional low-velocity anomaly with a north-south orientation, with a similar trench-like structure. It is shallower than The Ettlingen Line, around 1.5 m deep, with 2 to 3 m width. This low-velocity anomaly is visible on the previous 2D FWI (Fig. 3.14a) at a distance of around 30 to 35 m on the previous 2D FWI. However, considering the structure's location, which is close to the edge of the acquisition, it had been interpreted as a probable artifact previously. The 3D reconstruction we perform here shows that this low-velocity zone has a consistent structure along the north-south direction, making it much more likely an actual feature of the subsurface structure. There are now debates regarding the historical significance of this second trench-like structure.

On the MASW result, the indication of this trench-like structure is much weaker due to the lower resolution of the 3D estimation. However, its presence can be guessed from the smearing of low-velocity anomaly in the south-east part of the model (Fig. 3.15a).

Our multi-parameter reconstruction also makes it possible to describe the physical properties of the target better. In geotechnics, V_S is often used as a proxy of the soil compactness of the medium. Given the similar type of soil material in this experiment, lower V_S means a lower compaction degree. Thanks to our multi-parameter inversion, we can also estimate the value of the Poisson ratio ν . The Poisson ratio can give an estimation of water saturation tendency beside the compaction level. Within the trenches itself, we can see a variation of the Poisson's ratio. Assuming similar material was used to level the trench line, the higher Poisson's ratio might correlate with higher water saturation. It can be observed at the northwest part of the Ettlingen Line (Fig. 3.10l). The variation of the Poisson's ratio can also be interpreted as denoting the presence of fine heterogeneities inside the trench. The

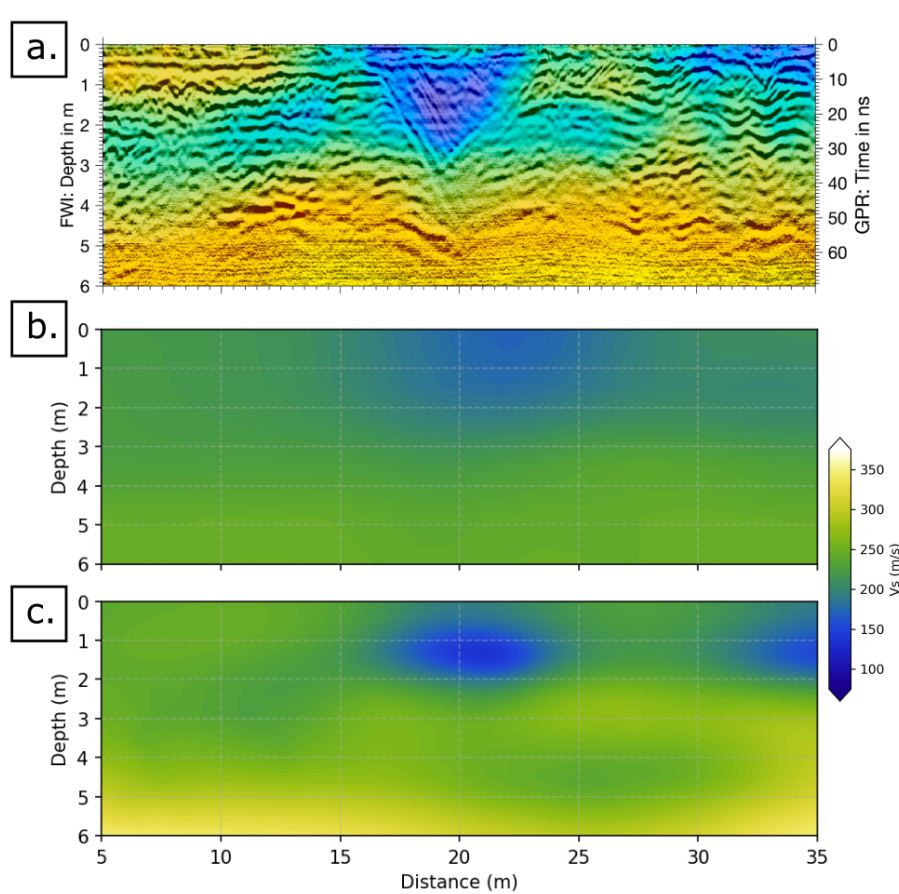


Figure 3.14: Vertical section of 3D GPR and 2D elastic joint inversion of Love and Rayleigh wave result taken from Wegscheider (2017) and Wittkamp et al. (2018) (a), 3D MASW by Pan et al. (2018) (c), and 3D elastic FWI starting from homogeneous model (c). The color-scale on (a) is unscaled, blue means lower velocity and yellow means higher velocity.

second trench-like structure does not show similar Poisson ratio variations, indicating a probably more homogeneous soil material within the trench.

In Figure 3.11, we present horizontal and vertical section of 3D model of the Ettlingen Line. The figures on the left represent V_S , and the figures on the right represent ν . These figures give a better view of the geometry of the trenches. The Ettlingen Line has a width ranging from 4 to 6 meters, and the depth ranging from 2 to 2.5 meters. This geometry is a common size for a war trench. Looking at the V_S profile of the inline vertical section gives information that the Ettlingen Line's structure is continuous throughout the model. The V_S of the Ettlingen is lower than the surrounding, below 140 m/s. The other trench-like structure is also continuous on the final reconstructed V_S . The structure is not as straight as the Ettlingen Line. Its width is narrower and shallower than the Ettlingen Line. It is around 2.5 meters and 1.5 meters for width and depth, respectively. The V_S on the other trench-like structure is slightly higher than the one inside the Ettlingen Line.

The right figures on Figure 3.11 show the final reconstructed Poisson's ratio at 65 Hz. Besides the higher Poisson's ratio at the trenches' location due to the different materials, compactness, or water saturation level, we observe an interesting behavior at a depth of 4 to 5 meters. There is a contrast of

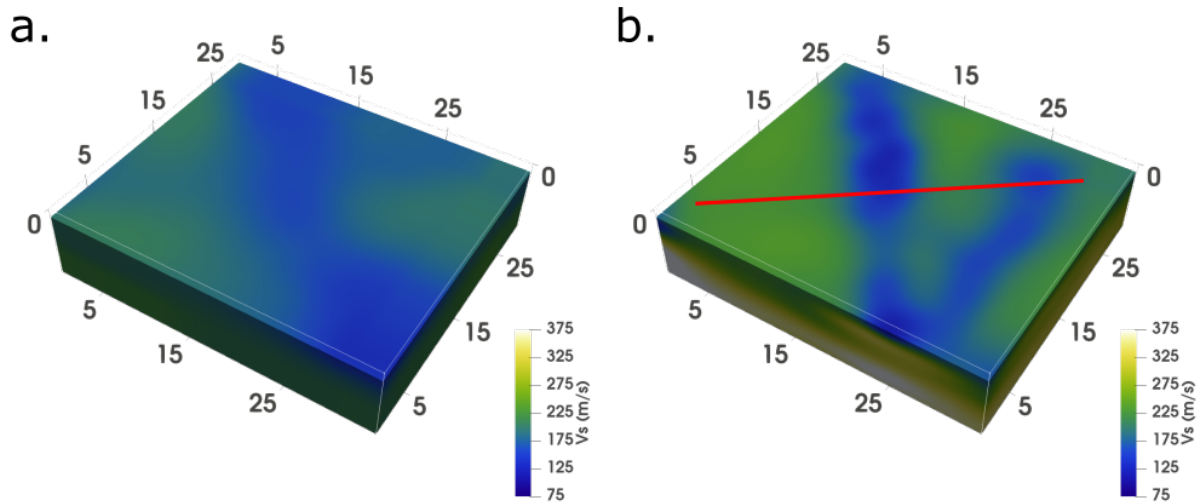


Figure 3.15: 3D V_S from previous MASW study by Pan et al. (2018) (left) and this study starting from homogeneous initial model (right). Red line represents the location of the GPR line on Figure 3.14.

the Poisson's ratio at this depth, from low to higher value. This feature probably depicts a possible higher water saturation or even the water table in the area.

3.5.2 Is it reasonable to start from a homogeneous model?

Initial model building is one of the key aspects to ensure the efficiency of the FWI and can be a highly time-consuming step of the FWI workflow. We have used here an initial homogeneous model, computed from very crude assumptions, advocating that the usable frequency content of the signal compared to the target's size was preventing in this case from any cycle skipping effects.

We perform an additional experiment to validate this assumption, where we use the 3D V_S MASW model from (Pan et al., 2018) as an initial model. We cut the model below 7 m depth, where a strong interface exists from the MASW result. Then we extrapolate the velocity value from the depth of 6.5 m. A fixed Poisson's ratio of 0.25 is used to estimate V_P . As we used before, the same Gardner relationship is taken to estimate the density from the initial model.

We then apply the exact same workflow like the one we have used using the homogeneous initial model. The reconstructed V_P and V_S from both starting models are presented in Figure 3.16. We observe that the difference between the two reconstructions is very weak, which confirms the fact that considering this type of target, with a sufficiently good quality data, a complex initial model building relying on tomography or analysis of surface wave dispersion is not needed. This observation is important for future near-surface FWI studies as it simplifies the FWI workflow greatly.

3.5.3 Elastic or viscoelastic FWI?

The shallow geology around the Ettlingen Line field is dominated by loose sediment and soil. In the seismic wave propagation perspective, uncompacted sediment shall present high attenuation. Previous studies in the area found that within the first meter, Q_S can be as low as 12. This low Q_S in the first meter is essential since the target is located very close to the surface. We perform a crude verification

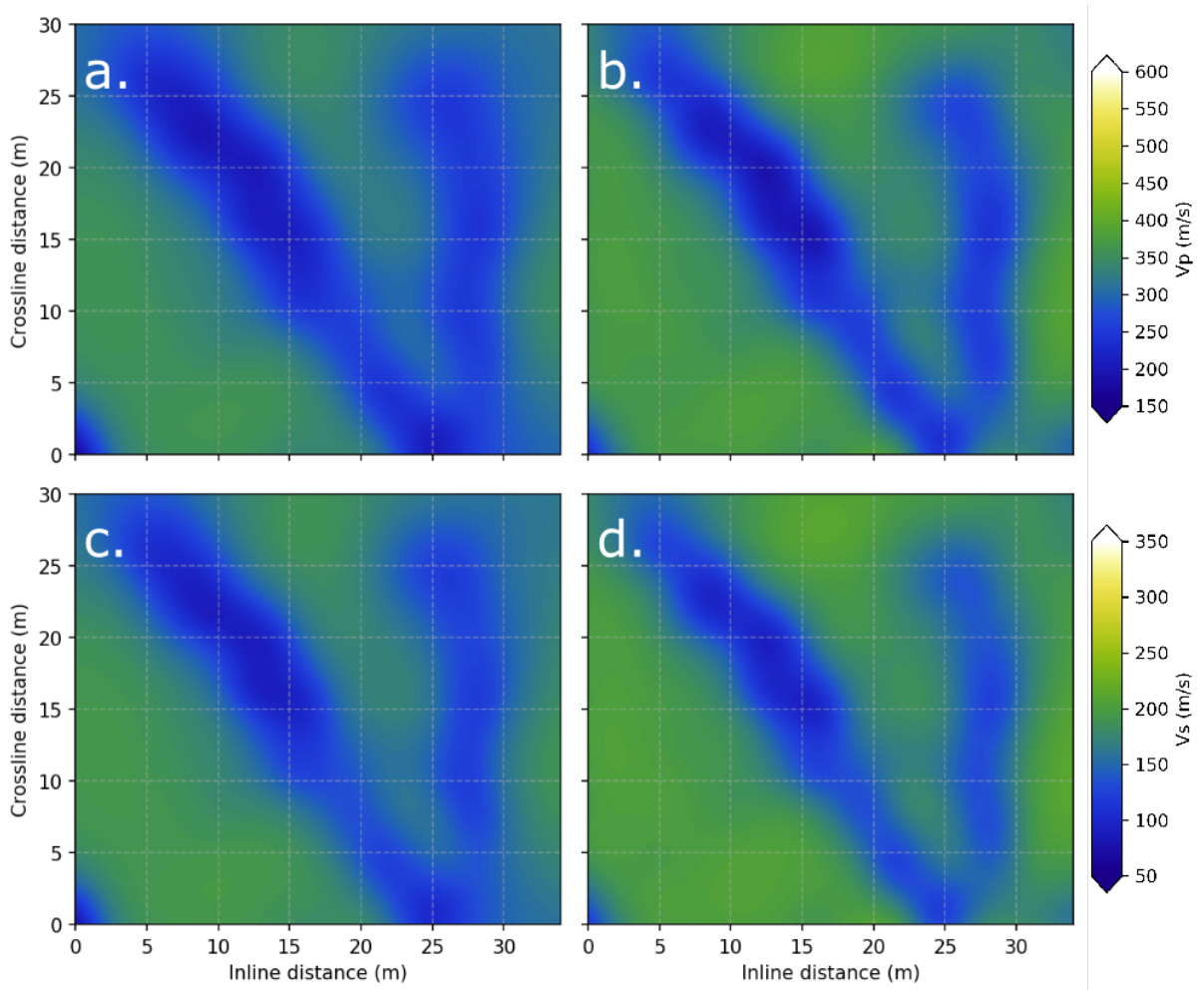


Figure 3.16: Horizontal slice of the inversion result at 1 m depth for both V_P (top row) and V_S (bottom row) use different initial models. Left slices represent final velocity model at 65 Hz starting from homogeneous model; whereas right slices represent final velocity model at 65 Hz starting from MASW V_S model.

of the overall Q_P value by comparing the P-wave amplitude versus offset (after geometrical spreading correction and a narrow bandpass filter between 50 and 80 Hz) with the theoretical amplitude decay given a constant Q_P model based on Kjartansson (1979) with a constant V_P of 170 m.s^{-1} at 65 Hz (Fig. 3.17). A Q_P value between 10 and 20 appears reasonable, which is consistent with the attenuation model we have used so far.

In figure 3.18 and 3.19, we present the reconstructed V_S and V_P velocities using both elastic (left) and viscoelastic modeling (right) on two different frequency bands (65 Hz at the top and 45 Hz at the bottom), starting from the homogeneous initial model. The inversion on the highest frequency band (65 Hz) generates significantly different models. While sharing a similar background model, the elastic FWI result display some additional smaller-scale features. On the contrary, the viscoelastic results exhibit a smoother and more spatially consistent aspect, with slightly higher velocity values. We also note that the divergence between elastic and viscoelastic FWI results appear only on the largest frequency band. Results obtained at 45 Hz are reasonably similar.

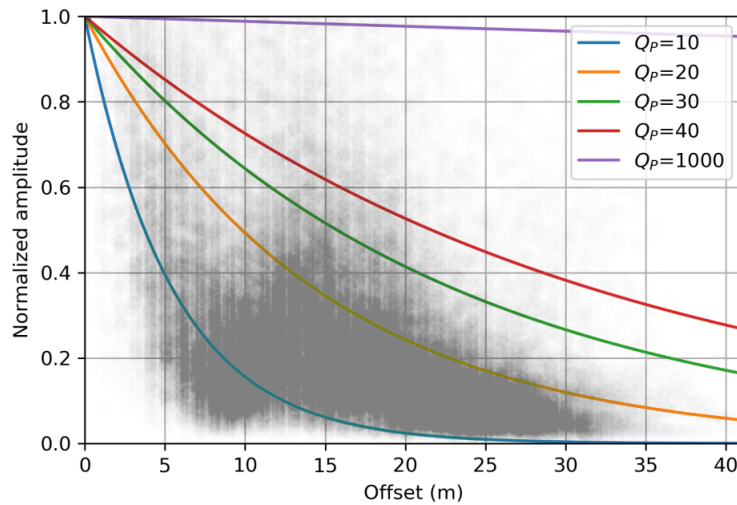


Figure 3.17: Normalized amplitude of P-wave with respect to the offset drawn as the scatter plot on a narrow bandpassed data centered at 65 Hz. The line plots represents theoretical amplitude decay given a constant Q_P model based on Kjartansson (1979) at 65 Hz. A geometrical spreading correction is applied prior to normalization.

We present several seismograms comparing the synthetic data, which are obtained using elastic and viscoelastic FWI with the observed data (Fig. 3.20). The amplitudes are normalized based on the maximum amplitude of each seismic section's longest offset to see the relative amplitude decay between each data. We can see a better relative amplitude decay at the first arrival of trace #5 to trace #10, but in general, the difference is not significant. The wave packets' travel time is very similar between elastic and viscoelastic FWI because the travel time difference has been compensated during the inversion.

We hypothesize that the additional small scale structures appearing in the elastic FWI result are artifacts due to physics's inaccuracy. For a sufficiently narrow frequency band (in our example up to 45 Hz), the data's attenuation influence is less dramatic, using elastic modeling is sufficiently accurate. On the contrary, at a higher frequency band, viscoelastic modeling seems to become essential. While viscoelastic FWI produces smooth and consistent velocity models, elastic FWI tends to introduce small scale artifacts to compensate for the inaccuracy of the wave propagation modeling engine it relies on.

3.5.4 Other limitations and prospects

This study demonstrates the 3D FWI application on the Ettlingen Line using 9C seismic data. However, there are several limitations related to the two-step strategy, initial model, source time function, data coverage, and modeling approach. It is essential to discuss these limitations better to understand the advantages and disadvantages of our approach.

The two steps FWI (parameter binding and non-linear model constraint) the model reconstruction on both V_P and V_S but leads to an increase in the relative computational cost related to the two FWI. The reconstruction of V_P itself is rather limited due to the stronger influence of V_S in the surface wave and lack of P-wave information in the data.

The source time function is one of the keys to obtain a good model reconstruction during FWI. In our experiment, we assume a known and fixed direction of the source time function (Table 3.1). We

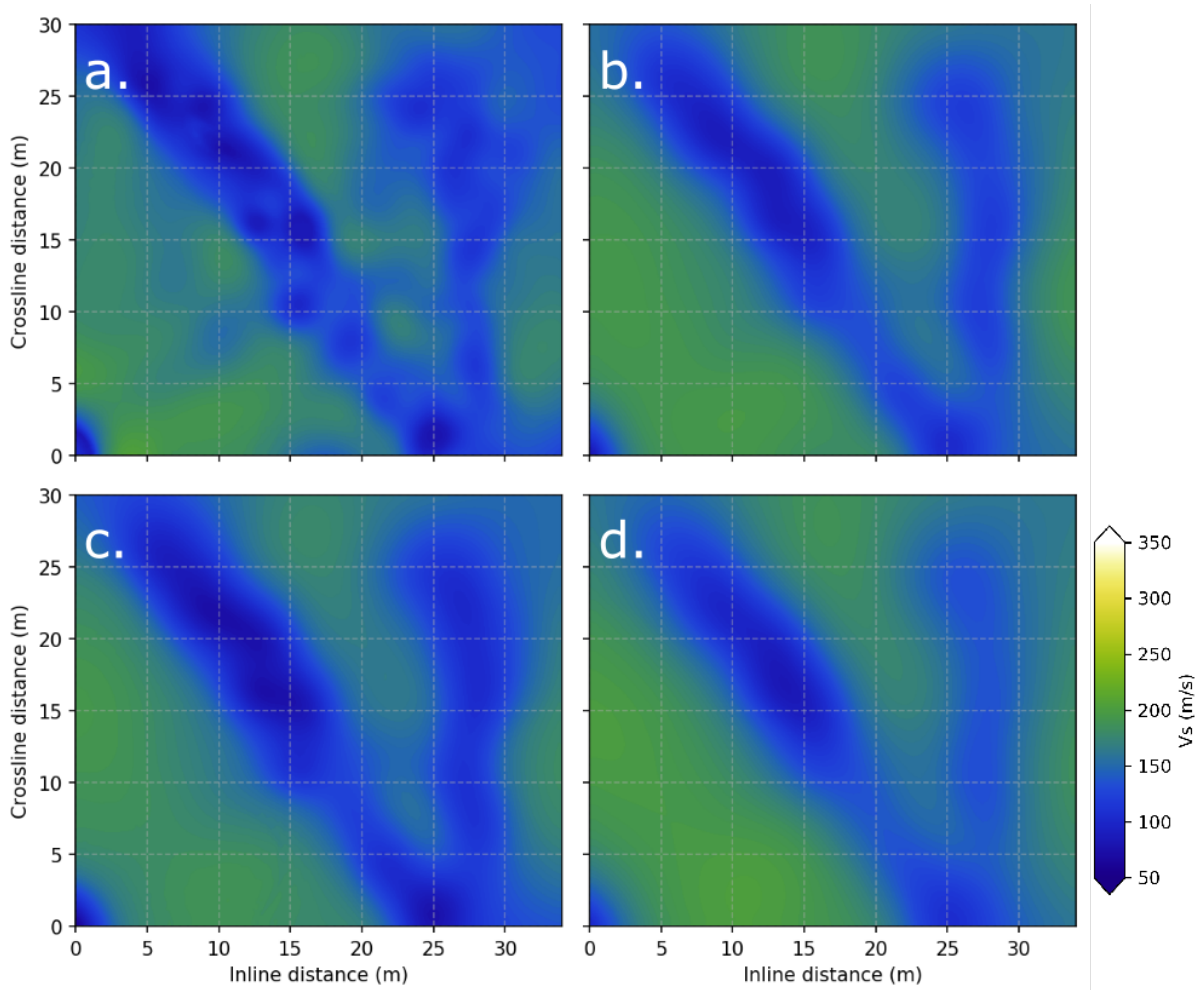


Figure 3.18: Horizontal slice of V_S from the FWI at 1 m depth for FWI with elastic medium (left column) and viscoelastic medium (right column). Top row images are the reconstructed V_S at 65 Hz, whereas 45 Hz for the bottom row images.

have minimized the local dependency of the source time function by performing normalization and the spatial weighting, but with better source estimation, we might be able to improve the result.

Good coverage of sources and receivers also plays an essential factor in the accurate model reconstruction. The receiver spacing (1 m), which is way less than the target (~ 5 m) width, ensures the information redundancy in terms of data, therefore enhancing the signal and helping the inversion. The availability of 9C data might also contribute towards the improvement of the model reconstruction. A more detailed study regarding multi-component data and source and receiver setup will be done on further study.

The viscoelastic FWI uses the attenuation model from the previous 2D seismic experiment. Although there is no significant landscape or geological changes between the acquisition and FWI usually does not require a very detailed attenuation model, a slight change of attenuation value might occur, and the 1D attenuation model might produce less satisfying results than a correct 3D attenuation model.

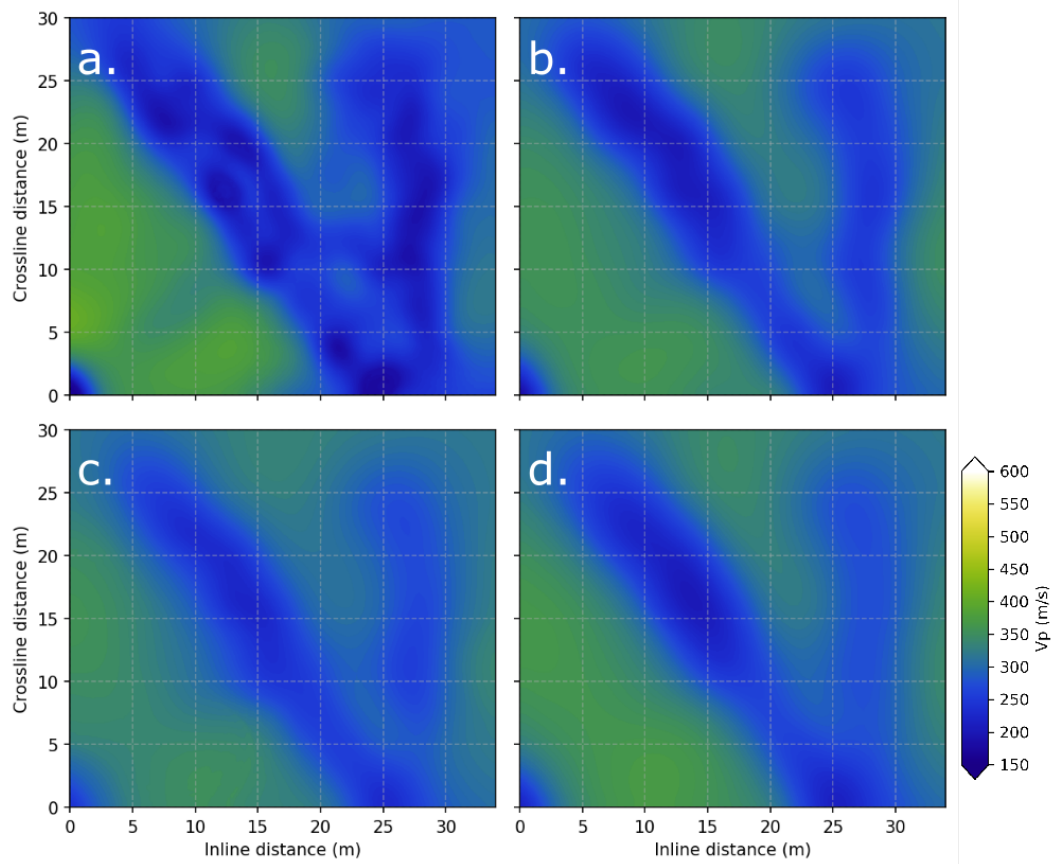


Figure 3.19: Horizontal slice of V_P from the FWI at 1 m depth for FWI with elastic medium (left column) and viscoelastic medium (right column). Top row images are the reconstructed V_P at 65 Hz, whereas 45 Hz for the bottom row images.

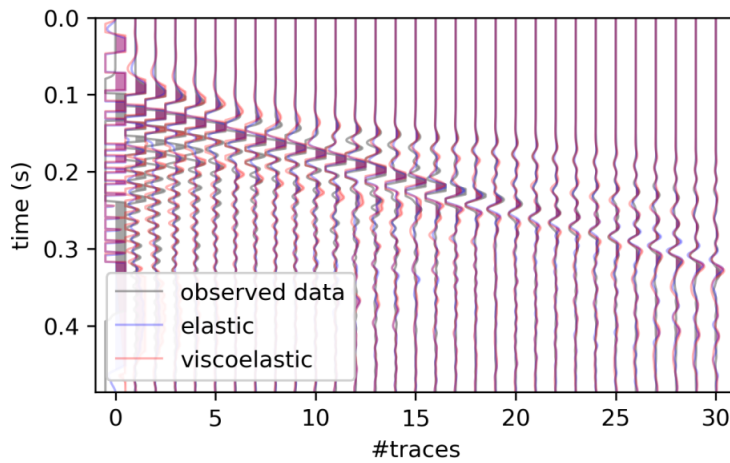


Figure 3.20: Relative amplitude decay on elastic and viscoelastic synthetic data compared with the observed data. The trace is normalized based on the maximum absolute amplitude of the longest offset data. The seismograms with the amplitude which overlapped with the neighboring seismogram are clipped.

3.6 Conclusions

We demonstrate an application of 3D Full Waveform Inversion for shallow-seismic scale. The target is the Ettlingen Line, an ancient war-trench built during the War of The Spanish Succession.

With the limited number of the equipment, we perform the 3D dense acquisition patch by patch. In consequence, we observe some data inconsistencies. We can reduce the inconsistencies through matching filters in the pre-processing stage. This process decreases the potential computational cost (up to the factor of 6) since the data can be treated as a single 3D dense acquisition.

The FWI follows a multi-scale approach with two specific strategies for each frequency band (the parameter binding and the non-linear model constraints). The inversion is performed up to 65 Hz with two initial models (homogeneous and MASW) and modeling approaches (elastic and viscoelastic). The result shows that we can start from a homogeneous initial model, thanks to sufficient low-frequency data. On the aspect of the modeling approach, both elastic and viscoelastic approach are comparable up to 45 Hz. At higher frequency, we observe differences between both approaches, where the elastic modeling produces some additional small scale features. We hypothesize that these additional features in elastic FWI are artifacts due to the physics's inaccuracy, thus advocating for the use of viscoelastic FWI.

From the archaeological point of view, our 3D FWI has reconstructed a high-resolution historical trench. The shape and geometry of the Ettlingen Line can be recovered. The width of the Ettlingen Line is around 5 meters, and the depth is around 2 meters. We are also able to reconstruct another trench-like structure, which was not detected previously. This structure's width is around 3 meters, and the depth is around 1.5 meters.

With the successful application of FWI using 9C seismic data on the Ettlingen Line, we would like to extend our study to analyze the interest of using multi-component data and each component's contribution toward FWI. Studying multi-component data might allow us to better design strategies for acquisition, data processing, and the FWI itself.

APPENDICES

3.A Parameter binding FWI

Full Waveform Inversion (FWI) problem with two inverted parameters (V_P and V_S) can be written in Lagrangian form

$$\begin{aligned} \mathcal{L}(V_S, V_P, \rho, u, d_{cal}, l_1, l_2) = & \frac{1}{2} \|d_{cal} - d_{obs}\|^2 - \\ & \langle l_1 | Ru - d_{cal} \rangle - \langle l_2 | A(V_P, V_S, \rho)u - s \rangle, \end{aligned} \quad (3.24)$$

where V_P and V_S is P and S wave velocity, u is the incident wavefield, d_{cal} is the synthetic data, l are the lagrangian multipliers, d_{obs} is the observed data, R is the sampling operator to extract the data at the receiver location, A is the forward problem operator, s is the source time function.

In the parameter binding strategy, we impose a hard-constrained V_P with respect to V_S with a linear operator ($V_P = \gamma V_S$). $\gamma(x, y, z)$ is a scaling factor between V_P and V_S . Introducing another hard-constraint modifies the Lagrangian form on Equation 3.24 as following

$$\begin{aligned} \mathcal{L}(V_S, V_P, \rho, u, d_{cal}, l_1, l_2, l_3) = & \frac{1}{2} \|d_{cal} - d_{obs}\|^2 \\ & - \langle l_1 | Ru - d_{cal} \rangle - \langle l_2 | A(V_P, V_S, \rho)u - s \rangle \\ & - \langle l_3 | V_P - \gamma V_S \rangle. \end{aligned} \quad (3.25)$$

The adjoint-state equation of the Lagrangian formulation can be solved by calculating $\frac{\partial \mathcal{L}}{\partial d_{cal}} = 0$, $\frac{\partial \mathcal{L}}{\partial u} = 0$, $\frac{\partial \mathcal{L}}{\partial V_P} = 0$ and can be written down as

$$l_1 = d_{obs} - d_{cal}, \quad (3.26)$$

$$A^\dagger l_2 = R^\dagger l_1, \quad (3.27)$$

$$l_3 = \left\langle l_2, \frac{\partial A(V_P, V_S, \rho)}{\partial V_P} u \right\rangle, \quad (3.28)$$

where l_1 is the residual between the synthetic data and the observed data, l_2 is the adjoint wavefield obtained by solving the adjoint wave equation with $R^\dagger l_1$ as the source term, and l_3 is zero-lag cross-correlation between the l_2 and \ddot{u} .

Finally, the gradient of the Lagrangian with respect to the V_S can be written as

$$\frac{\partial \mathcal{L}}{\partial V_S} = - \left\langle l_2, \frac{\partial A(V_P, V_S, \rho)}{\partial V_S} u \right\rangle + \gamma l_3. \quad (3.29)$$

3.B Non-linear model constraints FWI

In non-linear model constraints strategy, we would like to solve the following minimization problem

$$\begin{aligned} \min_{V_P, V_S} f(V_P, V_S) = & \frac{(\overline{V_P} - V_P)^2}{V_P^2} + \frac{(\overline{V_S} - V_S)^2}{V_S^2}, \\ \text{subject to} \quad & r_1 \leq V_P/V_S \leq r_2, \end{aligned} \quad (3.30)$$

where $\overline{V_P}$ and $\overline{V_S}$ is the updated V_P and V_S value given by the optimization for each iteration, V_P and V_S represent a projected value with respect to the r_1 and r_2 boundary.

There is exist an analytical solution for this problem when $V_P/V_S > r_2$

$$V_P = r_2 V_S \quad \text{and} \quad V_S = \frac{\overline{V_S} \overline{V_P} (r_2 \overline{V_S} + \overline{V_P})}{(r_2 \overline{V_S})^2 + \overline{V_P}^2}, \quad (3.31)$$

and when $V_P/V_S < r_1$

$$V_P = r_1 V_S \quad \text{and} \quad V_S = \frac{\overline{V_S} \overline{V_P} (r_1 \overline{V_S} + \overline{V_P})}{(r_1 \overline{V_S})^2 + \overline{V_P}^2}. \quad (3.32)$$

Following Trinh (2018), both constraints \mathcal{C}_1 and \mathcal{C}_2 (bound constraints, ratio constraints) can be solved using Dykstra algorithm (Algorithm 1).

Algorithm 1: Standard Dykstra algorithm

$x_0 = m^k + {}_k \Delta m_k$ and $p_0 = 0, q_0 = 0$
while not convergence and $k < n_{max}$ do
 $y_k = \mathcal{P}_{\mathcal{C}_1}(x_k + p_k)$
 $x_{k+1} = \mathcal{P}_{\mathcal{C}_2}(y_k + q_k)$
 $p_{k+1} = x_k + p_k - y_k$
 $q_{k+1} = y_k + q_k - x_{k+1}$

3.C Source estimation

In shallow-seismic data where the source is manually performed by the sledgehammer, there are several potential problems. The problems include a potential unbalanced in the relative source energy and a potential to over-estimating the source. Those problem might lead to both unbalance contribution of each source and insensitive inversion. Based on those problem, we perform two additional steps during the source estimation procedure.

In total there are three steps to obtain source time function for each source location:

1. raw source estimation $s_i(t)$ following Pratt (1999),
2. amplitude normalization, and
3. spatial weighting average.

The amplitude normalization aims to equalize the energy contribution on each source. We calculate the scaling factor c_i for each $s_i(t)$ as

$$c_i = n / \overline{s_i}(t), \quad (3.33)$$

where n is a constant normalization factor and $\overline{s_i}(t)$ is the average amplitude for source i (i, j , and k is the source's number). The scales are used to normalize both the source time function and the observed data.

The spatial weighting average is performed using a 2D spatial gaussian window. It is aimed to reduce the over estimation of the source by assuming similar source time function compared with the neighboring source, but still preserve some characteristics of each source location. The spatially weighted source $\hat{s}_i(t)$ is calculated from the scaled source ($\tilde{s}_i(t) = s_i(t)c_i$) and given as

$$\hat{s}_i(t) = \sum_{j=1}^N \tilde{s}_j(t) \frac{e^{\frac{1}{2} \frac{\tilde{s}_j^2}{\sigma}} / \sigma \sqrt{2\pi}}{\sum_{k=1}^N (e^{\frac{1}{2} \frac{\tilde{s}_k^2}{\sigma}} / \sigma \sqrt{2\pi})}. \quad (3.34)$$

where σ is the standard deviation of the gaussian function controlling the influence distance of the averaging function. In our experiment, we set 6 m as the σ .

3.D Computational cost

The calculation of this FWI experiment is performed using Irene KNL. It is a High Performance Computer (HPC) managed by TGCC in France. Irene KNL is based on Intel KNL processor with Knight-landing architecture. For each node, it has 68 cores, with 1.4 GHz CPU clock and 1.4GB RAM for each core. In practice, due to the limited memory of Irene KNL, we store the wavefield on a very high bandwidth disk (60 GB/s). The bandwidth is shared amongst the users therefore the Input/Output performance might differ from time to time and might affect the computational time.

The computational time needed to perform the whole set of FWI is 69119 and 41415 sequential hours for elastic and viscoelastic FWI, respectively (Table 3.2 and Table 5.6). Both tables represent the FWI which are started from the homogeneous initial model. The sequential hour represents the computational time needed to calculate a task only using a single processor, disregarding its memory requirement. V_S FWI represents FWI with parameter binding, whereas $V_S \& V_P$ represents FWI with non-linear model constraints. The CPU time which is required to estimate a single gradient increase with the increase of the degree of freedom, time step, and frequency band. The global CPU time, on the other hand, is highly influenced by the total number of the gradient as well as the time needed to perform the communication between the processor and the disk. Since we stored the resampled wavefield directly on the disk, the performance of the I/O also depends on the global I/O load on the whole HPC cluster.

The total CPU time is relatively expensive for shallow-seismic applications compared to another methodology (FATT, MASW). Nevertheless, when we look at the table, for the elastic FWI case almost 87% of the total computational hours were spent on the last two frequency bands. It means, with 9338 sequential hours, 47 Gigabytes of RAM, and 283 GB of fast storage for homogeneous initial model, we can already compute FWI up to 45 Hz and obtain resolution beyond FATT and MASW. It is currently not cheap for a personal workstation, but it is still feasible to be done and with the added benefit of the reconstruction of V_P .

Table 3.2: Computational cost for 3D FWI using elastic medium approximation.

No	FWI	N_{iter}	Time/ ∇	Seq. Time	Memory	Storage	NCPU	Elap. Time
1	15 Hz V_S	1	3.67	7.33	7559	7197	108	0.07
2	15 Hz $V_S&V_P$	5	3.67	32.99	7559	7191	108	0.31
3	25 Hz V_S	5	23.99	143.96	18530	45996	432	0.33
4	25 Hz $V_S&V_P$	17	23.47	610.23	18530	45996	432	1.41
5	35 Hz V_S	9	58.98	766.70	30472	118541	648	1.18
6	35 Hz $V_S&V_P$	9	59.11	591.08	30472	118541	648	0.91
7	45 Hz V_S	15	144.45	2311.14	47193	283256	972	2.38
8	45 Hz $V_S&V_P$	15	139.28	4874.95	47193	283256	972	5.02
9	55 Hz V_S	33	342.10	11973.38	75037	702491	1296	9.24
10	55 Hz $V_S&V_P$	25	337.99	10139.69	75037	702491	1296	7.82
11	65 Hz V_S	28	473.52	13731.96	88232	851449	3456	3.97
12	65 Hz $V_S&V_P$	12	460.32	23936.43	88232	851449	3456	6.93

The unit time is in hours. The total sequential CPU time (seq. time) is 69119 hours for all frequency bands on Irene KNL HPC (TGCC) to calculate from the homogeneous initial model. The memory and storage unit is in Megabytes (MB), and the indicated frequency is the highest frequency band starting from 3 Hz. The elapsed time (elap. time) is the time needed to perform the FWI in parallel.

Table 3.3: Computational cost for 3D FWI using viscoelastic medium approximation.

No	FWI	N_{iter}	Time/ ∇	Seq. Time	Memory	Storage	NCPU	Elap. Time
1	15 Hz V_S	1	7.81	15.63	9273	50382	108	0.14
2	15 Hz $V_S&V_P$	4	7.83	62.62	9273	50382	108	0.58
3	25 Hz V_S	23	25.83	697.51	15254	137909	864	0.81
4	25 Hz $V_S&V_P$	6	26.33	158.00	15254	137909	864	0.18
5	35 Hz V_S	23	109.27	2731.66	27672	494284	1296	2.11
6	35 Hz $V_S&V_P$	10	92.30	2769.14	27672	494284	1296	2.14
7	45 Hz V_S	10	285.66	2856.57	42878	1140998	1296	2.20
8	45 Hz $V_S&V_P$	11	327.20	3926.42	42878	1140998	1296	3.03
9	55 Hz V_S	14	424.94	7224.00	64184	2355901	2592	2.79
10	55 Hz $V_S&V_P$	1	537.10	537.10	64184	2355901	2592	0.21
11	65 Hz V_S	2	812.20	19492.88	81566	3497627	3240	6.02
12	65 Hz $V_S&V_P$	1	944.43	944.43	81566	3497627	3240	0.29

The unit time is in hours. The total sequential CPU time (seq. time) is 41415 hours for all frequency bands on Irene KNL HPC (TGCC) to calculate from the homogeneous initial model. The memory and storage unit is in Megabytes (MB), and the indicated frequency is the highest frequency band starting from 3 Hz. The elapsed time (elap. time) is the time needed to perform the FWI in parallel.

Chapter 4

Analysis of the use of multicomponent sources and receivers in the frame of shallow seismic Full Waveform Inversion

Contents

4.1	Introduction	89
4.2	Full Waveform Inversion	91
4.2.1	Elastic wave modeling	91
4.2.2	Inverse problem	91
4.2.3	SEM46 code	92
4.3	Sensitivity kernel investigation on multicomponent data	92
4.3.1	Sensitivity kernel	92
4.3.2	Synthetic model and experiment setup	93
4.3.3	Results	95
4.4	Application of multicomponent Full Waveform Inversion	98
4.4.1	Experiment setup	98
4.4.2	Assessment methods	103
4.4.3	Results	106
4.5	Acquisition's decimation	114
4.5.1	Source's and receiver's decimation setup	114
4.5.2	Results	114
4.6	Conclusions	121

In the previous chapter (Ch 3), we have designed a working and stable workflow of 3D elastic FWI. We have successfully reconstructed both V_P and V_S for the Ettlingen Line case study. In Chapter 3, we utilize all sources and receivers (9C seismic data) acquired on the dense grid acquisition. The result is high-resolution velocity models, in which we can see the Ettlingen Line and another new trench line-like structure. In addition, we can also see a strong horizontal velocity contrast at around 6 meters depth, which may be linked to the groundwater level, based on the previous research.

In this chapter, we answer the second main question listed in the problematics of my PhD work at the end of the General Introduction: the role and interest of multicomponent data for a near-surface target. There are three main experiments in this chapter. The first experiment analyzes the sensitivity kernel on each component (from 9C seismic) and wave packets (P, S, and surface waves) based on two simple synthetic models. Throughout this experiment, we ought to see that having different components gives a unique contribution. These results encourage us to continue with the second experiment.

In the second experiment, we perform 16 different inversions using different component combinations, starting from inversion using 1C, 3C, to 9C seismic data. Thanks to a working workflow described in Chapter 3, we can use a similar setup for all inversions in this chapter. Two different experiments are performed in this second problem, inversion based on synthetic models and inversion based on the field experiment. In this experiment, we can see the benefit of the horizontal component, amongst other results.

The third experiment is the inversion with the decimated acquisitions. In this experiment, there are nine different acquisition geometries with 16 inversions on each acquisition. With this experiment, we analyze in detail the effect of each component and multicomponent inversion. We also determine whether inversion with 1C seismic data and dense acquisition grid is better than the inversion using 9C seismic data and a coarse acquisition grid.

The content of this chapter is based on extended abstracts and paper:

- Irnaka, M., Brossier, R., and Métivier, L. (2018). 3x3C seismic's sensitivity analysis on near-surface towards Full Waveform Inversion. In *Expanded Abstracts, EAGE-HAGI 1st Asia Pacific Meeting on Near Surface Geoscience & Engineering (Yogyakarta)*.
- Irnaka, T. M., Brossier, R., Métivier, L., Bohlen, T., and Pan, Y. (2019b). Uncovering the effect of multi-component data on 9C 3D elastic FWI: Ettlingen line case study. *AGUFM*, 2019:S31D–0565.
- Irnaka, M., Brossier, R., and Métivier, L., Bohlen, T., and Pan, Y. (2020). Component analysis of 3D elastic 9C Full Waveform Inversion: Ettlingen line case study. In *SEG Technical Program Expanded Abstracts 2020*.
- Irnaka, T. M., Brossier, R., Métivier, L., Bohlen, T., and Pan, Y. (to be submitted). Analysis of the use of multicomponent sources and receivers in the frame of shallow seismic Full Waveform Inversion. *to be submitted to Geophysical Journal International*.

Abstract

Full Waveform Inversion (FWI) is one of the most popular seismic imaging techniques. In the exploration scale, FWI has become one of the industrial standards and proven to be accurate. Following that trend, FWI in shallow seismic scale has started to gain attraction in the past decade. Several publications have demonstrated and proposed workflow to tackle the challenges in shallow seismic scales, such as sparse and limited acquisition, weak signal to noise ratio, high complexity propagation due to the strong elastic effect, and strong attenuation. This article analyzes the effect of multicomponent data in a shallow seismic scale for 3D elastic FWI. The experiment's target is the Ettlingen Line (EL), a defensive trench-line built by the German Troop in 1707, located at Rheinstetten, Germany. We perform three different experiments to understand the effect of multicomponent data on FWI. The first experiment is a sensitivity kernel analysis of several wave packets (P-wave, S-wave, and surface wave) on a simple 3D model based on a Cartesian based direction of source and receiver. The second experiment is 3D elastic inversions based on synthetic (using Cartesian direction's source) and field data (using Galperin source) with various component combinations. Sixteen component combinations are analyzed for each case. In the third experiment, we perform the acquisition's decimation based on the second experiment. We demonstrate a significant benefit of multicomponent data FWI in terms of model and data misfit through those experiments. In a shallow seismic scale, the inversions with the horizontal components give a better depth reconstruction. Based on the acquisition's decimation, inversion using heavily decimated 9C seismic data still produce similar results compared to the inversion using 1C seismic on the full acquisition.

4.1 Introduction

Full Waveform Inversion (FWI) is a high-resolution seismic imaging technique which has been designed in the 1980s (Lailly, 1984; Tarantola, 1984a). The potential resolution of the FWI is up to half of the propagated wavelength (Wu and Toksöz, 1987). In the past years, thanks to the development of wide-angle and broadband frequency seismic acquisition devices, together with the High Performance Computing (HPC) platform development, FWI has been successfully applied at various scales, starting from laboratory scale (Bretaudeau et al., 2013b), engineering and environmental scale (Smithyman et al., 2009; Fathi et al., 2016; Nguyen and Tran, 2018; Smith et al., 2019), crustal-scale (Sirgue et al., 2010; Bleibinhaus and Hilberg, 2012; Etienne et al., 2012; Prioux et al., 2013b; Vigh et al., 2014; Górszczyk et al., 2017; He et al., 2019b; Trinh et al., 2019a), lithospheric scale (Tape et al., 2010; Beller et al., 2018; Lu et al., 2018), as well as global scale (Fichtner et al., 2008; French and Romanowicz, 2014; Modrak and Tromp, 2016).

Although FWI is successfully applied to a variety of targets and field data, it remains an ill-posed inverse problem. In practice, the uncertainty attached to the reconstructed model is significant. Besides the methodological development aiming at mitigating the ill-posedness of FWI (modification of misfit function or introducing the extension strategies), access to more complete data that can constrain FWI is also essential.

In this frame, multicomponent receiver, recording both P-waves with hydrophones and displacement with multi-directional geophones have started to be used in different applications (Choi et al., 2008; Robertsson et al., 2008; Sears et al., 2010; Prioux et al., 2013b; Vigh et al., 2014). At exploration scales and in marine environment, this multicomponent receivers are deployed on the sea-bottom (Ocean Bottom Cable). The additional displacement recording might open the way to reconstruct both

P-wave and S-wave velocities using viscoelastic modeling. In this case, the S-wave signal is indeed visible on the geophones while remaining absent on hydrophone data.

At shallow-seismic scale, multicomponent receivers have been shown to improve the reconstructed model. Nuber et al. (2017) proposes a way to efficiently design the acquisition through the solution of an optimal design problem for a 2D synthetic case. The optimized experimental design aims at predicting the most optimum source location for the seismic acquisition. They demonstrate that multicomponent data can increase the efficiency of the acquisition with a fewer number of sources. Smith et al. (2019) also perform both synthetic and field experiment with an underground tunnel as the target. Their synthetic test demonstrates that using multicomponent sources and multicomponent receivers can improve the image, especially at depth. In their field experiment, they use vertical sources while using two types of geophones. The first is vertical geophone, and the second is horizontal geophones, which were set longitudinally to the direction of the target. Thanks to the second horizontal geophones, they were able to reconstruct the underground tunnel better.

At shallow seismic scale, multicomponent sources have also been introduced. Classically, we only use vertical sources. This type of source can be easily produced by hitting a horizontal metal plate with a sledgehammer. Horizontal sources are not used in conventional acquisition. When it is performed, normally, the horizontal source requires a vertical metal plate hit by a horizontal force. Performing vertical to horizontal sources requires the metal plate's movement from the horizontal direction to the vertical direction and vice versa. This installation process might reduce the source's consistency and efficiency in terms of the source-ground coupling, location, and direction. Therefore, Schmelzbach et al. (2016) proposes a prismatic source. A prismatic source can produce two sources' directions in a single installation procedure and later can be rotated in the preprocessing step to produce the true vertical and horizontal component. The prismatic source has been later improved by adding the third direction. The new type of source is called the Galperin source (Häusler et al., 2018). The Galperin source contains three orthogonal source directions in a single installation. It can increase the data consistency, as well as the acquisition's efficiency.

This article is interested in analyzing the multicomponent source and receiver for a specific shallow-seismic target. Prior to the FWI application, we perform a preliminary investigation on the sensitivity kernel. On the FWI application, we use the Galperin sources and 3C (three-component) geophones, whereas, for the synthetic case, we use 3C sources that align with the Cartesian coordinate and 3C receivers. We focus on a specific data with an ancient war-trench as the main object to be reconstructed. The assessment method is performed qualitatively by examining the reconstructed model and quantitatively by calculating both data misfit and model misfit.

We give a brief introduction to the basic theory of wave propagation, the inverse problem, and the computer tools we use for this experiment. Afterward, we present three different experiments. The first experiment is the sensitivity kernel study to understand each wave type's effect in multicomponent data. The second is the synthetic and the field experiment of multicomponent FWI. A detailed comparison between different FWI with the different component combinations is performed. The third experiment uses the field data to assess the effect of source and receiver decimation on a single component, 3C, and 9C FWI.

4.2 Full Waveform Inversion

4.2.1 Elastic wave modeling

In shallow seismic scale, where the elastic effect is dominant, we use elastic wave propagation to model the wavefield. The elastic wave propagation can be described by the equation of motion and Hooke's law as

$$\begin{aligned}\rho\partial_{tt}u_i &= \partial_j\sigma_{ij} + f_i, \\ \sigma_{ij} &= c_{ijkl}\varepsilon_{kl} + \mathcal{T}_{ij},\end{aligned}\quad (4.1)$$

where $\rho = \rho(\mathbf{x})$ denotes the density, $\mathbf{u} = u(\mathbf{x}, t)$ is the displacement, $\sigma = \sigma(\mathbf{x}, t)$ and $\varepsilon = \varepsilon(\mathbf{x}, t)$ are second-order stress and strain tensor respectively. The external force is denoted by \mathbf{f} , and a possible stress failure as \mathcal{T} . The stiffness tensor is denoted by c_{ijkl} . We follow Einstein convention (summation over repeated indices) for these equations.

Using Voigt indexing and matrix notation, Equation 4.1 can be rewritten as

$$\rho\partial_{tt}\mathbf{u} - DCD^T\mathbf{u} = S, \quad (4.2)$$

where S is the external source, D is the spatial derivative operator

$$D = \begin{pmatrix} \partial_1 & 0 & 0 & 0 & \partial_3 & \partial_2 \\ 0 & \partial_2 & 0 & \partial_3 & 0 & \partial_1 \\ 0 & 0 & \partial_3 & \partial_2 & \partial_1 & 0 \end{pmatrix}, \quad (4.3)$$

and C is the stiffness tensor. In this study, we assume an isotropic medium, and C can be written as (Eq. 4.4) where λ and μ are the two Lamé parameters.

$$C = \begin{bmatrix} \lambda + 2\mu & \lambda & \lambda & 0 & 0 & 0 \\ \lambda & \lambda + 2\mu & \lambda & 0 & 0 & 0 \\ \lambda & \lambda & \lambda + 2\mu & 0 & 0 & 0 \\ 0 & 0 & 0 & \mu & 0 & 0 \\ 0 & 0 & 0 & 0 & \mu & 0 \\ 0 & 0 & 0 & 0 & 0 & \mu \end{bmatrix}. \quad (4.4)$$

4.2.2 Inverse problem

FWI is a local optimization technique which aims at minimizing an objective function $\chi(m)$ as

$$\begin{aligned}\chi(m) &= \frac{1}{2}\|d_{obs} - d_{cal}(m)\|^2, \\ d_{cal}(m) &= Ru(m), \\ A(m)u &= S,\end{aligned}\quad (4.5)$$

where $m = [\lambda \ \mu]$ is the model parameter, d_{obs} is the observed data, and d_{cal} is the calculated data, R is the extraction function of the wavefield u (as the particle velocity) at the receiver position, $A(m) = \rho\partial_{tt}\mathbf{u} - DCD^T\mathbf{u}$ is the forward modeling operator, and S is the source term. The optimal solution can be estimated using Newton-based method. An initial model (m_0) is updated within the iterative scheme

$$\begin{aligned}m_{k+1} &= m_k + \alpha_k\Delta m_k, \\ \Delta m_k &= -Q_k\nabla\chi(m_k),\end{aligned}\quad (4.6)$$

where k is the iteration number, and α_k is the step length obtained using a line search strategy at iteration k (Nocedal and Wright, 2006). In our study, Δm_k is the parameter update calculated as the product between the inverse Hessian (Q_k) estimated using l -BFGS (Byrd et al., 1995) and the gradient of the misfit function with respect to the parameters ($\nabla\chi(m_k)$).

The gradient ($\nabla\chi(m_k)$) is computed using the adjoint-state method (Plessix, 2006). In practice, $\nabla\chi(m_k)$ is the result of zero-lag cross-correlation between the adjoint displacement field ($l(m)$) and the incident displacement field ($\frac{\partial A}{\partial m}u(m)$)

$$\nabla\chi(m) = \frac{\partial\chi(m)}{\partial m} = \left\langle l(m), \frac{\partial A}{\partial m}u(m) \right\rangle. \quad (4.7)$$

We perform a multi-parameter FWI aiming at reconstructing both V_P and V_S , while keeping the density ρ fixed. Using the chain-rule, the gradient of any parameter p can be related to the gradient of the stiffness coefficient C_{ij}

$$\frac{\partial\chi(m)}{\partial p} = \sum_{i=1}^6 \sum_{j=1}^6 \frac{\partial\chi}{\partial C_{ij}} \frac{\partial C_{ij}}{\partial p} + \frac{\partial\chi}{\partial \rho} \frac{\partial \rho}{\partial p}, \quad (4.8)$$

where p can be replaced with V_P and V_S .

4.2.3 SEM46 code

The elastic modeling and inversion calculation is implemented in the SEM46 software (Trinh et al., 2019b). SEM46 is a full waveform modeling and inversion code based implementing (visco-)elastic wave propagation using a spectral element discretization. The code is linked to the SEISCOPE optimization toolbox for the solution of the local optimization problem (Métivier and Brossier, 2016). Spectral element method has the advantage of having an accurate representation of the free surface boundary due to the weak formulation of the wave equation. This accurate free surface modeling is essential for surface wave modeling in shallow seismic case.

SEM46 has several specificities. The first is the ease of the mesh design. The mesh can be designed quickly by automatically creating the mesh of the computational domain on a Cartesian based mesh. The second is an efficient and scalable two-levels MPI parallelism. The first level is on seismic sources, while the second level is on domain decomposition.

4.3 Sensitivity kernel investigation on multicomponent data

4.3.1 Sensitivity kernel

Conceptually, the sensitivity kernel is the gradient of the FWI misfit function using a single mono-component source/ receiver pair (Tromp et al., 2005). It illustrates the sensitivity of each model parameter with respect to the data of the source-receiver pair. In order to assess the sensitivity to specific part of the propagated wave, a window can be used on specific arrivals/phases to isolate them. In this experiment, we want to illustrate using schematic example, the sensitivity kernel of model parameters (V_P and V_S) to the different component of the data. It can be achieved by isolating several wave-packets on each component, from the P-wave window (t_P), the S-wave window (t_S), and the surface wave window (t_{RL}).

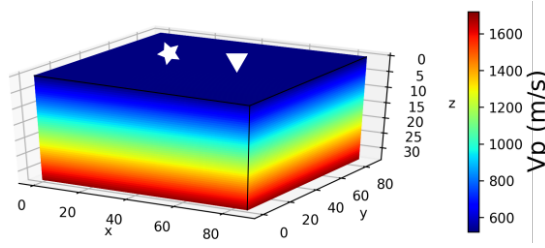


Figure 4.1: The synthetic 1D gradient model. The star symbol represents the source's location, whereas the inverted triangle represents the receiver's location. The dimension of the model is in meter.

4.3.2 Synthetic model and experiment setup

We take into account two synthetic models: 1D and 2D gradient model. Both models aim at better understanding the effect of their sensitivity kernels and their potential benefit on FWI.

4.3.2.1 Common experiment setup

The sensitivity kernel is calculated using the SEM46 code. Both models have a free surface boundary condition at the top of the model and absorbing boundary conditions on the other sides. We consider a single source-receiver pair with 25 m offset as the representation of a typical shallow seismic distance (Fig. 4.1). The source is a derivative of Ricker wavelet with a 100 Hz central frequency. Both synthetic sources and receivers have three components, resulting in 9C seismic data. In the following discussion, the source-receiver pair's component is denoted using two capital letters. The first and second capital letter are the source's direction and the receiver's direction, respectively.

4.3.2.2 1D gradient model

The 1D gradient model is referred to as Model I in the following. It is presented in Figure 4.1. It follows the affine model

$$V_P(z) = 36z + 520, \quad (4.9)$$

relating the depth (z) and V_P . The Poisson's ratio is kept constant at 0.25, whereas the density (ρ) is fixed to 1000 kgm^{-3} . This 1D gradient model is designed to have well-separated wave packets (P, S, and surface wave). The velocity model dimension is $30 \times 86 \times 86$ m in Z, X, and Y direction, respectively. Figure 4.1 shows the 3D velocity model. The star represents the source's location, whereas the inverted triangle is the receiver's location. Both source and receiver are located at the surface.

Figure 4.2 presents the seismic section, which is calculated using Model I on the ZZ component. The direction of the seismic section is aligned with the source-receiver pair for sensitivity kernel computation. The synthetic seismogram on the selected source-receiver pair is shown as a wiggle plot with an exaggerated amplitude. Using this model, we can see a clear separation between the P-wave window (blue line), S-wave window (green line), and the surface wave window (red line).

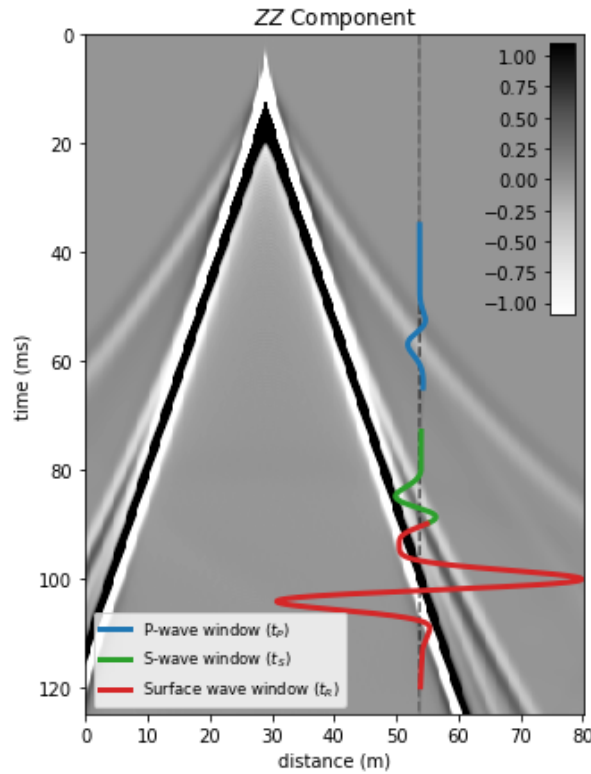


Figure 4.2: ZZ component of a synthetic data set on the Model I. The source-receiver pair with an offset of 25 m (represented by the grey dashed line) is used for the sensitivity kernel calculation. Each event window is denoted using a different color (blue for P wave, green for S wave, and red for the surface wave).

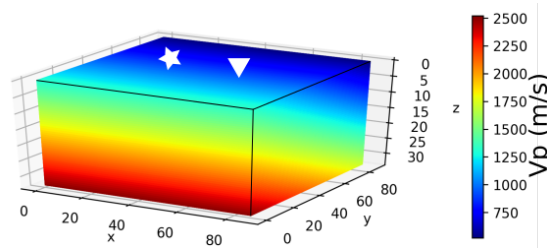


Figure 4.3: The synthetic 2D gradient model. The star symbol represents the source’s location, whereas the inverted triangle represents the receiver’s location. The dimension of the model is in meter.

4.3.2.3 2D gradient model

The 2D gradient model is referred to as Model II. It is presented in Figure 4.3. It is an extension of the 1D affine model. With the same physical dimension, the 2D gradient model is calculated following

$$V_P(y, z) = 36z - 18.5y + 1320. \quad (4.10)$$

Both Poisson’s ratio and the density are identical compared to Model I.

The result of the forward modeling using Model II can be seen in Figure 4.4. In this figure, the S-wave and the surface wave can not be separated anymore. This is the result of 2D variation of Model

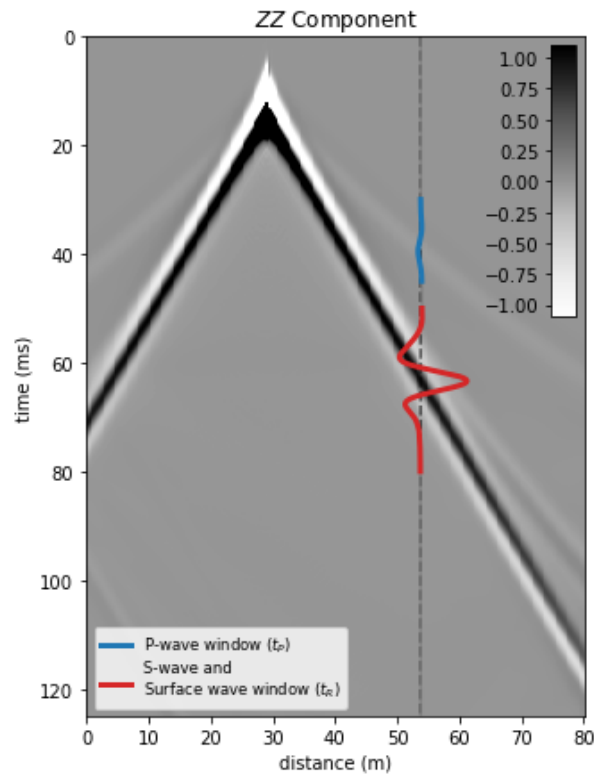


Figure 4.4: ZZ component of a synthetic data set on the Model II. The source-receiver pair with an offset of 25 m (represented by the grey dashed line) is used for the sensitivity kernel calculation. The P wave window is denoted by the blue line, whereas the S wave and surface wave are inseparable and denoted using the red line.

II, compared to the Model I. Therefore, we only have two windows, P-wave window (blue line) and the S-wave plus surface wave window (red line).

4.3.3 Results

We perform three sensitivity kernel analysis on Model I based on its event windows. The first result is shown in Figure 4.5. It contains the vertical section of the sensitivity kernels for the P-wave window. It displays sensitivity kernels for both V_P and V_S gradient for all 9C data. The P-wave window's sensitivity kernel display sensitivity with respect to both V_P and V_S parameters. It exhibits the potential to reconstruct V_S with the P-wave window. In this plot, we also observe the different characteristics of each component. ZZ component has a deeper penetration depth. On the other hand, the XX component has a stronger response close to the surface and less penetration depth. Looking at Figure 4.5, we see that 1C data (for example, only with ZZ component) only receive a fraction of information compared to the 9C dataset.

The second sensitivity kernel is calculated based on the S-wave window on Model I. Its vertical section can be seen in Figure 4.6. In this figure, we have a significant additional response on the YY component for the V_S gradient, alongside with the previous four components (ZZ, XZ, ZX, and XX). The sensitivity kernel on these four components can be related to the S_V wave propagation, whereas

ANALYSIS OF THE USE OF MULTICOMPONENT SOURCES AND RECEIVERS IN THE FRAME OF SHALLOW SEISMIC FULL WAVEFORM INVERSION

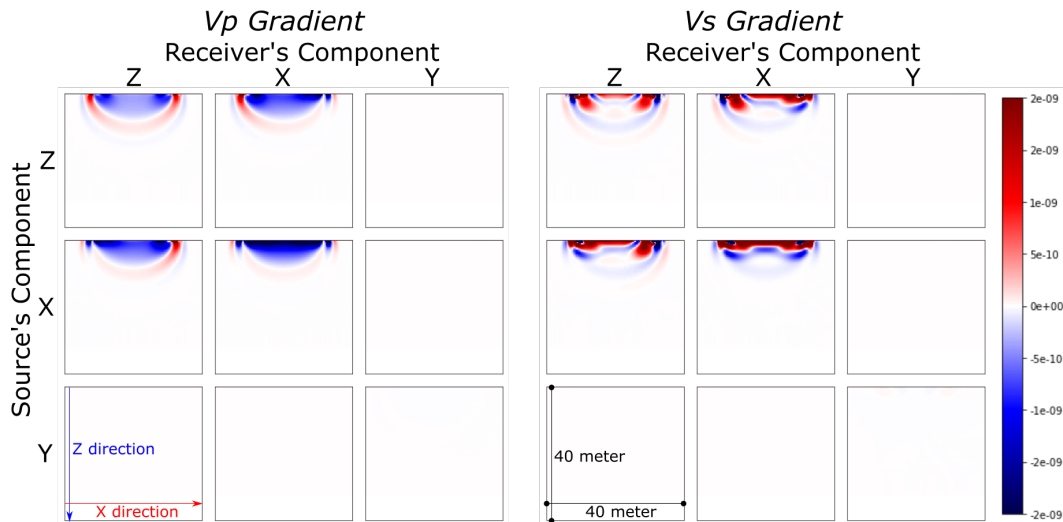


Figure 4.5: Vertical sections of the sensitivity kernel computed with Model I for P-wave window. The columns represent the receiver's components, the rows represent the source's components.

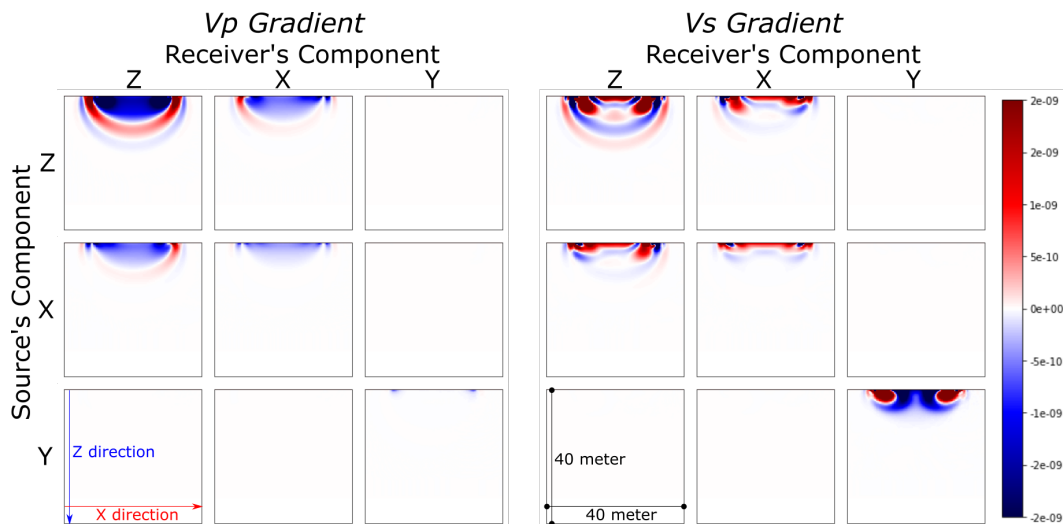


Figure 4.6: Vertical sections of the sensitivity kernel computed with Model I for S-wave window.

the sensitivity kernel on YY component is related to the S_H wave propagation. Note that the S_H wave has almost no sensitivity in V_P gradient, implying a weak dependency of S_H wave with the value of V_P .

Finally, the sensitivity kernels on the surface wave window (Fig. 4.7) exhibit a different shape. The main five components which are responsive for the V_S gradient are the same as for the previous time windows focused on P-wave and S-wave (ZZ, XZ, ZX, XX, and YY). The surface waves also do not contain any information on V_P , even close to the surface. Besides, in this 1D example, the sensitivity kernel of the Rayleigh wave and the Love wave are well-separated. The sensitivity kernel of the Rayleigh wave are shown in four components (ZZ, XZ, ZX, and XX), whereas the sensitivity kernel of the Love wave is shown in YY component. In general, the amplitude of the sensitivity kernel is mainly concentrated close to the surface, but the Love wave's sensitivity kernel has stronger sensitivity

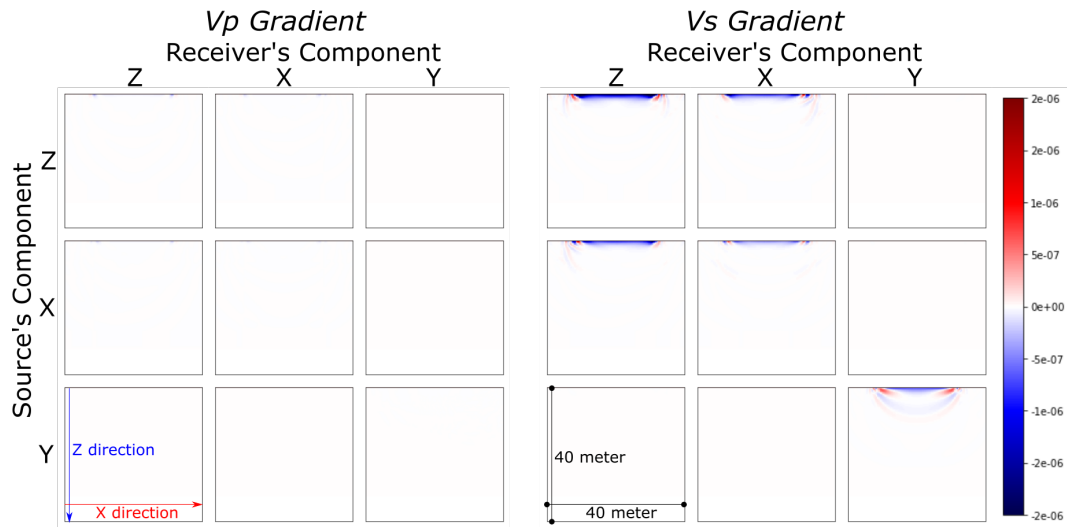


Figure 4.7: Vertical sections of the sensitivity kernel computed with Model I for surface wave window.

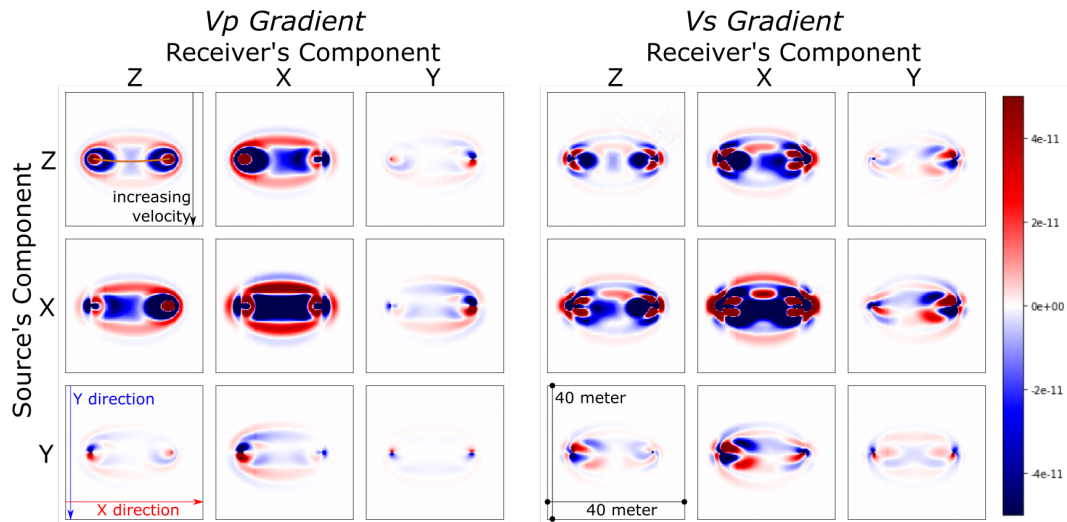


Figure 4.8: Horizontal sections of the sensitivity kernel computed with Model II for P-wave window.

at depth.

In this experiment, the amplitude range of the sensitivity kernels from the surface wave window is three order magnitude higher than the body wave window. Therefore a proper FWI strategy is required in order to exploit the information from the body wave. In the crustal scale, mitigation of the surface wave is very challenging. Different strategies have been proposed, such as treating the surface wave as the noise (the surface waves are removed from the dataset) (Bharti et al., 2016), interpret the surface wave using dispersion (Tawil et al., 2019), or using an accurate modeling to represent the surface wave (Wittkamp et al., 2018; He et al., 2019a; Trinh et al., 2019a). In our shallow seismic scale, the penetration depth of the surface waves correspond to the depth of the target. Therefore, we follow an FWI strategy which can take advantage of both surface waves and the body waves.

Figure 4.8 displays the horizontal section at the surface of the P-wave's sensitivity kernel window using Model II. The direction of the increasing velocity is annotated in the ZZ component of the V_P

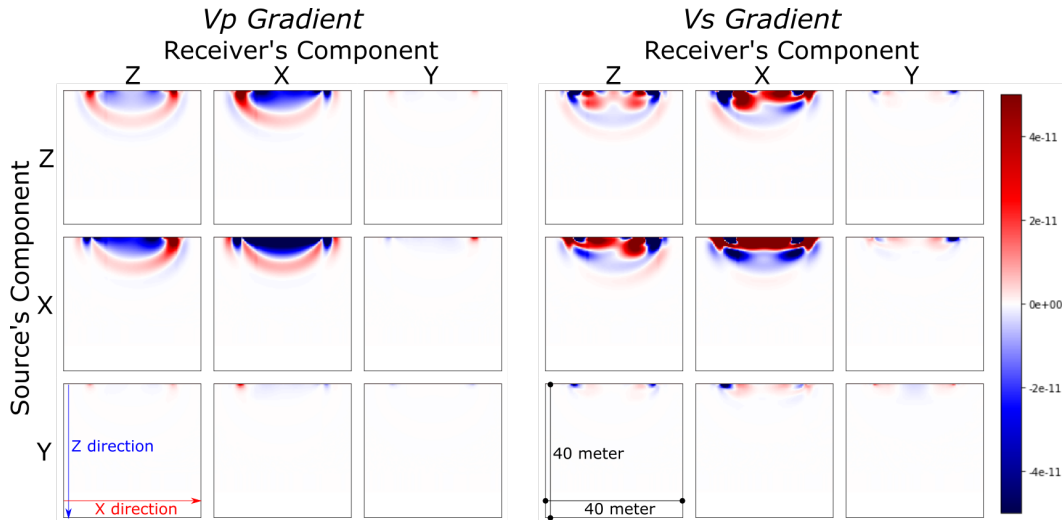


Figure 4.9: Vertical sections of the sensitivity kernel computed with Model II for P-wave window.

gradient. The ray-path between the source and receiver is also annotated on the same component.

Compared to the previous experiment, we have non-zero sensitivity kernel for all components. It is due to the fact that the direction of the polarization of the propagated wave is no longer as simple as the Model I. The same effect also apparent on the vertical section 4.9. The second time windows of the Model II, which contains both S-wave and the surface wave, also give similar result. It has non-zero sensitivity kernel for all components.

Throughout these experiments, we observe complementary information between components. We see that each component brings different information of the sensitivity kernel. The surface waves dominate the sensitivity kernel by three order of magnitude compared to the body wave's sensitivity kernel. From this simple analysis, we might expect that 9C seismic data should help in better constraining the FWI problem and makes possible to better reconstruct the subsurface mechanical properties.

4.4 Application of multicomponent Full Waveform Inversion

Sensitivity kernel is a bridge to comprehend the benefit of having multicomponent data in FWI. This section continues our experiment by performing 3D elastic FWI on two datasets: a synthetic and a field experiment.

4.4.1 Experiment setup

4.4.1.1 Target

Our experiment is based on the 3D 9C shallow seismic experiment at the Ettlingen Line's segment in Rheinstetten, Germany. The Ettlingen Line is a historical war trench built in 1707 during the War of the Spanish succession (Lang et al., 1907). The trench is located at the topsoil layer, which is the fluvial sediment from the Rhein river west of the acquisition zone. Several previous studies have been done focusing on the geometry reconstruction of the target (Wegscheider, 2017; Wittkamp et al., 2018; Pan



Figure 4.10: Basemap of the seismic data acquisition at Rheinstetten, Germany. The solid red line represents the existing trench line. The dashed red line represents the buried trench. A white box draws the area of the seismic acquisition.

et al., 2018; Irnaka et al., 2021). Figure 4.10 shows the base map of the buried trench. The solid red line represents the existing trench, whereas the dashed red line represents the buried trench. The white box depicts the seismic acquisition zone.

Figure 4.11 illustrates the acquisition geometry of the experiment. The acquisition spans 32 m inline and 28 m crossline, with 888 receivers and 36 source locations. The 3C geophones are located at the surface with 1 m spacing for both inline and crossline directions. In comparison, the 3C sources are deployed following a staggered pattern resulting in an effective minimum spacing around 5.66 m.

4.4.1.2 FWI Workflow

Choosing the correct modeling approximation for our particular case is crucial. The shallow seismic scale has a strong elastic effect and attenuation. The strong elastic effect is mainly due to the surface wave's presence, whereas the strong attenuation is due to the unconsolidated soil at shallow depth. In this case, viscoelastic modeling is the obvious choice. Additionally, with a sufficiently low frequency, the attenuation effect might be disregarded. Irnaka et al. (2021) has demonstrated that up to 45 Hz, the result between FWI using an elastic and viscoelastic medium is similar in this dataset (Fig. 4.12). In addition, using elastic approximation can significantly decrease the required computational cost.

The formulation in the Equation 4.5 to 4.8 are the fundamental of FWI. In practice, we need to design a specific multiparameter strategy because we want to reconstruct V_P and V_S . Our data is a surface wave dominated data and the body wave are mixed with the surface waves for a relatively short offset

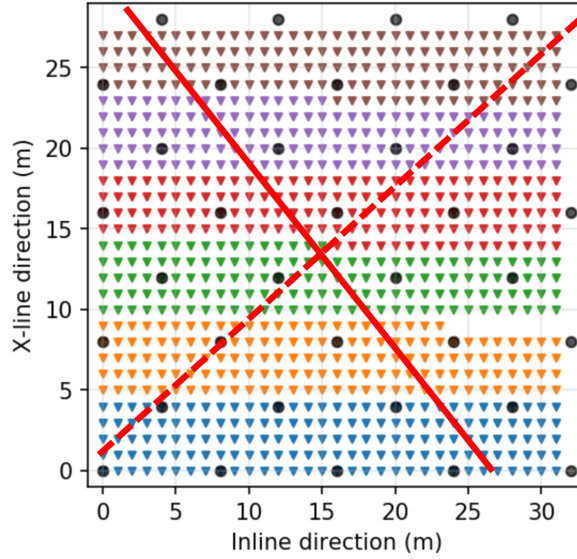


Figure 4.11: Layout of the acquisition grid for both synthetic and field experiments. The total number of receiver is 888 (triangles), the total number of source's location is 36 (circles). Solid and dashed red lines represent the parallel and perpendicular sections used in the following figures, respectively. The color of the receivers represents the acquisition subset, only for the field experiment.

seismic data we consider. Therefore, to exploit at best the data, and being able to reconstruct both V_P and V_S while having a simple enough initial model, we follow the FWI workflow for the shallow seismic scale proposed by Irnaka et al. (2021). It is a multi-scale approach with two successive inversions in each scale. The first is V_S only inversion with an imposed linear relation of V_P (parameter binding). The second is a multi-parameter V_P and V_S inversion with non-linear model constraints imposed on the ratio between V_P and V_S to ensure the solution remains in a space of physically meaningful models. We use Bessel gradient smoothing in our application. Bessel gradient smoothing is an anisotropic smoothing along interfaces injected as prior information (Trinh et al., 2017). In our application, we use coherent lengths of 0.1λ , 0.7λ , and 0.7λ with respect to the local velocity and dominant frequency in vertical, inline, and crossline direction, respectively. We also apply a standard depth preconditioner for each parameter's gradient.

Following the workflow given in Figure 4.13, we have been able to perform the inversion and reconstruct both V_P and V_S up to 65 Hz, starting from a homogeneous initial model (Irnaka et al., 2021). In this previous study, we have shown the 9C FWI has been able to reconstruct the buried Ettligen Line and also discover a trench-like anomaly that was not detected before (Fig. 4.12).

4.4.1.3 Initial model design

To build the initial V_P model, we pick the first P-wave arrival at the longest offset on the inline seismic section in the field data. A homogeneous V_P model with the value of 345 m.s^{-1} can be directly calculated. The other elastic parameters (V_S and ρ) are estimated using a fixed Poisson's ration of 0.25 and Gardner's relationship. The initial V_S value is 199 m.s^{-1} , whereas the initial ρ value is 1336 kg.m^{-3} . These models are used for both synthetic and field experiments.

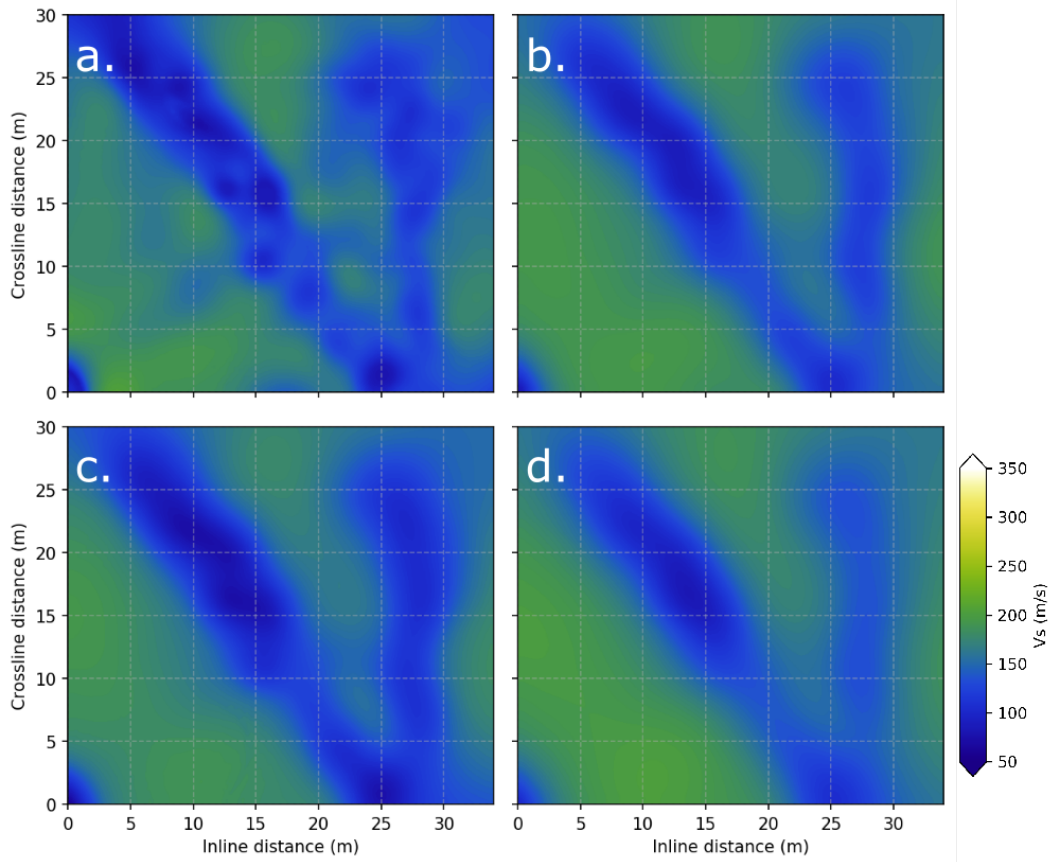


Figure 4.12: Example of FWI result between the elastic and viscoelastic medium. Horizontal slice of V_S from the FWI at 1 m depth for FWI with elastic medium (a and c) and viscoelastic medium (b and d). Top row images are the reconstructed V_S at 65 Hz (a and b), whereas 45 Hz for the bottom row images (c and d).

4.4.1.4 Source estimation

The source time function is estimated by assuming a known source and receiver direction. We also assume the sources to have a relatively consistent shape and a similar level of energy. In order to obtain the source time function, we follow three different steps: raw source estimation using the deconvolution formula following Pratt (1999), amplitude normalization to equalize the amplitude contribution of each source, and spatial weighting average to reduce the local effect and over-estimation of the source. Finally, we produce a single source time function for each location and direction of the source.

4.4.1.5 FWI settings

We perform inversions with the starting frequency band of 3 - 15 Hz. We increase the frequency band by 10 Hz increments for each frequency band. The highest frequency band in this experiment is 3 - 45 Hz.

We specify an initial ratio between V_P and V_S with a fixed value of 1.732 (which corresponds to a constant Poisson's ratio of 0.25). The ratio between V_P and V_S value is updated each time the

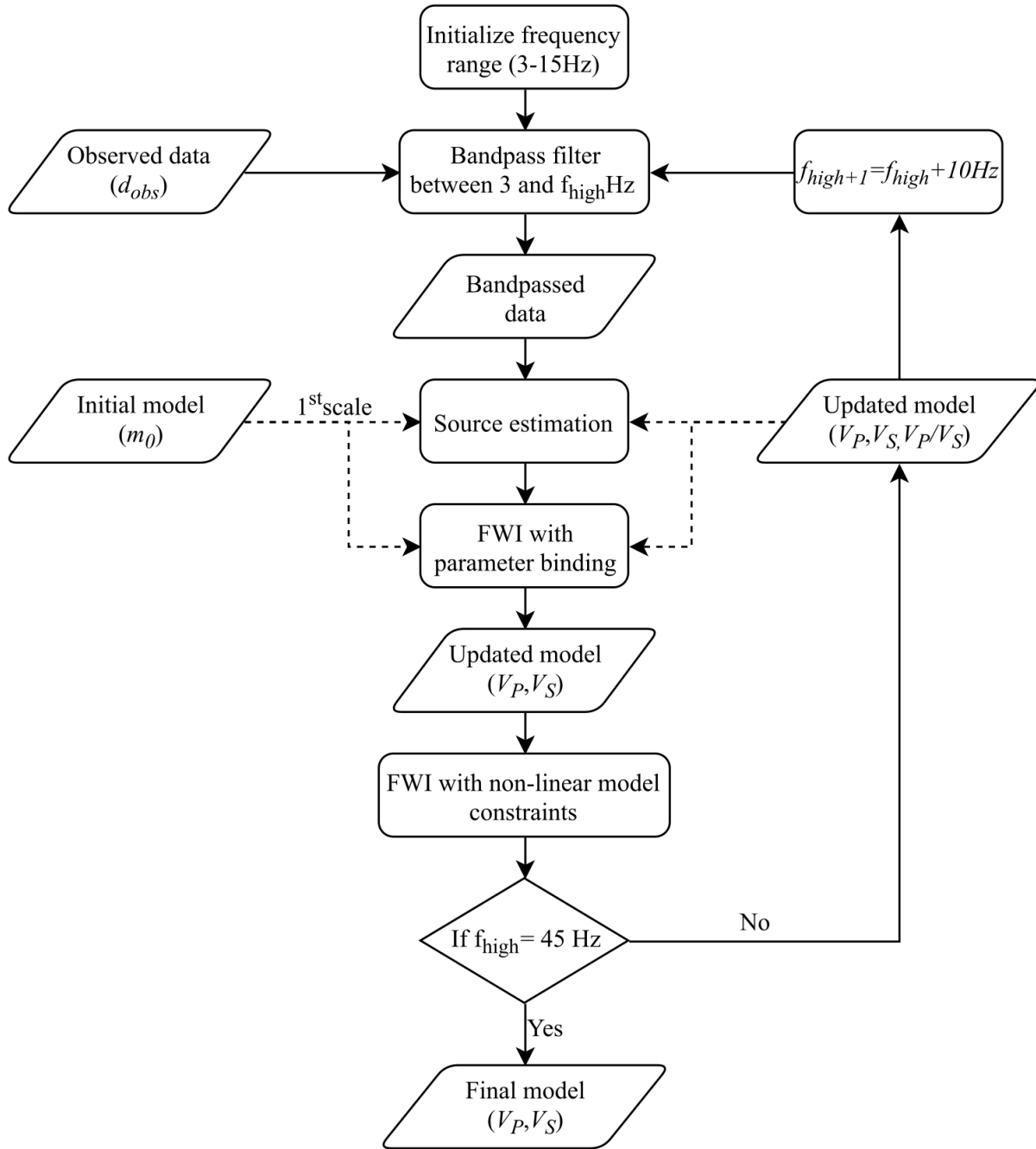


Figure 4.13: FWI workflow for shallow seismic application.

non-linear model constraints multi-parameter inversion is carried out (Fig. 4.13). The lower and upper boundary values we use are 100 m.s^{-1} and 2000 m.s^{-1} respectively for V_P , 50 m.s^{-1} and 800 m.s^{-1} respectively for V_S . The lower and upper boundary for V_P/V_S are 1.633 and 10, respectively. A short offset data muting, up to 1.5 m offset, is applied to remove unreliable data. For the field experiment, additional top window muting is applied to remove strong noise on some part of the data.

In terms of numerical optimization parameters, we set the maximum line search to 20, and the

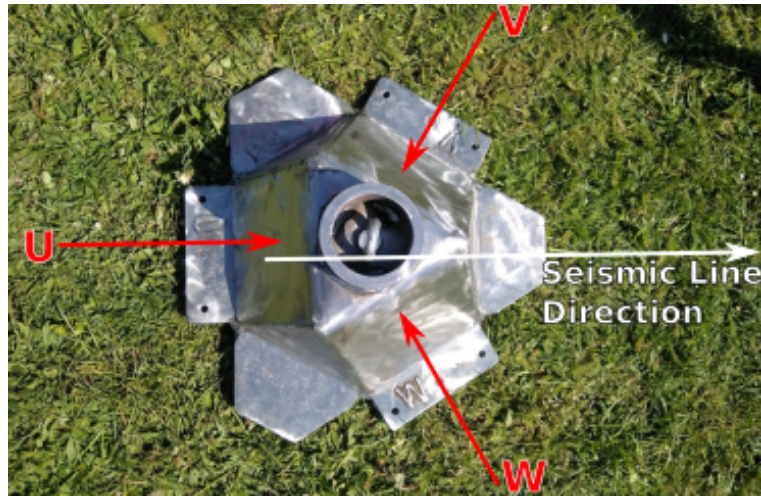


Figure 4.14: The Galperin source used in 9C seismic acquisition.

number of the stored gradient for l -BFGS to 10. The Bessel filter based gradient smoothing uses coherent lengths of 0.1λ , 0.7λ , and 0.7λ with respect to the local velocity and dominant frequency in vertical, inline, and crossline direction, respectively. A depth preconditioner is applied to the gradient with the power of 2 with respect to depth.

4.4.1.6 Synthetic experiment

The synthetic experiment is done based on a realistic 3D shallow seismic model. The true model is obtained from the previous 3D FWI application by Irnaka et al. (2021). The model has a dimension of $15 \times 34 \times 30$ in Z, X, and Y, respectively.

Similar to the sensitivity kernel study, we use 3C sources and receivers, which are aligned with the Cartesian axis. This model aims to mimic the field experiment with a classical type of source and receiver. The synthetic source time function is a Ricker wavelet with a 40 Hz central frequency.

4.4.1.7 Field experiment

The field experiment uses the Galperin source as the seismic source (Fig. 4.14), a multicomponent (3C) directional source designed for shallow seismic acquisition (Häusler et al., 2018). The receivers are 4.5 Hz 3C geophones installed at the surface. Due to a limited number of the equipment, the acquisition is performed in parts (as indicated by different receiver's colors in Fig. 4.11). Therefore, before performing the inversion, a data correction based on matching filters is carried out. The data acquisition and correction is written in detail by Irnaka et al. (2021).

4.4.2 Assessment methods

This section focuses on comparing the inversion result from the various component combinations, source, and receiver numbers. Therefore, we need some quantitative means to measure the quality of the inversion. We use the data misfit and the model misfit as the quantitative ways to measure the inversion quality. The detail of each method is explained in the following section.

4.4.2.1 Data misfit

The data misfit is calculated by measuring the difference between the synthetic and the observed data. In order to have a fair comparison between one case and another, we calculate a 9C synthetic seismic data based on each obtained model. For every case, we use an identical source time function, retrieved using a deconvolution formula (Pratt, 1999) based on the velocity model on 9C FWI on the full acquisition setup. The absolute misfit value (\mathcal{C}_d) can be calculated using a L_2 -norm for each component as

$$\mathcal{C}_d(d_{cal}) = \frac{1}{2} \|d_{obs} - d_{cal}\|^2, \quad (4.11)$$

where d_{obs} is the observed data, and d_{cal} is the calculated data. The result is nine different absolute misfit values for each inversion case (one per component).

The absolute misfit value is one way to represent the level of difference between the synthetic and the observed data. However, directly comparing the absolute misfit value can be misleading due to different content on each component. This bias makes it difficult to determine the performance of each inversion based on a specific component. Therefore, we propose an alternative way to display the data misfit. Instead of displaying the absolute misfit value directly, we present the grade of each component. Each component's grade is calculated by comparing the same component's absolute misfit value on all cases and sort it from the highest to the lowest misfit value. A higher grade means lower misfit value (better performance) only for the respective component.

4.4.2.2 Model misfit

The model misfit (\mathcal{C}_m) aims to quantify the distance between the reconstructed model and the reference model. It is formulated as a normalized L_2 -norm

$$\mathcal{C}_m(m) = \sum_{z=1}^{N_z} \sum_{x=1}^{N_x} \sum_{y=1}^{N_y} \frac{1}{2} \left\| \frac{w_{z,x,y}(m_{z,x,y}^* - m_{z,x,y})}{m_{z,x,y}^* N_z N_x N_y} \right\|^2, \quad (4.12)$$

where $m_{z,x,y}^*$ is the reference model, $m_{z,x,y}$ is the model obtained on each inversion, $w_{z,x,y}$ is the weight, N_z, N_x, N_y are the number of points in Z, X, Y directions. The normalization is essential to estimate a relative misfit value for different parameter's range.

The reference model is straightforward for the synthetic case. We can directly use the true model. Because we expect no spatial uncertainty in the reference model, we set the weight as a constant value 1.

For the field data experiment, the reference model is chosen as the mean of two models obtained using 3D 9C FWI up to 65 Hz starting from two different initial models (Irnaka et al., 2021). Figure 4.15 shows V_S model sections on horizontal and vertical sections, which was reconstructed using FWI starting from two different initial models (homogeneous model $V_{S_{homo}}$ and MASW model $V_{S_{MASW}}$ and using the full acquisition and components.

Figure 4.16 shows the mean difference μ_{V_S} and the standard deviation σ_{V_S} between the two reference V_S models as a function of depth. The standard deviation in this figure represents the variability of the reconstructed V_S between two models at each depth section. Close to the surface, due to the insensitivity of the surface wave in the inversion, it has higher standard deviation than at 1.5 m depth. Close to the surface, the value of V_S is more influenced by the initial model rather than the inversion itself.

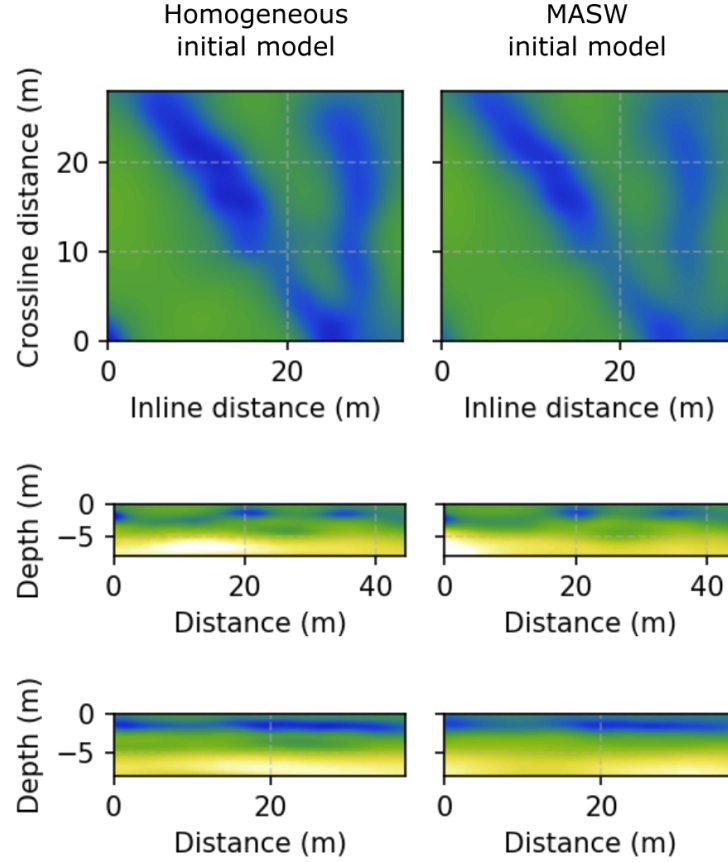


Figure 4.15: V_s model obtained using FWI starting from homogeneous initial model (left) and MASW initial model (right). The first row is the horizontal section at 1.5 m depth, the second row and the third row are the vertical section perpendicular and parallel with the Ettligen Line, respectively.

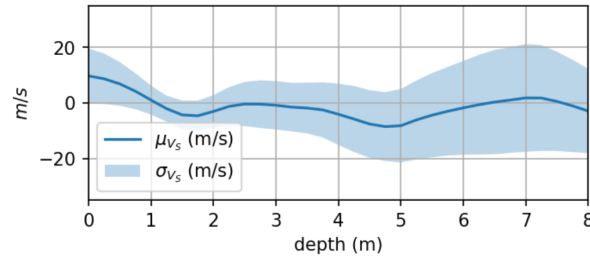


Figure 4.16: The average difference (blue line) and its standard deviation (light blue area) between two reference models in the field experiment.

This observation is similar to the high standard deviation at the deeper part of the model. Therefore, we decide to use the inverse of the standard deviation of the velocity models as the weight w

$$\frac{1}{w(z)} = \sqrt{\frac{1}{N_x N_y - 1} \sum_{x=1}^{N_x} \sum_{y=1}^{N_y} (\Delta_{V_S}(z, x, y) - \mu_{V_S}(z))^2}, \quad (4.13)$$

where Δ_{V_S} is the difference between two benchmark models ($V_{S_{hom}}(z, x, y) - V_{S_{MASW}}(z, x, y)$),

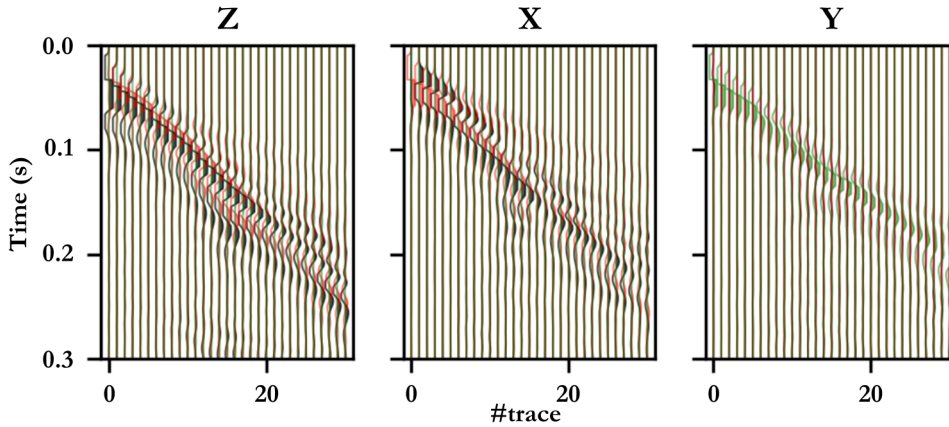


Figure 4.17: Synthetic data calculated using true velocity model on synthetic experiment. The source is located at position $x = 0$ m, and $y = 16$ m, and the receiver is located on inline direction at $y = 16$ m. Three subfigures represent different receiver's component, whereas the color on each figure represents source's component. Grey, red, and green seismograms are calculated using Z, X, and Y direction source, respectively.

$\mu_{V_S}(z)$ is the average between two models at each depth point.

4.4.3 Results

In this experiment, there are three types of inversion with different component combinations. FWI using single component, three components, and nine components. For single component inversion, we denote it in two ways. If we do not want to specify which component that is used, it is written as **1C FWI**. If we want to specify which component that is used, it is written as **two capital letters plus FWI suffix**. The first capital letter specifies the source component, whereas the second capital letter specifies the receiver component. For example, **UZ FWI** means the inversion which is carried out using single component data which is excited at U source direction and recorded by Z receiver component. For three component inversion, we also denote it in two ways. Suppose we do not want to specify which components that are used; it is written as **3C FWI**. However, if we want to specify which components that are used, it is written as **capital letter with subscript plus FWI suffix**. For example, **Z_{REC} FWI** means 3C FWI using the data which is excited using 3C sources and only recorded using Z component receivers. On the other hand, **W_{SRC} FWI** means 3C FWI using the data which is excited only using W direction sources and recorded using 3C receivers. For nine component inversion, we always denote it as **9C FWI**. In another case, when we want to discuss a specific component in model or data misfit for any inversion, we will use the **two capital letters** format without the 'FWI' suffix. For example, YX component refers to a data or model misfit, which is excited using Y component source and X component receiver.

4.4.3.1 Synthetic experiment

A shot gather for three receiver components from the synthetic data is presented in Figure 4.17. The receiver's components are shown in separate subfigure, whereas the source's components are shown in different colors (grey, red, and green for Z, X, and Y sources' direction, respectively). With the

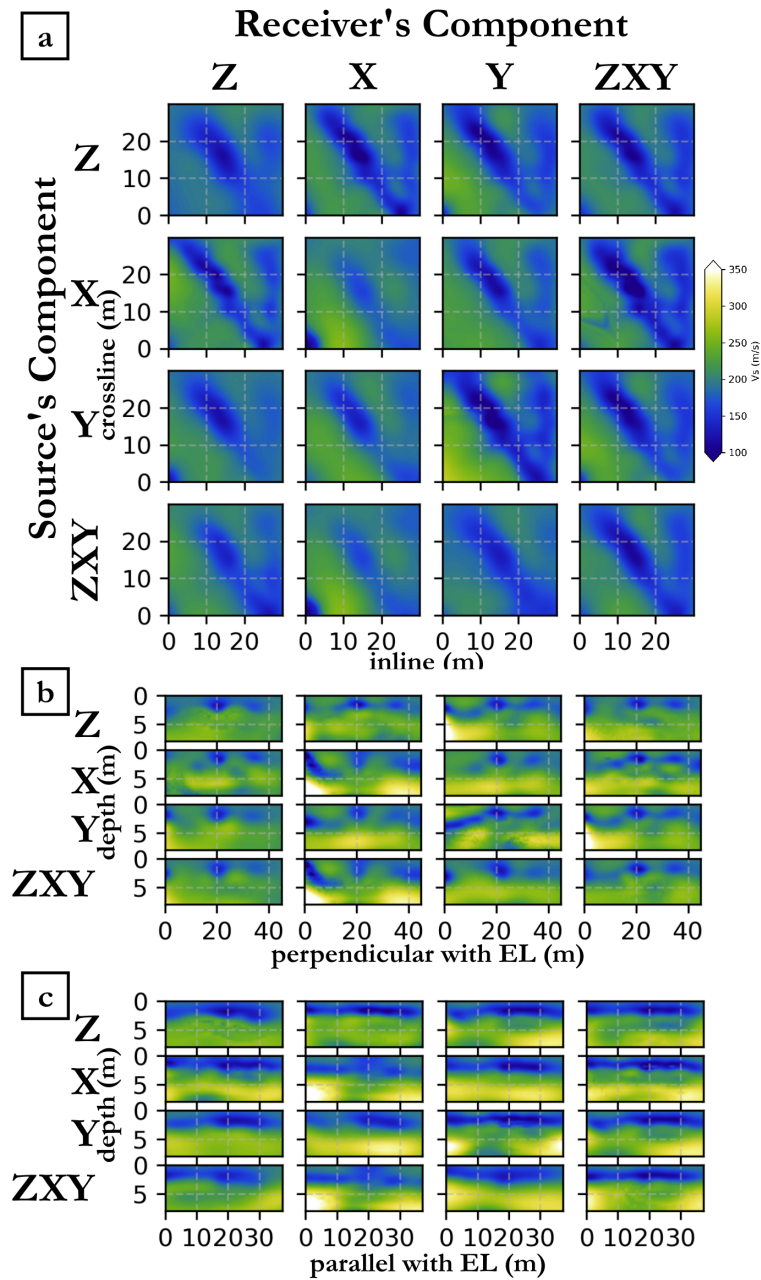


Figure 4.18: Reconstructed V_S from 16 inversions with various component combinations on the synthetic test. The top figure (a) represents horizontal slice at 1.5 m, middle (b) and bottom right (c) figures represent the vertical slice perpendicular and parallel to the Ettligen Line (EL), respectively. For each figure block, there are 16 different inversions, the rows represent the Galperin source's component, whereas the columns represent the receiver's component.

relatively simple synthetic model, the wavefields in the receiver's component Z and X are dominated by the Rayleigh waves. On the other hand, the receiver's component Y is dominated by the Love wave.

The reconstructed V_S from all 16 inversions is represented in Figure 4.18. The receiver's component is indicated by the column, whereas the row indicates the source's component. The top set of the figure

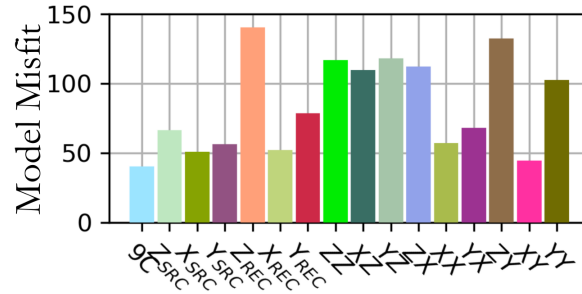


Figure 4.19: Weighted least-squares V_S model misfit for 9C and 3C FWI, and 1C FWI with respect to the reference model for the synthetic case. The behavior is similar compare to the field data, using horizontal component yield lower model misfit.

represents horizontal sections at 1.5 m depth. The middle set represents vertical sections perpendicular to the targeted trench, whereas the bottom set of the figure represents vertical sections parallel with the main anomaly.

Visual inspection of the figure reveals the inability to produce a good depth reconstruction when we only take into account the vertical component (ZZ, ZX, ZY, XZ, and YZ) compared to the case where one horizontal component is taken into account. This observation agrees with the model misfit (Fig. 4.19), where the 1C FWI with vertical component exhibits a high model misfit. Even with 3C source with a single vertical receiver’s component (Z_{REC} FWI), we can see high model misfit due to a limited number of multicomponent sources. This behavior is confirmed by the Z_{SRC} FWI experiment, where this time only vertical sources are used, however with 3 components receivers, thus including horizontal receiver components. It gives a lower model misfit, and the high-velocity layer at depth is partially recovered.

The importance of the horizontal source and receiver components can be linked to the previous sensitivity kernel study. Love wave, has a weaker sensitivity kernel’s decay than Rayleigh wave; therefore, the Love wave is more sensitive to V_S at depth part than the Rayleigh wave. The Love wave’s influence should be present in all horizontal components due to the source and receiver’s distribution. In addition, we have more information thanks to the presence of the radial component of the Rayleigh wave.

Despite the dense acquisition and a significant number of sources and receivers, some artifacts can be observed in these inversion results. The result of YY FWI, although it yields a proper model reconstruction at the 1.5 m horizontal section, fails to produce a satisfactory vertical slice result. We show that 1C FWI may not be ideal, even when it is based on the horizontal source and receiver components.

Figure 4.20 represents the absolute data misfit (a) and its corresponding misfit grade (b). ZZ, XX, and YY components for all inversions have the highest absolute misfit value. Those components have two order of magnitude absolute misfit value compared to the other components (Fig. 4.20c). The presence of those dominant components may drive the inversion due to the highest misfit value. In practice, when we have a relatively simple subsurface structure, we can focus on recording those three components since the waves are mainly recorded on those three components. In this synthetic example, analyzing the absolute data misfit is sufficient to see the horizontal components’ influence. Consistent with the previous results, the inversions that consider only the vertical source or receiver have a higher absolute misfit than the inversions that consider the horizontal components.

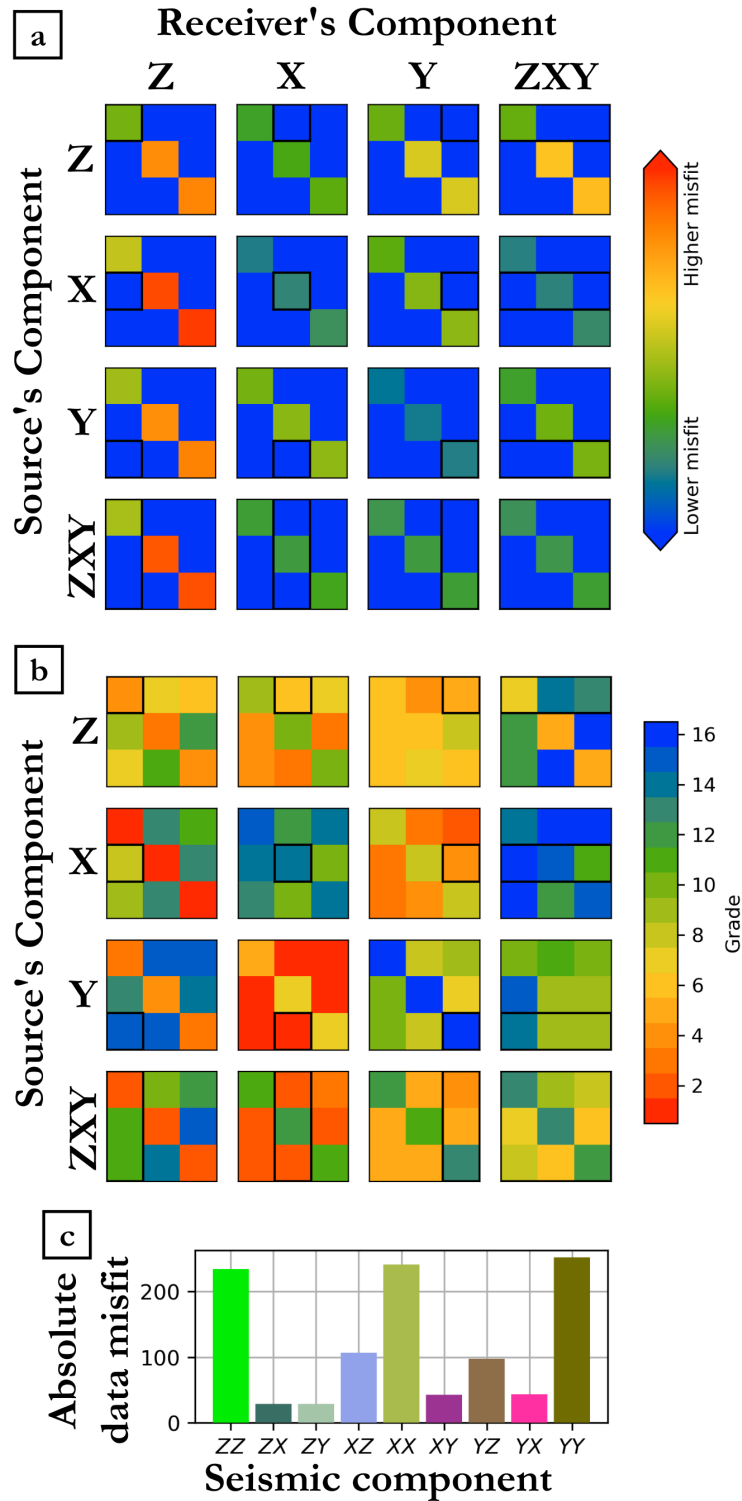


Figure 4.20: Color representation of the absolute misfit (a) and grade of component misfit (b) from all sources on the field data application. Bar plot of the absolute data misfit on 9C FWI (c).

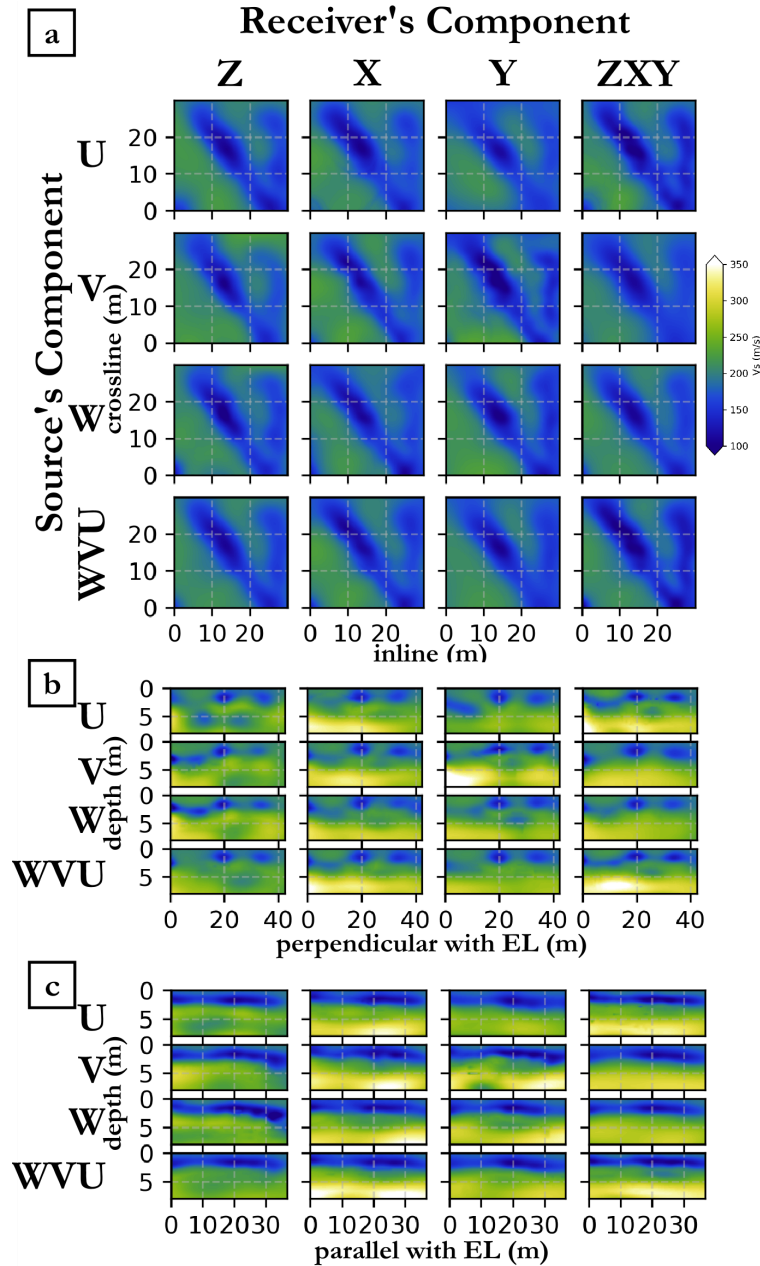


Figure 4.21: Reconstructed V_S from 16 inversions with various component combinations on field data application. The top figure (a) represents horizontal slice at 1.5 m, middle (b) and bottom right (c) figures represent the vertical slice perpendicular and parallel to the Ettligen Line (EL), respectively. For each figure block, there are 16 different inversions, the rows represent the Galperin source's component, whereas the columns represent the receiver's component.

4.4.3.2 Field experiment

The component analysis from the field experiment produces 16 different reconstructed V_P and V_S models. Figure 4.21 shows the reconstructed V_S on all 16 inversions. The top figures represent the horizontal slices at 1.5 m depth, the middle figures represent the vertical slices perpendicular to the

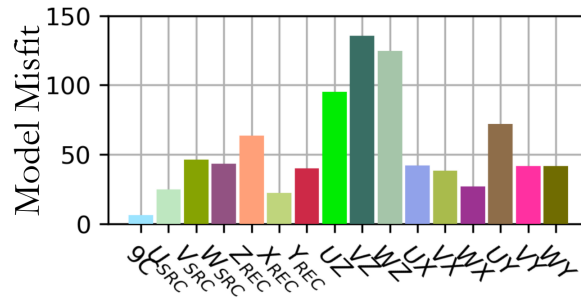


Figure 4.22: Weighted least-squares V_S model misfit for 9C and 3C FWI, and 1C FWI to the reference model for the field data application. Model misfits that consider the horizontal component receiver give significantly lower model misfit than the vertical one. Inversions using 1C source and 3C receiver give relatively similar misfits, whereas inversions using 3C source and 1C receiver give lower misfits on the horizontal component receiver. The vertical only receiver (Z_{REC}) has a higher misfit than the other 3C FWI, but it has a significantly lower misfit than 1C FWI using the vertical component.

Ettlingen Line, whereas the bottom figures represent the vertical slices parallel to the Ettlingen Line. The location of the vertical sections is displayed in Figure 4.11.

The horizontal slices show consistent shapes between all inversion results. Both the Ettlingen Line and the other trench-like structure can be recovered. The other trench-like structure can be recognized by a low-velocity anomaly at the horizontal section's right side. The consistent shapes depict a well-constrained problem due to the sufficient data and effective workflow. Through a more detailed analysis, the Ettlingen Line's shape is more consistently recovered than the other trench-like structure (the second trench). This observation corresponds with the fact that the second trench is located close to the acquisition's edge. Assuming the 9C FWI is the best-reconstructed model, we can see a more detailed structure on the second trench. Some results are similar to the 9C FWI (e.g., U_{SRC} FWI and VY FWI), and some are dissimilar (e.g., VZ FWI).

The vertical slices show more dramatic differences than the horizontal ones. It can be seen in both vertical sections. Starting from the depth of 5 m and deeper, we can observe significant model reconstruction differences, especially for the inversion using only vertical receivers (e.g., UZ , VZ , WZ , and Z_{REC} FWI). The velocity models deeper than 5 m depth on those inversions only have few updates than their initial models. The inversions, which take into account the horizontal components, generally have better depth reconstruction. From this point, we can see the importance of the horizontal components in the shallow seismic experiment. There are two exceptions for UY and WY FWI, where the model reconstruction at depth is not as good as the other inversion using horizontal components. This observation is later discussed in the data misfit.

Based on the visual inspection, there are some hints about the preferred component for FWI. Almost all inversions with the horizontal component receiver show a better model reconstruction than the vertical component receiver.

Contrary to the synthetic experiment, where 1C FWI with the vertical source gives a disadvantage, the Galperin source seems more beneficial in terms of the depth reconstruction. The Galperin sources' slanted directions mix horizontal and vertical components, resulting in the ability to have more diverse information.

The model misfit supports the observation of the reconstructed model in Figure 4.21. Presented as

a bar chart in Figure 4.22, the plot shows the model misfit for all 16 inversions. Amongst all the model misfit's largest three are the UZ, VZ, and WZ FWI. The values agree with Figure 4.21, in which the inversion results using the horizontal components have better model reconstruction at depth. On the other hand, the Z_{REC} FWI has a relatively lower model misfit than the previous three, even though it only considers the vertical receivers. This low model misfit corresponds to the fact that the Z_{REC} FWI better reconstructs the velocity model in the shallow part of the model.

The data misfits are presented as color matrices for both plots (the absolute data misfit and the misfit grade). We can observe similar patterns for all inversions in the absolute data misfit (Fig. 4.23a).

In this experiment, 9C FWI has the highest misfit grade for almost all components (Fig. 4.23b). The inversions with multicomponent receivers (U_{SRC} , V_{SRC} , and W_{SRC}) are the second best results. Even though they lack a multicomponent source, they have sufficiently dense 3C receivers. Some inversions with multicomponent sources (X_{REC} and Y_{REC}) are generally better than 1C FWI. Z_{REC} FWI demonstrates that even if we use multicomponent sources, the misfit grade might be worse than 1C FWI if we only consider the vertical component receiver.

From this experiment, several conclusions can be drawn. The first is that the horizontal components play an essential role in the model reconstruction. The second is that multicomponent data can produce a better-reconstructed model due to the better constraint and model's illumination. The third is the fact that the Galperin source has better 1C FWI's performance than the 1C FWI using the Cartesian source. Overall, 9C FWI produces a better model reconstruction than the 1C or 3C FWI in the synthetic experiment. In the field experiment, 9C FWI yields the best data and model misfit. However, there is bias in terms of the model misfit, because the reference model is determined from 9C FWI at a higher frequency.

In the next section, we assess the limit of the multicomponent inversion given a decimated number of the source and receiver. Using the decimated acquisition, we can see whether it is better to have coarse acquisition but multicomponent data or a dense acquisition with single component data.

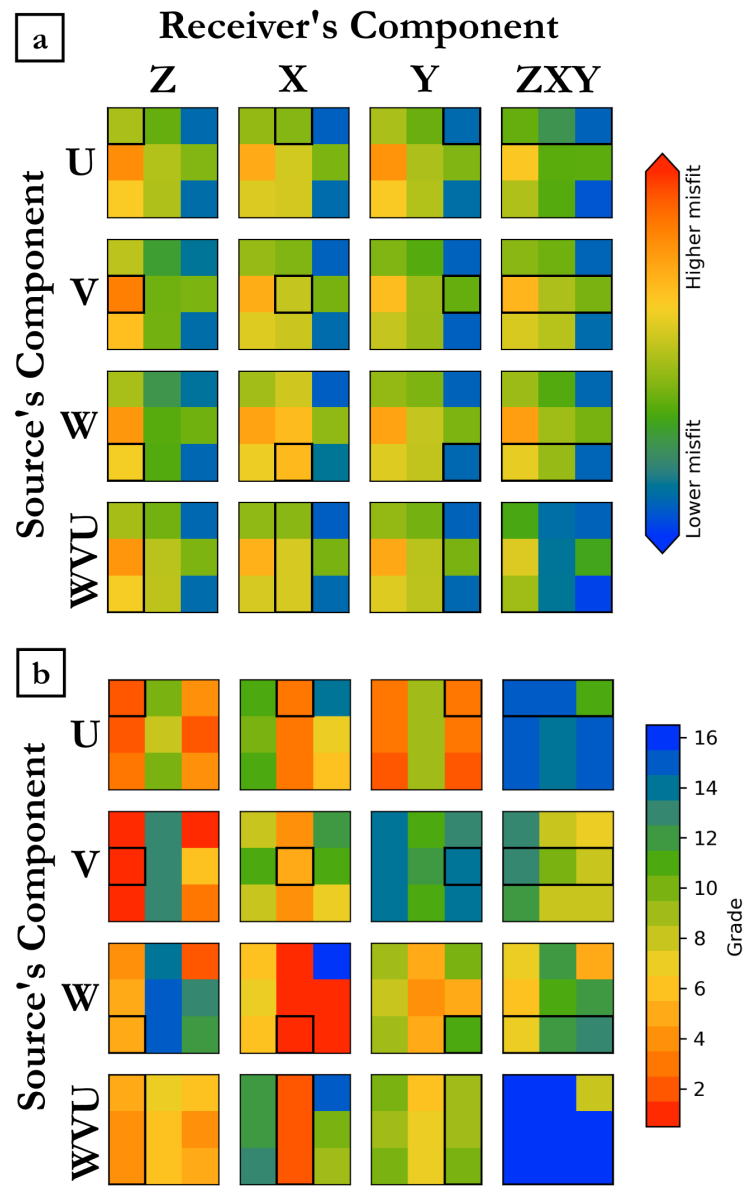


Figure 4.23: Color representation of the absolute misfit (a) and grade of component misfit (b) from all sources on the field data application. Each figure consists of 16 independent inversions with a different component combination. For each inversion, we have a 3 by 3 matrix, and the colors represent the misfit for each component (the rows are the sources' component, whereas the columns are the receivers' component.), the black rectangles represent the component combination which is used during the inversion. The absolute misfit matrix (a) represents the true calculated misfit value. Higher grade (b) means better data misfit compared to the same component on different inversion.

4.5 Acquisition's decimation

4.5.1 Source's and receiver's decimation setup

We perform decimation on source and receiver while keeping the equivalent aperture of the acquisition. With that consideration, we can see that the outer-most acquisition of the decimated acquisition is located approximately in the same area. Figure 4.24 represents all nine different combinations of the decimated source and receiver.

Figure 4.24 shows three level of decimations for the sources (orange circles) and receivers (blue triangles). We decimate the source from 36 to 10 and 5 source's locations. With the source's original position, it is quite challenging to maintain the original aperture, but we manage to select several outermost sources even when we only keep 5 sources. In terms of the receiver's location, due to the dense and regular spacings, we can easily decimate the receiver by a factor of two and four for each direction, resulting in three acquisition geometries with 855, 217, and 42 receivers.

We can compare the decimated acquisition spacing with the wavenumber of the anomaly. Based on the 9C FWI application using the full acquisition dataset (36 sources and 855 receivers), we obtain $V_S = 100 \text{ m.s}^{-1}$ within the Ettlingen Line. Given 45 Hz as the highest frequency, we have $\lambda = 1.9 \text{ m}$ as the minimal wavelength in the trench. The width of the anomaly is around 2 to 5 m (1.05 to 2.5 λ). The receiver's decimation gives us a spacing of 1, 2, and 4 m (or 0.52, 1.05, and 2.10 λ). The decimated sources' spacing is 5.65 and 11.31 m (or 2.97 and 5.95 λ) for the first two. The last decimated sources do not have an equivalent spacing, but it is ranging from 8 to 22 m (or 4.21 to 11.58 λ).

For each case of the decimation, we performed inversions for 16 different component combinations. In total, we perform 144 different inversions. We follow the same inversion workflow and procedure that is shown in Figure 4.13.

4.5.2 Results

The horizontal sections of the reconstructed V_S at 1.5 m depth from all inversions can be seen in Figure 4.25. With the decreasing source's number, we can see more apparent degradations on 1C FWI compared to 3C and 9C FWI. More in detail, these degradations are even more visible on 1C FWI with the horizontal component than the vertical component. For example WX FWI and WZ FWI with 5 sources and 42 receivers (Fig. 4.25). This observation shows a more robust resilience of the inversions with vertical component receiver at shallow depth.

The receiver's decimation also degrades the final reconstructed model, but not as severe as the source's decimation. The severity of the degradation is related to the receiver's spacing on the decimated setup. Note that the largest receiver's spacing is around the same as the size of the anomaly. In this case, the inversions using the largest receiver's spacing still produce decent anomaly reconstructions (with the densest source) but with a more visible acquisition footprint. We can see it in VY FWI with 36 sources and 42 receiver in Figure 4.25. One could introduce stronger gradient smoothing to mitigate this issue. However, the stronger gradient smoothing may slow down the inversion's convergence.

Multicomponent inversions (3C and 9C FWI) shows less degradation than the 1C FWI. In this experiment, 9C FWI shows the best result compare to 1C and 3C FWI with the same number of sources and receivers. In addition, 9C FWI also do not suffer from any acquisition footprint.

The vertical sections of reconstructed V_S at $x = 15 \text{ m}$ in crossline direction is shown in Figure 4.26. These vertical sections show similar result regarding to the inversion's resolvability using horizontal

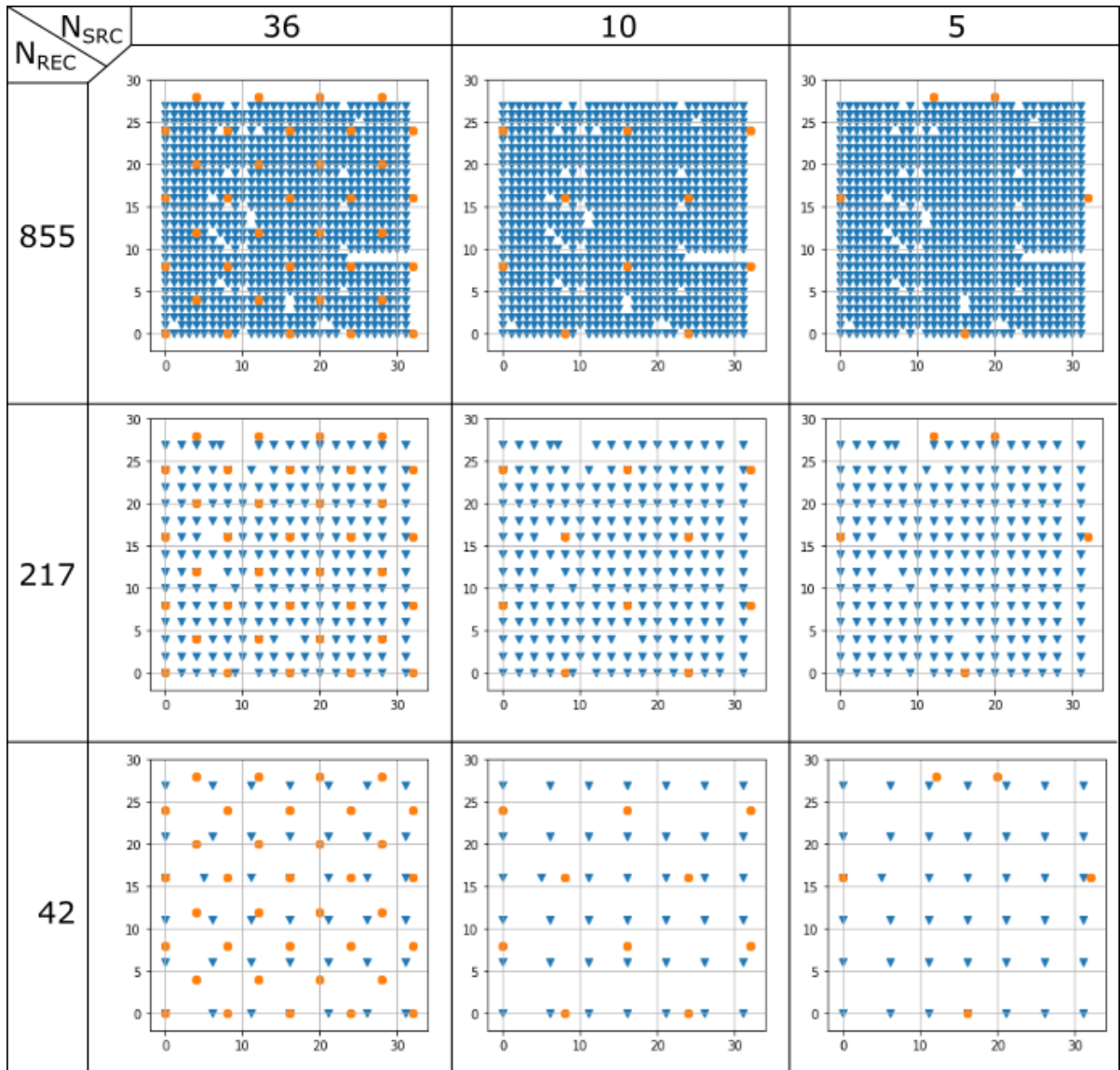


Figure 4.24: Source and receiver decimation of the Ettlingen Line field dataset. We decimate the source and receiver while keep the aperture of the acquisition to remain almost the same. N_{REC} and N_{SRC} represent the total number of sources and receivers, respectively. The notation below the N_{REC} is the decimated inline and crossline grid. Orange circles represent the source's location, whereas the blue triangles represent the receiver's location.

components with respect to depth. The results show that the depth reconstruction is better when the horizontal components are taken into account. However, the results degrade with fewer number of sources and receivers. In this experiment, the best trade-off can be seen in the inversions with 217 receivers and 10 sources. With this setup, we can save the acquisition time by a factor of four for the receiver's installation and 3.6 for the source's installation while still obtain an acceptable reconstructed model. Observing these horizontal and vertical sections shows that the vertical receivers are more sensitive to the shallow model reconstructions, whereas the horizontal receivers are more sensitive to the deeper model reconstructions.

ANALYSIS OF THE USE OF MULTICOMPONENT SOURCES AND RECEIVERS IN THE FRAME OF SHALLOW SEISMIC FULL WAVEFORM INVERSION

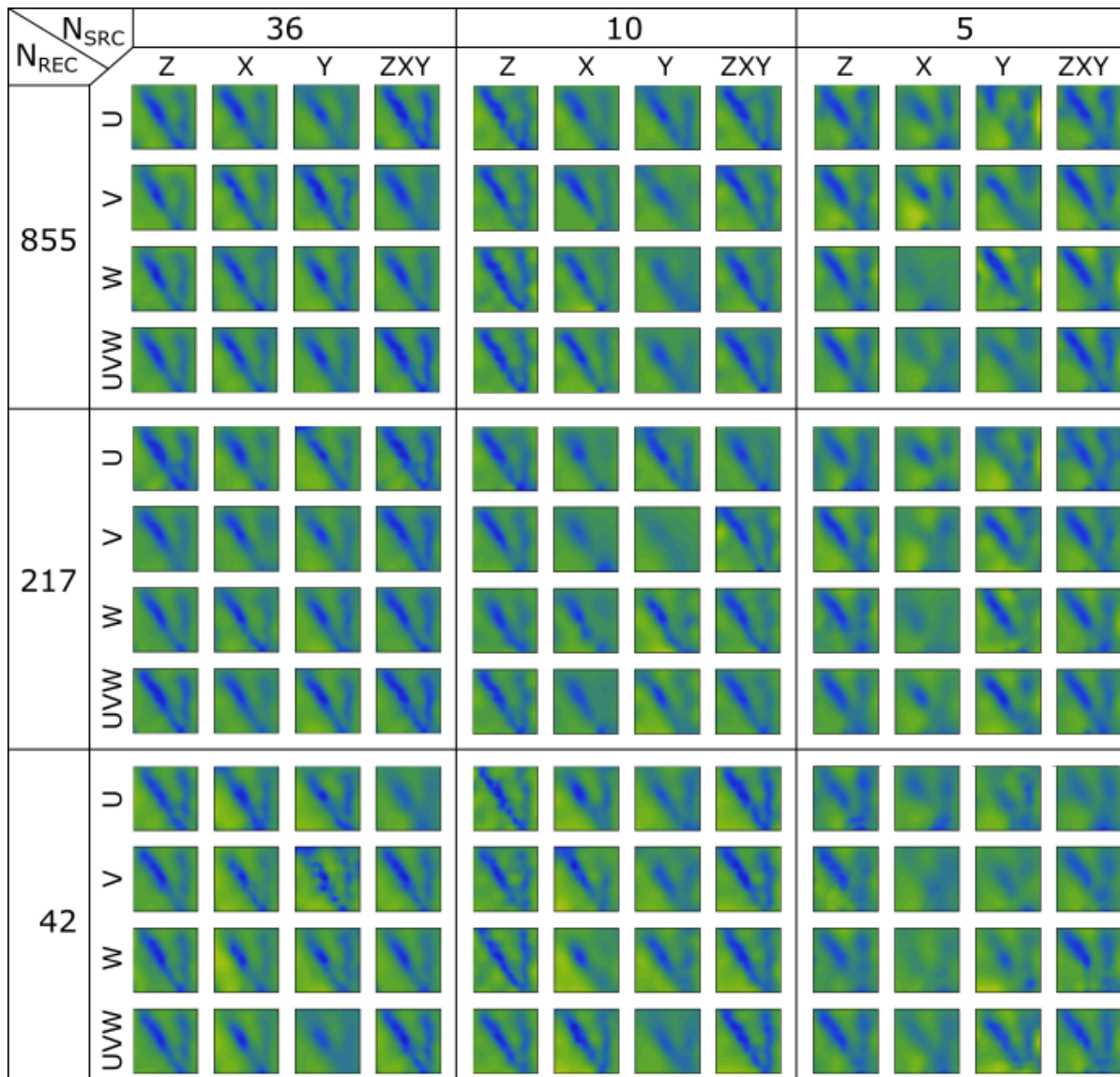


Figure 4.25: Horizontal section of the reconstructed V_S from all combination of source and receiver decimation at 1.5 m depth.

Qualitative interpretation from Figure 4.25 and 4.26 can be confirmed quantitatively by calculating the corresponding model misfit. The model misfit of all inversions are presented in Figure 4.27. Each color represents the model misfit for each inversion, with blue is the lowest and red is the highest model misfit.

Without sufficiently dense sources and receivers, 1C FWI using the horizontal receiver's component generally yields higher model misfits. The example can be seen in the inversions with 5 sources and 42 receivers. In this set of inversions, UY, VX, VY, WX, and WY FWI have higher model misfit than UZ, VZ, and WZ. This is contradictory with the inversion's results using 36 sources and 855 receivers, where 1C inversions using horizontal receiver component yield better model misfit than 1C inversions using vertical receiver component. This observations are related to fact that in dense enough acquisition, inversions using the horizontal component are able to both reconstruct the shallow anomaly

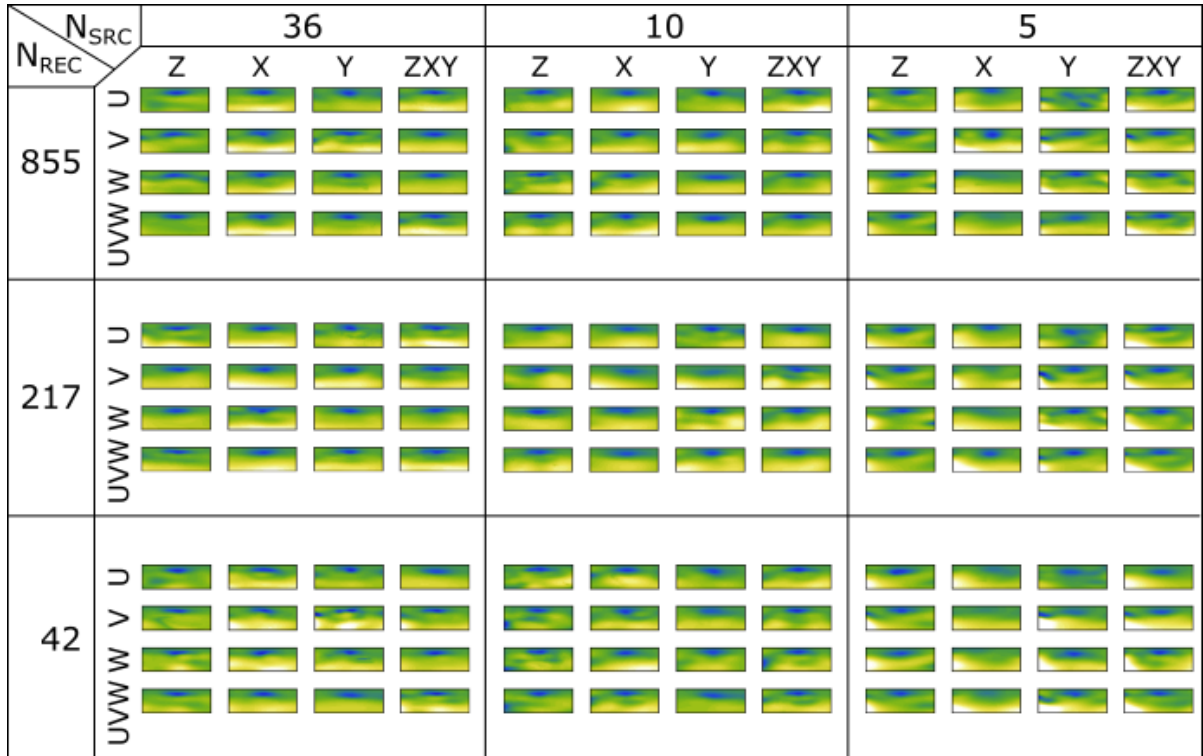


Figure 4.26: Vertical sections of the reconstructed V_S from all combination of source and receiver decimation. These sections are located at $x = 15$ m in crossline direction.

(The Ettlingen Line) and deeper part of the model. On the contrary, the inversions using the horizontal component with less number of sources and receivers are successfully reconstruct the deeper part of the model, but fail to reconstruct the shallow anomaly. In 3C FWI using horizontal receiver (X_{REC} and Y_{REC}), the previously mentioned effect is not so dramatic, thanks to the presence of multicomponent sources.

With the same number of sources and receivers, 9C FWI results always have the lowest model misfit. Aside from that, 9C FWI results also follow the expected behavior. Their model misfits increase when we reduce the number of sources or receivers. These observations are not visible in 1C FWI results. In 1C FWI results, reducing the number of sources or receivers is not always translated into lower model misfit. For example, VX FWI with 10 sources and 42 receivers has higher model misfit than VX FWI with 5 sources and 42 receivers. A similar observation also can be observed in 3C FWI, X_{REC} with 10 sources and 42 receivers has higher model misfit than X_{REC} with 5 sources and 42 receivers. These observations leads to a remark that 9C FWI is more robust than 1C and 3C FWI.

The data misfits of the source and receiver decimation experiments are shown as the absolute data misfit for each inversion result (Fig. 4.28). The color scale is scaled globally among all inversion cases and components. The lowest absolute misfit is represented as blue and the highest absolute misfit is represented as red. The absolute data misfits in Figure 4.28 show similar patterns between each inversion case. Thus, it is easier to assess the data misfit using the total absolute data misfit from all 9 components data because of these similarities. The representation of the total absolute data misfit is shown in Figure 4.29.

In some cases, the inversions fail to produce a sufficiently accurate models even if the data misfits

ANALYSIS OF THE USE OF MULTICOMPONENT SOURCES AND RECEIVERS IN THE FRAME OF SHALLOW SEISMIC FULL WAVEFORM INVERSION

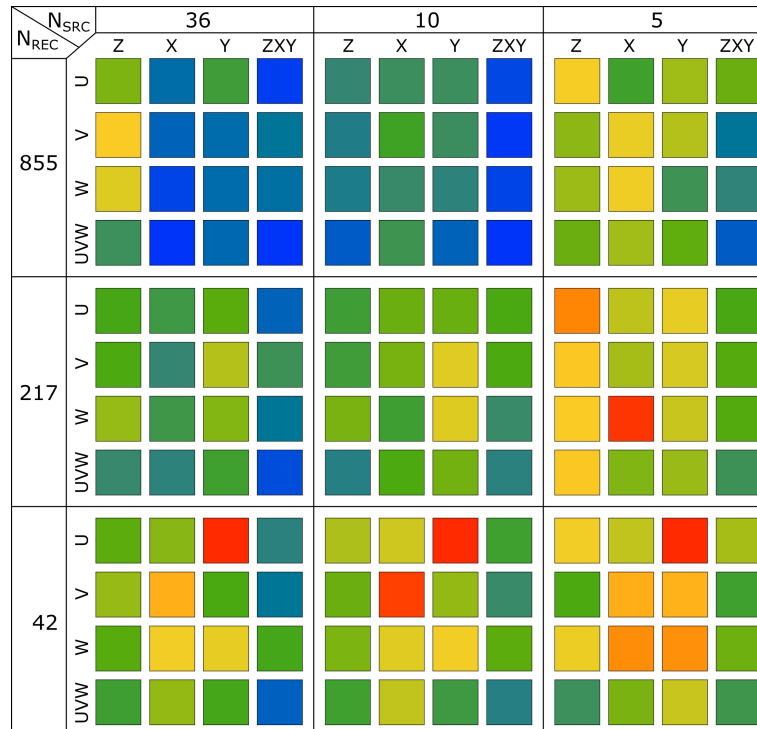


Figure 4.27: Model misfit from the decimated source and receiver setup. Each color represents the model misfit for each inversion, with blue means the lowest and red is the highest model misfit.

are low. Some of the examples are WX FWI with 5 sources and 217 receivers, UY FWI with 36 sources and 42 receivers, UY FWI with 10 sources and 42 receivers, as well as UY FWI with 5 sources and 42 receivers.

With the decimation (lower number of sources or receivers), the inversion using horizontal component receivers has lower data misfits. The lower data misfit on the horizontal component receivers might correspond with the higher level of data complexity. The vertical component receivers have simpler propagated waves and stronger responses. The stronger responses are observed for VZ and WZ component receivers, indicated in Fig. 4.28). Due to the amplitude bias, as demonstrated in Figure 4.28, the lower data misfit does not necessarily mean a better model misfit. However, the confidence of having good data misfit and model misfit is increased when we incorporate multicomponent data.

One extreme example is shown in Figure 4.30. With 5 Galperin sources and 42 3C geophones, we need fewer equipment numbers and less acquisition time compared to the UZ FWI on the full acquisition setup. The required installation times are reduced by a factor of 20 and 7 for the receivers and sources, respectively. It also has a potential reduction of acquisition time by a factor of 2.4, coming from the total number of source's components. The computational time also has a potential gain of 2.4 from the total source component's ratio. The model reconstruction is comparable at 1.5 m depth. At depth, the reconstruction is equally bad, UZ FWI fails to reconstruct high velocity layer at the bottom of the model, whereas 9C FWI only reconstruct it partially. Therefore, we conclude that 9C FWI with the least source's and receiver's numbers still produce a comparable result with the 1C FWI (especially UZ FWI) with the full setup for this particular case.

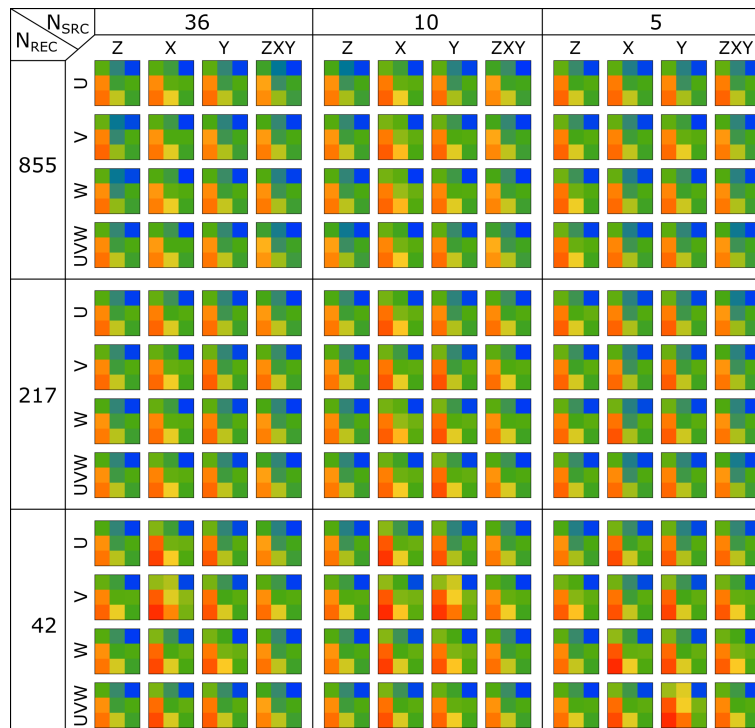


Figure 4.28: Absolute data misfit of all components and experiments from the decimated source and receiver setup. The color is scaled globally. The lowest absolute misfit is represented as blue and the highest is represented as red.

ANALYSIS OF THE USE OF MULTICOMPONENT SOURCES AND RECEIVERS IN THE FRAME OF SHALLOW SEISMIC FULL WAVEFORM INVERSION

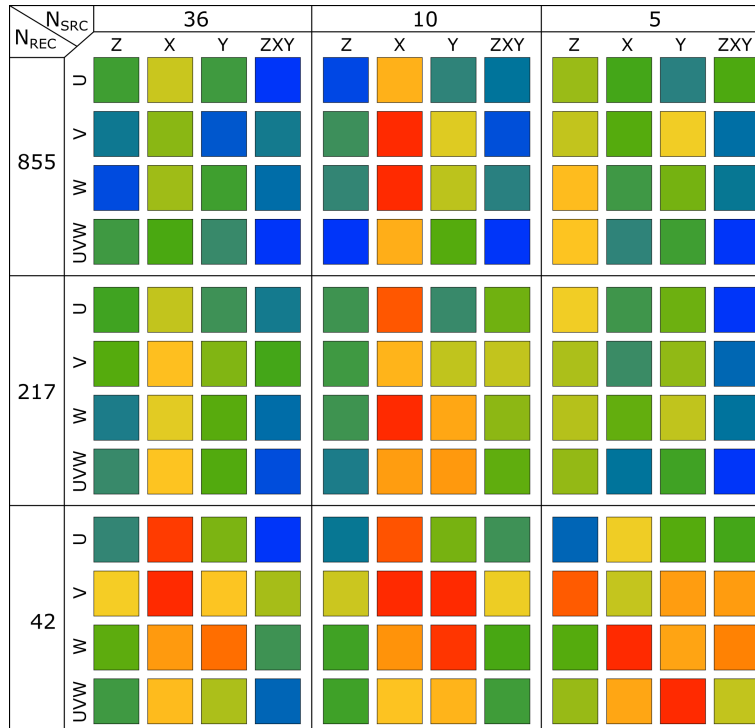


Figure 4.29: The total absolute data misfit on each inversion from the decimated source and receiver setup. The color is scaled globally. The lowest absolute misfit is represented as blue and the highest is represented as red.

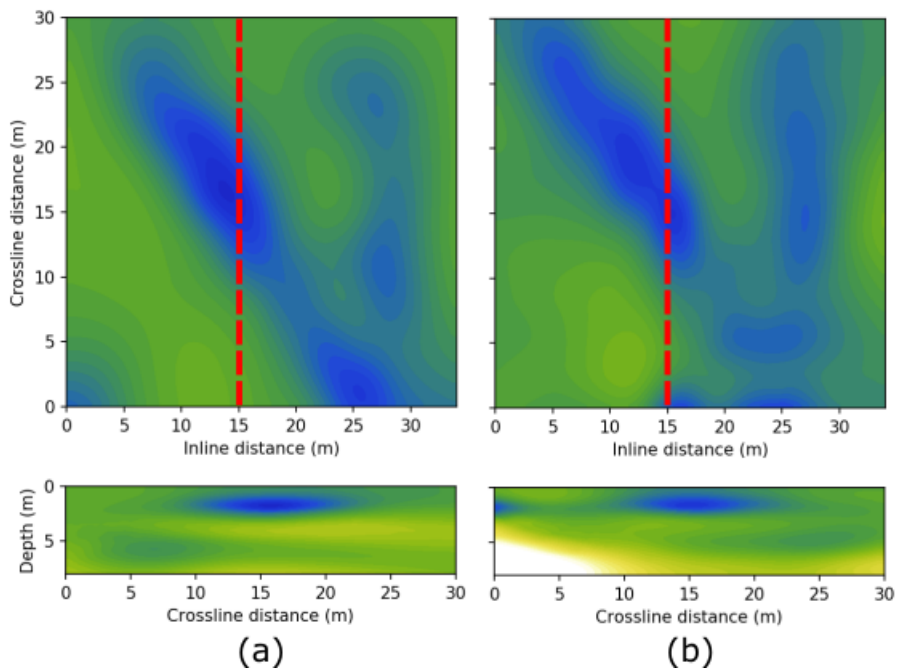


Figure 4.30: The reconstructed V_S on UZ FWI using the full acquisition setup (a). The reconstructed V_S on 9C FWI using 5 sources and 42 receivers (b). Top figures are the horizontal slices at 1.5 m depth. Bottom figures are the inline vertical slices at $x = 15$ m.

4.6 Conclusions

With the increasing popularity of the Full Waveform Inversion (FWI), the question regarding the effectiveness of using multicomponent data also increases. In this article, we perform extensive experiments to better understand the benefit of using multicomponent data in FWI. These experiments can also provide general guidelines for future shallow seismic experiments.

The sensitivity kernel analysis on simple synthetic models and several event windows shows that incorporating multicomponent data gives complementary information to improve the inversion. In shallow seismic, the surface waves have a strong response close to the surface and decay exponentially towards the depth. The surface waves also have a very weak sensitivity towards V_P but strong sensitivity to V_S parameter. In addition, our experiments show that the Love wave's sensitivity kernel has a stronger V_S sensitivity at depth than the Rayleigh wave. We also observed strong amplitude differences between the surface waves and the body waves. Therefore, a careful strategy needs to be implemented in order to have a decent V_P reconstruction.

Given a relatively dense acquisition, we perform an analysis of the inversions with various component combinations. The result shows that the inversions using multicomponent data (3C and 9C FWI) yield comparable reconstructed models at shallow depth, shown by synthetic and field data. The reconstruction at the deeper part of the model improves by incorporating the horizontal component. This result is supported by visual observation, model misfit, and data misfit. The additional depth resolution on inversion with the horizontal component can be linked with the additional information gathered from the Love wave's sensitivity at depth and the radial component of the Rayleigh wave. These observations agree with the earlier observation of the sensitivity kernel of the Love and Rayleigh wave.

The data misfit on the horizontal component inversion on a decimated source or receiver is higher due to the propagated wavefield's complexity. Using this experiment, we demonstrate that higher data misfit is not necessarily a higher model misfit.

The source and receiver's decimation gives a more evident benefit of using multicomponent data. In general, 1C FWI has a higher chance of producing a less accurate model even when the data misfit is low. Incorporating multicomponent data also can decrease the model misfit by a significant margin, especially for the 9C dataset. In this experiment, 9C FWI can still produce a decent lateral resolution at a shallow depth, even with minimal sources and receivers.

Chapter 5

The source subsampling and encoding toolbox

Contents

5.1	Introduction	125
5.2	Theory	126
5.2.1	Source encoding	126
5.2.2	Subsampling on sources	127
5.2.3	Code implementation	128
5.3	Application on the Ettlingen Line data	131
5.3.1	Parameter setup	131
5.3.2	Results	137
5.4	Conclusions	140
5.A	Computational time tables	141

5.1 Introduction

FWI is known for its demanding computational cost. Since its early development in the 1980s Tarantola (1984b), the computational cost is one major barricade, aside from the acquisition technology. Several factors contribute to the total computational cost in FWI. The first factor is related to the modeling and inversion engine. An accurate waveform modeling requires a more complex PDE and numerical discretization method. In some cases, both PDE and the numerical discretization method can be simplified but still have sufficient accuracy. One example is given in the marine environment, where a (visco)acoustic approximation is considered sufficient to represent the seismic data recorded using hydrophones. A suitable choice of numerical discretization also plays an important role. For example, the finite difference method is considered sufficient in the acoustic approximated medium with flat topography. However, these workarounds are sometimes not applicable to more complex cases. On-shore seismic acquisition with a thin low-velocity layer and complex topography is one of the examples (Trinh et al., 2019a). This type of case requires a better representation of physics, which leads to a more expensive computational cost.

The second reason is related to the practical aspects. With the development of the acquisition technology, it is now more affordable to perform a larger size acquisition, moving towards 3D instead of 2D, and having multicomponent sources. Those factors can increase computational cost demand. Aside from that, the development of data acquisition and processing enables us to have broadband data, which raises the interest of performing the inversion with even higher frequency, leading to an increased computational cost.

At the beginning of my PhD project, I was also aware that my project would involve 3D elastic medium. With the framework of exploration scale, I also aware that the computational cost is one of the limiting factors to extract most of the information from the seismic dataset. Therefore, we have planned to mitigate the problem through two popular techniques that have been used in the seismic imaging community, namely source encoding and subsampling on sources. Romero et al. (2000) introduced source encoding for the seismic migration application based on the source superposition concept. He proposes a technique to reduce the computational cost in performing seismic migration. This technique is later commonly used, especially in the exploration scales (Krebs et al., 2009; Ben Hadj Ali et al., 2011; Schuster et al., 2011; Haber et al., 2012; Castellanos et al., 2015). The second method is subsampling on sources. Instead of the superposition technique, subsampling on sources dynamically select some sources from the main pool of sources. This type of source decimation might yield a comparable result assuming that the medium is already oversampled with many sources. Ha and Shin (2013) performed a sensitivity test on the subsampling technique and shows that the random and cyclic source selection are the best subsampling technique. Both methods can reduce the computational cost by reducing the total number of forward and adjoint problems that need to be solved.

In the following section, I describe a short concept of the source encoding and subsampling on sources that I created. Then, I explain the implementation of the source subsampling and encoding toolbox. Afterward, a small field experiment is performed to assess the toolbox's potential benefit for a shallow seismic scale.

5.2 Theory

5.2.1 Source encoding

The source encoding method can be seen as a superposition of the recorded data from many sources in both synthetic (d_{cal}) and observed data (d_{obs}). The implementation of the source encoding in the synthetic data is performed by modifying the source time function into a supersource \tilde{s}_k through a convolution operation in time domain or multiplication in frequency domain given by

$$\tilde{s}_k(\omega) = \sum_{i=1}^{N_S} \kappa_i^k(\omega) s_i(\omega), \quad (5.1)$$

where k ($k \in 1, 2, \dots, K$) represents the index of the supersource, K is the total number of supersources, and κ is the encoding key (Castellanos et al., 2015). In ideal case, the quantities κ_i^k is random complex scalars and should follow

$$\mathbb{E}[\kappa_i^* \kappa_j] = \delta_{i,j}, \quad (5.2)$$

where \mathbb{E} is the expectation of κ , and δ_{ij} is the Kronecker delta. This equation implies that a perfect encoding key should be mutually exclusive to each other. Considering the new vector of encoded source $\tilde{\mathbf{S}}$, the second order viscoelastic wave equation in Chapter 1 is transformed into

$$\begin{aligned} \rho \partial_{tt} \tilde{\mathbf{u}} &= DC D^T \tilde{\mathbf{u}} - DC^R \sum_{\Lambda=1}^L \psi_{\Lambda} + \tilde{\mathbf{S}}, \\ \partial_t \psi_{\Lambda} + w_{\Lambda} \psi_{\Lambda} &= y_{\Lambda} w_{\Lambda} D^T \tilde{\mathbf{u}}, \quad \text{with } \Lambda = 1, \dots, L, \end{aligned} \quad (5.3)$$

where $\tilde{\mathbf{u}}$ is the encoded incident wavefield. The encoded synthetic data $\tilde{\mathbf{d}}_{cal}$ can be extracted using the same extraction operation R as

$$\tilde{\mathbf{d}}_{cal} = R \tilde{\mathbf{u}}. \quad (5.4)$$

The encoding should be performed for the observed data as well. Due to its linear operation in the frequency domain, the observed data \mathbf{d}_{obs} can be encoded using similar operation with the Equation 5.1 as

$$\tilde{\mathbf{d}}_{obs}(\omega) = \sum_{i=1}^{N_S} \kappa_i^k(\omega) \mathbf{d}_{obs_i}(\omega). \quad (5.5)$$

The new misfit function is now compare between two encoded seismic data as

$$\chi(\mathbf{m}) = \frac{1}{2} \left\| \tilde{\mathbf{d}}_{cal} - \tilde{\mathbf{d}}_{obs} \right\|^2 \quad (5.6)$$

Source encoding introduces substantial crosstalk between sources. Based on several experiments and sensitivity tests, Krebs et al. (2009) have demonstrated that a random scalar value of +1 or -1 is the most efficient encoding key. With a singular value, the convolution in Equation 5.1 and 5.5 can be simplified into a multiplication of either +1 or -1 in time domain. Krebs et al. (2009) also suggested to perform re-encoding as often as possible to minimize the crosstalk. Performing re-encoding breaks the numerical optimization flow because the objects that we compare in Equation 5.6 are different. In steepest descent (Nocedal and Wright, 2006), where the gradient calculation solely relies on the current iteration, performing re-encoding requires no modification. However, the other second-order numerical

optimization also takes into account the previous gradients. In this case, the optimization is also needed to be restarted along with the re-encoding.

On l -BFGS method, Rao and Wang (2017) proposed an alternative to both stable descent direction and minimal crosstalk. This method divides the l iterations into two parts, invariant and re-encoding steps. During the invariant steps, no re-encoding is performed to ensure a stable descent direction. Afterward, during the re-encoding steps, the data is re-encoded every iteration to reduce the crosstalk.

5.2.2 Subsampling on sources

Subsampling on sources dynamically selects a subset of sources from the sources' pool. The number of incidents and adjoint problems is also reduced through the source selection. In contrast with the source encoding, the subsampling on sources does not introduce any non-physical crosstalk. However, subsampling on sources reduces the amount of information that is taken into account in each iteration. In a sufficiently dense acquisition where the medium is densely sampled, subsampling on sources can reduce computational time without sacrificing the results. Ha and Shin (2013) presented a comparison between subsampling strategies. He suggests that random and cyclic subsampling on sources give the best result. The random and cyclic subsampling on sources is illustrated in Figure 5.1. Warner et al. (2013) demonstrate a successful example of subsampling on sources technique, followed by many other examples (Kamath et al., 2020; Pladys et al., 2020).

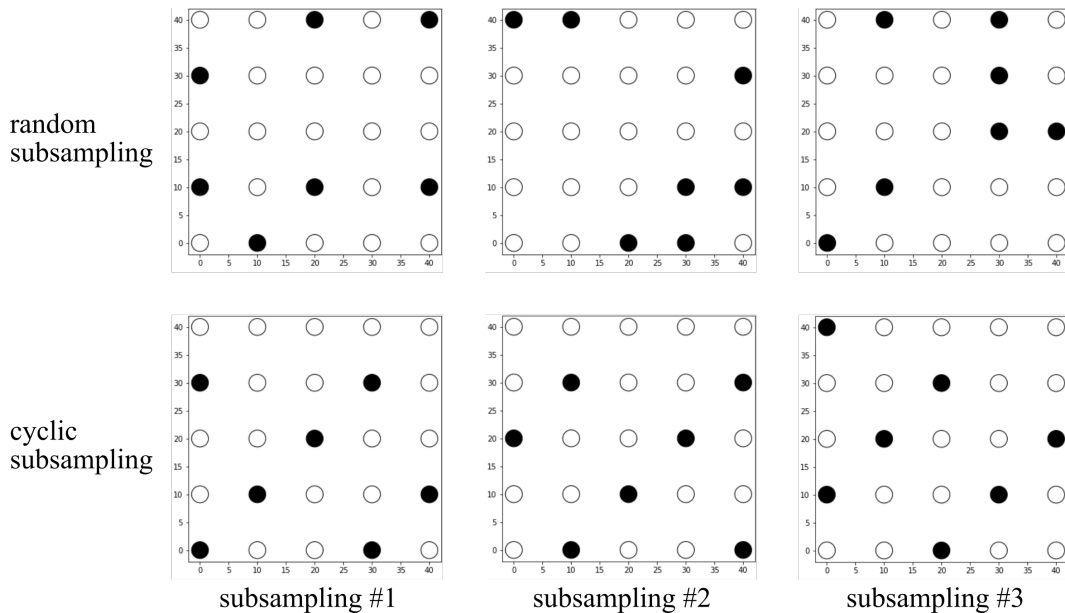


Figure 5.1: Illustration of random (first row), and cyclic subsampling on sources (second row). Filled circles are the selected sources.

Similar to the source encoding counterpart, re-subsampling is necessary to include the new dataset into the inversion. With re-subsampling, a numerical optimization restart is also required for the second-order optimization methods.

Algorithm 2: Initialization phase

Result: $\tilde{\mathbf{d}}_{obs}$ and $\tilde{\mathbf{S}}$
 Variables declaration and memory allocation;
 Read input files for encoding toolbox;
 Read acquisition files ;
 Execute encoding subroutine;

5.2.3 Code implementation

The source subsampling and encoding toolbox are written in Fortran as an independent library and coupled with two SEISCOPE codes. The toolbox is divided into three main parts: the initialization subroutine, the encoding and subsampling subroutine, and the main program's communication. The initialization phase (Alg. 2) mainly focus on the memory allocation, scan the acquisition information, and perform the first encoding/subsampling. The encoding phase is firstly executed during the initialization phase and later executed when re-encoding, or re-subsampling is activated (Alg. 3). The third step is communication and integration with the main FWI subroutine (Alg. 4). Besides the main three steps, other smaller subroutines are implemented in our subsampling and encoding toolbox, which are source partition, random number generator, and same source position check.

Algorithm 3: Encoding and subsampling phase

Result: $\tilde{\mathbf{d}}_{obs}$ and $\tilde{\mathbf{S}}$
 Variables declaration and memory allocation;
if *initialization phase or re-encoding is activated or re-subsample is activated* **then**
 if *Random seed file is not exist* **then** Create random seed file;
 Read random seed file;
 if *Subsampling is activated* **then** Subsample sources;
 if *Source partition is activated* **then** Perform source partition;
 Distribute the source to the available processors;
 if *source encoding is activated* **then**
 Generate encoding keys κ ;
 Read the observed data \mathbf{d}_{obs} ;
 Read the source time function \mathbf{S} ;
 Perform source encoding and obtain $\tilde{\mathbf{d}}_{obs}$ and $\tilde{\mathbf{S}}$;
 else
 Do nothing
 end
else
 Do nothing
end

5.2.3.1 Source partition

Introducing the source encoding into the inversion introduce non-physical crosstalk. Instead of combining it directly, Romero et al. (2000) introduce phase encoding to reduce the amount of crosstalk between

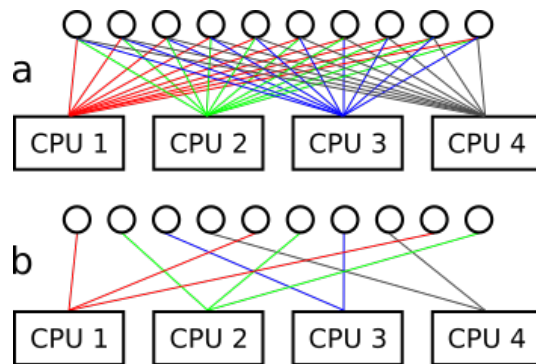


Figure 5.2: Illustration of the source encoding without (a) and with source partition (b). Each circle represents a single source and each rectangle represents each processors. In this illustration, we assume that there is no domain decomposition (each CPU perform a single simulation). The lines with the same colors depicts the relation between the source and the simulation.

different sources. The study from Krebs et al. (2009) show a further analysis of different phase encoding keys and decide that $+1$ or -1 scalar encoding keys are the most robust one. However, when many sources are taken into account, $+1$ or -1 scalar encoding keys are not sufficient, and heavy crosstalk could occur. Therefore, I propose another way to reduce the amount of crosstalk by reducing the total number of encoded sources in a single simulation. Instead of having all sources in each simulation (Fig. 5.2a), the source partition subroutine allows us to split the total number of the sources into a smaller supersource on each simulation (Fig. 5.2b).

5.2.3.2 Random Number Generator

The random number is generated using a built-in Fortran function `RANDOM_NUMBER()`. In order to have random numbers that are accessible to all processors, we need to determine a common random seed. In this Encoding Toolbox, the variable `seed` is an integer array with a length of 33. The length is arbitrarily chosen to accommodate different seed length requirements on several different compilers. Later, the seed is stored in the disk; therefore, all processors might have access to the same `seed` files and variables. In our implementation, the `seed` can be automatically written by the toolbox or manually defined by the user. The seeds generated by the toolbox is written on the disk with the prefix name 'seed'.

5.2.3.3 Same source position check

The source subsampling and encoding toolbox also perform the same source position check. Performing source encoding on several sources at the same location might increase the amount of crosstalk, especially when the type of sources or the directions are different. This check put the source with the same location on a different source partition.

Algorithm 4: Communication phase in a basic inversion subroutine

```

Initialization of FWI subroutine;
if Encoding is activated or subsampling is activated then
    | Execute initialization phase subroutine (Alg. 2) ;
    | Copy  $\tilde{\mathbf{d}}_{obs}$  and  $\tilde{\mathbf{S}}$  to the local variables if necessary;
    | Copy the acquisition information to the local variables;
else
    | Perform regular data reading ( $\mathbf{S}$ ,  $\mathbf{d}_{obs}$ , and acquisition);
end
Compute forward problem, gradient, and the cost function;
while inversion is not converged and inversion id not failed do
    | Execute the optimization toolbox (Métivier and Brossier, 2016);
    if new iteration then
        | if Encoding is activated or subsampling is activated then
            | Check whether optimization restart is required;
            | if l-BFGS optimization then
                | Check whether the iteration is invariant or not (Rao and Wang, 2017);
            | else
                | Do nothing
            | end
            | if gradient computation is required then
                | Compute forward problem, gradient, and the cost function;
            | else
                | Do nothing
            | end
            | if optimization restart or not in invariant iteration then
                | Execute source encoding/subsampling subroutine (Alg. 3);
                | Copy  $\tilde{\mathbf{d}}_{obs}$  and  $\tilde{\mathbf{S}}$  to the local variables if necessary;
                | Copy the new acquisition information to the local variables;
                | if optimization restart then
                    | Compute forward problem, gradient, and the cost function;
                | else
                    | Do nothing
                | end
                | Set optimization restart to FALSE;
                | Set the invariant iteration to TRUE;
            | else
                | Do nothing
            | end
        | else
            | Do nothing
        | end
    | end
    | Do nothing
end
end

```

5.3 Application on the Ettlingen Line data

5.3.1 Parameter setup

The source subsampling and encoding toolbox are tested on the existing field experiment. We use the 3D 9C Ettlingen Line seismic data for this purpose. Our goal is to test the feasibility of performing 3D FWI using the 9C dataset on the viscoelastic medium within a reasonable computational cost margin. We follow the same workflow as it has been proposed in Section 3.3.2.3 and main parameter setup in Section 4.4.1 for field experiment.

Common experiment setup

We perform five different tests concerning source encoding and subsampling on sources. We illustrate the subsampled or encoded sources using a selected source map plot given in Figure 5.3. For each subsampling and encoding, there are three lines of circles plot. Each line represents the Galperin source direction in U, V, and W from top to bottom, respectively (Fig. 5.3a). Each circle illustrates a single source with a particular direction and location. Circles with the same color on each subsampling and encoding plot represent a common source in a single wave propagation simulation or encoded into a common supersource (Fig. 5.3b).

There are several common parameters used in our experiment. A random +1 or -1 encoding is used for source encoding, whereas random subsampling is used for subsampling on sources. The numerical optimization is restarted every five iterations, and the encoding keys are randomly re-generated. All receiver components (Z, X, and Y) are also considered.

Figure 5.4 shows a synthetic seismic section that is calculated without source encoding or subsampling on sources in a single simulation. This synthetic data is the Z component of the first source location (source coordinate of $x = 0$ and $y = 0$) using the U source component. This figure can be used as a comparison with the other seismic sections in our experiments.

In all experiments, we aim to seek the possibility of an affordable inversion for the Ettlingen Line field experiment. We aim to perform 3D FWI on a viscoelastic medium using SEM46 with a limited resource and a time constraint. In this case, we target an inversion that can be performed using 16 core processors, 32 GB RAM, and big but not unlimited non-volatile storage. The non-volatile storage is considered big but not unlimited because it is easily expandable. We show later that, while the non-volatile storage requirement is relatively high, it is still affordable. Several non-volatile storage examples are the hard disk, Solid State Drive (SSD), and Intel Optane. It is essential that considering high-speed non-volatile storage is essential because the inversion requires intensive I/O operations. For our experiments, we limit the maximum CPU time up to 10 days using 16 processors. Note that 10 days is just an arbitrary value representing a week and a half of inversion. It is equivalent to a total maximum sequential CPU time of 2688 hours.

The experiments are performed using Irene KNL Nodes, a high-performance computing machine provided by the TGCC. KNL Nodes is the second generation of Intel Xeon Phi processor with the code name of Knight Landing. Intel Xeon Phi itself is based on Many Integrated Core (MIC) architecture. For each node, there is a single CPU with 68 cores with a clock of 1.4 GHz. Each node has 96 GB of RAM, leading to 1.4 GB of RAM per core. In terms of the non-volatile memory, Irene KNL uses a very high bandwidth of 60 GB/s, shared with all active users.

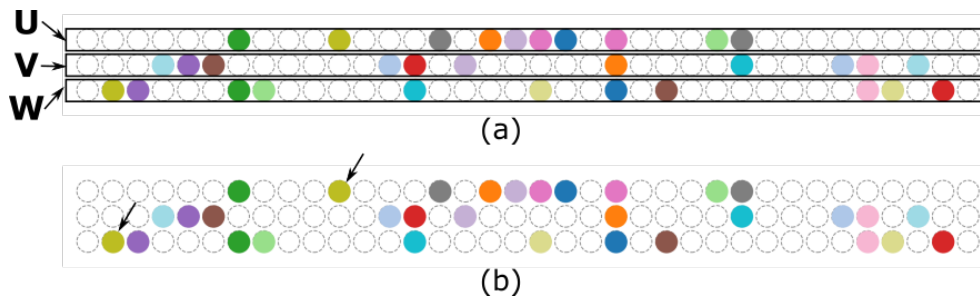


Figure 5.3: A guide to understand the selected source map plot. This plot is the representation of the selected source for source encoding and subsampling on sources. Each circle represents a single source location and direction. Filled circles depict the selected sources, whereas blank circles represent discarded sources. Each line represents the source directions (a). Black arrows in (b) show an example of sources taken into account in a single simulation. The same color indicates a common source in a single simulation.

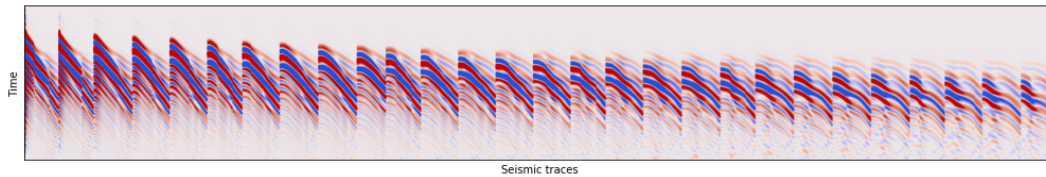


Figure 5.4: Normal synthetic seismic section without source encoding and subsampling on sources. The figure indicates the first source location recorded in z -direction. The location of the source is coincide with first seismic trace.



Figure 5.5: Selected sources of the full source encoding for all frequency bands on case 1.

The detail of each different cases are presented below:

Case 1: Full source encoding using all source directions

The first test is a full source encoding using all source directions on each forward problem. For each wave propagation simulations, all 108 sources are taken into account. It is indicated by the same circle's color in Figure 5.5. There are a total of 16 encoded seismic simulations with different encoding keys. Figure 5.6 shows the encoded seismic section in a single wave's propagation's simulation in Z component. Due to multicomponent sources, there are three different sources at the same location, which might increase the crosstalk between these sources.

Case 2: Full source encoding using V source directions

In this second case, instead of using all source directions, we only consider the V component source (Fig. 5.7). By selecting a single source direction, we can avoid heavy crosstalk between sources at the same location. Figure 5.8 shows the encoded seismic source.

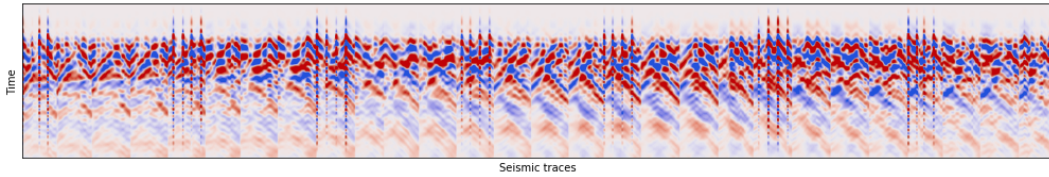


Figure 5.6: Synthetic encoded seismic section on all 108 sources calculated on a single wave propagation's simulation (case 1).

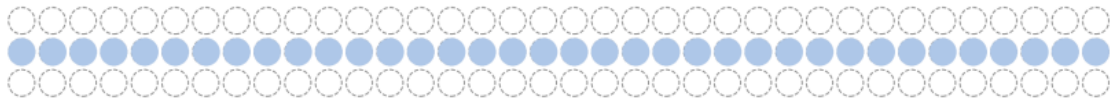


Figure 5.7: Selected sources of the full source encoding for all frequency bands on case 2. Note that only sources with V direction are selected.

Case 3: Partitioned source encoding

Instead of reducing crosstalk reduction by having the same encoded source with a different encoding key, we can have a source encoding with partitioned source by separating sources into several different simulations (Fig. 5.2). In this case, 108 sources are divided into 16 different simulations. Each simulation consists of 6 to 7 random sources. Figure 5.9 shows the selected sources map throughout the inversion. Each frequency band has a minimum of two sets of selected sources map due to two inversions (V_S only and multiparameter inversion). If the frequency band has more than two selected source maps, it means the encoding is performed more than once. This setup might reduce spatial crosstalk between the receiver. Figure 5.10 shows a better spatial separation between sources.

Case 4: Full subsampling on sources

In this setup, we only consider 16 different sources for each iteration. The component and location of sources are randomly selected. Different from the source encoding, subsampling on sources does not suffer from the crosstalk between sources. Figure 5.11 shows the subsampled source. Our field experiment is a good candidate for the subsampling on sources because of the dense acquisition. Chapter 4 also shows a promising result with a decimated source. The seismic section of the subsampled source can be seen in Figure 5.12. The seismic waveform is simpler than the source encoded case. However, the source location and component are different compared to Figure 5.4 due to the random source selection.

Case 5: Source encoding + subsampling on sources

We perform another experiment by combining both methods to take advantage of the subsampling on sources and source encoding. We consider two sources for each simulation. Because we restrict ourselves to 16 simulations, only 32 sources can be taken into account. Therefore, random subsampling is performed in order to select the source pool to be encoded. Figure 5.13 shows the selected sources on the first 3 frequency bands. Figure 5.14 shows the encoded seismic section on a single simulation. We can observe minimal crosstalk compared to the other encoding technique.

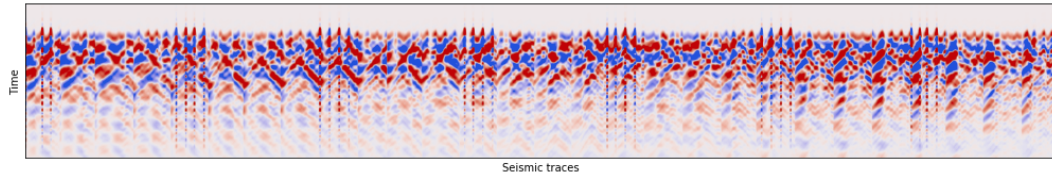


Figure 5.8: Synthetic encoded seismic section on 36 sources with V direction calculated on a single simulation (case 2).

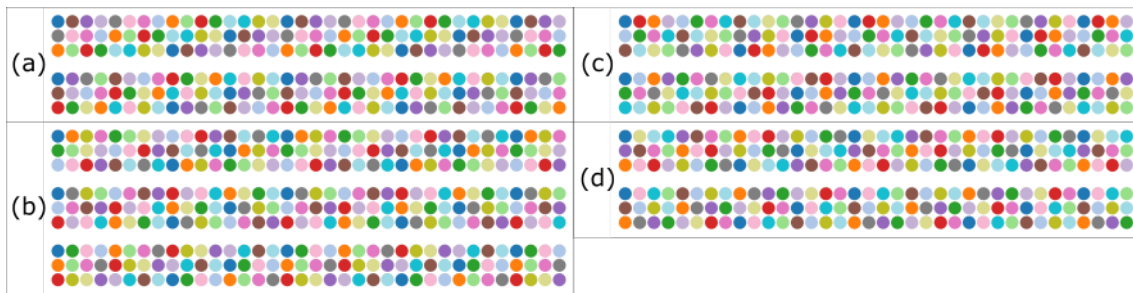


Figure 5.9: Selected sources of the partitioned source encoding for 3 - 15 Hz (a), 3 - 25 Hz (b), 3 - 35 Hz (c), and 3 - 45 Hz (d) frequency band on case 3. Each frequency band might have multiple re-encoding, depicted by multiple set of plots.

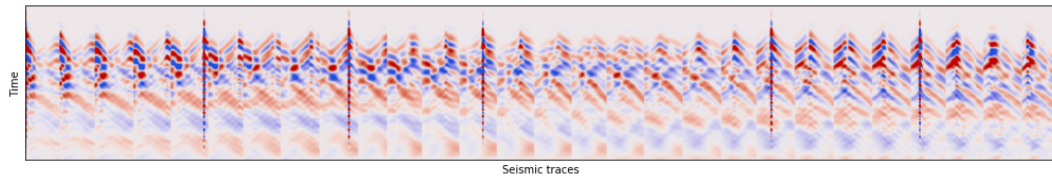


Figure 5.10: Synthetic encoded seismic section on 7 sources calculated on a single simulation (case 3). The selected sources is determined using sequential partition.

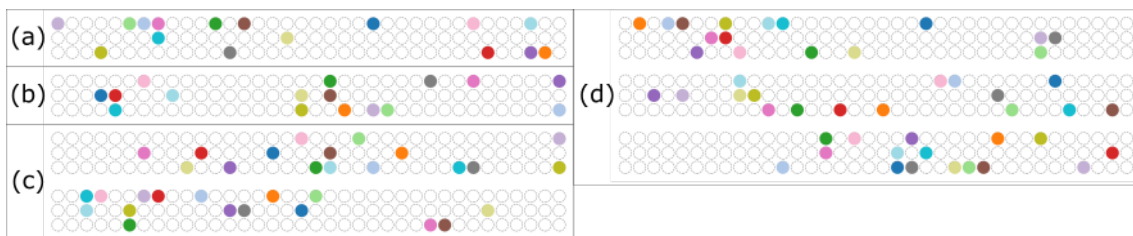


Figure 5.11: Selected sources of the full subsampling on sources for 3 - 15 Hz (a), 3 - 25 Hz (b), 3 - 35 Hz (c), and 3 - 45 Hz (d) frequency band on case 4. Each frequency band might have multiple re-encoding, depicted by multiple set of plots.

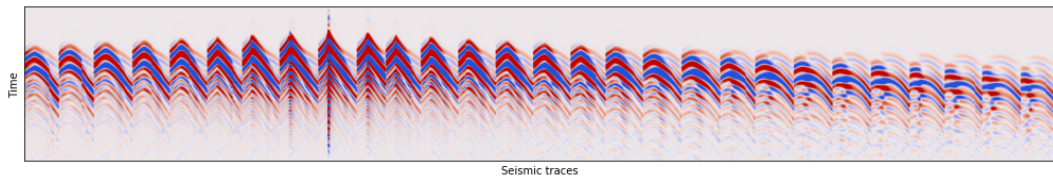


Figure 5.12: Subsampled seismic section on a single simulation (case 4). There is only one selected source for each simulation.

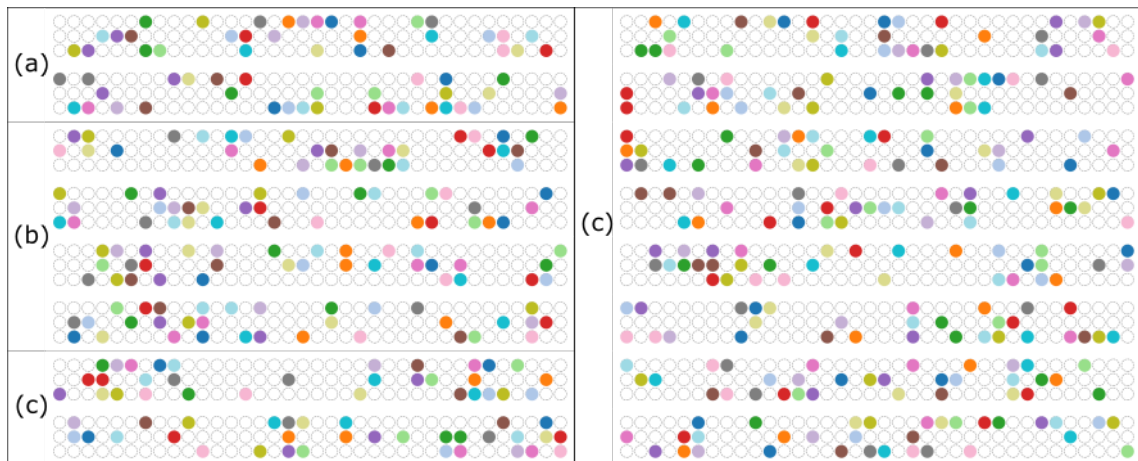


Figure 5.13: Selected sources of the full source encoding for 3 - 15 Hz (a), 3 - 25 Hz (b), and 3 - 35 Hz (c) frequency band on case 5. Each frequency band might have multiple re-encoding, depicted by multiple set of plots.

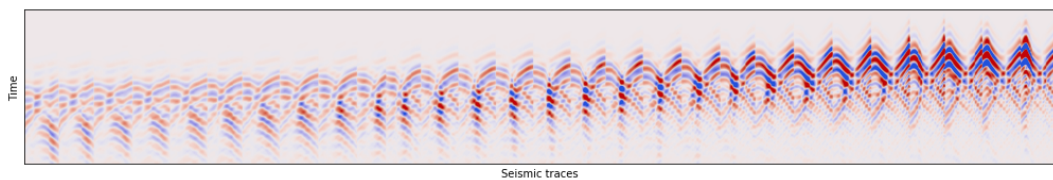


Figure 5.14: Subsampled and encoded seismic section on a single simulation (case 5). There are two selected sources for each simulation.

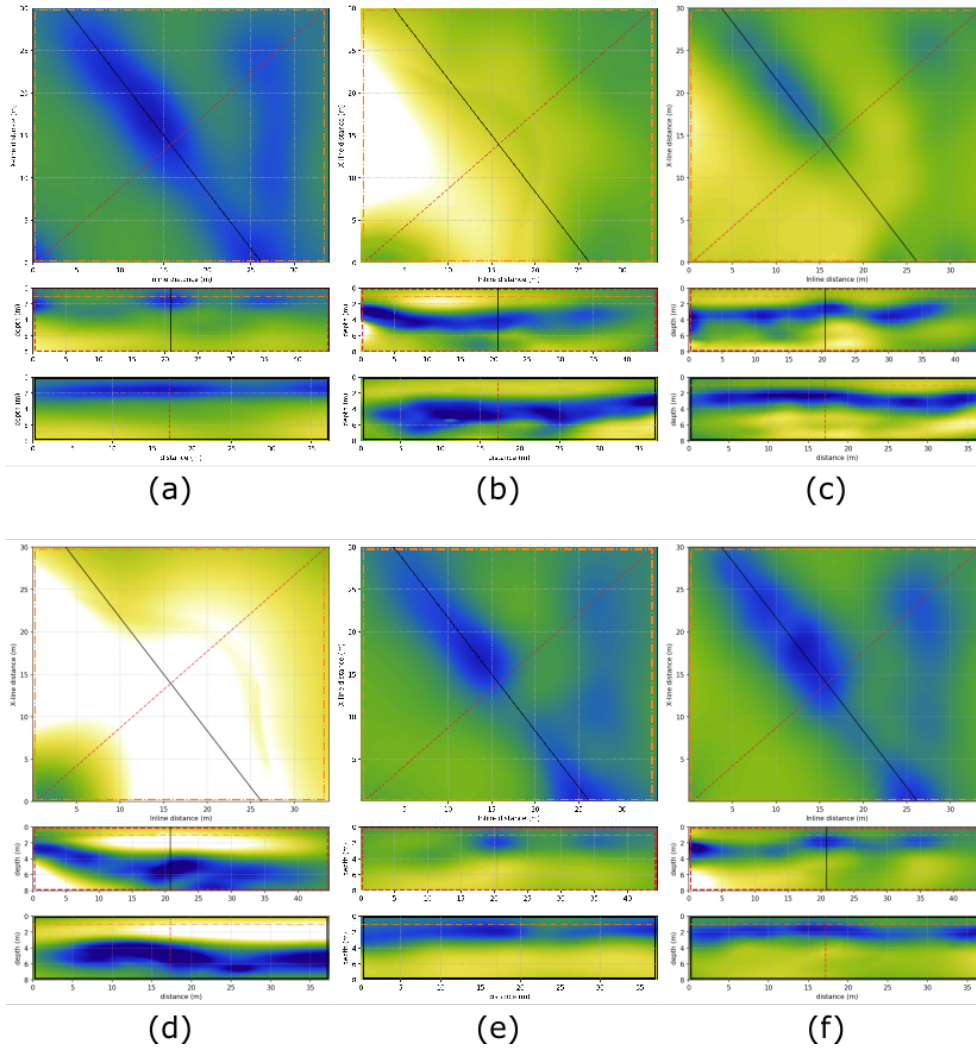


Figure 5.15: Reconstructed V_S models which are obtained using standard FWI on a full acquisition setup (a), full source encoding (b), source encoding on SRC_V (c), partitioned source encoding (d), subsampling on sources (e), and source encoding + subsampling on sources (f).

Table 5.1: Summary of the total computational time and model misfit for each case. The time is in days of the equivalent machine, whereas the model misfit is a unitless quantity to measure the similarity between the reference and reconstructed model. The reference model (first row) is obtained from the reconstructed V_S at 45 Hz from Chapter 3.

Case	Total computational time (day)	Model misfit (unitless quantity)
Ref.	34.4	36
1	2.1	2476
2	8.3	1415
3	6.5	5591
4	5.1	190
5	7.6	253

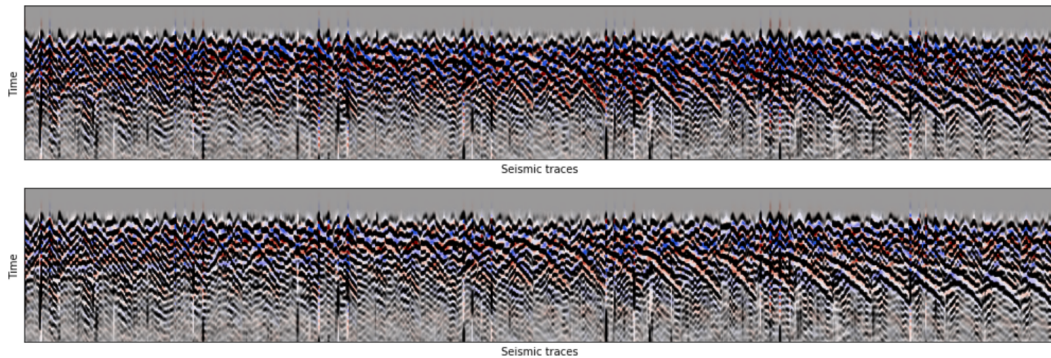


Figure 5.16: Data fit between the observed and synthetic data on Case 1. The synthetic data is calculated using the initial model (top) and final reconstructed model (bottom). A good data fit is indicated by the pair of black and blue. The presence of red can be associated with a bad data fit.

5.3.2 Results

Figure 5.15 shows the reconstructed V_S at 45 Hz. The reference model in Figure 5.15a is obtained from the multiparameter inversion using full acquisition (Chapter 3). The reconstructed V_S for Case 1 to 5 can be seen in Figure 5.15b to f. Table 5.1 shows a short summary of the equivalent total calculation time and the model misfit. The model misfit is calculated using the same formulation of model misfit in Chapter 4. The equivalent total computational times are given in day and represent the computational time using 16 processors on all four frequency bands.

Figure 5.16 to 5.20 shows the data fit between the observed and synthetic data. The synthetic data on the top figures are calculated using the initial velocity models, whereas the synthetic data on the bottom figures are calculated using the final reconstructed models. The synthetic data is drawn using the blue to the red color scale. Blue represents the positive amplitude in the synthetic data. The observed data is drawn using the black to the transparent color scale. Black represents negative amplitudes in the observed data. When the data phase is perfectly matched, a combination of black and blue colors is shown in the plot. Therefore, the presence of red color is related to a bad data fit.

From the reconstructed V_S model (Fig. 5.15b), the full source encoding in **Case 1** fails to produce satisfactory results. Laterally at 1.5 m depth, it cannot reconstruct the two main archaeological objects (the Ettlingen Line and other trench-like structure on the right of the model). Vertically, it also fails to produce a meaningful result. There are very high-velocity values close to the surface and a missing high-velocity layer at depth. Even though the computational time is the cheapest amongst the other experiments, the model misfit is the second highest (Table 5.1). The data fit plot in Figure 5.16 shows almost no perceptible improvement for this seismic section. The seismic sections show heavy crosstalk between sources. Having a limited number of encoded data (only 16 in this case) and multiple sources at a single receiver does not help the inversion.

The **second case** focuses on reducing the crosstalk by avoiding multiple sources in a single location. With this approach, we can see a notable improvement in the reconstructed V_S model (Fig. 5.15c). Laterally at 1.5 m depth, the low-velocity value due to the Ettlingen Line is visible. The reconstruction of the other trench-like structure is weaker than the Ettlingen Line. The vertical sections show a bit of improvement compared to Case 1. A high-velocity layer at the bottom of the model is better reconstructed than the one in Case 1. Even with these improvements, the V_S model is still far from the reference model. A large model misfit indicates it.

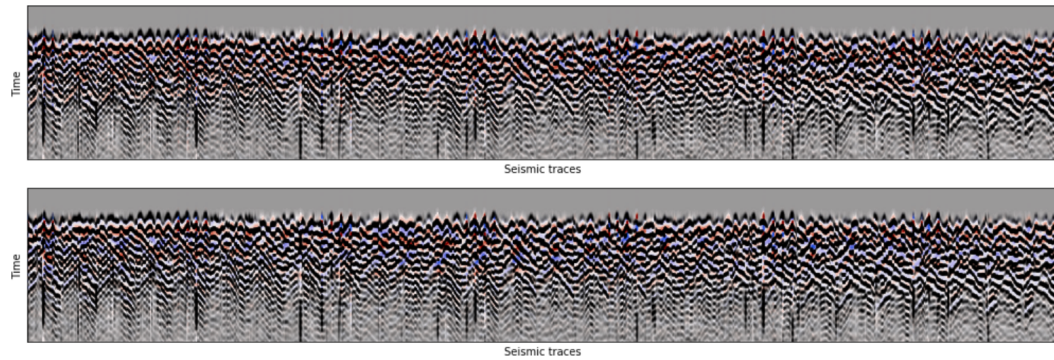


Figure 5.17: Data fit between the observed and synthetic data on Case 2. The synthetic data is calculated using the initial model (top) and final reconstructed model (bottom). A good data fit is indicated by the pair of black and blue. The presence of red can be associated with a bad data fit.

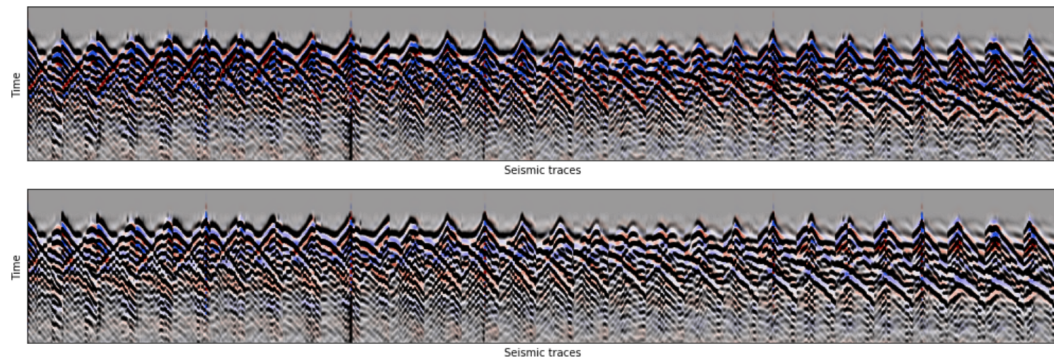


Figure 5.18: Data fit between the observed and synthetic data on Case 3. The synthetic data is calculated using the initial model (top) and final reconstructed model (bottom). A good data fit is indicated by the pair of black and blue. The presence of red can be associated with a bad data fit.

In terms of the computational time, Case 2 has the highest compared to the other experiments (Table 5.1), but still four times faster than the one used to reconstruct the reference model. From the visual inspection (Fig. 5.17), there is no significant improvement, especially for this seismic section. Nevertheless, we demonstrate that using a single component source improves the model reconstruction.

The **Case 3** has the highest model misfit (Table 5.1). The reconstructed model is the worst compared to the other experiments (Fig. 5.15d). The trick of reducing crosstalk by separating some sources into different simulation seems to reduce the amount of crosstalk in a single section. It is shown in Figure 5.18. The data fit after the inversion seems to degrade compared to the initial model. We hypothesize that due to the lack of redundancy properties given by the first two cases, the inversion is not working as intended. In this case, for each iteration, every single source is only encoded once, whereas, in the first two cases, each source is encoded multiple times according to the total number of simulations. There might be a good exercise to implement an update to the toolbox to performed both partitioned source encoding with a given amount of encoded source redundancy.

The subsampling on sources (**Case 4**) is, by far, provides the best-reconstructed model in terms of the model misfit with a significant reduction of the computational time (Table 5.1). From the reconstructed V_S model (Fig. 5.15e), we can observe a clear reconstruction of both archaeological features.

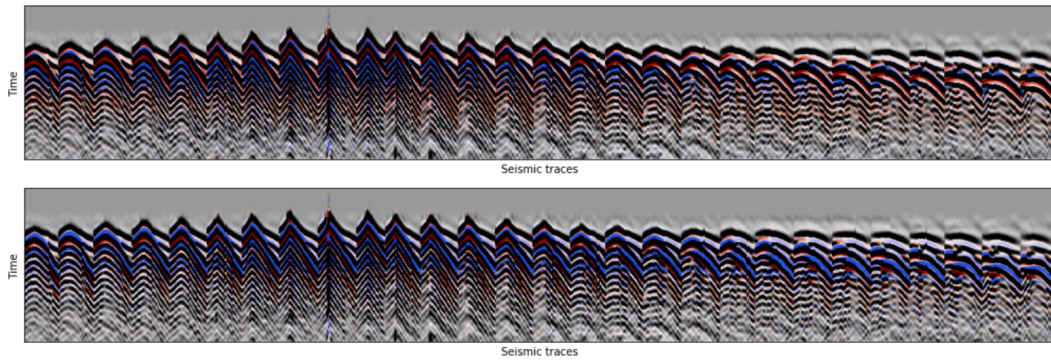


Figure 5.19: Data fit between the observed and synthetic data on Case 4. The synthetic data is calculated using the initial model (top) and final reconstructed model (bottom). A good data fit is indicated by the pair of black and blue. The presence of red can be associated with a bad data fit.

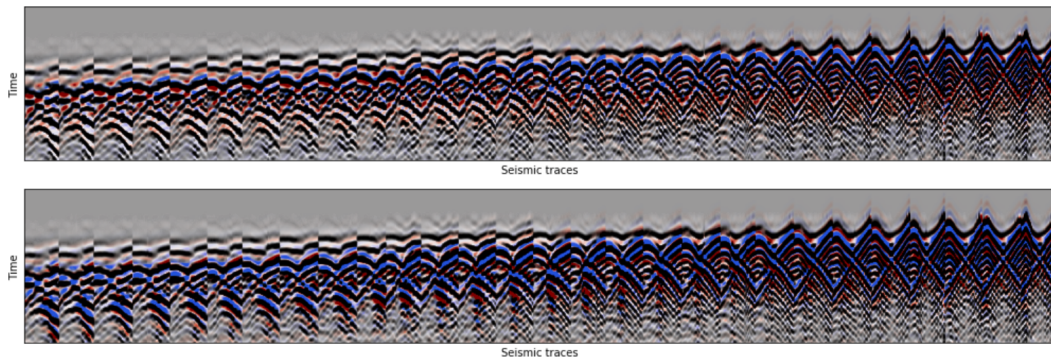


Figure 5.20: Data fit between the observed and synthetic data on Case 5. The synthetic data is calculated using the initial model (top) and final reconstructed model (bottom). A good data fit is indicated by the pair of black and blue. The presence of red can be associated with a bad data fit.

The background velocity model is better estimated than in the first three experiments. Overall, the lateral and vertical model reconstructions also show a good agreement with the reference model. The significant improvement can also be seen in the data fit (Fig. 5.19). The blue-black pair of color is more dominantly presented in the final reconstructed model than the initial model. Having already dense acquisition is an important factor as well. As I have discussed in detail in Chapter 4, we can perform a heavy acquisition decimation and still obtain a reasonably good result. With the subsampling on the source, we can cut down the computational cost while maintaining sufficient accuracy.

The last case (**Case 5**) is the combination of subsampling on sources and source encoding. With only two sources per simulation, in the beginning, I expect benefit coming from both subsampling on sources and source encoding. With a minimal crosstalk source encoding due to the number of sources per simulation, we may consider more sources on each iteration. Despite that, we can limit the maximum number of sources taken into account through subsampling on the source. In practice, even with a minimal source encoding crosstalk, it may degrade the result of the inversion.

The reconstructed V_S model of Case 5 is similar to Case 4, thanks to the subsampling technique (Fig. 5.15f). However, several degradations can also be observed, such as the velocity variation at depth. This degradation is worse when we consider the computational time. Case 5 is 50% more expensive

than Case 4 with worse model misfit (Table 5.1). Even if we can gain a significant improvement in terms of the data fit (Fig 5.20), the increase of the computational cost and model misfit makes this strategy unappealing.

Overall, source encoding strategies fail to produce a satisfactory result for our shallow seismic case, even with several available options in the current toolbox. We hypothesize that these failures are related to the complex waveform shape due to the strong elastic effects. Avoiding multiple sources in a single location and adding more encoded source redundancy improves source encoded inversion quality. However, those strategies still fail to produce satisfactory results in our experiments.

Subsampling on sources, on the other hand, produce reasonable models with a significant cost reduction. Our experiment shows the reduction of computational cost by a factor of 6.75 compared to the reference model with a full acquisition setup. Subsampling on sources is effective due to the dense acquisition. The potential reduction is also shown in the analysis of source and receiver decimation in Chapter 4.

5.4 Conclusions

We illustrate the source subsampling and encoding toolbox's development, which can automatically manage source encoding and subsampling on sources within the FWI framework. The toolbox is independent and can be easily implemented into the modeling and inversion engine. The full Encoding toolbox is integrated into SEM46, whereas the partial encoding toolbox that manages the subsampling on sources is integrated into TOYxDAC. TOYxDAC is an acoustic modeling and inversion engine based on the finite difference method developed by the SEISCOPE consortium.

We observe potential benefits and limitations through five different inversions using source encoding and subsampling on sources techniques. In our shallow seismic experiments, source encoding fails to produce acceptable reconstructed parameters when multiple sources in a single location are taken into account in a single simulation. It also fails when the inversion lacks the encoded source's redundancy. If both factors are honored, we can see that the source encoding strategy yields imperfect reconstructed models but still interpretable. We hypothesize that the source encoding's failures are affected by the complexity of the encoded seismic data. In shallow seismic with a short distance between source and receiver, the data is tightly packed with complex waveform due to the strong elastic effects. On the other hand, the subsampling on sources shows a more promising result in shallow seismic applications. We can reconstruct an acceptable V_S model with a significantly lower computational cost, thanks to the dense acquisition data.

Aside from the Ettlingen Line application, this source encoding and source subsampling toolbox has also been used by other researchers in our group. Pladys et al. (2019) and Pladys et al. (2020) show two FWI applications using optimal transport misfit function for exploration scale. They implemented the partial Encoding toolbox into TOYxDAC (only subsampling on sources is supported in this implementation). With a good misfit function and a proper workflow, they can gain a significant resolution improvement for V_P .

APPENDIX

5.A Computational time tables

This appendix contains more detailed information regarding the computational time required to perform source encoding and subsampling toolbox cases on the 3D 9C Ettlingen Line seismic dataset.

Table 5.2: Computational cost for 3D FWI using full source encoding on all sources (case 1).

No	FWI	N_{iter}	Time/ ∇	Seq. Time	Memory	Storage	N_{CPU}	El. Time	Eq. Time
1	15 Hz V_S	1	1.01	3.04	1373	3255	16	0.19	0.19
2	15 Hz $V_S&V_P$	3	0.96	10.58	1373	3255	16	0.66	0.66
3	25 Hz V_S	5	3.10	18.58	2201	10813	128	0.15	1.16
4	25 Hz $V_S&V_P$	1	3.35	10.04	2201	10813	128	0.08	0.63
5	35 Hz V_S	1	11.84	35.53	4533	67735	192	0.19	2.22
6	35 Hz $V_S&V_P$	2	11.63	46.51	4533	67735	192	0.24	2.91
7	45 Hz V_S	4	70.45	352.27	9166	329148	256	1.38	22.02
8	45 Hz $V_S&V_P$	4	64.39	321.95	9166	329148	256	1.26	20.12

The unit time is in hours. The total sequential CPU time (seq. time) is 798 hours for four frequency bands on Irene KNL HPC (TGCC) to perform an inversion starting from the homogeneous initial model. The memory and storage unit is in Megabytes (MB), and the indicated frequency is the highest frequency band starting from 3 Hz. The elapsed time (el. time) is the time needed to perform the FWI in parallel. Equivalence time (eq. time) is the estimated elapsed time on 16 CPU workstation. The total equivalence time is 50 hours (2.1 days).

Table 5.3: Computational cost for 3D FWI using source encoding on all V direction sources (case 2).

No	FWI	N_{iter}	Time/ ∇	Seq. Time	Memory	Storage	N_{CPU}	El. Time	Eq. Time
1	15 Hz V_S	1	0.98	2.94	1246	3255	16	0.18	0.18
2	15 Hz $V_S&V_P$	1	1.08	4.32	1246	3255	16	0.27	0.27
3	25 Hz V_S	1	15.65	46.96	4804	93648	128	0.37	2.93
4	25 Hz $V_S&V_P$	1	16.78	50.33	4804	93648	128	0.39	3.15
5	35 Hz V_S	1	19.07	57.22	4856	99277	192	0.30	3.58
6	35 Hz $V_S&V_P$	1	18.22	54.65	4856	99277	192	0.28	3.42
7	45 Hz V_S	20	47.80	1481.72	7458	287219	256	5.79	92.61
8	45 Hz $V_S&V_P$	25	44.25	1504.53	7458	287219	256	5.88	94.03

The unit time is in hours. The total sequential CPU time (seq. time) is 3202 hours for four frequency bands on Irene KNL HPC (TGCC) to perform an inversion starting from the homogeneous initial model. The memory and storage unit is in Megabytes (MB), and the indicated frequency is the highest frequency band starting from 3 Hz. The elapsed time (el. time) is the time needed to perform the FWI in parallel. Equivalence time (eq. time) is the estimated elapsed time on 16 CPU workstation. The total equivalence time is 200 hours (8.3 days).

Table 5.4: Computational cost for 3D FWI using partitioned source encoding (case 3).

No	FWI	N_{iter}	Time/ ∇	Seq. Time	Memory	Storage	N_{CPU}	El. Time	Eq. Time
1	15 Hz V_S	1	1.07	3.21	1246	3255	16	0.20	0.20
2	15 Hz $V_S \& V_P$	2	1.01	5.04	1246	3255	16	0.32	0.32
3	25 Hz V_S	6	8.79	87.90	3306	41145	128	0.69	5.49
4	25 Hz $V_S \& V_P$	1	8.48	25.44	3306	41145	128	0.20	1.59
5	35 Hz V_S	3	30.96	123.86	5903	164167	192	0.65	7.74
6	35 Hz $V_S \& V_P$	3	24.35	97.39	5903	164167	192	0.51	6.09
7	45 Hz V_S	1	236.68	710.03	18115	2203480	256	2.77	44.38
8	45 Hz $V_S \& V_P$	4	238.26	1429.57	18115	2203480	256	5.58	89.35

The unit time is in hours. The total sequential CPU time (seq. time) is 2482 hours for four frequency bands on Irene KNL HPC (TGCC) to perform an inversion starting from the homogeneous initial model. The memory and storage unit is in Megabytes (MB), and the indicated frequency is the highest frequency band starting from 3 Hz. The elapsed time (el. time) is the time needed to perform the FWI in parallel. Equivalence time (eq. time) is the estimated elapsed time on 16 CPU workstation. The total equivalence time is 155 hours (6.5 days).

Table 5.5: Computational cost for 3D FWI using partitioned subsampling on sources (case 4).

No	FWI	N_{iter}	Time/ ∇	Seq. Time	Memory	Storage	N_{CPU}	El. Time	Eq. Time
1	15 Hz V_S	1	0.97	2.91	1373	3255	16	0.18	0.18
2	15 Hz $V_S \& V_P$	3	0.99	10.87	1373	3255	16	0.68	0.68
3	25 Hz V_S	3	2.65	13.23	2134	10083	128	0.10	0.83
4	25 Hz $V_S \& V_P$	2	2.84	11.35	2134	10083	128	0.09	0.71
5	35 Hz V_S	6	6.31	44.19	3428	32878	192	0.23	2.76
6	35 Hz $V_S \& V_P$	6	6.51	208.24	3428	32878	192	1.08	13.01
7	45 Hz V_S	6	28.64	801.79	5905	128432	256	3.13	50.11
8	45 Hz $V_S \& V_P$	7	29.96	868.93	5905	128432	256	3.39	54.31

The unit time is in hours. The total sequential CPU time (seq. time) is 1961 hours for four frequency bands on Irene KNL HPC (TGCC) to perform an inversion starting from the homogeneous initial model. The memory and storage unit is in Megabytes (MB), and the indicated frequency is the highest frequency band starting from 3 Hz. The elapsed time (el. time) is the time needed to perform the FWI in parallel. Equivalence time (eq. time) is the estimated elapsed time on 16 CPU workstation. The total equivalence time is 123 hours (5.1 days).

Table 5.6: Computational cost for 3D FWI using partitioned source encoding and subsampling on sources (case 5).

No	FWI	N_{iter}	Time/ ∇	Seq. Time	Memory	Storage	N_{CPU}	El. Time	Eq. Time
1	15 Hz V_S	1	1.02	3.05	1246	3255	16	0.19	0.19
2	15 Hz $V_S \& V_P$	1	1.10	3.30	1246	3255	16	0.21	0.21
3	25 Hz V_S	11	2.30	39.06	1789	7998	128	0.31	2.44
4	25 Hz $V_S \& V_P$	1	2.72	8.16	1789	7998	128	0.06	0.51
5	35 Hz V_S	4	9.31	46.57	3471	45132	192	0.24	2.91
6	35 Hz $V_S \& V_P$	40	9.98	558.92	3471	45132	192	2.91	34.93
7	45 Hz V_S	16	42.83	1242.04	7417	282487	256	4.85	77.63
8	45 Hz $V_S \& V_P$	18	42.05	1051.24	7417	282487	256	4.11	65.70

The unit time is in hours. The total sequential CPU time (seq. time) is 2952 hours for four frequency bands on Irene KNL HPC (TGCC) to perform an inversion starting from the homogeneous initial model. The memory and storage unit is in Megabytes (MB), and the indicated frequency is the highest frequency band starting from 3 Hz. The elapsed time (el. time) is the time needed to perform the FWI in parallel. Equivalence time (eq. time) is the estimated elapsed time on 16 CPU workstation. The total equivalence time is 184 hours (7.6 days).

Conclusions and prospects

Conclusions

This manuscript aims to tackle specific challenges of 3D multicomponent elastic multiparameter FWI in a particular shallow seismic experiment. At the beginning of the manuscript, we introduce the wave propagation inside two different rheologies (elastic and viscoelastic), the numerical method to discretize and perform wave modeling, and the numerical optimization to perform an iterative inversion. In chapter 2, I review the main field object of this manuscript, the Ettlingen Line. I discuss the history of the Ettlingen Line and previous experiments that have been performed in the area. I also discuss our 3D dense seismic acquisition alongside the small preprocessing step required before the inversion. The application of 3D 9C multiparameter FWI using the viscoelastic medium is described in Chapter 3. In this chapter, we are able to propose a consistent workflow to obtain V_P and V_S models and able to reconstruct the subsurface model of The Ettlingen Line alongside the other trench-like structure. The effect of multicomponent data in FWI is later discussed in Chapter 4, where I perform a sensitivity kernel analysis, inversions with various component combination, and acquisition decimations. The last chapter, Chapter 5, discussed another experiment and implementation that has been done during my study. Notably, the implementation of the source subsampling and encoding toolbox.

Throughout this study, several important remarks are interesting to be discussed in-depth:

- **Feasibility of performing 3D 9C dense seismic acquisition**

Performing 3D multicomponent dense seismic acquisition is an exhaustive experiment. One needs to prepare many resources, mainly in terms of the source's type and the receiver's number. The Prismatic and Galperin source allows us to perform shallow seismic multicomponent seismic acquisition more efficient with high repeatability. In this manuscript, I also illustrate that we can perform a relatively dense acquisition with the limited equipment, thanks to the matching filters. However, the utilization of matching filters still requires another dataset. This dataset needs to be acquired on the full acquisition area and treated as the reference data. We also have to be aware that, in some noisy data, the matching filter may end up enhancing the noise instead of the signal, which leads to an unphysical result.

- **3D multiparameter FWI in shallow seismic scale**

Strong elastic effects dominate shallow seismic data in the form of surface waves. With the short distance between the source and receiver, the body waves are difficult to be separated from the surface waves. In this manuscript, I show a strategy to perform a multiparameter inversion, starting from simple models. Our approach relies on a multi-scale strategy with two successive inversions on each scale. The first inversion is a hard-constrained V_P with respect to V_S with a

linear relationship leading to a constant Poisson's ratio ν throughout the first inversion. With a hard-constrained V_P , we are able to start the inversion from a simple initial model while keeping the V_P and V_S value within a reasonable physical limit, constrained by a constant Poisson's ratio. The second inversion is a multiparameter inversion for both V_P and V_S with an additional constraint of Poisson's ratio. In this inversion, the Poisson's ratio may not exceed a designated limit. With this inversion, we will have the update of both parameters. The updated model has an updated Poisson's ratio, which can be used by the next scale's (higher frequency) inversion.

We illustrate several FWI applications for the Ettligen Line data up to 65 Hz. The first batch of the inversion is two 3D 9C inversions using two different initial models, homogeneous and MASW models. We show that using our workflow, we can obtain a very similar reconstructed V_P and V_S . This demonstration is essential for future near-surface FWI studies as it may simplify the procedure to build the initial model. The second batch of the inversion is related to the rheology choice (viscoelastic or elastic). We test 3D 9C inversions using both elastic and viscoelastic medium. Our results show that the inversion using an elastic medium is still acceptable at the lower frequency band in terms of the model reconstruction since the attenuation effect is not as significant as the higher frequency. Performing inversion using an elastic approach might also decrease the computational time. In our case, both results are comparable up to 45 Hz, with a 30% computational time decrease if we consider an elastic medium.

Aside from the technical point of view, through these inversions, we are able to perform a 3D high-resolution reconstruction of the Ettligen Line. All four experiments using different initial models and rheologies successfully reconstruct the geometry of the target. Based on these reconstructed models, the Ettligen Line has an approximate width of 5 meters and a depth of around 2 meters. We are also able to reconstruct another trench-like structure, which was not detected previously. This new structure has 3 meters in width and 1.5 meters in depth. We gain an additional resolution benefit; therefore, the archaeologist might have additional information to investigate this historic structure further.

- **Impact of multicomponent data towards FWI**

The increase of affordability to perform a dense multicomponent seismic acquisition drives us to study the effect of multicomponent data on the FWI. The aim is to understand better and efficiently perform future multicomponent seismic data acquisition, which is suitable for FWI.

The sensitivity kernel analysis of 9C synthetic seismic data on each component demonstrates several interesting observations. Each component yields a unique sensitivity kernel, leading to complementary information if more components are used during the inversion. The strong amplitude of the surface wave in the seismogram is reflected in the sensitivity kernel. Our experiment shows a massive amplitude difference between the sensitivity kernel from the body wave and the surface wave to three orders of magnitude.

In the second experiment, we perform multiple inversions with various component combinations. The result shows that multicomponent data (3C and 9C) has a comparable reconstructed model at shallow depth, shown by synthetic and field data, but not at a deeper part of the model. The depth reconstruction is more related to the horizontal component's presence instead of the receiver's component. The depth resolution increase can be linked with the additional information from the Love wave and the Rayleigh wave's radial component.

The acquisition's decimation in the third experiment shows that 9C seismic data can still produce a relatively good result with heavy source and receiver decimation, while 1C and 3C data fail to

produce satisfactory results. This experiment demonstrates that 9C FWI with heavily decimated data can produce a comparable result with the 1C using a full dense acquisition recorded using the vertical component. Based on these experiments, performing a coarse grid acquisition while having multicomponent data might be more favorable than a dense 1C seismic acquisition.

- **Reducing computational cost through subsampling on sources**

Using the source subsampling and encoding toolbox, we are able to perform several multiparameter FWI experiments based on viscoelastic medium. Source encoding fails to produce a meaningful result. A heavy source's crosstalk causes this failure in shallow seismic scale in complex waveforms. In our case, complex waveforms are mainly dominated by surface waves. Source subsampling, on the other hand, yields a promising result. It has a relatively good lateral and vertical model reconstruction with a significant decrease of computational cost (~ 6.75 times compared to the full acquisition).

Prospects

Throughout this manuscript, we have presented a detailed FWI study in a particular shallow seismic target. With this result, we can still see several potential prospects.

FWI parameterization. In the context of this PhD thesis, we only choose two reconstructed parameters, V_P , and V_S . The density, Q_P , and Q_S are not reconstructed. Those three parameters might bring important information regarding the soil and rock properties. Knowing that the medium in our experiment possibly consists of soil and rock, we may expect a strong density and quality factor contrast between the soil and the rock.

In acoustic data, density is more difficult to reconstruct in short offset due to the similarity of the radiation pattern with V_P (Forgues and Lambaré, 1997; Virieux and Operto, 2009). Despite that, Przebindowska et al. (2012) and Bai and Yingst (2014) show that an accurate density model might improve the overall reconstruction of V_P in the acoustic case. As an alternative, applying a hard constrained density with respect to the V_P or V_S during the inversion could be the way to update the density passively. We could follow the empirical relationship similar to Gardner et al. (1974) or Lindseth (1979), in order to estimate the density from V_P or V_S (Miller and Stewart, 1991; Potter et al., 1998).

In our experiment, the attenuation model is obtained from an independent experiment (Gao et al., 2020). Following Virieux and Operto (2009), an accurate velocity model is suggested prior to the further inversion of the attenuation model. Accurate velocity models are required before reconstructing Q_P and Q_S in order to discriminate between the intrinsic and extrinsic attenuation.

Misfit selection. In this experiment, we only consider the standard least-square misfit function. We show that using the least-square misfit function, we are already able to produce a meaningful result. However, several other misfit functions exist, which might be suitable for a near-surface scale.

Frequency-dependent difference in phase traveltimes (Tape, 2009) is one alternative of misfit function. In one application, Lu et al. (2020) shows that this misfit function is also suitable for reconstructing surface wave features extracted from the ambient noise tomography. This misfit function focuses on the phase information without the bias from the amplitude. Despite the successful examples in the ambient noise data, there is a question of whether this misfit function is beneficial to the surface wave data. In the exploration scale, He et al. (2019b) also shows an interesting example of the optimal transport misfit function usage. They can interpret both body wave and surface wave in onshore data application, based

on an elastic VTI media. Even if the optimal transport strategy's initial focus is to minimize the cycle skip problem, it has an intrinsic behavior that might be suitable for near-surface scale. Optimal transport allows the balance between low energy (body wave) and high energy (surface wave) information in the seismic data. Therefore, the application of optimal transport has the potential to improve the result, especially in terms of V_P .

Exploiting high-frequency content. In this manuscript, we only perform inversion up to 65 Hz for the first batch of inversions (Chapter 3) and 45 Hz for the component analysis (Chapter 4). From the signal to noise ratio (SNR) calculation in Figure 3.5, we observe a relatively high usable frequency with high SNR up to 145 Hz. However, in our viscoelastic inversion, there is no significant update beyond 65 Hz. This observation raises the question of whether high-frequency data is accessible. Do we need an even denser seismic acquisition in order to utilize the higher frequency fully? Or do we need more accurate parameters (density, Q_P , Q_S)?

Acquisition strategy. Our seismic experiment focuses on the 3D dense acquisition using a multicomponent source and receiver. This manuscript shows that considering a heterogeneous seismic acquisition is possible and applicable as long as we have a reference acquisition. The data correction can be performed using matching filters, as presented in Chapter 2. Therefore, in order to improve the inversion results, we might be able to perform multiple seismic acquisitions in the form of a 2D and 3D acquisition grid. The 3D acquisition can be located in the target location, whereas the 2D seismic lines can be performed with a longer offset. The longer offset in those 2D seismic lines might improve the model reconstruction, especially at depth. The result of the analysis of multicomponent also encourages the future near-surface acquisition to take benefit of multicomponent source and receiver. By doing so, we might be able to perform a coarser but bigger 3D acquisition grid.

List of Figures

1	The simplified illustration of the 3D internal structure of the Earth as a layered model (a). The simplified 2D section structure of the Earth and the examples of the body wave's seismic phases (b). The names of the raypath is given by the wave type, the propagated layer, and the interaction with the discontinuities (Stein and Wysession, 2003).	2
2	Example on an earthquake recorded using a multicomponent seismometer (Lee et al., 2002). The horizontal component is rotated to the longitudinal and transverse direction with respect to the earthquake. Red arrows indicate the first arrival of the P-wave. Blue arrows indicate the first arrival of S-wave. Cyan blocks represent the surface waves. Green blocks represent the windows data for full waveform inversion (FWI). Note that in FWI, all parts of the dataset are taken into account.	2
3	Particle motion of P-wave (a), S_V -wave (b), Rayleigh wave (c), and Love Wave (d). The direction of the propagation is from the left to the right of the model. The S-wave is consist of two different polarizations S_V and S_H -waves. In this illustration, only S_V -wave is given. After Everett (2013).	3
4	Example of 3D acoustic FWI from (Operto et al., 2015). Top figures represent the initial V_P models from the reflection tomography, bottom figures represent the final reconstructed V_P models using FWI. Left and right figures represent the horizontal sections at 150 m and 1050 m depth, respectively.	4
5	Example of global FWI showing the vertically polarized V_S perturbations in the initial mantle model S362ANI (left) and the reconstructed model using FWI - GLAD-M15 (right) at 250 km depth. Notable slabs and hotspots enhanced in the reconstructed model are marked. This image is taken from Bozdağ et al. (2016).	5
6	2D FWI in shallow seismic experiment (Köhn et al., 2018).	7
7	The replica of Zhang Heng seismoscope featured in Chabot Space and Science center in Oakland, California (Wikipedia contributors, 2020b).	8
8	A sample of hydrophone, a pressure sensitive seismic recorder device. It is usually used in marine environment (Wikipedia contributors, 2020a).	8
9	Ocean bottom cable (OBC), courtesy of Magseis (Duey, 2017) (a). 1C (b), and 3C geophone made by SENSOR Netherland (c) (GFZ, 2020).	9
10	Example of three orthogonal vector sources which can produce 9C seismic data when recorded using 3C receivers (Hardage et al., 2011).	10

LIST OF FIGURES

1.1	The physical model Ω in Cartesian coordinate is divided into a set of tensorial element $\Omega_e (e = 1, \dots, 4)$ (a). Example of GLL points in 2D element with interpolation order $N = 4$ (b).	20
1.2	Sufficient decrease condition (a) and the curvature condition (b). Two condition for satisfying the Wolfe condition. The picture is adapted from Nocedal and Wright (2006).	29
1.3	The logo of SEM46 (Brossier and Trinh, 2017).	31
2.1	The original shape of the trench (a), the shape of the existing trench (b), and the current shape of the buried trench (c) redrawn from Lang et al. (1907). The trench's existing shape is smoother due to erosion, and the wooden palisade wall also does not exist anymore. Our target is the buried trench (c) in which I do not know any more the boundary and the geometry of the original trench.	35
2.2	Photo of the information panel of the Ettlingen Line showing the old map between the period of winter 1707 to 1708 (a). Modern map of Karlsruhe and Ettlingen taken from Google Maps in October 2020 (b). The red circle indicates the preserved area of the trench and the approximate location of the field experiment. At the time of the Ettlingen Line's construction, the city of Karlsruhe has not been founded.	36
2.3	Basemap of the acquisition at Rheinstetten (a). Red solid line represents the existing location of the trench, red dashed line represents the possible buried location of the trench line, and the white rectangle represents seismic acquisition location. The existing V-shaped trench of the Ettlingen Line at the south-east of the study area (b). Blue circle in (a) represents the approximate location of the photo, whereas its translucent cone depicts the estimated field of view of the photo in (b).	37
2.4	Basemap of the acquisition at the Ettlingen Line, Rheinstetten from the previous geophysical experiments. The Red dashed line represents the possible buried location of the trench line. The white rectangle represents seismic acquisition location on Pan et al. (2018) and the study on this PhD thesis. The blue line represents the approximate location of the seismic line in Binnig (2015). The Green rectangle represents the approximate location of the GPR survey in Wegscheider (2017). The purple line depicts the seismic acquisition line in Wittkamp et al. (2018).	39
2.5	Reconstructed V_S on seismic profile 1 (a) and 2 (b) taken from Binnig (2015). The location of each profile can be seen on Figure. 2.4. The vertical lines on each subfigure correspond to the depth profile with the same color. The black dashed lines at the edge of the model are the perfectly matched layer (PML).	39
2.6	Reconstructed V_S overlaid with the GPR section on profile 3 taken from Wittkamp et al. (2018). The GPR experiment was performed by Wegscheider (2017).	39
2.7	3D reconstructed V_S from MASW data processing by Pan et al. (2018). The Ettlingen Line is indicated by a low velocity zone.	40
2.8	The Galperin source used in 9C seismic acquisition (a), and its schematic explaining the three principal orthogonal direction of the source (b) (Häusler et al., 2018).	41
2.9	The Galperin source used in 9C seismic acquisition (a), and its schematic explaining the three principal orthogonal direction of the source (b) (Häusler et al., 2018).	43
2.10	Seismic data acquisition at the Ettlingen Line field. The figure shows the Galperin source is hit by the sledgehammer.	43

2.11 Coarse grid acquisition (a) and dense grid acquisition (b). Triangles represent receiver’s locations, whereas circles represent source’s locations. Different receiver’s color shows different acquisition time; 1st day = blue, 2nd day = orange, 3rd day = green, 4th day = red, 5th day = purple and brown. 44

2.12 Signal (orange) and noise (blue) spectrum together with its standard deviation of Ettlingen Line 9C seismic data (a). SNR_{dB} of the seismic data (b). The good signal ($SNR_{dB} > 27$) ranging from 15 Hz (green line) to 145 Hz (red line). I started our FWI from 3 Hz (orange line) based on the strong coherent signal. They grey hatches represents unreliable SNR estimation. 45

2.13 Seismic data before data correction (a) shows travel time shift between acquisition’s subsets, and after data correction (b) where the data is more consistent. 46

2.14 Seismic data before data correction (a), and after data correction (b). This seismic line is taken from the first crossline on the first source location on UZ component. Red vertical lines represent acquisition subset separation. Consistency improvements can be seen on the corrected data. 46

3.1 Basemap of the acquisition at Rheinstetten. Red solid line represents the existing location of the trench, red dashed line represents the possible buried location of the trench line, and the white rectangle represents seismic acquisition location. 55

3.2 The original shape of the trench (a), the current shape of trench (b), and the current shape of buried trench (c) redrawn from Lang et al. (1907). In general, the current shape is smoother due to erosion. The wood palisade wall also do not exist anymore. Our target is the buried trench in which we do not know anymore the boundary and the geometry of the original trench. 56

3.3 The Galperin source used in 9C seismic acquisition (a), and its schematic explaining the three principal orthogonal direction of the source (b) (Häusler et al., 2018). 56

3.4 Coarse grid acquisition (a) and dense grid acquisition (b). Triangles represent receiver’s locations, whereas circles represent source’s locations. Different receiver’s color shows different acquisition time; 1st day = blue, 2nd day = orange, 3rd day = green, 4th day = red, 5th day = purple and brown. 58

3.5 Signal (orange) and noise (blue) spectrum together with its standard deviation of Ettlingen Line 9C seismic data (a). SNR_{dB} of the seismic data (b). The good signal ($SNR_{dB} > 27$) ranging from 15 Hz (green line) to 145 Hz (red line). We started our FWI from 3 Hz (orange line) based on the strong coherent signal. They grey hatches represents unreliable SNR estimation. 59

3.6 Seismic data before data correction (a) shows travel time shift between acquisition’s subsets, and after data correction (b) where the data is more consistent. 59

3.7 Seismic data before data correction (a), and after data correction (b). This seismic line is taken from the first crossline on the first source location on UZ component. Red vertical lines represent acquisition subset separation. Consistency improvements can be seen on the corrected data. 59

3.8 Seismic section on the first source location with U source direction. This seismic section is used to estimate the V_P for the homogeneous initial model. Red dashed line represents the direct P-wave arrival from the estimated homogeneous model. 66

LIST OF FIGURES

3.9 The proposed FWI Workflow for shallow-seismic application. We test this workflow with 9C data on Ettlingen Line case. 68

3.10 Reconstructed parameters (V_S at the top row, V_P at the middle row, and ν at the bottom row) at 1 m depth section. Each column is associated with a specific FWI stage (initial model on the 1st column, 3-25 Hz band on the 2nd column, 3-45 Hz band on the 3rd column, 3-65 Hz band on the 4th column). 69

3.11 A horizontal slice of reconstructed V_S (left) and Poisson’s ratio ν (right) at 1 m depth shows clear presence of the Ettlingen Line trench as well as a trench-like structure with north-south direction (top). Vertical slice of reconstructed V_S perpendicular (middle) and parallel (bottom) with the direction of Ettlingen Line. 70

3.12 First V_S gradient at 3-25 Hz frequency band. The top figure represents a horizontal slice at 2m depth, the middle figure represents a vertical crossline section AB , and the bottom figure represents a vertical inline section CD . Cyan rectangles on each figure depict the positive value which correspond with the presence of the low velocity anomaly of the Ettlingen Line. 71

3.13 Comparison between 9C observed data (grey) and 9C calculated data (red) in (a) the initial model (b) the reconstructed model. A trace by trace normalization is used to plot the data. The larger overlap between red and grey in the final model shows a better data match. 71

3.14 Vertical section of 3D GPR and 2D elastic joint inversion of Love and Rayleigh wave result taken from Wegscheider (2017) and Wittkamp et al. (2018) (a), 3D MASW by Pan et al. (2018) (c), and 3D elastic FWI starting from homogeneous model (c). The color-scale on (a) is unscaled, blue means lower velocity and yellow means higher velocity. 73

3.15 3D V_S from previous MASW study by Pan et al. (2018) (left) and this study starting from homogeneous initial model (right). Red line represents the location of the GPR line on Figure 3.14. 74

3.16 Horizontal slice of the inversion result at 1 m depth for both V_P (top row) and V_S (bottom row) use different initial models. Left slices represent final velocity model at 65 Hz starting from homogeneous model; whereas right slices represent final velocity model at 65 Hz starting from MASW V_S model. 75

3.17 Normalized amplitude of P-wave with respect to the offset drawn as the scatter plot on a narrow bandpassed data centered at 65 Hz. The line plots represents theoretical amplitude decay given a constant Q_P model based on Kjartansson (1979) at 65 Hz. A geometrical spreading correction is applied prior to normalization. 76

3.18 Horizontal slice of V_S from the FWI at 1 m depth for FWI with elastic medium (left column) and viscoelastic medium (right column). Top row images are the reconstructed V_S at 65 Hz, whereas 45 Hz for the bottom row images. 77

3.19 Horizontal slice of V_P from the FWI at 1 m depth for FWI with elastic medium (left column) and viscoelastic medium (right column). Top row images are the reconstructed V_P at 65 Hz, whereas 45 Hz for the bottom row images. 78

3.20 Relative amplitude decay on elastic and viscoelastic synthetic data compared with the observed data. The trace is normalized based on the maximum absolute amplitude of the longest offset data. The seismograms with the amplitude which overlapped with the neighboring seismogram are clipped. 78

4.1 The synthetic 1D gradient model. The star symbol represents the source’s location, whereas the inverted triangle represents the receiver’s location. The dimension of the model is in meter. 93

4.2 ZZ component of a synthetic data set on the Model I. The source-receiver pair with an offset of 25 m (represented by the grey dashed line) is used for the sensitivity kernel calculation. Each event window is denoted using a different color (blue for P wave, green for S wave, and red for the surface wave). 94

4.3 The synthetic 2D gradient model. The star symbol represents the source’s location, whereas the inverted triangle represents the receiver’s location. The dimension of the model is in meter. 94

4.4 ZZ component of a synthetic data set on the Model II. The source-receiver pair with an offset of 25 m (represented by the grey dashed line) is used for the sensitivity kernel calculation. The P wave window is denoted by the blue line, whereas the S wave and surface wave are inseparable and denoted using the red line. 95

4.5 Vertical sections of the sensitivity kernel computed with Model I for P-wave window. The columns represent the receiver’s components, the rows represent the source’s components. 96

4.6 Vertical sections of the sensitivity kernel computed with Model I for S-wave window. 96

4.7 Vertical sections of the sensitivity kernel computed with Model I for surface wave window. 97

4.8 Horizontal sections of the sensitivity kernel computed with Model II for P-wave window. 97

4.9 Vertical sections of the sensitivity kernel computed with Model II for P-wave window. 98

4.10 Basemap of the seismic data acquisition at Rheinstetten, Germany. The solid red line represents the existing trench line. The dashed red line represents the buried trench. A white box draws the area of the seismic acquisition. 99

4.11 Layout of the acquisition grid for both synthetic and field experiments. The total number of receiver is 888 (triangles), the total number of source’s location is 36 (circles). Solid and dashed red lines represent the parallel and perpendicular sections used in the following figures, respectively. The color of the receivers represents the acquisition subset, only for the field experiment. 100

4.12 Example of FWI result between the elastic and viscoelastic medium. Horizontal slice of V_S from the FWI at 1 m depth for FWI with elastic medium (a and c) and viscoelastic medium (b and d). Top row images are the reconstructed V_S at 65 Hz (a and b), whereas 45 Hz for the bottom row images (c and d). 101

4.13 FWI workflow for shallow seismic application. 102

4.14 The Galperin source used in 9C seismic acquisition. 103

LIST OF FIGURES

4.15 V_S model obtained using FWI starting from homogeneous initial model (left) and MASW initial model (right). The first row is the horizontal section at 1.5 m depth, the second row and the third row are the vertical section perpendicular and parallel with the Ettlingen Line, respectively. 105

4.16 The average difference (blue line) and its standard deviation (light blue area) between two reference models in the field experiment. 105

4.17 Synthetic data calculated using true velocity model on synthetic experiment. The source is located at position $x = 0$ m, and $y = 16$ m, and the receiver is located on inline direction at $y = 16$ m. Three subfigures represent different receiver's component, whereas the color on each figure represents source's component. Grey, red, and green seismograms are calculated using Z, X, and Y direction source, respectively. 106

4.18 Reconstructed V_S from 16 inversions with various component combinations on the synthetic test. The top figure (a) represents horizontal slice at 1.5 m, middle (b) and bottom right (c) figures represent the vertical slice perpendicular and parallel to the Ettlingen Line (EL), respectively. For each figure block, there are 16 different inversions, the rows represent the Galperin source's component, whereas the columns represent the receiver's component. 107

4.19 Weighted least-squares V_S model misfit for 9C and 3C FWI, and 1C FWI with respect to the reference model for the synthetic case. The behavior is similar compare to the field data, using horizontal component yield lower model misfit. 108

4.20 Color representation of the absolute misfit (a) and grade of component misfit (b) from all sources on the field data application. Bar plot of the absolute data misfit on 9C FWI (c). 109

4.21 Reconstructed V_S from 16 inversions with various component combinations on field data application. The top figure (a) represents horizontal slice at 1.5 m, middle (b) and bottom right (c) figures represent the vertical slice perpendicular and parallel to the Ettlingen Line (EL), respectively. For each figure block, there are 16 different inversions, the rows represent the Galperin source's component, whereas the columns represent the receiver's component. 110

4.22 Weighted least-squares V_S model misfit for 9C and 3C FWI, and 1C FWI to the reference model for the field data application. Model misfits that consider the horizontal component receiver give significantly lower model misfit than the vertical one. Inversions using 1C source and 3C receiver give relatively similar misfits, whereas inversions using 3C source and 1C receiver give lower misfits on the horizontal component receiver. The vertical only receiver (Z_{REC}) has a higher misfit than the other 3C FWI, but it has a significantly lower misfit than 1C FWI using the vertical component. 111

4.23 Color representation of the absolute misfit (a) and grade of component misfit (b) from all sources on the field data application. Each figure consists of 16 independent inversions with a different component combination. For each inversion, we have a 3 by 3 matrix, and the colors represent the misfit for each component (the rows are the sources' component, whereas the columns are the receivers' component.), the black rectangles represent the component combination which is used during the inversion. The absolute misfit matrix (a) represents the true calculated misfit value. Higher grade (b) means better data misfit compared to the same component on different inversion. 113

4.24 Source and receiver decimation of the Ettlingen Line field dataset. We decimate the source and receiver while keep the aperture of the acquisition to remain almost the same. N_{REC} and N_{SRC} represent the total number of sources and receivers, respectively. The notation below the N_{REC} is the decimated inline and crossline grid. Orange circles represent the source's location, whereas the blue triangles represent the receiver's location. 115

4.25 Horizontal section of the reconstructed V_S from all combination of source and receiver decimation at 1.5 m depth. 116

4.26 Vertical sections of the reconstructed V_S from all combination of source and receiver decimation. These sections are located at $x = 15$ m in crossline direction. 117

4.27 Model misfit from the decimated source and receiver setup. Each color represents the model misfit for each inversion, with blue means the lowest and red is the highest model misfit. 118

4.28 Absolute data misfit of all components and experiments from the decimated source and receiver setup. The color is scaled globally. The lowest absolute misfit is represented as blue and the highest is represented as red. 119

4.29 The total absolute data misfit on each inversion from the decimated source and receiver setup. The color is scaled globally. The lowest absolute misfit is represented as blue and the highest is represented as red. 120

4.30 The reconstructed V_S on UZ FWI using the full acquisition setup (a). The reconstructed V_S on 9C FWI using 5 sources and 42 receivers (b). Top figures are the horizontal slices at 1.5 m depth. Bottom figures are the inline vertical slices at $x = 15$ m. 120

5.1 Illustration of random (first row), and cyclic subsampling on sources (second row). Filled circles are the selected sources. 127

5.2 Illustration of the source encoding without (a) and with source partition (b). Each circle represents a single source and each rectangle represents each processors. In this illustration, we assume that there is no domain decomposition (each CPU perform a single simulation). The lines with the same colors depicts the relation between the source and the simulation. 129

5.3 A guide to understand the selected source map plot. This plot is the representation of the selected source for source encoding and subsampling on sources. Each circle represents a single source location and direction. Filled circles depict the selected sources, whereas blank circles represent discarded sources. Each line represents the source directions (a). Black arrows in (b) show an example of sources taken into account in a single simulation. The same color indicates a common source in a single simulation. 132

5.4 Normal synthetic seismic section without source encoding and subsampling on sources. The figure indicates the first source location recorded in z -direction. The location of the source is coincide with first seismic trace. 132

5.5 Selected sources of the full source encoding for all frequency bands on case 1. 132

5.6 Synthetic encoded seismic section on all 108 sources calculated on a single wave propagation's simulation (case 1). 133

5.7 Selected sources of the full source encoding for all frequency bands on case 2. Note that only sources with V direction are selected. 133

LIST OF FIGURES

5.8 Synthetic encoded seismic section on 36 sources with V direction calculated on a single simulation (case 2). 134

5.9 Selected sources of the partitioned source encoding for 3 - 15 Hz (a), 3 - 25 Hz (b), 3 - 35 Hz (c), and 3 - 45 Hz (d) frequency band on case 3. Each frequency band might have multiple re-encoding, depicted by multiple set of plots. 134

5.10 Synthetic encoded seismic section on 7 sources calculated on a single simulation (case 3). The selected sources is determined using sequential partition. 134

5.11 Selected sources of the full subsampling on sources for 3 - 15 Hz (a), 3 - 25 Hz (b), 3 - 35 Hz (c), and 3 - 45 Hz (d) frequency band on case 4. Each frequency band might have multiple re-encoding, depicted by multiple set of plots. 134

5.12 Subsampled seismic section on a single simulation (case 4). There is only one selected source for each simulation. 135

5.13 Selected sources of the full source encoding for 3 - 15 Hz (a), 3 - 25 Hz (b), and 3 - 35 Hz (c) frequency band on case 5. Each frequency band might have multiple re-encoding, depicted by multiple set of plots. 135

5.14 Subsampled and encoded seismic section on a single simulation (case 5). There are two selected sources for each simulation. 135

5.15 Reconstructed V_S models which are obtained using standard FWI on a full acquisition setup (a), full source encoding (b), source encoding on SRC_V (c), partitioned source encoding (d), subsampling on sources (e), and source encoding + subsampling on sources (f). 136

5.16 Data fit between the observed and synthetic data on Case 1. The synthetic data is calculated using the initial model (top) and final reconstructed model (bottom). A good data fit is indicated by the pair of black and blue. The presence of red can be associated with a bad data fit. 137

5.17 Data fit between the observed and synthetic data on Case 2. The synthetic data is calculated using the initial model (top) and final reconstructed model (bottom). A good data fit is indicated by the pair of black and blue. The presence of red can be associated with a bad data fit. 138

5.18 Data fit between the observed and synthetic data on Case 3. The synthetic data is calculated using the initial model (top) and final reconstructed model (bottom). A good data fit is indicated by the pair of black and blue. The presence of red can be associated with a bad data fit. 138

5.19 Data fit between the observed and synthetic data on Case 4. The synthetic data is calculated using the initial model (top) and final reconstructed model (bottom). A good data fit is indicated by the pair of black and blue. The presence of red can be associated with a bad data fit. 139

5.20 Data fit between the observed and synthetic data on Case 5. The synthetic data is calculated using the initial model (top) and final reconstructed model (bottom). A good data fit is indicated by the pair of black and blue. The presence of red can be associated with a bad data fit. 139

Bibliography

- Agudo, O. C., da Silva, N. V., Warner, M., and Morgan, J. (2018). Acoustic full-waveform inversion in an elastic world. *Geophysics*, 0(ja):1–62.
- Aki, K., Christoffersson, A., Husebye, E., and Powell, C. (1974). Three-dimensional seismic velocity anomalies in the crust and upper-mantle under the usgs, california seismic array. *Eos Trans. AGU*, 56:1145.
- Allred, B., Daniels, J. J., and Ehsani, M. R. (2008). *Handbook of agricultural geophysics*. CRC Press.
- Babuska, V. and Cara, M. (1991). *Seismic Anisotropy in the Earth*. Boston: Kluwer Academic Publishers.
- Bai, J. and Yingst, D. (2014). Simultaneous inversion of velocity and density in time-domain full waveform inversion. In *SEG Technical Program Expanded Abstracts*, pages 922–927. SEG.
- Barnes, C. and Charara, M. (2008). Full-waveform inversion results when using acoustic approximation instead of elastic medium. *SEG Technical Program Expanded Abstracts*, 27(1):1895–1899.
- Beller, S., Monteiller, V., Operto, S., Nolet, G., Paul, A., and Zhao, L. (2018). Lithospheric architecture of the south-western alps revealed by multi-parameter teleseismic full-waveform inversion. *Geophysical Journal International*, 212(2):1369–1388.
- Ben Hadj Ali, H., Operto, S., and Virieux, J. (2011). An efficient frequency-domain full waveform inversion method using simultaneous encoded sources. *Geophysics*, 76(4):R109.
- Bharti, S., Stopin, A., Solano, C. A. P., Plessix, R.-E., Lutz, J., Al-Qadeeri, B., Dashti, Q., Narhari, S., Kolawole, O. O., et al. (2016). Application of an anisotropic elastic multiparameter waveform inversion on a land data set from north kuwait. In *2016 SEG International Exposition and Annual Meeting*. Society of Exploration Geophysicists.
- Binnig, M. (2015). Full waveform inversion of shallow seismic rayleigh waves to characterize the "ettlinger linie". Master's thesis, Karlsruhe Institute of Technology.
- Blanch, J., Robertson, J. O. A., and Symes, W. W. (1995). Modeling of a constant Q: Methodology and algorithm for an efficient and optimally inexpensive viscoelastic technique. *Geophysics*, 60:176–184.
- Bleibinhaus, F. and Hilberg, S. (2012). Shape and structure of the Salzach Valley, Austria, from seismic traveltime tomography and full waveform inversion. *Geophysical Journal International*.

BIBLIOGRAPHY

- Bohlen, T. and Saenger, E. H. (2006). Accuracy of heterogeneous staggered-grid finite-difference modeling of Rayleigh waves. *Geophysics*, 71:109–115.
- Borisov, D., Gao, F., Williamson, P., and Tromp, J. (2019). Application of 2d full-waveform inversion on exploration land data. *Geophysics*, 85(2):1–57.
- Borisov, D., Modrak, R., Gao, F., and Tromp, J. (2018). 3d elastic full-waveform inversion of surface waves in the presence of irregular topography using an envelope-based misfit function. *Geophysics*, 83(1):R1–R11.
- Boyle, J. P. and Dykstra, R. L. (1986). A method for finding projections onto the intersection of convex sets in Hilbert spaces. In Dykstra, R., Robertson, T., and Wright, F. T., editors, *Advances in Order Restricted Statistical Inference: Proceedings of the Symposium on Order Restricted Statistical Inference held in Iowa City, Iowa, September 11–13, 1985*, pages 28–47. Springer New York, New York, NY.
- Bozdağ, E., Peter, D., Lefebvre, M., Komatitsch, D., Tromp, J., Hill, J., Podhorszki, N., and Pugmire, D. (2016). Global adjoint tomography: first-generation model. *Geophysical Journal International*, 207(3):1739–1766.
- Brethaud, F., Brossier, R., Leparoux, D., Abraham, O., and Virieux, J. (2013a). 2D elastic full waveform imaging of the near surface: Application to synthetic and a physical modelling data sets. *Near Surface Geophysics*, 11:307–316.
- Brethaud, F., Brossier, R., Leparoux, D., Abraham, O., and Virieux, J. (2013b). 2D elastic full waveform imaging of the near surface: Application to synthetic and a physical modelling data sets. *Near Surface Geophysics*, 11:307–316.
- Brossier, R. and Trinh, P. T. (2017). *SEM46 Manual Version 2.1*. SEISCOPE Consortium.
- Bunks, C., Salek, F. M., Zaleski, S., and Chavent, G. (1995). Multiscale seismic waveform inversion. *Geophysics*, 60(5):1457–1473.
- Byrd, R. H., Lu, P., and Nocedal, J. (1995). A limited memory algorithm for bound constrained optimization. *SIAM Journal on Scientific and Statistical Computing*, 16:1190–1208.
- Canuto, C., Hussaini, M. Y., Quarteroni, A., and Zang, T. A. (2006). *Spectral Methods Fundamentals in Single Domains*. Springer.
- Carcione, J., Kosloff, D., and Kosloff, R. (1988). Wave propagation simulation in a linear viscoacoustic medium. *Geophysical Journal International*, 93(2):393–401.
- Cardarelli, E., Cercato, M., Cerreto, A., and Di Filippo, G. (2010). Electrical resistivity and seismic refraction tomography to detect buried cavities. *Geophysical Prospecting*, 58(4):685–695.
- Cary, P. and Chapman, C. (1988). Automatic 1-D waveform inversion of marine seismic refraction data. *Geophysical Journal of the Royal Astronomical Society*, 93:527–546.
- Castellanos, C., Métivier, L., Operto, S., Brossier, R., and Virieux, J. (2015). Fast full waveform inversion with source encoding and second-order optimization methods. *Geophysical Journal International*, 200(2):720–744.

- Cerjan, C. D., Kosloff, D., and Reshef, M. (1985). A non-reflecting boundary condition for direct acoustic and elastic wave equations. *Geophysics*, 50:705–708.
- Chapman, M., Martin, J., Olgun, C., and Beale, J. (2006). Site-response models for charleston, south carolina, and vicinity developed from shallow geotechnical investigations. *Bulletin of the Seismological Society of America*, 96(2):467–489.
- Choi, Y., Min, D., and Shin, C. (2008). Two-dimensional waveform inversion of multi-component data in acoustic-elastic coupled media. *Geophysical Prospecting*, 56(6):863–881.
- Claerbout, J. (1971). Towards a unified theory of reflector mapping. *Geophysics*, 36:467–481.
- Cruse, E., Pica, A., Noble, M., McDonald, J., and Tarantola, A. (1990). Robust elastic non-linear waveform inversion: application to real data. *Geophysics*, 55:527–538.
- de la Puente, J., Ferrer, M., Hanzich, M., Castillo, J. E., and Cela, J. M. (2014). Mimetic seismic wave modeling including topography on deformed staggered grids. *Geophysics*, 79(3):T125–T141.
- Deville, M., Fischer, P., and Mund, E. (2002). *High Order Methods for Incompressible Fluid Flow*. Cambridge University Press.
- Dewey, J. and Byerly, P. (1969). The early history of seismometry (to 1900). *Bulletin of the Seismological Society of America*, 59(1):183–227.
- Duey, R. (2017). A new breed of ocean-bottom seismic. *Hart Energy*.
- El Yadari, N., Ernst, F., and Mulder, W. (2008). Near-surface attenuation estimation using wave-propagation modeling near-surface attenuation estimation. *Geophysics*, 73(6):U27–U37.
- Emmerich, H. and Korn, M. (1987). Incorporation of attenuation into time-domain computation of seismic wavefield. *Geophysics*, 52:1252–1264.
- Etienne, V., Hu, G., Operto, S., Virieux, J., Barkved, O., and Kommedal, J. (2012). Three-dimensional acoustic full waveform inversion: algorithm and application to Valhall. In *Expanded Abstracts, 74th Annual EAGE Conference & Exhibition, Copenhagen*. EAGE.
- Everett, M. E. (2013). *Near-surface applied geophysics*. Cambridge University Press.
- Faccioli, E. F., Paolucci, R., and Quarteroni, A. (1997). 2D and 3D elastic wave propagation by a pseudo-spectral domain decomposition method. *Journal of Seismology*, 1:237–251.
- Fathi, A., Poursartip, B., Stokoe II, K. H., and Kallivokas, L. F. (2016). Three-dimensional p-and s-wave velocity profiling of geotechnical sites using full-waveform inversion driven by field data. *Soil Dynamics and Earthquake Engineering*, 87:63–81.
- Fichtner, A., Kennett, B. L. N., Igel, H., and Bunge, H. P. (2008). Theoretical background for continental- and global-scale full-waveform inversion in the time-frequency domain. *Geophysical Journal International*, 175:665–685.
- Forgues, E. and Lambaré, G. (1997). Parameterization study for acoustic and elastic ray+born inversion. *Journal of Seismic Exploration*, 6:253–278.

BIBLIOGRAPHY

- Foti, S., Sambuelli, L., Socco, V. L., and Strobbia, C. (2003). Experiments of joint acquisition of seismic refraction and surface wave data. *Near surface geophysics*, 1(3):119–129.
- French, S. W. and Romanowicz, B. A. (2014). Whole-mantle radially anisotropic shear velocity structure from spectral-element waveform tomography. *Geophysical Journal International*.
- Gao, F., Levander, A. R., Pratt, R. G., Zelt, C. A., and Fradelizio, G. L. (2006). Waveform tomography at a groundwater contamination site: Vsp-surface data set. *Geophysics*, 71(1):H1–H11.
- Gao, F., Levander, A. R., Pratt, R. G., Zelt, C. A., and Fradelizio, G. L. (2007). Waveform tomography at a groundwater contamination site: surface reflection data. *Geophysics*, 72(5):G45–G55.
- Gao, L., Pan, Y., and Bohlen, T. (2020). 2-d multiparameter viscoelastic shallow-seismic full-waveform inversion: reconstruction tests and first field-data application. *Geophysical Journal International*, 222(1):560–571.
- Gao, L., Pan, Y., Tian, G., and Xia, J. (2018). Estimating q factor from multi-mode shallow-seismic surface waves. *Pure and Applied Geophysics*, 175(8):2609–2622.
- Gardner, G. H. F., Gardner, L. W., and Gregory, A. R. (1974). Formation velocity and density—the diagnostic basics for stratigraphic traps. *Geophysics*, 39:770–780.
- Gauthier, O., Virieux, J., and Tarantola, A. (1986). Two-dimensional nonlinear inversion of seismic waveforms: numerical results. *Geophysics*, 51(7):1387–1403.
- GFZ (2020). Seismic Pool. <https://www.gfz-potsdam.de/en/section/geophysical-deep-sounding/infrastructure/geophysical-instrument-pool-potsdam-gipp/pool-components/seismic-pool/>.
- Göktürkler, G., Balkaya, Ç., and Erhan, Z. (2008). Geophysical investigation of a landslide: The altındağ landslide site, izmir (western turkey). *Journal of Applied Geophysics*, 65(2):84–96.
- Górszczyk, A., Operto, S., and Malinowski, M. (2017). Toward a robust workflow for deep crustal imaging by FWI of OBS data: The eastern nankai trough revisited. *Journal of Geophysical Research: Solid Earth*, 122(6):4601–4630.
- Ha, W. and Shin, C. (2013). Efficient laplace-domain full waveform inversion using a cyclic shot subsampling method. *Geophysics*, 78(2):R37–R46.
- Haber, E., Chung, M., and Herrmann, F. (2012). An effective method for parameter estimation with PDE constraints with Multiple Right-Hand Sides. *SIAM Journal on Optimization*, 22(3):739–757.
- Hardage, B. A., DeAngelo, M. V., Murray, P. E., and Sava, D. (2011). *Multicomponent seismic technology*. Society of Exploration Geophysicists.
- Hauksson, E. and Shearer, P. M. (2006). Attenuation models (q_p and q_s) in three dimensions of the southern california crust: Inferred fluid saturation at seismogenic depths. *Journal of Geophysical Research: Solid Earth*, 111(B5).
- Häusler, M., Schmelzbach, C., and Sollberger, D. (2018). The galperin source: A novel efficient multicomponent seismic source. *Geophysics*, 83(6):P19–P27.

- He, W., Brossier, R., Métivier, L., and Plessix, R. (2019a). Land seismic multi-parameter FWI in elastic VTI media by simultaneously interpreting body waves and surface waves. In *Expanded Abstracts, 81th Annual EAGE Conference & Exhibition, London*, page Tu R08 09. EAGE.
- He, W., Brossier, R., Métivier, L., and Plessix, R.-É. (2019b). Land seismic multi-parameter full waveform inversion in elastic VTI media by simultaneously interpreting body waves and surface waves with an optimal transport based objective function. *Geophysical Journal International*, 219(3):1970–1988.
- Hüttner, R., Konrad, H., and Zitzmann, A. (1968). Geologische übersichtskarte 1: 200000, blatt cc7110 mannheim. *Bundesanstalt für Geowissenschaften und Rohstoffe in Zusammenarbeit mit den Geologischen Landesämtern der Bundesrepublik Deutschland und benachbarter Staaten*.
- Irnaka, M., Brossier, R., and Métivier, L. (2018). 3x3c seismic's sensitivity analysis on near-surface towards full waveform inversion. In *Expanded Abstracts, EAGE-HAGI 1st Asia Pacific Meeting on Near Surface Geoscience & Engineering (Yogyakarta)*.
- Irnaka, T. M., Brossier, R., Métivier, L., Bohlen, T., and Pan, Y. (2021). 3D 9C Full Waveform Inversion for Shallow Seismic Target: Ettlingen Line Case Study. *Geophysical Journal International*.
- Jarchow, C. M. and Thompson, G. A. (1989). The nature of the mohorovicic discontinuity. *Annual Review of Earth and Planetary Sciences*, 17(1):475–506.
- Jin, S., Madariaga, R., Virieux, J., and Lambaré, G. (1991). Two dimensional asymptotic iterative elastic inversion. In *Expanded Abstracts*, volume SI5.6, pages 1013–1016. Society of Exploration Geophysics.
- Kamath, N., Brossier, R., Metivier, L., Pladys, A., and Yang, P. (2020). Multiparameter full-waveform inversion of 3D OBC data from the valhall field. *Geophysics*, in press.
- Kamath, N. and Tsvankin, I. (2013). Full-waveform inversion of multicomponent data for horizontally layered vti media for horizontally layered vti media. *Geophysics*, 78(5):WC113–WC121.
- Kjartansson, E. (1979). Constant Q-wave propagation and attenuation. *Journal of Geophysical Research*, 84(B9):4737–4748.
- Köhn, D., Meier, T., Fehr, M., De Nil, D., and Auras, M. (2016). Application of 2d elastic rayleigh waveform inversion to ultrasonic laboratory and field data. *Near Surface Geophysics*, 14(5):461–476.
- Köhn, D., Wilken, D., De Nil, D., Wunderlich, T., Rabbel, W., and Werther, L. (2018). 2d full waveform inversion applied to a strongly-dispersive love wave field dataset. In *80th EAGE Conference and Exhibition 2018*.
- Köhn, D., Wilken, D., De Nil, D., Wunderlich, T., Rabbel, W., Werther, L., Schmidt, J., Zielhofer, C., and Linzen, S. (2019). Comparison of time-domain sh waveform inversion strategies based on sequential low and bandpass filtered data for improved resolution in near-surface prospecting. *Journal of Applied Geophysics*, 160:69–83.
- Komatitsch, D. (1997). *Méthodes spectrales et éléments spectraux pour l'équation de l'élastodynamique 2D et 3D en milieu hétérogène*. PhD thesis, Institut de Géophysique du Globe de Paris.

BIBLIOGRAPHY

- Komatitsch, D., Barnes, C., and Tromp, J. (2000). Simulation of anisotropic wave propagation based upon a spectral element method. *Geophysics*, 65(4):1251–1260.
- Komatitsch, D. and Tromp, J. (1999). Introduction to the spectral element method for three-dimensional seismic wave propagation. *Geophysical Journal International*, 139(3):806–822.
- Komatitsch, D. and Vilotte, J. P. (1998). The spectral element method: an efficient tool to simulate the seismic response of 2D and 3D geological structures. *Bulletin of the Seismological Society of America*, 88:368–392.
- Kouroussis, G., Verlinden, O., and Conti, C. (2011). Finite-Dynamic Model for Infinite Media: Corrected Solution of Viscous Boundary Efficiency. *Journal of Engineering Mechanics*, 137(7):509–511.
- Kramer, S. (1996). Geotechnical earthquake engineering. prentice-hall, inc. *New Jersey*, pages 348–422.
- Krebs, J., Anderson, J., Hinkley, D., Neelamani, R., Lee, S., Baumstein, A., and Lacasse, M. D. (2009). Fast full-wavefield seismic inversion using encoded sources. *Geophysics*, 74(6):WCC105–WCC116.
- LaFehr, T. (1980). Gravity method. *Geophysics*, 45(11):1634–1639.
- Lailly, P. (1983). The seismic inverse problem as a sequence of before stack migrations. In Bednar, R. and Weglein, editors, *Conference on Inverse Scattering, Theory and application, Society for Industrial and Applied Mathematics, Philadelphia*, pages 206–220.
- Lailly, P. (1984). The seismic inverse problem as a sequence of before stack migrations. In Bednar, R. and Weglein, editors, *Conference on Inverse Scattering, SIAM, Philadelphia*, pages 206–220. Soc. Ind. appl. Math.
- Lambaré, G., Virieux, J., Madariaga, R., and Jin, S. (1992). Iterative asymptotic inversion in the acoustic approximation. *Geophysics*, 57:1138–1154.
- Lamert, A. and Friederich, W. (2019). Full waveform inversion for advance exploration of ground properties in mechanized tunneling. *International Journal of Civil Engineering*, 17(1):19–32.
- Lang, K. et al. (1907). *Die Ettlinger Linien und ihre Geschichte*. Selbstverlag der Stadt Ettlingen.
- Lay, T. and Wallace, T. C. (1995). *Modern global seismology*. Academic Press.
- Lee, W., Jennings, P., Kisslinger, C., and (eds), H. K. (2002). *International Handbook of Earthquake and Engineering Seismology*. Academic Press.
- Li, Y. and Oldenburg, D. W. (1998). 3-D inversion of gravity data. *Geophysics*, 63(1):109–119.
- Lindseth, R. O. (1979). Synthetic sonic logs—a process for stratigraphic interpretation. *Geophysics*, 44:3–26.
- Lu, Y., Stehly, L., Brossier, R., Paul, A., and ng Group, A. W. (2020). Imaging Alpine crust using ambient noise wave-equation tomography. *Geophysical Journal International*, 222(1):69–85.

- Lu, Y., Stehly, L., Paul, A., and Group, A. W. (2018). High-resolution surface wave tomography of the european crust and uppermost mantle from ambient seismic noise. *Geophysical Journal International*, 214(2):1136–1150.
- Lysmer, J. and Kuhlemeyer, R. (1969). Finite Dynamic Model for Infinite Media. *Journal of the Engineering Mechanics Division*, 95(EM4):859–877.
- Martínez, K. and Mendoza, J. A. (2011). Urban seismic site investigations for a new metro in central copenhagen: Near surface imaging using reflection, refraction and vsp methods. *Physics and Chemistry of the Earth, Parts A/B/C*, 36(16):1228–1236.
- Métivier, L. and Brossier, R. (2016). The seiscopes optimization toolbox: A large-scale nonlinear optimization library based on reverse communication. *Geophysics*, 81(2):F11–F25.
- Miller, S. L. and Stewart, R. R. (1991). The relationship between elastic-wave velocities and density in sedimentary rocks: A proposal. *Crewes Res. Rep.*, pages 260–273.
- Moczo, P. (1989). Finite-difference technique for SH waves in 2D media using irregular grids: application to the seismic response problem. *Geophysical Journal International*, 99:321–329.
- Moczo, P., Bystricky, E., Carcione, J. M., and Bouchon, M. (1997). Hybrid modeling of P-SV seismic motion at inhomogeneous viscoelastic topographic structures. *Bulletin of the Seismological Society of America*, 87:1305–1323.
- Moczo, P. and Kristek, J. (2005). On the rheological models used for time-domain methods of seismic wave propagation. *Geophysical Research Letters*, 32(1).
- Modrak, R., Borisov, D., Lefebvre, M., and Tromp, J. (2018). The seisflows framework for waveform inversion: Rapid prototyping and hpc applications. *Computers and Geosciences*, 115:88–95.
- Modrak, R. and Tromp, J. (2016). Seismic waveform inversion best practices: regional, global and exploration test cases. *Geophysical Journal International*, 206(3):1864–1889.
- Mohorovicic, A. (1909). Das beben vom 8. x. 1909. *Jb. Met. Obs. Zagreb (Agram)*, 9:1–63.
- Nabighian, M. N., Grauch, V., Hansen, R., LaFehr, T., Li, Y., Peirce, J. W., Phillips, J. D., and Ruder, M. (2005). The historical development of the magnetic method in exploration. *Geophysics*, 70(6):33ND–61ND.
- Nguyen, T. D. and Tran, K. T. (2018). Site characterization with 3d elastic full-waveform tomography. *Geophysics*, 83(5):R389–R400.
- Nocedal, J. and Wright, S. J. (2006). *Numerical Optimization*. Springer, 2nd edition.
- Nuber, A., Manukyan, E., and Maurer, H. (2017). Optimizing measurement geometry for seismic near-surface full waveform inversion. *Geophysical Journal International*, 210(3):1909–1921.
- Oldham, R. (1906). The constitution of the earth. *Quarterly Journal of the Geological Society of London*, 62:456–475.
- Operto, S., Miniussi, A., Brossier, R., Combe, L., Métivier, L., Monteiller, V., Ribodetti, A., and Virieux, J. (2015). Efficient 3-D frequency-domain mono-parameter full-waveform inversion of ocean-bottom cable data: application to Valhall in the visco-acoustic vertical transverse isotropic approximation. *Geophysical Journal International*, 202(2):1362–1391.

- Palmer, D. (1980). *The generalized reciprocal method of seismic refraction interpretation*. Society of Exploration Geophysicists.
- Pan, Y., Gao, L., and Bohlen, T. (2019). High-resolution characterization of near-surface structures by surface-wave inversions: from dispersion curve to full waveform. *Surveys in Geophysics*, 40(2):167–195.
- Pan, Y., Schaneng, S., Steinweg, T., and Bohlen, T. (2018). Estimating s-wave velocities from 3d 9-component shallow seismic data using local rayleigh-wave dispersion curves – a field study. *Journal of Applied Geophysics*, 159:532–539.
- Parasnis, D. S. (1962). *Principles of Applied Geophysics*. Chapman and Hall.
- Park, C., Miller, R., and Xia, J. (1999). Multichannel analysis of surface waves. *Geophysics*, 64:800–808.
- Pegah, E. and Liu, H. (2016). Application of near-surface seismic refraction tomography and multichannel analysis of surface waves for geotechnical site characterizations: A case study. *Engineering Geology*, 208:100–113.
- Peter, D., Komatitsch, D., Luo, Y., Martin, R., Le Goff, N., Casarotti, E., Le Loher, P., Magnoni, F., Liu, Q., Blitz, C., Nissen-Meyer, T., Basini, P., and Tromp, J. (2011). Forward and adjoint simulations of seismic wave propagation on fully unstructured hexahedral meshes. *Geophysical Journal International*, 186(2):721–739.
- Peters, B. and Herrmann, F. J. (2017). Constraints versus penalties for edge-preserving full-waveform inversion. *The Leading Edge*, 36(1):94–100.
- Petersson, N. A. and Sjögreen, B. (2015). Wave propagation in anisotropic elastic materials and curvilinear coordinates using a summation-by-parts finite difference method. *Journal of Computational Physics*, 299:820 – 841.
- Pladys, A., Brossier, R., Irnaka, M., Kamath, N., and Métivier, L. (2019). Assessment of optimal transport based fwi: 3d obc valhall case study. In *SEG Technical Program Expanded Abstracts 2019*, pages 1295–1299. Society of Exploration Geophysicists.
- Pladys, A., Brossier, R., and Métivier, L. (2020). Graph space optimal transport based FWI: 3D OBC valhall case study. In *SEG Technical Program Expanded Abstracts 2020*.
- Plessix, R. E. (2006). A review of the adjoint-state method for computing the gradient of a functional with geophysical applications. *Geophysical Journal International*, 167(2):495–503.
- Potter, C. C., Dey, A. K., and Stewart, R. R. (1998). Density prediction using P-and S-wave sonic velocities. Technical report, CREWES.
- Pratt, R. G. (1999). Seismic waveform inversion in the frequency domain, part I: theory and verification in a physical scale model. *Geophysics*, 64:888–901.
- Prieux, V., Brossier, R., Operto, S., and Virieux, J. (2013a). Multiparameter full waveform inversion of multicomponent OBC data from Valhall. Part 1: imaging compressional wavespeed, density and attenuation. *Geophysical Journal International*, 194(3):1640–1664.

- Prieux, V., Brossier, R., Operto, S., and Virieux, J. (2013b). Multiparameter full waveform inversion of multicomponent OBC data from valhall. Part 2: imaging compressional and shear-wave velocities. *Geophysical Journal International*, 194(3):1665–1681.
- Przebindowska, A., Kurzmann, A., Köhn, D., and Bohlen, T. (2012). The role of density in acoustic full waveform inversion of marine reflection seismics. In *74th EAGE Conference and Exhibition incorporating EUROPEC 2012*.
- Rao, Y. and Wang, Y. (2017). Seismic waveform tomography with shot-encoding using a restarted l-bfgs algorithm. *Scientific Reports*, 7.
- Reford, M. (1980). Magnetic method. *Geophysics*, 45(11):1640–1658.
- Roberts, J. C. and Asten, M. W. (2004). Resolving a velocity inversion at the geotechnical scale using the microtremor (passive seismic) survey method. *Exploration geophysics*, 35(1):14–18.
- Robertsson, J., Moore, I., Vassallo, M., Özdemir, K., van Manen, D. J., and Özbek, A. (2008). On the use of multicomponent streamer recordings for reconstruction of pressure wavefields in the crossline direction. *Geophysics*, 73(5):A45–A49.
- Robertsson, J. O. A. (1996). A numerical free-surface condition for elastic/viscoelastic finite-difference modeling in the presence of topography. *Geophysics*, 61:1921–1934.
- Romanowicz, B. and Dziewonski, A. (2010). *Seismology and Structure of the Earth: Treatise on Geophysics*, volume 1. Elsevier.
- Romdhane, A., Grandjean, G., Brossier, R., Réjiba, F., Operto, S., and Virieux, J. (2011). Shallow structures characterization by 2d elastic waveform inversion. *Geophysics*, 76(3):R81.
- Romero, L. A., Ghiglia, D. C., Ober, C. C., and Morton, S. A. (2000). Phase encoding of shot records in prestack migration. *Geophysics*, 65, (2):426–436.
- Samyn, K., Travelletti, J., Bitri, A., Grandjean, G., and Malet, J.-P. (2012). Characterization of a landslide geometry using 3d seismic refraction travelttime tomography: The la valette landslide case history. *Journal of Applied Geophysics*, 86:120–132.
- Schmelzbach, C., Sollberger, D., Greenhalgh, S., Horstmeyer, H., Maurer, H., and Robertsson, J. (2016). 9C seismic data acquisition for near-surface applications: recording, waveform reciprocity and 4C rotation. In *78th EAGE Conference and Exhibition 2016-Workshops*.
- Schuster, G. T., Wang, X., Huang, Y., Dai, W., and C., B. (2011). Theory of multisource crosstalk reduction by phase encoded statics. *Geophysical Journal International*, 184:1289–303.
- Sears, T., Singh, S., and Barton, P. (2008). Elastic full waveform inversion of multi-component OBC seismic data. *Geophysical Prospecting*, 56(6):843–862.
- Sears, T. J., Barton, P. J., and Singh, S. C. (2010). Elastic full waveform inversion of multicomponent ocean-bottom cable seismic data: Application to alba field, u. k. north sea. *Geophysics*, 75(6):R109–R119.
- Signanini, P. and Torrese, P. (2004). Application of high resolution shear-wave seismic methods to a geotechnical problem. *Bulletin of Engineering Geology and the Environment*, 63(4):329–336.

BIBLIOGRAPHY

- Sirgue, L., Barkved, O. I., Dellinger, J., Etgen, J., Albertin, U., and Kommedal, J. H. (2010). Full waveform inversion: the next leap forward in imaging at Valhall. *First Break*, 28:65–70.
- Smith, J. A., Borisov, D., Cudney, H., Miller, R. D., Modrak, R., Moran, M., Peterie, S. L., Sloan, S. D., Tromp, J., and Wang, Y. (2019). Tunnel detection at yuma proving ground, arizona, usa—part 2: 3d full-waveform inversion experimentstunnel detection at ypg—part 2: 3d fwi. *Geophysics*, 84(1):B95–B108.
- Smithyman, B., Pratt, R. G., Hayles, J., and Wittebolle, R. (2009). Detecting near-surface objects with seismic waveform tomography. *Geophysics*, 74(6):WCC119–WCC127.
- Stein, S. and Wysession, M. (2003). *An Introduction to Seismology, Earthquakes and Earth Structure*. Blackwell Publishing.
- Stewart, I., Williams, J., and Walker, C. (1997). Seismic refraction in relation to geotechnical information for (road) construction contracts. *Geological Society, London, Engineering Geology Special Publications*, 12(1):383–390.
- Stokoe, K. H., Santamarina, J. C., et al. (2000). Seismic-wave-based testing in geotechnical engineering. In *ISRM International Symposium*. International Society for Rock Mechanics and Rock Engineering.
- Tape, C., Liu, Q., Maggi, A., and Tromp, J. (2010). Seismic tomography of the southern California crust based on spectral-element and adjoint methods. *Geophysical Journal International*, 180:433–462.
- Tape, C. H. (2009). *Seismic tomography of southern California using adjoint methods*. PhD thesis, California Institute of Technology.
- Tarantola, A. (1984a). Inversion of seismic reflection data in the acoustic approximation. *Geophysics*, 49(8):1259–1266.
- Tarantola, A. (1984b). Linearized inversion of seismic reflection data. *Geophysical Prospecting*, 32:998–1015.
- Tawil, M., Socco, L. V., and Anjom, F. K. (2019). Surface wave tomography applied to oil and gas data.
- Telford, W. M., Geldart, L. P., and Sheriff, R. E. (1990). *Applied Geophysics - Second Edition*. Cambridge University Press.
- Trinh, P., Brossier, R., Lemaistre, L., Métivier, L., and Virieux, J. (2019a). 3d elastic fwi with a non-linear model constraint: Application to a real complex onshore dataset. In *Expanded Abstracts, 81th Annual EAGE Conference & Exhibition, London*, page Th P01 07. EAGE.
- Trinh, P. T. (2018). *3D Multi-parameters Full Waveform Inversion for challenging land targets*. PhD thesis, University Grenoble Alpes.
- Trinh, P. T., Brossier, R., Métivier, L., Tavard, L., and Virieux, J. (2018). Data-windowing hierarchy in multi-parameter elastic fwi: 3d synthetic foothills case study. In *Expanded Abstracts, 80th Annual EAGE Meeting (Copenhagen)*.
- Trinh, P. T., Brossier, R., Métivier, L., Tavard, L., and Virieux, J. (2019b). Efficient 3D time-domain elastic and viscoelastic Full Waveform Inversion using a spectral-element method on flexible Cartesian-based mesh. *Geophysics*, 84(1):R75–R97.

- Trinh, P. T., Brossier, R., Métivier, L., Virieux, J., and Wellington, P. (2017). Bessel smoothing filter for spectral element mesh. *Geophysical Journal International*, 209(3):1489–1512.
- Tromp, J., Tape, C., and Liu, Q. (2005). Seismic tomography, adjoint methods, time reversal and banana-doughnut kernels. *Geophysical Journal International*, 160:195–216.
- Vafidis, A., Manakou, M., Kritikakis, G., Voganatsis, D., Sarris, A., and Kalpaxis, T. (2003). Mapping the ancient port at the archaeological site of itanos (greece) using shallow seismic methods. *Archaeological Prospection*, 10(3):163–173.
- van Driel, M. and Nissen-Meyer, T. (2014). Optimized viscoelastic wave propagation for weakly dissipative media. *Geophysical Journal International*, 199(2):1078–1093.
- Vigh, D., Jiao, K., Watts, D., and Sun, D. (2014). Elastic full-waveform inversion application using multicomponent measurements of seismic data collection. *Geophysics*, 79(2):R63–R77.
- Virieux, J. and Operto, S. (2009). An overview of full waveform inversion in exploration geophysics. *Geophysics*, 74(6):WCC1–WCC26.
- Wang, Y., Miller, R. D., Peterie, S. L., Sloan, S. D., Moran, M. L., Cudney, H. H., Smith, J. A., Borisov, D., Modrak, R., and Tromp, J. (2019). Tunnel detection at yuma proving ground, arizona, usa—part 1: 2d full-waveform inversion experiment. *Geophysics*, 84(1):B95–B105.
- Warner, M., Ratcliffe, A., Nangoo, T., Morgan, J., Umpleby, A., Shah, N., Vinje, V., Stekl, I., Guasch, L., Win, C., Conroy, G., and Bertrand, A. (2013). Anisotropic 3D full-waveform inversion. *Geophysics*, 78(2):R59–R80.
- Wegscheider, S. (2017). Abbildung der ettlinger linie auf dem segelflugplatz rheinstetten mittels georadar. Master’s thesis, Karlsruhe Institute of Technology.
- Weil, M. H., DeJong, J. T., Martinez, B. C., and Mortensen, B. M. (2012). Seismic and resistivity measurements for real-time monitoring of microbially induced calcite precipitation in sand. *Geotechnical Testing Journal*, 35(2):330–341.
- Wikipedia contributors (2020a). Hydrophone — Wikipedia, the free encyclopedia. <https://en.wikipedia.org/w/index.php?title=Hydrophone&oldid=982558209>. [Online; accessed 14-October-2020].
- Wikipedia contributors (2020b). Zhang heng — Wikipedia, the free encyclopedia. https://en.wikipedia.org/w/index.php?title=Zhang_Heng&oldid=978105050. [Online; accessed 17-September-2020].
- Wittkamp, F., Athanasopoulos, N., and Bohlen, T. (2018). Individual and joint 2-d elastic full-waveform inversion of rayleigh and love waves. *Geophysical Journal International*, 216(1):350–364.
- Wolfe, P. (1969). Convergence conditions for ascent methods. *SIAM Review*, 11.
- Wu, R. S. and Toksöz, M. N. (1987). Diffraction tomography and multisource holography applied to seismic imaging. *Geophysics*, 52:11–25.
- Wynn, J. C. (1986). A review of geophysical methods used in archaeology. *Geoarchaeology*, 1(3):245–257.

BIBLIOGRAPHY

- Xia, J., Xu, Y., Miller, R. D., and Ivanov, J. (2012). Estimation of near-surface quality factors by constrained inversion of rayleigh-wave attenuation coefficients. *Journal of Applied Geophysics*, 82:137–144.
- Yang, P., Brossier, R., Métivier, L., and Virieux, J. (2016). A review on the systematic formulation of 3D multiparameter full waveform inversion in viscoelastic medium. *Geophysical Journal International*, 207(1):129–149.
- Zhang, W. and Chen, X. (2006). Traction image method for irregular free surface boundaries in finite difference seismic wave simulation. *Geophysical Journal International*, 167(1):337–353.

